Development of anion exchange membranes for aqueous organic redox and zinc slurry-air flow batteries

Misgina Tilahun Tsehaye

▶ To cite this version:

Misgina Tilahun Tsehaye. Development of anion exchange membranes for aqueous organic redox and zinc slurry-air flow batteries. Chemical and Process Engineering. Université Grenoble Alpes [2020-..], 2021. English. NNT : 2021GRALI046 . tel-03292028

HAL Id: tel-03292028

https://theses.hal.science/tel-03292028

Submitted on 20 Jul 2021

THÈSE

Pour obtenir le grade de

DOCTEUR DE L'UNIVERSITE GRENOBLE ALPES

Spécialité : **Matériaux, Mécanique, Génie civil, Electrochimie**

Arrêté ministériel : 25 mai 2016

Présentée par

Misgina Tilahun TSEHAYE

Thèse dirigée par **Fannie ALLOIN**, Directrice de recherche, CNRS
et codirigée par **Cristina IOJOIU**, Directrice de recherche, CNRS

Préparée au sein du **Laboratoire d'Electrochimie et de Physicochimie des Matériaux et des Interfaces.**
dans **École doctorale Ingénierie -Matériaux, Mécanique, Environnement, Energétique, Procédés, Production (I-MEP2).**

Membranes échangeuses d'anions pour technologies de batteries à flux : batterie redox-organique et Zinc-Air

Thèse soutenue publiquement le **12 Avril 2021**
devant le jury composé de :

Monsieur Lionel FLANDIN
Professeur, Université Savoie Mont Blanc, Président
Monsieur Emmanuel BAUDRIN
Professeur, UFR de Pharmacie – UPJV, Rapporteur
Madame Odile FICHET
Professeur, Université Cergy Pontoise, Rapporteur
Monsieur Mathieu ETIENNE
Directeur de recherche, CNRS, Examinateur
Monsieur Steven LE VOT
Maitre de Conférences, Université Montpellier, Examinateur
Madame Fannie ALLOIN
Directeur de recherche, CNRS, Directrice de thèse
Madame Cristina IOJOIU
Directeur de recherche, CNRS, Co-Directrice de thèse

DISSERTATION

To obtain the degree of

DOCTOR FROM GRENOBLE ALPES UNIVERSITY

Speciality: **Materials, Mechanics, Civil Engineering, Electrochemistry**

Ministerial decree: 25 may 2016

Presented by

Misgina Tilahun TSEHAYE

Thesis supervised by **Fannie ALLOIN**, research director, CNRS
and co-supervised by **Cristina IOJOIU**, research director, CNRS

Prepared at **Laboratory of Electrochemistry and Physical Chemistry of Materials and Interfaces (LEPMI).**

Doctoral School of Engineering – Materials, Mechanics, Environment, Energy, Procedures, Production (I-MEP2)

Development of Anion Exchange Membranes for Aqueous Organic Redox and Zinc Slurry-Air Flow Batteries

Dissertation defended publicly on **April 12, 2021**,
in front of the jury comprising of:

Mr. Lionel FLANDIN
Professor, Savoie Mont Blanc University, President
Mr. Emmanuel BAUDRIN
Professor, UPJV - UFR OF PHARMACY, Reviewer
Ms. Odile FICHET
Professor, University of Cergy-Pontoise, Reviewer
Mr. Mathieu ETIENNE
Research director, CNRS, Examiner
Mr. Steven LE VOT
Lecturer, University of Montpellier, Examiner
Ms. Fannie ALLOIN
Research director, CNRS, Thesis director
Ms. Cristina IOJOIU
Research director, CNRS, Thesis co-director

Abbreviations

AEM	Anion exchange membrane
AFM	Atomic force microscopy
AORFBs	Aqueous organic redox flow batteries
AIBN	2,2′-Azobis(2-methylpropionitrile)
CE	Coulombic efficiency
CEM	Cation exchange membrane
CV	Cyclic voltammetry
DABCO	1,4-diazabicyclo[2.2. 2]octane
DAPCl	Diallylpiperidinium chloride
DMAC	Dimethylacetamide
DMSO	Dimethyl sulfoxide
DSC	Differential scanning calorimetry
EE	Energy efficiency
EIS	Electrochemical impedance spectroscopy
FTIR	Fourier-transform infrared spectroscopy
IEC	Ion exchange capacity
MV	Methyl viologen
NBS	*N*-Bromosuccinimide
NMP	*N*-Methyl-2-pyrrolidone
NMR	Nuclear magnetic resonance
PBI	Polybenzimidazole
PP	Polypropylene
PPO	Poly(2,6-dimethyl-1,4-phenylene oxide)
QA	Quaternary ammonium
RFB	Redox flow battery
SEM	Scanning electron microscopy
TGA	Thermogravimetric analysis
THF	Tetrahydrofuran
TMA	Trimethylamine
TMA-TEMPO	*N*,*N*,*N*-2,2,6,6-heptamethylpiperi-dinyl oxy-4-ammonium chloride
VE	Voltage efficiency
WU	Water uptake

Abstract

Redox flow batteries, in particular, aqueous organic redox flow batteries (AORFBs) and zinc (Zn) slurry-air flow batteries are considered to be very attractive candidates for large-scale electricity storage due to their safety and environmental friendliness, economic feasibility and high storage capacity. In these batteries, the membrane allows the transport of ions between the catholyte and the anolyte while providing a physical barrier between the two compartments in order to prevent electrical short circuits. The performance, lifespan and cost of these batteries are greatly affected by the physicochemical properties and type of the employed membrane. However, a critical discussion of the state-of-the-art studies on membranes showed that the research and development of appropriate membranes for these batteries has received insufficient attention.

In this PhD thesis, aiming at first understanding the correlations between the membranes properties and cell performances, commercial porous and prepared anion exchange membranes were *ex-situ* characterized and tested in the Zn slurry-air flow battery and AORFB, respectively. This was followed by various membrane synthesis and modification strategies to prepare membranes with reduced active species crossover and improved battery performances. The results in this work not only contribute to the basic understanding of the relationship between membrane properties and RFBs performances but also greatly contribute to the future market of the RFBs with low cost and high performance.

Keywords: Anion exchange membranes, Aqueous organic redox flow battery, Zinc slurry-air flow battery, Structure-property relation, Battery test

Résumé

Les batteries à flux redox, en particulier, les batteries à flux redox aqueux organiques (AORFB) et les batteries Zn-air sont considérées comme des candidats très intéressants pour le stockage d'électricité à grande échelle en raison de leur sécurité élevée, de leur impact environnemental faible, de leur faisabilité économique et de leur forte capacité de stockage. Dans ces batteries, la membrane permet le transport des ions entre l'anolyte et le catholyte tout en assurant une barrière physique entre les deux compartiments afin d'éviter les courts-circuits électriques. Les performances, la durée de vie et le coût de ces batteries sont fortement affectés par les propriétés physico-chimiques des membranes employées. Cependant, l'étude de l'état de l'art montre que la recherche et le développement de membranes spécifiques pour ces batteries ne sont encore pas assez importants.

Dans ce manuscrit, visant à mettre en évidence les corrélations entre les propriétés des membranes et les performances en systèmes, des membranes denses échangeuses d'anions et des membranes poreuses commerciales modifiées par un ionomère ont été préparées, caractérisées et testées dans les batteries AORFB et Zn-air. Cette étude a été menée sur différentes familles de membranes, obtenues par diverses stratégies de synthèse ou de modifications de membranes poreuses, afin d'obtenir des membranes à forte conductivité et faiblement perméables aux espèces actives et ainsi améliorer les performances en batterie. Les résultats de ces travaux contribuent non seulement à avancer dans la compréhension de la relation entre les propriétés de la membrane et les performances des RFB, mais également au développement futur des RFB à faible coût et hautes performances.

Mots clés : Membranes échangeuses d'anions, batteries à flux redox, batterie à flux redox organique aqueux, batterie Zn-air, relation structure-propriété, tests en batteries à flux redox

Acknowledgment

First of all, I would like to express my gratitude to my family for their unconditional support and constant encouragement.

I would like to express my sincere appreciation and gratitude to my thesis supervisors, Dr. Cristina IOJOJU and Dr. Fannie ALLOIN for their invaluable guidance and support throughout my thesis work. Dr. Cristina was highly involved in this thesis work starting from its inception till the end. You are one of the very few supervisors with an open door policy and available to students almost all the time. I have learned a lot about polymer synthesis and characterization from your deep understanding and experience. I have to appreciate the contribution made by Dr. Fannie ALLOIN especially on the electrochemistry part. The critical questions raised at certain stages were important for improving the quality of the thesis. Equally important are the fruitful comments you gave me after reading my manuscripts and reports with a dedication which were very helpful and an important input to the success of my thesis work.

My special thanks go to my friends and colleagues at LEPMI, including Sajad RAHIMI, Ngoc Anh TRAN, Adriana CAPOZZI, Caterina SANSONE, Régis PORHIEL, Ibrahim SHALAYEL, Huu Dat NGUYEN, Thi Khanh Ly Nguyen, Hoang Phuong Khanh Ngo, Yunfan SHAO, Getachew TEKLAY, Faiz AHMED, Tanguy PICARD, Justine SOLIER, Gregoire VANSSE, Delphine YETIM, Rakesh Khatokar Amarnath, Roselyne Jeanne-Brou, James ISAAC, Philippe DUMAZ and Nicolas Magne-tang. It has been great to work with all of you at the lab during my three years stay.

I should acknowledge the coordinators of FlowCamp for making this challenging and amazing project a reality. I would like to extend my appreciation to my FlowCamp mentors, including Dr. Tobias JANOSCHKA, Dr. Mateusz DONTEN and Dr. Peter FISCHER. The discussions we had at the “meet the mentor” sessions were helpful for me to discuss my results and question I had and plan my works accordingly. In addition, I would like to thank Dr. Tobias JANOSCHKA and Dr. Mateusz DONTEN for allowing me do a secondment at their respective companies.

I would also like to say thank you to all the Flowcamp early-stage researchers (ESRs), especially to those who were working on the aqueous organic redox and Zn slurry-air flow batteries (Diego Josué Milián Izeppi, Ricardo P. M. Duarte, Diego del Olmo and Gael Mourouga). I would like to express my heartfelt appreciation to Xian YANG and Nak Heon Choi who I was working in close collaboration.

I should also mention Ms. Laure Cointeaux (NMR), Mr. Vincent MARTIN (AAS), Mr. Nicolas SERGENT (FTIR), Mr. Fabien VOLPI (AFM), Ms. Francine ROUSSEL (SEM) and Professor Jean Claude LEPRETRE (FTIR) for helping me with different sample analyses.

Last but not least, I'd like to express my gratitude to Professor Emmanuel BAUDRIN, Professor Odile FICHET, Dr. Mathieu ETIENNE, and Dr. Steven LE VOT, members of my PhD thesis committee, for their willingness to serve on the committee and for their comments and suggestions that helped improve the PhD thesis report.

Misgina Tilahun TSEHAYE

Table of Content

Chapter 1: Scope of the thesis work and co-authorship statement

Renewable energy storages, mainly solar and wind, generate intermittent electrical power depending on the time (day/night) and climatic factors [1]. One strategy to address the intermittency is by coupling them with an appropriate energy storage device. Among them, redox-flow batteries (RFBs) are promising electrochemical energy storage systems since they exhibit high efficiency, room temperature operation, long charge/discharge cycles and independent energy/power sizing [2].

The thesis work took place from April 2018 to April 2021 under research and training project, FlowCamp, funded by the European Union's Marie Skłodowska-Curie programme, in which three different RFBs (Zn slurry-air RFB, aqueous organic RFB (AORFB) and H_2/Br RFB) which meet different demands of the market were being developed and optimized. Zn slurry-air flow battery presents high-potential energy storages because of its high energy capacity, environmental friendliness and economic viability. Whereas, the organic and H_2/Br_2 RFBs are known for their environmental friendliness (since it uses organic redox species in aqueous electrolytes) and high power densities, respectively.

FlowCamp involves 15 PhD students and 11 partner organizations from 8 different countries. In this project, five PhD students work on the different components, including membrane, redox-active species (electrolyte), cell design, modelling, electrode and sealing of one of the batteries. My PhD thesis focuses on the design, synthesis and characterization of anion exchange membranes for aqueous organic redox and zinc slurry-air flow batteries. Anion exchange membranes are an important part of these batteries since they conduct charge-carrier ion and prevent mixing of redox-active species. Therefore, the lifespan, performance and stability of these batteries are influenced by the membranes used. However, despite the importance of the membranes, they remain to be less investigated. Membranes that were designed for other applications are commonly used in these batteries.

The thesis is divided into two parts. Membrane development and characterization for the AORFBs are presented first (part I). Whereas, the next section is focused on the synthesis of membranes for Zn slurry-air flow batteries. In both systems, first a detailed state-of-the-art studies on membranes for AORFB and Zn-air batteries are summarized and critically discussed. The membranes developed are *ex-situ* characterized in terms of ionic conductivity, selectivity and stability and are then tested in the AORFB (in collaboration with JenaBatteries GmbH, Germany) and Zn slurry-air flow battery (in collaboration with Fraunhofer ICT, Germany). In this thesis, in both battery systems, the main effort has been given to understanding and investigating the correlations between membrane properties and RFBs performance. This was followed by various membrane synthesis strategies and optimization to prepare RFBs with improved cell performance.

Chapters and co-authorship statement:

Chapter 2: **State-of-the-art membranes for neutral aqueous organic redox flow batteries**. The first two pages of the introduction are taken from our mini-review paper “Prospects for Anion-Exchange Membranes in Alkali Metal–Air Batteries” published in *Energies* [3] by Misgina Tilahun TSEHAYE, Fannie ALLOIN and Cristina IOJOIU. The other part is intended to be submitted for publication with a title of recent progress on membranes for aqueous organic redox flow battery.

Chapter 3: Study of Anion exchange membrane properties incorporating *N*-spirocyclic quaternary ammonium cation and aqueous organic redox flow battery performance. The polymer, monomer and membrane preparation and *ex-situ* characterization were done by Misgina Tilahun TSEHAYE. Battery testing was performed at JenaBatteries (Jena, Germany) by Xian YANG, who also wrote the cell test and characterization part of the manuscript. Misgina Tilahun TSEHAYE wrote the remaining parts of the manuscript, involved in the interpretation of the battery performance and compiled the work. This manuscript has been published in Membranes [4].

Chapter 4: **Anion exchange membranes with high power density and energy efficiency in neutral aqueous organic redox flow battery**. Similar to the work in chapter 3, the membrane design, preparation and *ex-situ* characterization was done at LEPMI (CNRS, France) by Misgina Tilahun TSEHAYE. Battery testing was done at JenaBatteries (Jena, Germany) by Xian YANG, who also wrote the cell test and characterization part of the manuscript. Misgina Tilahun TSEHAYE wrote the other remaining parts of the manuscript, involved in the interpretation of the battery performance and compiled the work. This manuscript is currently being written and will be submitted for publication.

Chapter 5: **Membranes for zinc-air batteries: Recent progress, challenges and perspectives.** This work is adapted from our review paper published in the Journal of Power Sources [5]. The manuscript was written by Misgina Tilahun TSEHAYE. All co-authors have contributed to the work by editing the manuscript.

Chapter 6: **Porous and modified porous membranes for Zinc slurry-air flow battery**. Misgina Tilahun TSEHAYE performed the polymer synthesis, membrane preparation and ex-situ characterizations, while the battery testing was performed at Fraunhofer ICT (Karlsruhe, Germany) by Nak Heon Choi. Misgina Tilahun TSEHAYE interpreted all of the data and wrote the complete manuscript. This manuscript has been published in Molecules [6].

Chapter 7: **Anion exchange membranes based on poly(phenylene oxide) with a spacer incorporating N-Spirocyclic quaternary ammonium cation via UV irradiation for zinc slurry-air flow batteries**. Misgina Tilahun TSEHAYE performed the polymer, monomer and membrane synthesis and ex-situ characterization, while the battery test was performed at Fraunhofer ICT (Karlsruhe, Germany) by Nak Heon Choi. Misgina Tilahun TSEHAYE interpreted all of the data and wrote the complete manuscript. This manuscript is currently being written and will be submitted for publication in Journal of Membrane Science.

Chapter 8: **Conclusion and perspectives.**

Funding: This project has received funding from the European Union's Horizon 2020 research and innovation programme under the Marie Skłodowska-Curie Grant Agreement no. 765289.

References

[1] K. Engeland, M. Borga, J.-D. Creutin, B. François, M.-H. Ramos, J.-P. Vidal, Space-time variability of climate variables and intermittent renewable electricity production – A review, Renew. Sustain. Energy Rev. 79 (2017) 600–617. https://doi.org/10.1016/j.rser.2017.05.046.

[2] P. Alotto, M. Guarnieri, F. Moro, Redox flow batteries for the storage of renewable energy: A review, Renew. Sustain. Energy Rev. 29 (2014) 325–335. https://doi.org/10.1016/j.rser.2013.08.001.

[3] M.T. Tsehaye, F. Alloin, C. Iojoiu, Prospects for Anion-Exchange Membranes in Alkali Metal–Air Batteries, Energies. 12 (2019) 4702. https://doi.org/10.3390/en12244702.

[4] M. Tsehaye, X. Yang, T. Janoschka, M. Hager, U. Schubert, F. Alloin, C. Iojoiu, Study of Anion Exchange Membrane Properties Incorporating N-spirocyclic Quaternary Ammonium Cations and Aqueous Organic Redox Flow Battery Performance, Membranes (Basel). 11 (2021) 367. https://doi.org/10.3390/membranes11050367.

[5] M.T. Tsehaye, F. Alloin, C. Iojoiu, R.A. Tufa, D. Aili, P. Fischer, S. Velizarov, Membranes for zinc-air batteries: Recent progress, challenges and perspectives, J. Power Sources. 475 (2020) 228689. https://doi.org/10.1016/j.jpowsour.2020.228689.

[6] M.T. Tsehaye, G. Teklay Gebreslassie, N. Heon Choi, D. Milian, V. Martin, P. Fischer, J. Tübke, N. El Kissi, M.L. Donten, F. Alloin, C. Iojoiu, Pristine and Modified Porous Membranes for Zinc Slurry–Air Flow Battery, Molecules. 26 (2021) 4062. https://doi.org/10.3390/molecules26134062.

Part-I: Membranes for Aqueous Organic Redox Flow Batteries

Chapter 2: State-of-the-art membranes for neutral aqueous organic redox flow batteries

1. Introduction

1.1. Role of energy storage in renewable energy

The gradual depletion of fossil fuels and environmental concerns associated with their use have been challenging the energy sector. Thus, vast development and deployment of sustainable renewable energy sources, such as solar and wind are required [1]. Wind and solar are the world's fastest-growing energy sources [2]. Despite their economic feasibility and environmental friendliness, their intermittent nature and geographical limitations are the major challenges for their full employment as next-generation energy sources. To counteract their fluctuating energy outputs and, thus improving the stability of the electrical grid, efficient and stable electrical energy storage is needed [3–5].

Over the years, various electrical energy storages have been identified and used. Currently, lithium (Li)-ion and lead (Pb)-acid batteries are the leading employed energy storage technologies. Li-ion battery is playing an important role in our daily lives as it is the most commercialized system and commonly used battery in electric vehicles and electronics today. Unfortunately, its high cost per kWh and recent concern over its safety have restricted its application, thus calling for the development of new storage technology for next-generation [3,6,7]. The thermal runaway of the cell which leads to the whole battery pack failure is believed to be caused by mechanical, electrical, or thermal abuses [8]. Moreover, its energy density is only about 100-200 Wh Kg^{-1}, which cannot achieve the requirements of large stationary applications, especially for long-term utilization [9]. Similarly, Pb-acid batteries are well-established electrochemical energy storage for stationary applications [10]. However, they have a low energy density (30-50 Wh kg^{-1}), low cycling life (500-1000 cycles) and are dependent on toxic Pb [11,12]. Therefore, new energy storage technologies, which are safe and high energy density systems are desired. Figure 1 shows the chemistries and principal components of Pb-acid and Li-ion batteries.

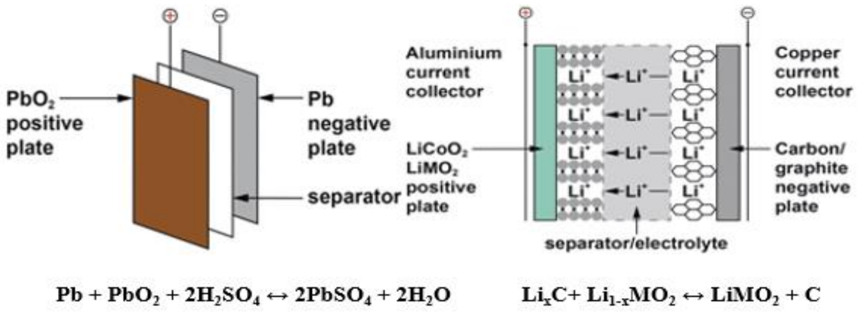

Figure 1: Chemistries and principal components of Pb-acid (left) and Li-ion (right) batteries [10].

Several other electrochemical energy storage candidates, including metal-air batteries and redox-flow batteries (RFBs), such as vanadium and organic RFBs have been developed. Metal-air batteries are promising and competitive high-energy alternatives to Li-ion batteries [13]. Metal-air batteries are high energy density electrochemical cells that use air at the cathode and metal as the anode with aqueous electrolyte [14]. Therefore, they can be applicable in a wide range of energy transfer stations and energy storage device applications, including automotive and larger passenger vehicles and a large station for stationary application. However, despite their promising capacities, they have not fulfilled their full potentials due to several challenges in their anode, air cathode and membrane components [15].

1.2. Redox flow batteries

Another promising electrochemical energy storage devices replacement to Li-ion and Pb-acid technologies are RFBs, in particular aqueous organic RFBs, which are one of the batteries investigated in this thesis work. A short introduction to the basic working principles, components, main parameters and classification of the systems are introduced in this section. Flow batteries store energy using redox-active species via electrochemical reactions [16]. RFBs are an attractive choice for large-scale energy storage alternatives because of their ability to separate power and energy, and operate at ambient temperature and pressure [17–21]. In such batteries, the redox-active molecules, which are dissolved in liquid supporting electrolytes, are used on the anode (called anolyte) and cathode (called catholyte) compartments during the discharge.

Generally speaking, the performance of RFBs can be expressed by their energy density, power density, energy efficiency and cycling stability. These parameters are affected by several factors, mainly by the design of the battery, active materials and membrane employed, to mention a few. The equations used to determine these parameters are summarized in Table 1. The theoretical energy density which indicates the amount of charge stored depends on mainly three parameters: (i) cell voltage (redox potential difference between the catholyte and anolyte), (ii) solubility of the redox-active species and (iii) number of electrons involved in the oxidation-reduction reactions, which governs the functioning of RFBs.

Table 1: Main parameters in RFBs.

Parameters	Unit	Equation	Terms
Cell voltage (E_{cell})	Volt (V)	$E_{cell} = E_{positive} – E_{negative}$	$E_{positive}$ and $E_{negative}$ are the potential at the positive and negative electrodes, respectively.
Volumetric capacity (C)	Ah L^{-1}	$C = \frac{m\ x\ n\ x\ F}{M\ x\ V}$	m = mass (g), n = number of electrons, F = Faraday’s constant (Unit conversion: A·h = 3600 C), M = molar mass, V = volume. E = energy density, U = E_{cell} - RI.
Theoretical energy density (E)	Wh L^{-1}	$E = C\ x\ U$	
Coulombic efficiency (CE)	%	$CE = \frac{t_d}{t_c}\ x\ 100\%$	t_d is the discharging time, and t_c is the charging time.
Voltage efficiency (VE)	%	$VE = \frac{U_d}{U_c}\ x\ 100\%$	U_d = average discharging voltage and U_c = average charging voltage when the same current was used for charging and discharging.
Energy efficiency (EE)	%	$EE = CE\ x\ VE$	
Current density	mA cm^{-2}	$J = \frac{I}{A}$	I = discharge current, U = output potential and A = active surface area of the membrane.
Power density	mW cm^{-2}	Power density = J x U	

The power density of the battery depends on several parameters, including the voltage, internal resistance of cell (resistance of the electrolyte, electrodes and connectors), kinetics of the redox reactions and operation factors, including temperature, flow rate and flow field used [22]. The cycling stability, on the other hand, depends on the (electro)chemical stability and degree of crossover of redox species.

Until recently, the electroactive materials used in aqueous RFBs have been limited to transition metal redox couples, such as Vanadium RFB (VRFB) (stores energy by employing vanadium redox couples: V^{2+}/V^{3+} in the negative and V^{4+}/V^{5+} in the positive half-cells) (electrochemical reactions are shown in Table 2), which is one of the most commonly used RFB systems [23–25]. In VRFBs, VO_2 +/VO^{2+} and V^{2+}/V^{3+} are used as catholyte and anolyte active species, respectively. These are separated by a membrane. Figure 2 presents the redox reaction during the charge and discharge processes in VRFB.

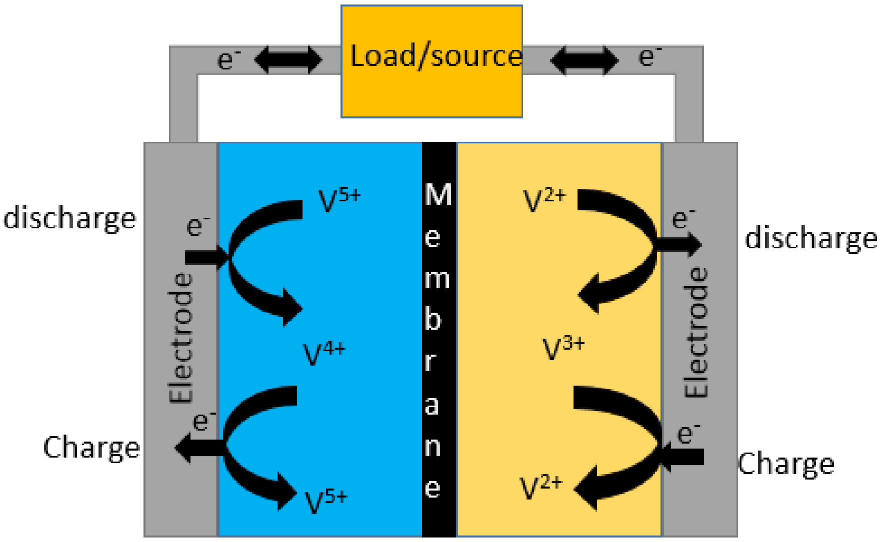

Figure 2: VRFB reaction during the charge and discharge processes [26].

Table 2: Electrochemical reaction in vanadium redox battery.

Reaction in the catholyte side	$VO_2^+ + 2H^+ + e^- \leftrightarrow VO^{2+} + H_2O$
Reaction in the anolyte side	$V^{2+} \leftrightarrow V^{3+} + e^-$
Cell reaction	$V^{2+} + VO_2^+ + 2H^+ \leftrightarrow VO^{2+} + V^{3+} + H_2O$

In the conventional aqueous RFBs, there are limited active materials choices and they are mostly expensive. The widespread adoption of the VRFB system has been limited due to the high cost of vanadium [27] and limited energy density of the system (about 20-60 Wh L^{-1}) due to the low solubility of vanadium ion in the electrolyte (2.0 - 3.0 M) [28–30]. Thus, cheap and large-scale energy storage is highly needed.

1.3. Aqueous organic redox flow batteries

The idea of replacing the corrosive molecules used in the other RFBs with new environmentally benign aqueous soluble redox couples, which exhibit fast electrochemical reaction kinetics, has received increasing research interest in recent years [31,32]. Redox-active organic molecules in the application of RFBs have been identified as promising energy storage devices because of their diverse molecular moieties, high structural tenability, a wide range of redox potentials, material abundance and low material cost [29,33,34]. In the past few years, various organic materials-based chemistries have been developed. As shown in Figure 3, organic RFBs (ORFBs) can be classified as aqueous ORFBs (AORFBs), non-aqueous ORFBs (NAORFBs), and hybrid aqueous/non-aqueous ORFBs (HORFBs) based on the solvent used in the electrolyte [22]. Furthermore, depending on the pH of the electrolyte, AORFBs can be classified into acidic, basic and neutral. Compared to NAORFBs, the AORFBs provide relatively low-cost electrolyte, high ionic conductivity and fast kinetics [35,36].

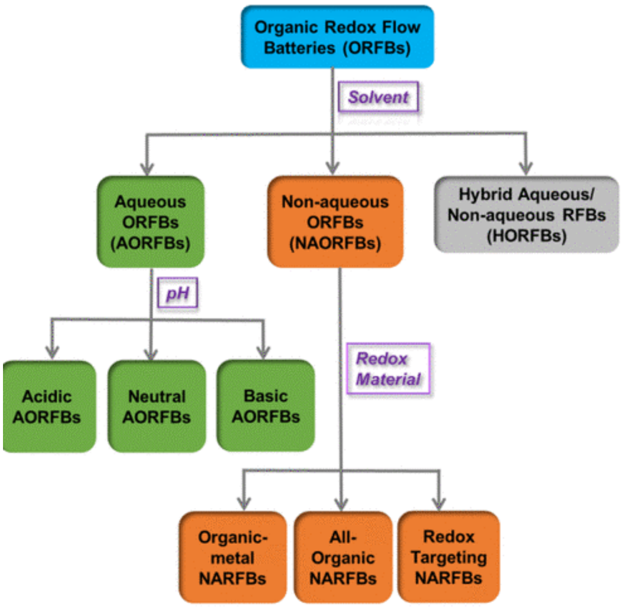

Figure 3: Classification of organic redox flow batteries (ORFBs) [22].

1.3.1. Redox-active species in AORFBs

A typical AORFB consists of redox-active materials, membrane and electrode (Figure 4). Various catholyte and anolyte active species, including the well-known active species, such as quinone, anthraquinone, viologen, TEMPO, ferrocene and alloxazine ferrocene have been studied and reported in the literature. A number of molecular designing strategies of the organic redox-active materials have been employed in order to increase their solubility, cell voltage, stability, chemical reversibility, cyclability and performance at a high charge rate (C-rate) [34,37]. This renders to enhance the power and energy density of AORFBs and this technology becomes a promising electrochemical energy storage devices [38]. The addition of electron-withdrawing groups (for e.g., SO_3^-) and electron-donating groups (for e.g., OH^-) has been reported to shift the potential to forward (positive) and backward (negative) directions, respectively. Whereas, ammonium groups have been shown to increase both the solubility and electrochemical reaction kinetics [31]. For instance, the tuning of redox potential and solubility of quinone via substitution of the side groups has been explored with density functional theory [39,40]. A good review of the redox-active materials in AORFBs can be found in the literature [29,31,34,41].

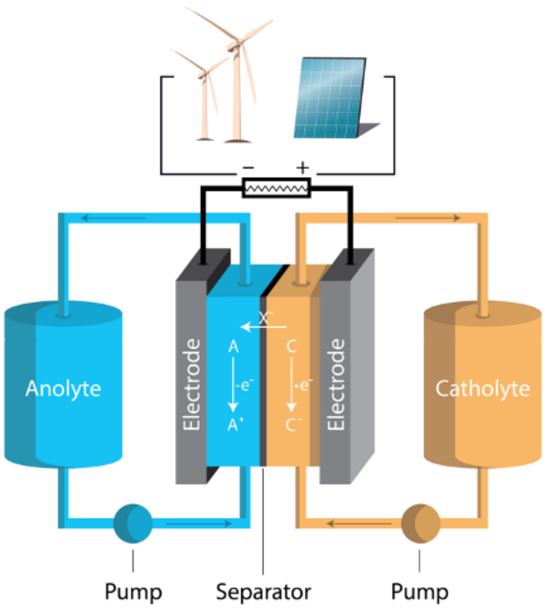

Figure 4: A schematic diagram of AORFBs [42].

One of the promising active anolyte molecules for AORFBs are viologen because of their low cost, high solubility in water, fast electrochemical kinetics and stability at neutral conditions [43–45]. Various viologen derivative employing AORFBs, including 1.2 V methyl viologen (MV, anolyte)/ 4-hydroxy-2,2,6,6-tetramethylpiperidin-1-oxyl (4-HO-TEMPO, catholyte) [43], *N*,*N*′-dimethyl-4,4-bipyridinium dichloride (MV)/ N,N,N-2,2,6,6-heptamethylpiperidinyl oxy-4-ammonium chloride (TEMPTMA) [4] have been reported in the literature. The former MV/4-HO-TEMPO based AORFB with a cell voltage of 1.25 V was reported to cycle for 100 cycles with coulombic efficiency of about 100% and operate at high current densities (20 to 100 mA cm^{-2}). Due to the good solubility of both active materials, the TEMPTMA/MV battery has been reported to deliver high energy density (38 Wh L^{-1} at 1.4 V of cell voltage) [4]. With peak current density of up to 200 mA cm^{-2}, it was reported to be a promising candidate for high-power applications.

1.3.2. Membranes for AORFBs

The membrane in AORFBs is used for the conduction of charge-carrying ions and prevention of cross-contamination of redox-active chemicals and short-circuit. The membranes should exhibit high chemical and electrochemical stabilities in the medium used, especially in the case of alkaline and acidic media. The membrane used depends on the type of medium, charge carrier ions and redox couples. Generally speaking, due to the higher conductivities (migrations) of H^+ or OH^- than that of K^+, Na^+ or Cl^-, the operating current density used (which is closely related to the membrane used) in acidic or basic media based AORFBs is higher than that of neutral AORFBs [46]. Thus, the former AORFBs could deliver higher power densities than the later ones. Moreover, cell potential and solubility of the redox couple depends on the pH of the media. On the other hand, compared to the alkaline and acidic AORFBs, the non-corrosive nature of neutral AORFBs is less aggressive for most membranes, thus the membrane could have a longer lifespan and cyclic stability. The key requirements and characteristics of the membranes used in neutral AORFBs are discussed in section 2. A summary of recent advances in membranes for neutral AORFBs is discussed in section 3. Strategies for overcoming the remaining issues are also highlighted. Lastly, a conclusion and perspective for understanding membrane-cell relations and developing membranes for high-performance AORFB systems are provided in section 4. Moreover, thesis works planned to fill the research gaps in this topic are outlined.

2. Requirements and characteristics of membranes used in AORFBs

The main properties of membranes that affect the battery performance and life span will be discussed in this section. These parameters include ion conductivity, redox-active species crossover, chemical and mechanical stabilities. Additionally, the cost of the membrane is discussed since it affects the overall cost of the battery. In each subsection, strategies for optimizing those key properties are forwarded.

2.1. Membrane resistance (ionic conductivity)

Since the main function of the membrane is ion conduction, a membrane with high ion conductivity or low resistance is needed for enhancing the power density and voltage efficiency of the battery. In general, membrane resistance depends on its thickness and ion exchange capacity (IEC). IEC (in meq g^{-1}) is the amount of ion-exchange groups in a gram of dry membrane. Membranes with low thickness and high IEC deliver low membrane resistance [29]. Therefore, the most straightforward method to increase the ionic conductivity of a given membrane is to increase its IEC. IEC of a membrane is determined by titration of counter ion or by spectra analysis i.e. nuclear magnetic resonance (NMR).

In a recent study, five commercial AEMs (Neosepta® AFX, Neosepta® AHA, Selemion® AMV, Selemion® ASV, and Selemion® DSV) with different IEC and thickness were tested in AORFB containing N, N'-dimethyl- 4,4'-bipyridinium dichloride (MV) as the redox-active species in the anolyte, and 4-hydroxy-2,2,6,6-tetramethylpiperidine 1-oxyl (TEMPO) as the active species in the catholyte [47]. These membranes were designed for acid recovery applications. As shown in Table 3, the Selemion® DSV exhibited the lowest area resistance since it has the lowest thickness and one of the highest IEC among the investigated membranes. Whereas, the membrane with the lowest IEC and highest thickness, Neosepta® AHA exhibited the highest area resistance (4.8 Ω cm^2).

Table 3: Selemion® and Neosepta® AEMs properties and area resistance.

Company	Membrane	Thickness (μm)	IEC (meq g^{-1})	Area resistance (Ω cm^2)* [47]
Asahi, Japan	Selemion® DSV	93	2.0	1.16
	Selemion® AMV	104	1.9	2.27
	Selemion® ASV	110	2.1	4.76
Astom, Japan	Neosepta® AFX	137	1.3	1.24
	Neosepta® AHA	190	1.1	4.81

*The ionic resistances of the membranes were determined using electrochemical impedance spectroscopy in a Swagelok-style cell following immersing them in 1.5 M NaCl for one week.

Voltage efficiencies (VE) of the batteries containing the different membranes are shown in Figure 5. Figure 5a and b show the VE of the membranes as a function of cycle number and area resistance of the membranes, respectively. The VE of the batteries was found to depend on the cell resistances and their associated ohmic losses, a linear correlation between VE and the area resistance was reported. As expected, DSV and AFX, membranes with the lowest area resistances displayed the highest VE (about 75%) among the tested membranes after 100 cycles. Whereas AHA and ASV, membranes with high cell resistances exhibited the lowest VE. Moreover, DSV and AFX produced RFBs with coulombic efficiencies of above 98%, while the other batteries yielded slightly lower.

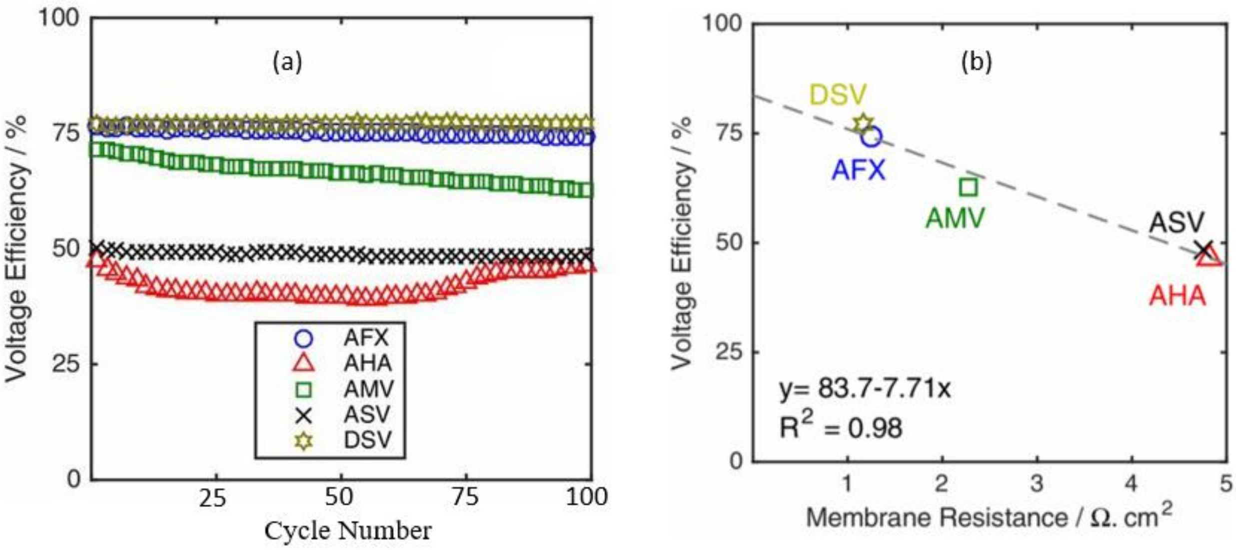

Figure 5: Voltage efficiency for 100 cycles (a) and 100th cycle vs. membrane area-specific resistance (b) [47].

A similar impact of cell resistance on voltage and energy efficiency of AORFB employing FcNCl (ferrocenylmethyl)trimethylammonium chloride and MV has been reported by Hu et al.,[48]. In this study, DSV, AMV and ASV-based cell displayed area resistance (in 2 M NaCl) of 1.13, 2.8 and 4.86 Ω cm^2, respectively, which is similar to the previously discussed finding [47]. Slightly lower cell resistance was found when KCl is used as an electrolyte. The thinnest DSV membrane (which exhibited the lowest cell resistance among the tested membranes) exhibited the best battery performance, energy efficiency and power density (discussed in section 3). For example, at 60 mA cm^{-2}, the Selemion® DSV-employing cell exhibited higher energy efficiency (76%) than that of AMV-based (60%) and ASV-based (44%) cells.

Moreover, four commercial AEMs from Fumatech (Germany), namely the FAA-3-PE30®, FAP-PK-3130®, FAS-30® and FAA-3® have been tested in an AORFB employing 0.5 M MV and TEMPO-based polymers with 1.5 M $NaCl_{aq.}$ as electrolytes [49]. The membranes were intended for desalination application. The FAA-3-50® membrane exhibited the lowest area resistance of 1.67 Ω cm^2. This is in agreement with the high IEC of the membrane compared to the others (Table 4). Due to its lowest electric cell resistance, the FAA-3-50® AEM delivered the best cell performance (see section 3 for detailed battery performance). Table 4 summarizes the properties and area resistance of the membranes.

Table 4: Fumatech AEMs properties and area resistance in an AORFB [49].

Company	Membrane	Thickness (µm)	IEC (mmol g^{-1})	Area resistance (Ω cm$^{2)}$
Fumatech, Germany	Fumasep® FAA-3-PE30	20 - 30	1.4 - 1.6	9.62
	Fumasep® FAP-PK-130	110 - 140	1.1 - 1.4	7.77
	Fumasep® FAS-30	25 - 35	0.3 - 0.6	3.32
	Fumasep® FAA-3-50	45 – 55	1.6 - 2.1	1.67

*All information other than the in-situ area resistance were taken from the manufacturer technical data sheet.

2.2. Redox-active species crossover

In asymmetric RFBs, cross-contamination of redox-active species causes capacity fade. In addition to the permeation of active material through the membrane, capacity fade can also be caused by chemical decomposition of the active organic species and electrolyte leakage. The chemical degradation mechanism and lifetime of electrolytes in AORFBs, with the main focus on capacity fade, has been discussed elsewhere [50]. In this review work, the authors classified capacity fade rates in AORFs into extremely low (≤0.02%/day), low (0.02–0.1%/day), moderate (0.1–1%/day) and high (>1%/day) groups depending on the percentage of capacity fade per day. Active organic molecules decomposition which results in loss of redox activity could take place through various mechanisms, including nucleophilic addition/substitution, disproportionation to redox-inactive center, dimerization/polymerization and tautomerization, depending on nature, the structure of the reactant and the pH of the electrolyte used (Scheme 1).

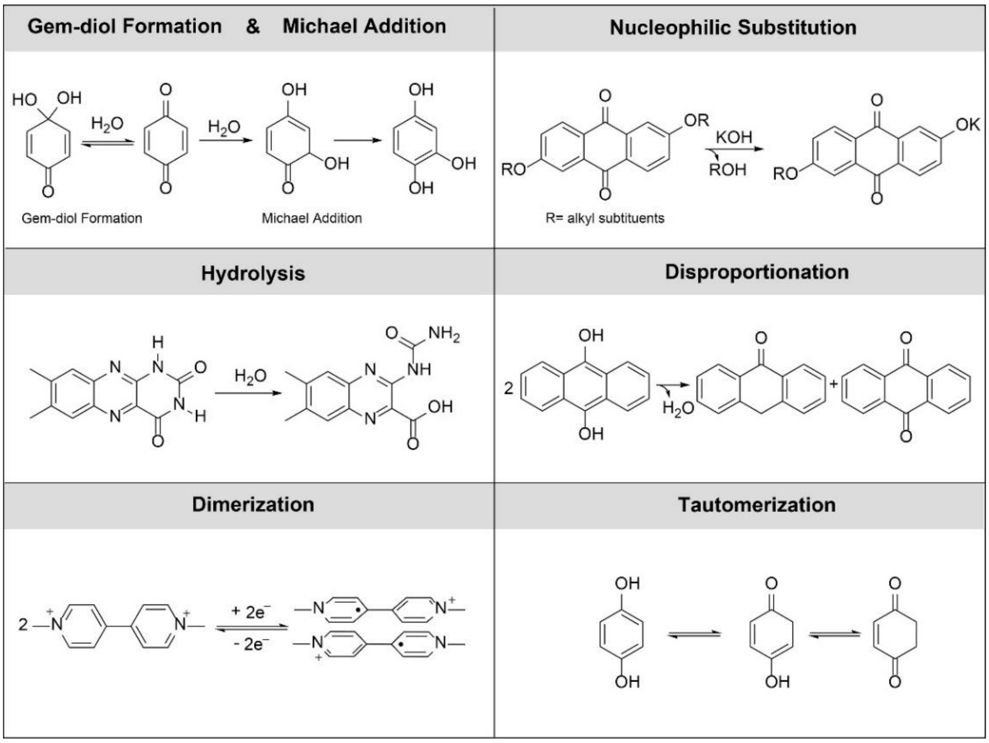

Scheme 1: Common chemical decomposition mechanisms for redox-active molecules [50].

The permeation/crossover of active species through a membrane is another main cause of capacity fade [51]. This can be caused by the physical crossover of the species due to the high permeability of membrane to those species and/or due to the membrane aging and/or pinholes within manufacturing defects. A diffusion cell composed of two cells, separated by a membrane, is usually used to study the permeability of the active species through the membranes, level of *ex-situ* membrane permeability. Voltammetric or UV-Vis analysis of the active species is usually used to determine the concentration crossing through the membrane. However, there is no standardized protocol on the concentration which should be used to balance the ionic strength of the solutions at the receiving and donating sides. Different protocols (type, volume and concentration of species on the receiving and donating compartments) have been used in the literature [47,52,53]. This calls for a standardized protocol to be used by researchers so that the reported results can be compared.

The permeability P of the redox active species (cm^2 s^{-1}) can be calculated from Fick's law [54]:

$$P = \frac{\ln(1 - \frac{2C_r}{C_o})(-\frac{Vl}{2A})}{t}$$

Where C_r and C_o are the concentration (M) at the receiving and donating side, respectively. A and l are the effective area (cm^2) and membrane thickness (cm), respectively. V (mL) is the initial volume of the receiving side and t (s) is the sampling time.

For instance, the permeabilities of bis(3-trimethylammonio)propyl viologen tetrachloride (BTMAP-Vi), bis((3-trimethylammonio)propyl)ferrocene dichloride (BTMAP-FC) and MV through Selemion® DSV membrane were reported to be 6.7×10^{-10} cm^2 s^{-1}, 6.2×10^{-10} cm^2 s^{-1} and 3.4×10^{-9} cm^2 s^{-1}, respectively. Slightly higher permeability value (9.5×10^{-10} cm^2 s^{-1}) were reported for BTMAP-Vi through a prepared PPO-based AEM in another study [53]. Whereas the permeability of TMAP-TEMPO electrolytes through the same membrane was found to be 3.4×10^{-9} cm^2 s^{-1}, thus more than 5 times higher. The capacity retention was reported to be 90.4%. The high diffusion process was suggested to be due to the swelling of the membranes and the small size of the TMAP-TEMPO species (crossover process accounted for 56% of the capacity fade). In a different study, Liu et al., [43] reported a water–based MV/4HO-TEMPO flow battery with an AEM (120 µm thickness, pore size <10 Å, Selemion) displayed a high apparent capacity fade (~28%/day), which is recoverable. However, no chemical analysis was performed on the cycled electrolytes. Moreover, the specific Selemion membrane used was not mentioned.

To better understand the impact of crossover on the capacity retention of a cycling battery, based on the permeability values and assuming the same set of conditions, Beh et al., [52] used the following equation to predict the time (year) for 50% capacity loss ($\tau_{50\%}$):

$$\tau_{50\%} = \frac{i_c \, \mathrm{l} \, t_d \; ln(\frac{1}{0.5})}{P \, C \, n \, F}$$

where P is permeability, i_c is the cycling current density (mA/cm^2), l is the membrane thickness, td is the discharge time (h). And C is the concentration of electroactive species (M), n is the number of electrons per mole of redox-active species (e^-) and F is Faraday's constant. For instance, based on the permeability reported above [52], it would take 2.1, 10.8 and 11.6 years, respectively, for the crossover of MV, BTMAP-Vi and BTMAP-Fc through the Selemion® DSV membrane used and cause a 50% loss in cell capacity.

The capacity retentions of TEMPO/MV-based AORFBs employing five different commercial AEMs (Neosepta® AFX and Neosepta® AHA, and Selemion® AMV, Selemion® ASV and Selemion® DSV) after 100 cycles at 50 mA/cm^2 were reported [47]. The capacity fade was mainly attributed to the crossover of the redox-active species through the membranes. The crossovers of TEMPO and MV through the membranes were dominated by the different transport mechanisms, including pressure-driven flow, diffusion, migration, or electroosmotic drag. Membranes with higher IEC (and water uptake) displayed lower fluxes of electroosmotic drag as the cation might repel redox-active species with the same charge. For example, Neosepta® AHA, the worst-performing membrane because of its lowest IEC and water uptake, displayed the lowest diffusion coefficients and highest electroosmotic drag for the redox-active species. This shows the need for preparing a membrane with optimized IEC and water uptake. However, there was a difference between the maximum crossover of redox-active species determined theoretically and experimentally especially in the case of the Selemion® DSV membrane (Figure 6). As the membrane chemistry and structure are not known, it is difficult to predict the crossover merely from the membrane properties.

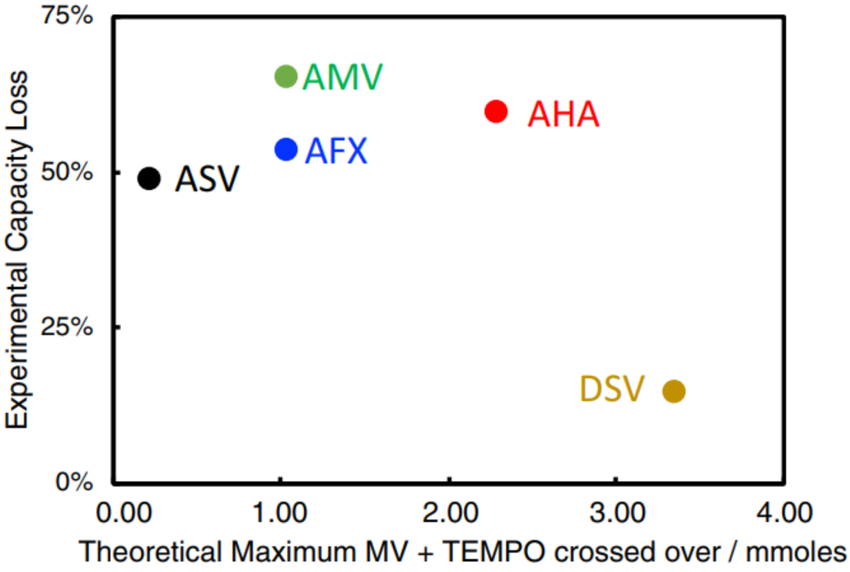

Figure 6: Experimental capacity losses *vs* theoretical number of moles crossed over [47].

2.3. Chemical and electrochemical stability

The chemical stability of a membrane in the given electrolyte and condition can be studied by comparing the performance and structure of the membrane before and after immersing the membrane in the prepared solution for a certain period of time. Microscopic and mechanical properties comparison can be done to investigate and study possible morphological and mechanical degradation of the membrane. Another way is to compare the membranes IEC and conductivity before and after the immersion.

However, in this system, usually a non-corrosive electrolyte (neutral medium) is used. Therefore, the chemical stability of commonly used AEMs, which are prepared for aggressive acidic and basic environments are expected to work well. Nevertheless, long term investigation of electrolyte-membrane interaction should be studied for a possible reactivity between certain active groups. There are various mechanisms in which a reaction between the electrolyte/redox-active species and the membrane could take place. One possible way is the oxidation of secondary and tertiary amines groups present in the membrane by the nitrox radicals as shown in Figure 7 [55].

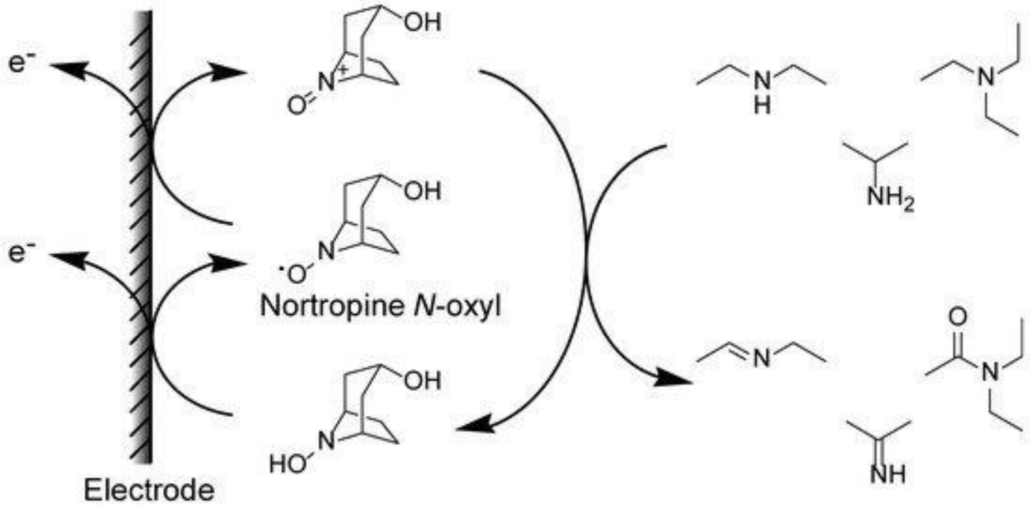

Figure 7: Electrochemical reactions of nortropine *N*-oxyl with different amines [55].

An intense visual discoloration of Nafion® (NR212) membrane after cycling in an AORFB based on dihydroxyphenazine sulfonic acid (DHPS) was reported in the literature [56]. This was suggested to be due to a possible reactivity of DHPS with the Nafion® or crossover of the species through the membrane inducing a capacity fade. As a result, an increase in the membrane resistance after cycling was reported.

2.4. Mechanical strength

A membrane with high mechanical strength is necessary for a continuous safe operation of the battery. The polymeric membrane mechanical properties depend on its tensile strength, elastic modulus and ductility [57]. During cell assembly, the membranes must be mechanically robust to withstand the winding process tension and stacking stress. Besides, during a flow battery, depending on the flow rate and type of active redox species, the electrolyte will continuously contact the membrane.

However, as discussed previously thickness of a membrane, in addition to its IEC determines the membrane/cell resistance. Usually, the internal electrical resistance of a thin membrane is low, however too low thickness might have a negative effect on the mechanical strength of the membrane. On the other hand, thicker membranes have good mechanical properties with better battery safety. However, very thick membranes normally induce high internal resistance. Therefore, an optimum membrane thickness (usually between 20 and 50 μm) is needed for long rechargeable batteries operation [58]. In addition to thickness, IEC and polymer backbone (molecular weight and type) of the membrane affect its mechanical property.

2.5. Membrane cost

To realize a wide deployment of renewable energy with a convenient energy storage system, it is necessary that the cost of the energy source and storage technology together are comparable or lower than the other energy sources, such as fossil fuels. Thus, it is important to produce a feasible AORFB at a low cost. Usually, the capital cost of electricity storage is expressed in terms of capital cost per kWh (\$/kW) [37]. In addition to installation material costs, maintenance is also important. The European Strategic Energy Technology Plan (SET Plan) aims to develop cheap and high durability (10,000 cycles and 20 years lifetime) (stationary) energy storage by 2030 [59].

In order to achieve this goal, low–cost membranes are required. Nowadays, polymer electrolyte-based state-of-the-art ion-exchange membranes (typically, Nafion®) accounts for about 30-40% of the VRFBs stack [60,61]. Generally speaking, the final cost of a membrane is determined by both the raw materials used and synthesis procedures. Low cost and sustainable raw materials and processes should therefore be used.

AEMs usually used in AORFBs, such as Fumatech® FAA-3-50, Selemion® DSV and Selemion® AMV are sold at \$17.00 for a 10 cm × 10 cm [62] and 392 \$/m^2 [63], respectively. Thus, the use of Fumatech® membrane would reduce the cost of the membrane by about 30-70% compared to using Nafion® [49]. Another possible option is the use of porous membranes, which is only 5%-10% of Nafion®'s cost [45].

3. Recent progress in membranes for neutral AORFBs

The membrane-type used in AORFB depends on various factors, such as the chemistry/pH, nature and molecular size of the redox-active species/electrolytes, charge carrier ion, availability and cost of the membrane. Although the catholyte and anolyte could be conceptually separated by a porous membrane, the smaller sized organic species can pass through the larger pores of the membrane. Various membrane types including cation-exchange membranes (CEM), AEMs, porous membranes, composite membranes and inorganic membranes have been tested in AORFBs. Usually, AEMs are composed of an anionic conducting polymer i.e. a polymer backbone onto which cationic groups are covalently bound. This makes the membrane capable of selectively allowing the passage of anions while blocking the passage of cations.

The previous Tables 3 and 4 summarize a list of the available commercial AEMs that are commonly used in neutral AORFBs, showing the limited availability of such membranes. Almost all of them were developed for other applications, such as desalination. Moreover, only limited research works on the synthesis of membranes for AORFBs have been reported. The performance of AORFBs employing the different membranes is summarized in Table 5. The table contains reported battery performance in terms of energy efficiency, coulombic efficiency voltage efficiency, peak power density and cycle numbers. In this part, the commercial membranes are first reported. The results and improvement obtained by using lab-made membranes are presented at last.

In 2015, Janoschka [45] used a cellulose-based porous dialysis membrane with a molecular weight cut-off (MWCO) of 6000 g mol^{-1} in a polymerized viologen/nitroxide radical-based AORFB (Figure 8 a and b). NaCl (aq.) was employed as a supporting electrolyte. The cell displayed a capacity fade rate of 0.75% per day. This moderate capacity fade rate was due to the fact that the polymerized actives redox species used had molecular masses of three times higher than that of the MWCO of the porous membrane. The cells were reported to be able to charge and discharge at a current density up to 40 mA cm^{-2} with an energy efficiency of 75-80%. Figure 8 c and d show the capacity retention of the polymer-based RFB as a function of current density and cycle number.

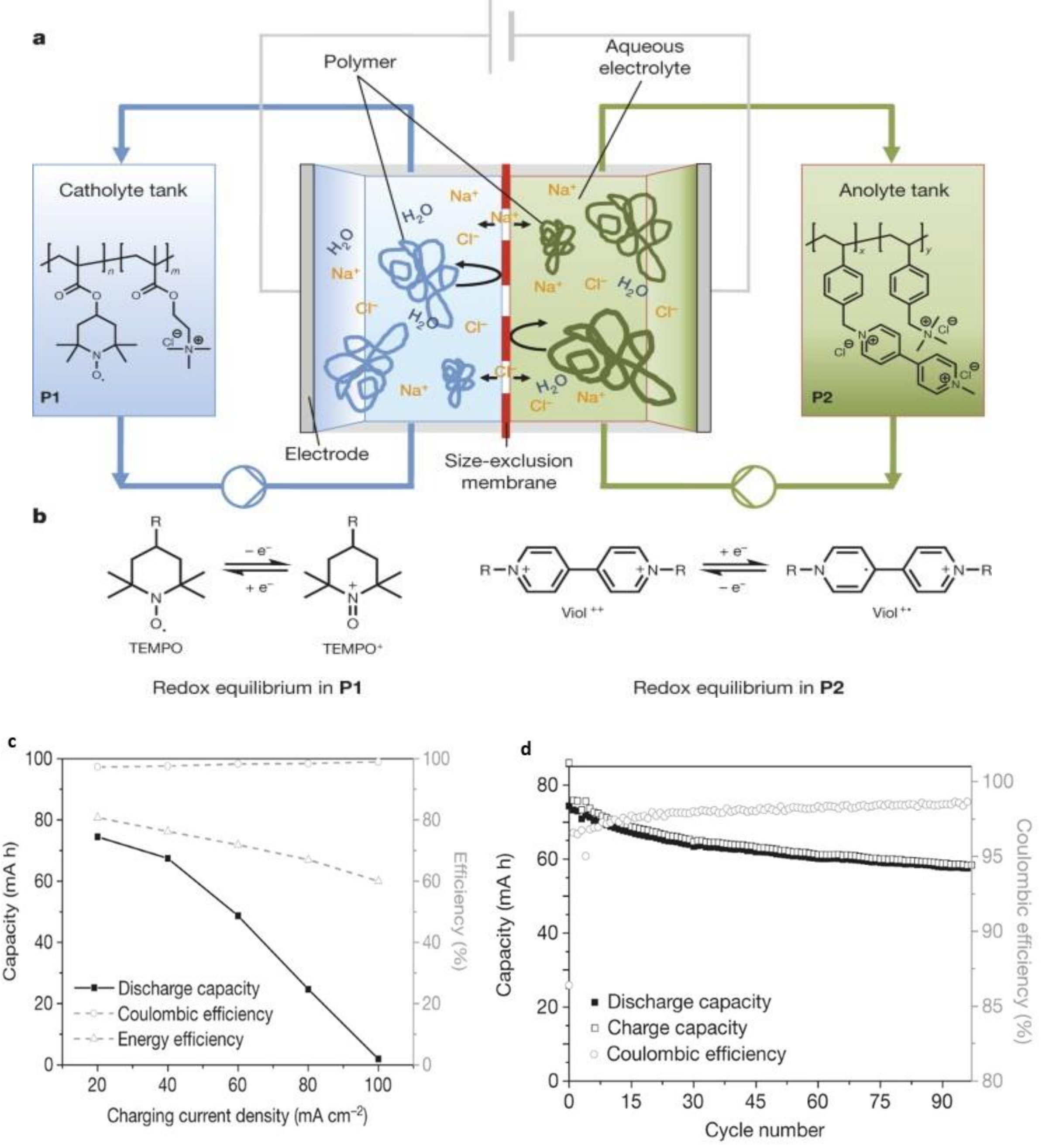

Figure 8: (a) schematic representation of the AORFB, (b) electrode reactions, and capacity as a function of (c) charging current density and (d) cycle number [45].

Similarly, as discussed in section 2.1, Hagemann et al.,[49] tested four Fumatech AEMs (FAA-3-PE30®, FAP-PK-3130®, FAS-30® and FAA-3-50®) in a neutral cell where TEMPO containing polymer poly(2,2,6,6-tetramethylpiperidinyloxy-4-yl methacrylate-*co*-[2-(methacryloyloxy)ethyl]trimethyl ammonium chloride) and a low-molar-mass compound (MV, 0.5 M) were used as a catholyte and anolyte redox-active materials, respectively, in an aqueous NaCl solution. It was cycled in a voltage window of 0.80-1.35 V. Figure 9 shows the capacity retention, voltage, coulombic and energy efficiencies as a function of current density used (between 1 and 16 mA cm^{-2}) for the four membranes. Due to their low electric cell resistance (see Table 4), the cells employing FAA-3-50® and FAS-30® membranes displayed better overall battery performance than the other two systems. In particular, as shown in Figure 9 c and d, the cells employing the former membranes delivered excellent coulombic (up to 97%) and energy efficiencies (80-87% at above 1 mA cm^{-2}). Furthermore, combined with optimized flow rate and salt concentration, the FAA-3-50®-based battery exhibited an energy efficiency of 85% and coulombic efficiency up to 95% after 100 cycles at a low current density of 5 mA cm^{-2}. Due to the increase in the potential gap between the charging and discharging plateaus associated with the polarization phenomenon, the voltage efficiency decreases linearly with increasing of current density whereas the coulombic efficiency increased in a parabolic pattern in four of the cell test. On the other hand, the charging capacities of all cell tests were reported to decrease with increasing current densities.

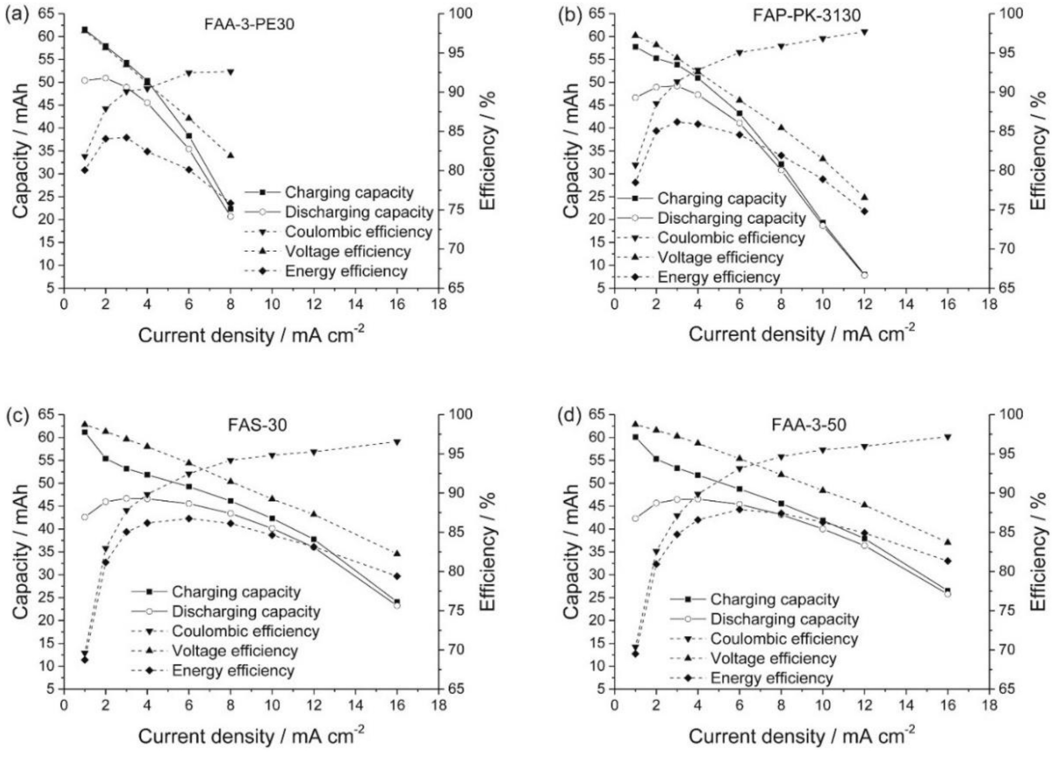

Figure 9: Battery performance of an AORFB employing (a) Fumasep® FAA-3-PE30, (b) Fumasep® FAP-PK-3130, (c) Fumasep® FAS-30 and (d) Fumasep® FAA-3-50 AEM [49].

Moreover, three commercial Selemion® DSV, AMV and ASV AEMs (NaCl/KCl as supporting electrolytes) were tested in a neutral FcNCl/MV-based AORFB, where FcNCl is (ferrocenylmethyl)trimethylammonium chloride [48]. The properties of the membranes are given in Table 3. The Selemion® DSV AEM based cell exhibited better overall performance, energy efficiency of 79% at 60 mA cm^{-2} and power density of 123 mW cm^{-2}. The battery performance, in terms of capacity, voltage, energy efficiencies and power density as a function of cycle number or current density is summarized in Figure 10. The thinnest Selemion® DSV membrane (which exhibited the lowest cell resistance among the tested membranes) exhibited the best battery performance, capacity utilization, energy efficiency and power density. For example, at 60 mA cm^{-2}, the Selemion® DSV-employing cell exhibited higher energy efficiency (76%) than that of Selemion® AMV-based (60%) and Selemion® ASV-based (44%) cells. As shown in Figure 10d, the Selemion® DSV/NaCl-employing cell delivered the highest peak power density of 113 mW cm^{-2} at about 200 mA cm^{-2}, whereas the same cell employing AMV exhibited a much lower peak power density (66 mW cm^{-2} at 114 mA cm^{-2}).

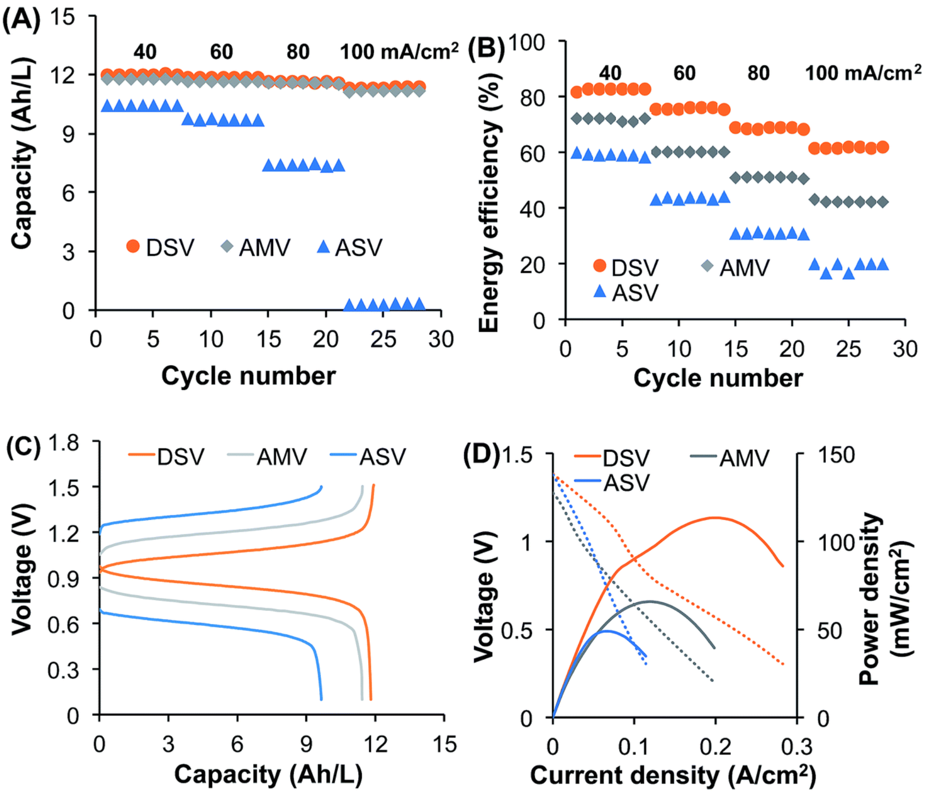

Figure 10: FcNCl/MV AORFBs with three commercial AEMs: (a) capacity *vs* cycle number, (b) energy efficiency *vs* cycle number, (c) Voltage profile *vs.* capacity at 60 mA cm^{-2} and (d) polarization and peak power density curves [48].

Furthermore, in addition to these commercial membranes, a cheap (\$9/m^2) AEM based on poly(phenylene) oxide) (PPO) and trimethylamine (TMA) was prepared and tested in a pH-neutral TMAP-TEMPO and BTMAP-Vi based AORFB. The cell exhibited an energy efficiency of 81% at a current density of 40 mA cm^{-2} with coulombic efficiency of ~100% for 800 consecutive cycles. Moreover, the cell delivered 95 mW cm^{-2} at about 100% state of charge [53].

The performance of AORFBs employing different membranes is summarized in Table 5. The table contains reported battery performance in terms of energy efficiency, coulombic efficiency, voltage efficiency, peak power density and cycle numbers. It must be noted that only membranes-employed in a neutral AORFBs are summarized. As shown in the Table, only a limited number of AEMs are reported. Indeed, more attention is given to the development of new redox-active species. However, to fully implement these devices, there is a need for the development and optimization of appropriate membranes as well. Few points on the direction to achieve these goals are discussed in the perspective section (4.2).

Table 5: Cell performance in neutral aqueous-based redox flow batteries using different membranes.

Membrane	Redox couple	Capacity retention per cycle (%)	Performance	Ref.
Selemion® DSV	BTMAP-Vi/BTMAP-Fc (~ 0.75 V), (0.75 M/1.0 M)	99.9989	> 500 cycles, 60 mW cm^{-2}	[52]
Selemion® AEM	MV/4-HO-TEMPO in 1.5 M NaCl (~ 1.25 V) (0.5 M/0.5 M)	99.88	>100 cycles, CE ~ 100%, EE : 62.5% at 60 mA cm^{-2}	[43]
Fumasep® FAA-3-PE-30 AEM	TEMPTMA/MV in 1.5 M NaCl (~ 1.40 V), (2.0 M/2.0 M)	~99.963	>100 cycles, ~ 250 mW cm^{-2}	[4]
Cellulose-based dialysis membrane	TEMPO/Viologen in 2 M NaCl (~ 1.15 v) (0.37 M/0.37 M)	~99.74	>10000 cycles ; ~ 100 mW cm^{-2}	[45]
Selemion® AMV	FcNCl or FcN$_2$Br2/MV in 2 M NaCl (~ 1.0 V) (0.5 M/0.5 M)	99.987	~ 700 cycles, ~ 125 mW cm^{-2} EE : 60%	[64]
Selemion® DSV	FcNCl/MV in KCl	99.955	EE: 85% at 40 mA cm^{-2} and 73% at 80 mA cm^{-2} ~ 122.7 mW cm^{-2}	[48]
Selemion® AMV	FcNCl/MV in KCl	99.971	EE: 76% at 40 mA cm^{-2} and 56.5% at 80 mA cm^{-2} ~ 74.1 mW cm^{-2}	
Selemion® ASV	FcNCl/MV in KCl	99.961	EE: 62% at 40 mA cm^{-2} and 35% at 80 mA/cm^{2} ~ 67.2 mW cm^{-2}	
Selemion® AMV	[(NPr)2V]Br$_4$/FcNCl in NaCl	99.99	100 cycles, 92 mW cm^{-2} CE : > 99% EE :59% at 60 mA cm^{-2}	[65]
	[(Me)(NPr)V]Cl$_3$/FcNCl	99.82%	CE :> 99%, EE : 65% at 60 mA cm^{-2}	

FAA-3-50®	TEMPO containing copolymer/MV in 1.5 M NaCl (1.3 V) 0.5 M		> 100 cycles, CE ~ 95%, EE : 85%	[49]
Selemion® DSV	TEMPO/MV in 1.5 M NaCl		100th cycle, VE ~76%	[47]
Selemion® DMV			100th cycle, VE ~62.5%	
Neosepta® AFX			100th cycle, VE ~76%	
Selemion® ASV			100th cycle, VE ~50%	
Neosepta® AHA			100th cycle, VE ~49%	
Nafion 212®	$(SPr)_2V/KI$	99.99%	CE ~100%, EE : 67%,	[66]
PPO and TMA based AEM	TMAP-TEMPO/BTMAP-Vi	99.988%	> 800 cycles, CE : 100%, EE : 81% at 40 mA cm^{-2},	[53]

Abbreviations**:** 1,1′-bis(3-sulfonatopropyl)-4,4′-bipyridinium, $(SPr)_2V$, 1-methyl-10-[3-(trimethylammonio)propyl]-4,40-bipyridinium trichloride, $[(Me)(NPr)V]Cl_3$, 1,1′-Bis[3-(trimethylamonium)propyl]-4,4′-bipyridinium Tetrachloride, $[(NPr)_2V]Cl_4$.

4. Conclusion, perspectives and thesis plan

4.1. Conclusion

Neutral pH AORBs are promising energy storage devices for various appealing reasons, such as safe, low-cost electrolytes and environmental friendliness. In such system, membrane, one of the critical component of the AORFB is used to separate the redox-active species and conducts the charge carrier ion. It affects the performance, lifespan and cost of the AORFBs. The membranes should exhibit low resistance, be impermeable to the redox-active species, high chemical stability and mechanical strength. Moreover, the membrane should be available at a reasonable price.

However, due to the fact that the technology is still at an early stage of development, compared to other energy storage systems, and the less attention given to the membrane, compared to the other components, remains to be a less developed component. The area resistances of various commercial membranes were found to depend on both the IEC and thickness of the membranes. Overall, due to their low electric resistance, Selemion® DSV and Fumatech® FAA-3-50 have been reported to perform better in neutral AORFBs among the tested commercial membranes.

Commercial membranes developed for desalination and acid-base recovery applications are often used. As a result, the crossover of redox-active species is widely reported as those membranes are not specifically designed for this system. Moreover, there are limited choices of commercially available AEMs that can be readily used in the system. On top of that, the high-cost of state-of-the-art membranes is a bottleneck for the widespread adoption of AORFB [67]. Therefore, the development of alternative low-cost appropriate (ion-selective) membranes for this system is needed.

4.2. Perspectives and thesis plan

To address the expensive cost and limited selectivity of state-of-the-art commercial membranes, we believe there is a need for detailed correlations study between the various membrane (with defined chemistry and structure) properties and cell cycling performances as well as stability and crossover, and preparing high performance membrane accordingly.

Understanding the correlation between the various membrane properties and cell cycling performance and stability in a controlled and systematic way should be done as this would help to develop an optimized membrane with high performance. Once a clear understanding of the membrane properties and cell performance is established, development of a battery with high performance (capacity retention, coulombic efficiency, energy efficiency and power density) by employing low-cost membranes should be the next target. This would require optimizing several properties of the membranes, such as IEC, ionic conductivity, water uptake, swelling degree, mechanical, chemical stability, redox-active species permeability and interaction with electrolyte. Various strategies, such as crosslinking, surface modification, lowering IEC and controlling ionic channels or pore size could be employed to minimize water uptake, thus minimize or avoid cross-contamination of redox-active species.

Last but not least, the membrane should be synthesized in an environmentally friendly synthetic method and a reasonable low cost. A general strategy to lower the cost of the membrane is to use economical raw materials and prepare the membrane in an optimized simple way. This is due to the fact that AORFBs are chosen over other electrochemical storage devices because of their environmental friendliness and possibly lower cost.

In this thesis, as part of the FlowCamp project, neutral AORFB based on water-soluble redox-active species, TMA-TEMPO (N,N,N-2,2,6,6-heptamethylpiperi-dinyl oxy-4-ammonium chloride) (catholyte) and dimethyl viologen (MV, N,N'-dimethyl- 4,4'-bipyridinium dichloride) (anolyte) (Scheme 2) are used [4]. The redox-active species have been demonstrated as stable and high performing in the system developed by a FlowCamp project partner – JenaBatteries GmbH (Jena, Germany), a spin-off from the University of Jena (Germany). However, in this thesis work, only the membrane part will be studied in order to further improve the cell performance.

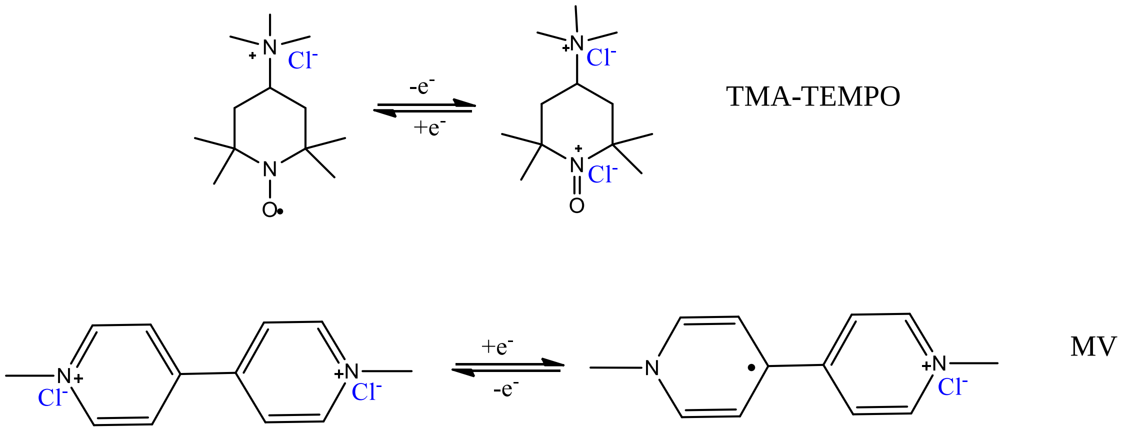

Scheme 2: Representation of the electrode reactions employed in the TMA-TEMPO (catholyte) /MV (anolyte) RFB.

Following summarizing and a critical analysis of the state-of-the-art studies on membranes for pH-neutral AORFBs, in this thesis work, to address the above-mentioned issues of membranes used in (TMA-TEMPO/MV) AORFBs, two research works were performed. In the first work, series of membranes were synthesized and the correlations between the membrane properties (such as IEC and water uptake) and cell performance (such as cell resistance, capacity fade, coulombic and energy efficiencies) were investigated. This work is discussed in chapter 3. In the second work, based on the finding obtained on the first work, various membrane synthesis strategies were followed to prepared a membrane with optimized properties, that is conductive and low-water uptake membrane which delivered excellent battery performance (discussed in chapter 4).

References

[1] X. Wei, W. Pan, W. Duan, A. Hollas, Z. Yang, B. Li, Z. Nie, J. Liu, D. Reed, W. Wang, V. Sprenkle, Materials and Systems for Organic Redox Flow Batteries: Status and Challenges, ACS Energy Lett. 2 (2017) 2187–2204. doi:10.1021/acsenergylett.7b00650.

[2] L.E. Singer, D. Peterson, International energy outlook 2010, 2011.

[3] Z. Chang, X. Zhang, Introduction to Metal-Air Batteries: Theory and Basic Principles, in: Met. Batter., Wiley-VCH Verlag GmbH & Co. KGaA, Weinheim, Germany, 2018: pp. 1–9. doi:10.1002/9783527807666.ch1.

[4] T. Janoschka, N. Martin, M.D. Hager, U.S. Schubert, An Aqueous Redox-Flow Battery with High Capacity and Power: The TEMPTMA/MV System, Angew. Chemie Int. Ed. 55 (2016) 14427–14430. doi:10.1002/anie.201606472.

[5] F. Cheng, J. Chen, Metal–air batteries: from oxygen reduction electrochemistry to cathode catalysts, Chem. Soc. Rev. 41 (2012) 2172. doi:10.1039/c1cs15228a.

[6] A. Mauger, C.M. Julien, Critical review on lithium-ion batteries: are they safe? Sustainable?, Ionics (Kiel). 23 (2017) 1933–1947. doi:10.1007/s11581-017-2177-8.

[7] G.E. Blomgren, The Development and Future of Lithium Ion Batteries, J. Electrochem. Soc. 164 (2017) A5019–A5025. doi:10.1149/2.0251701jes.

[8] X. Feng, M. Ouyang, X. Liu, L. Lu, Y. Xia, X. He, Thermal runaway mechanism of lithium ion battery for electric vehicles: A review, Energy Storage Mater. 10 (2018) 246–267. doi:10.1016/j.ensm.2017.05.013.

[9] P.G. Bruce, S.A. Freunberger, L.J. Hardwick, J.-M. Tarascon, Li–O2 and Li–S batteries with high energy storage, Nat. Mater. 11 (2012) 19–29. doi:10.1038/nmat3191.

[10] G.J. May, A. Davidson, B. Monahov, Lead batteries for utility energy storage: A review, J. Energy Storage. 15 (2018) 145–157. doi:10.1016/j.est.2017.11.008.

[11] B. Pinnangudi, M. Kuykendal, S. Bhadra, Smart Grid Energy Storage, in: Power Grid, Elsevier, 2017: pp. 93–135. doi:10.1016/B978-0-12-805321-8.00004-5.

[12] M. Beaudin, H. Zareipour, A. Schellenberglabe, W. Rosehart, Energy storage for mitigating the variability of renewable electricity sources: An updated review, Energy Sustain. Dev. 14 (2010) 302–314. doi:10.1016/j.esd.2010.09.007.

[13] S. Sankarasubramanian, J. Kahky, V. Ramani, Tuning anion solvation energetics enhances potassium–oxygen battery performance, Proc. Natl. Acad. Sci. 116 (2019) 14899–14904. doi:10.1073/pnas.1901329116.

[14] X. Zhang, X.-G. Wang, Z. Xie, Z. Zhou, Recent progress in rechargeable alkali metal–air batteries, Green Energy Environ. 1 (2016) 4–17. doi:10.1016/j.gee.2016.04.004.

[15] Y. Li, J. Lu, Metal–Air Batteries: Will They Be the Future Electrochemical Energy Storage Device of Choice?, ACS Energy Lett. 2 (2017) 1370–1377. doi:10.1021/acsenergylett.7b00119.

[16] H. Zhao, Q. Wu, S. Hu, H. Xu, C.N. Rasmussen, Review of energy storage system for wind power integration support, Appl. Energy. 137 (2015) 545–553. doi:10.1016/j.apenergy.2014.04.103.

[17] E. Sánchez-Díez, E. Ventosa, M. Guarnieri, A. Trovò, C. Flox, R. Marcilla, F. Soavi, P. Mazur, E. Aranzabe, R. Ferret, Redox flow batteries: Status and perspective towards sustainable stationary energy storage, J. Power Sources. 481 (2021) 228804. doi:10.1016/j.jpowsour.2020.228804.

[18] A.N. Colli, P. Peljo, H.H. Girault, High energy density MnO 4 − /MnO 4 2− redox couple for alkaline redox flow batteries, Chem. Commun. 52 (2016) 14039–14042. doi:10.1039/C6CC08070G.

[19] S. Roe, C. Menictas, M. Skyllas-Kazacos, A High Energy Density Vanadium Redox Flow Battery with 3 M Vanadium Electrolyte, J. Electrochem. Soc. 163 (2016) A5023–A5028. doi:10.1149/2.0041601jes.

[20] Z. Yang, J. Zhang, M.C.W. Kintner-Meyer, X. Lu, D. Choi, J.P. Lemmon, J. Liu, Electrochemical Energy Storage for Green Grid, Chem. Rev. 111 (2011) 3577–3613. doi:10.1021/cr100290v.

[21] B. Dunn, H. Kamath, J.-M. Tarascon, Electrical Energy Storage for the Grid: A Battery of Choices, Science (80-.). 334 (2011) 928–935. doi:10.1126/science.1212741.

[22] J. Luo, B. Hu, M. Hu, Y. Zhao, T.L. Liu, Status and Prospects of Organic Redox Flow Batteries toward Sustainable Energy Storage, ACS Energy Lett. 4 (2019) 2220–2240. doi:10.1021/acsenergylett.9b01332.

[23] M. Park, J. Ryu, W. Wang, J. Cho, Material design and engineering of next-generation flow-battery technologies, Nat. Rev. Mater. 2 (2017) 16080. doi:10.1038/natrevmats.2016.80.

[24] E. Sum, M. Skyllas-Kazacos, A study of the V(II)/V(III) redox couple for redox flow cell applications, J. Power Sources. 15 (1985) 179–190. doi:10.1016/0378-7753(85)80071-9.

[25] E. Sum, M. Rychcik, M. Skyllas-kazacos, Investigation of the V(V)/V(IV) system for use in the positive half-cell of a redox battery, J. Power Sources. 16 (1985) 85–95. doi:10.1016/0378-7753(85)80082-3.

[26] C. Blanc, A. Rufer, Understanding the Vanadium Redox Flow Batteries, in: Paths to Sustain. Energy, InTech, 2010. doi:10.5772/13338.

[27] X. Luo, J. Wang, M. Dooner, J. Clarke, Overview of current development in electrical energy storage technologies and the application potential in power system operation, Appl. Energy. 137 (2015) 511–536. doi:10.1016/j.apenergy.2014.09.081.

[28] R. Chen, S. Kim, Z. Chang, Redox Flow Batteries: Fundamentals and Applications, in: Redox - Princ. Adv. Appl., InTech, 2017. doi:10.5772/intechopen.68752.

[29] H. Chen, G. Cong, Y.-C. Lu, Recent progress in organic redox flow batteries: Active materials, electrolytes and membranes, J. Energy Chem. 27 (2018) 1304–1325. doi:10.1016/j.jechem.2018.02.009.

[30] L. Li, S. Kim, W. Wang, M. Vijayakumar, Z. Nie, B. Chen, J. Zhang, G. Xia, J. Hu, G. Graff, J. Liu, Z. Yang, A Stable Vanadium Redox-Flow Battery with High Energy Density for Large-Scale Energy Storage, Adv. Energy Mater. 1 (2011) 394–400. doi:10.1002/aenm.201100008.

[31] V. Singh, S. Kim, J. Kang, H.R. Byon, Aqueous organic redox flow batteries, Nano Res. 12 (2019) 1988–2001. doi:10.1007/s12274-019-2355-2.

[32] W. Wang, V. Sprenkle, Redox flow batteries go organic, Nat. Chem. 8 (2016) 204–206. doi:10.1038/nchem.2466.

[33] B. Huskinson, M.P. Marshak, C. Suh, S. Er, M.R. Gerhardt, C.J. Galvin, X. Chen, A. Aspuru-Guzik, R.G. Gordon, M.J. Aziz, A metal-free organic–inorganic aqueous flow battery, Nature. 505 (2014) 195–198. doi:10.1038/nature12909.

[34] J. Winsberg, T. Hagemann, T. Janoschka, M.D. Hager, U.S. Schubert, Redox-Flow Batteries: From Metals to Organic Redox-Active Materials, Angew. Chemie Int. Ed. 56 (2017) 686–711. doi:10.1002/anie.201604925.

[35] J. Noack, N. Roznyatovskaya, T. Herr, P. Fischer, The Chemistry of Redox-Flow Batteries, Angew. Chemie Int. Ed. 54 (2015) 9776–9809. doi:10.1002/anie.201410823.

[36] Y. Wang, P. He, H. Zhou, Li-Redox Flow Batteries Based on Hybrid Electrolytes: At the Cross Road between Li-ion and Redox Flow Batteries, Adv. Energy Mater. 2 (2012) 770–779. doi:10.1002/aenm.201200100.

[37] K. Wedege, E. Dražević, D. Konya, A. Bentien, Organic Redox Species in Aqueous Flow Batteries: Redox Potentials, Chemical Stability and Solubility, Sci. Rep. 6 (2016) 39101. doi:10.1038/srep39101.

[38] J.A. Kowalski, L. Su, J.D. Milshtein, F.R. Brushett, Recent advances in molecular engineering of redox active organic molecules for nonaqueous flow batteries, Curr. Opin. Chem. Eng. 13 (2016) 45–52. doi:10.1016/j.coche.2016.08.002.

[39] J.E. Bachman, L.A. Curtiss, R.S. Assary, Investigation of the Redox Chemistry of Anthraquinone Derivatives Using Density Functional Theory, J. Phys. Chem. A. 118 (2014) 8852–8860. doi:10.1021/jp5060777.

[40] S. Er, C. Suh, M.P. Marshak, A. Aspuru-Guzik, Computational design of molecules for an all-quinone redox flow battery, Chem. Sci. 6 (2015) 885–893. doi:10.1039/C4SC03030C.

[41] S. Gentil, D. Reynard, H.H. Girault, Aqueous organic and redox-mediated redox flow batteries: a review, Curr. Opin. Electrochem. 21 (2020) 7–13. doi:10.1016/j.coelec.2019.12.006.

[42] M. Li, Z. Rhodes, J.R. Cabrera-Pardo, S.D. Minteer, Recent advancements in rational design of non-aqueous organic redox flow batteries, Sustain. Energy Fuels. 4 (2020) 4370–4389. doi:10.1039/D0SE00800A.

[43] T. Liu, X. Wei, Z. Nie, V. Sprenkle, W. Wang, A Total Organic Aqueous Redox Flow Battery Employing a Low Cost and Sustainable Methyl Viologen Anolyte and 4-HO-TEMPO Catholyte, Adv. Energy Mater. 6 (2016) 1501449. doi:10.1002/aenm.201501449.

[44] B. Hu, Y. Tang, J. Luo, G. Grove, Y. Guo, T.L. Liu, Improved radical stability of viologen anolytes in aqueous organic redox flow batteries, Chem. Commun. 54 (2018) 6871–6874. doi:10.1039/C8CC02336K.

[45] T. Janoschka, N. Martin, U. Martin, C. Friebe, S. Morgenstern, H. Hiller, M.D. Hager, U.S. Schubert, An aqueous, polymer-based redox-flow battery using non-corrosive, safe, and low-cost materials, Nature. 527 (2015) 78–81. doi:10.1038/nature15746.

[46] Z. Yuan, H. Zhang, X. Li, Ion conducting membranes for aqueous flow battery systems, Chem. Commun. 54 (2018) 7570–7588. doi:10.1039/C8CC03058H.

[47] L.J. Small, H.D. Pratt, T.M. Anderson, Crossover in Membranes for Aqueous Soluble Organic Redox Flow Batteries, J. Electrochem. Soc. 166 (2019) A2536–A2542. doi:10.1149/2.0681912jes.

[48] B. Hu, C. Seefeldt, C. DeBruler, T.L. Liu, Boosting the energy efficiency and power performance of neutral aqueous organic redox flow batteries, J. Mater. Chem. A. 5 (2017) 22137–22145. doi:10.1039/C7TA06573F.

[49] T. Hagemann, J. Winsberg, M. Grube, I. Nischang, T. Janoschka, N. Martin, M.D. Hager, U.S. Schubert, An aqueous all-organic redox-flow battery employing a (2,2,6,6-tetramethylpiperidin-1-yl)oxyl-containing polymer as catholyte and dimethyl viologen dichloride as anolyte, J. Power Sources. 378 (2018) 546–554. doi:10.1016/j.jpowsour.2017.09.007.

[50] D.G. Kwabi, Y. Ji, M.J. Aziz, Electrolyte Lifetime in Aqueous Organic Redox Flow Batteries: A Critical Review, Chem. Rev. 120 (2020) 6467–6489. doi:10.1021/acs.chemrev.9b00599.

[51] R. Darling, K. Gallagher, W. Xie, L. Su, F. Brushett, Transport Property Requirements for Flow Battery Separators, J. Electrochem. Soc. 163 (2016) A5029–A5040. doi:10.1149/2.0051601jes.

[52] E.S. Beh, D. De Porcellinis, R.L. Gracia, K.T. Xia, R.G. Gordon, M.J. Aziz, A Neutral pH Aqueous Organic–Organometallic Redox Flow Battery with Extremely High Capacity Retention, ACS Energy Lett. 2 (2017) 639–644. doi:10.1021/acsenergylett.7b00019.

[53] Y. Li, Y. Liu, Z. Xu, Z. Yang, Poly(phenylene oxide)-Based Ion-Exchange Membranes for Aqueous Organic Redox Flow Battery, Ind. Eng. Chem. Res. 58 (2019) 10707–10712. doi:10.1021/acs.iecr.9b01377.

[54] W. Xie, J. Cook, H.B. Park, B.D. Freeman, C.H. Lee, J.E. McGrath, Fundamental salt and water transport properties in directly copolymerized disulfonated poly(arylene ether sulfone) random copolymers, Polymer (Guildf). 52 (2011) 2032–2043. doi:10.1016/j.polymer.2011.02.006.

[55] K. Sato, T. Ono, Y. Sasano, F. Sato, M. Kumano, K. Yoshida, T. Dairaku, Y. Iwabuchi, Y. Kashiwagi, Electrochemical Oxidation of Amines Using a Nitroxyl Radical Catalyst and the Electroanalysis of Lidocaine, Catalysts. 8 (2018) 649. doi:10.3390/catal8120649.

[56] A. Hollas, X. Wei, V. Murugesan, Z. Nie, B. Li, D. Reed, J. Liu, V. Sprenkle, W. Wang, A biomimetic high-capacity phenazine-based anolyte for aqueous organic redox flow batteries, Nat. Energy. 3 (2018) 508–514. doi:10.1038/s41560-018-0167-3.

[57] R. Narducci, J.-F. Chailan, A. Fahs, L. Pasquini, M.L. Di Vona, P. Knauth, Mechanical properties of anion exchange membranes by combination of tensile stress-strain tests and dynamic mechanical analysis, J. Polym. Sci. Part B Polym. Phys. 54 (2016) 1180–1187. doi:10.1002/polb.24025.

[58] H. Lee, M. Yanilmaz, O. Toprakci, K. Fu, X. Zhang, A review of recent developments in membrane separators for rechargeable lithium-ion batteries, Energy Environ. Sci. 7 (2014) 3857–3886. doi:10.1039/C4EE01432D.

[59] EUROPA - Batteries for e-Mobility and Stationary Storage (ongoing work) | SETIS - European Commission, (n.d.). https://setis.ec.europa.eu/implementing-integrated-set-plan/batteries-e-mobility-and-stationary-storage-ongoing-work (accessed January 30, 2021).

[60] C. Minke, U. Kunz, T. Turek, Techno-economic assessment of novel vanadium redox flow batteries with large-area cells, J. Power Sources. 361 (2017) 105–114. doi:10.1016/j.jpowsour.2017.06.066.

[61] V. Viswanathan, A. Crawford, D. Stephenson, S. Kim, W. Wang, B. Li, G. Coffey, E. Thomsen, G. Graff, P. Balducci, M. Kintner-Meyer, V. Sprenkle, Cost and performance model for redox flow batteries, J. Power Sources. 247 (2014) 1040–1051. doi:10.1016/j.jpowsour.2012.12.023.

[62] Fumasep® Membrane Types Redox-Flow-Batteries, No Title, (n.d.). https://fuelcellstore.com/spec-sheets/fumasep-faa-3-50-technical-specifications.pdf (accessed January 30, 2021).

[63] FOR BLUE SELEMION | Products | AGC Engineering, (n.d.). https://www.agec.co.jp/eng/product/selemion/ (accessed January 30, 2021).

[64] B. Hu, C. DeBruler, Z. Rhodes, T.L. Liu, Long-Cycling Aqueous Organic Redox Flow Battery (AORFB) toward Sustainable and Safe Energy Storage, J. Am. Chem. Soc. 139 (2017) 1207–1214. doi:10.1021/jacs.6b10984.

[65] C. DeBruler, B. Hu, J. Moss, X. Liu, J. Luo, Y. Sun, T.L. Liu, Designer Two-Electron Storage Viologen Anolyte Materials for Neutral Aqueous Organic Redox Flow Batteries, Chem. 3 (2017) 961–978. doi:10.1016/j.chempr.2017.11.001.

[66] C. DeBruler, B. Hu, J. Moss, J. Luo, T.L. Liu, A Sulfonate-Functionalized Viologen Enabling Neutral Cation Exchange, Aqueous Organic Redox Flow Batteries toward Renewable Energy Storage, ACS Energy Lett. 3 (2018) 663–668. doi:10.1021/acsenergylett.7b01302.

[67] C. Minke, T. Turek, Economics of vanadium redox flow battery membranes, J. Power Sources. 286 (2015) 247–257. doi:10.1016/j.jpowsour.2015.03.144.

Chapter 3: Study of Anion exchange membrane properties incorporating *N*-Spirocyclic quaternary ammonium cation and aqueous organic redox flow battery performance

1. Introduction

Redox flow batteries (RFB) are promising large-scale energy storage devices for many reasons, such as the power and energy are independently scalable, they allow for modular production, operate at ambient temperature and are environmentally benign [1–4]. In recent years, organic redox flow batteries (ORFBs) have grown and became very promising candidates to fulfill the requirements of ‘‘green’’, safe and sustainable energy storage [5]. Among them, aqueous ORFBs (AORFBs), which use water as solvent, are of high interest for both industry and academia [6–11]. Particularly, near neutral pH AORFB employing water-soluble dimethyl viologen (MV, *N,N*’-dimethyl- 4,4’-bipyridinium dichloride) (anolyte) and TMA-TEMPO (*N,N,N*-2,2,6,6-heptamethylpiperi-dinyl oxy-4-ammonium chloride) (catholyte) molecules has been demonstrated as a stable and high performing flow battery system [12]. A relatively high capacity of 54 Ah L^{-1} giving a total energy density of 38 Wh L^{-1} at a cell voltage of 1.4 V has been reported using TMA-TEMPO (2.3 M)/MV (2.4 M) as the active materials [12]. The relatively high energy density of this system is due to the high solubility of both active materials. Furthermore, the solubility of the organic active materials and, hence, energy density can be further improved by modifying the functional group or tuning the composition of the supporting electrolytes [13,14].

Over the years, most of the research efforts have been focused on the redox-active organic compounds only [16,17]. However, the membrane that is separating the catholyte and anolyte, has been identified as one of the major obstacles in the deployment of various RFBs [15]. The battery performance is strongly defined by the membrane, since the key roles of the membrane is to avoid the mixing of redox-active species and to conduct charge carrying ions (e.g., Cl^- ion for TMA-TEMPO/MV system) for the electrochemical reaction. In other words, for a high power density battery, a membrane with high ionic conductivity is required, while for a high coulombic efficiency and capacity retention, the membrane should avoid the cross-contamination of active species. Additionally, a well performant membrane should possess certain properties: (i) low ohmic resistance, (ii) good mechanical stability, (iii) good chemical stability, (iv) chemical inertness and (v) acceptable cost [5,22–24]. In spite, the state-of-the-art ORFB systems mostly use commercial membranes developed for other applications [12,18–21] that are not optimized for this type of flow battery.

The transport phenomena through a membrane used in RFBs are more complex and challenging as compared to those involved in others broadly studied systems such as fuel cells, as more ionic species are involved in transport activities driven by diffusion, osmosis and migration [17]. Therefore, to optimize the cell performance and to develop adapted membranes, there is a need to understand the correlation between polymer structure/membrane properties/transport phenomena and its influence on the overall cell performance. After all, it is the polymer structure (backbone, ionic moieties, ion exchange capacity (IEC), etc.) and microstructure of the membrane that endow the membrane with the different properties.

However, to date, only two systematic studies were reported on the influence of the cell performance parameters in ORFBs by cell/membrane resistance and crossover/membrane selectivity [25,26] , respectively. In 2017, Bo Hu et al. [25] performed a systematic study on the effects of commercial ion exchange membranes (Selemion® AMV, DSV, ASV) and supporting electrolytes (NaCl, KCl) on the cell resistance and cell performance of a neutral aqueous ORFB (FcNCl/MV). It turned out that the thinnest membrane DSV with the lowest area resistance displayed the best current dependent performance, energy efficiency and power density. This work emphasized the battery resistance as the primary factor to reach high battery performance. However, the crossover issue was neglected and the potential impact of the membrane structure was not studied. In 2019, Leo J. Small et al. [26] compared the performances of five different kinds of commercial AEMs (AFX, AHA, AMV, ASV, DSV) in TEMPO/MV based ORFB. Taking into consideration the cumulative contributions of pressure-driven flow, osmosis of solvent and redox-active species, migration and the electroosmotic drag, capacity loss of each membrane was traced back to their corresponding water content and IEC. However, since different commercial membranes (different polymer, cation, design and preparation procedures) were used, it is difficult to solely attribute the variation to the IEC of the membranes.

In this work, poly-(phenylene oxide) (PPO) was chosen as polymer backbone because of its good mechanical strength, good chemical stability and commercial availability in large quantities [27]. Moreover, it offers versatile synthetic routes and can be easily adjusted to meet various application requirements [28]. Recently, *N*-spirocyclic quaternary ammonium (QA) cations have been reported to be more chemically stable (against elimination and ring-opening substitution reactions) than other ammonium species due to their geometric constraints (unfavorable bond angles and lengths) in the reaction transition states [29]. Despite of this, very few AEMs bearing such *N*-spirocyclic QA cations were reported [30–32] because of the challenge to attach it to the polymer backbone [30,33].

Herein, we first provide a simple and convenient synthetic method to incorporate the N-spirocyclic QA to the membrane structure via a rapid UV irradiation approach. The PPO polymer backbone was first functionalized with methylbenzyldiallylammonium groups (PPO-Q) via a two-step process and then crosslinked in the presence of *N*, *N*-diallylpiperidinum chloride (DAPCl) via UV-induced free radical polymerization. Five membranes with different IECs were synthetized by varying the feed ratio of the DAPCl and PPO-Q. Subsequently, the membranes were characterized in terms of IEC, thickness, water uptake and chloride conductivity before they were used into battery test cell. Besides, for the assessment of the reproducibility of the improved synthetic method, three samples of each membrane type were tested in the TMA-TEMPO/MV based ORFB system and their charge/discharge cycling performance were recorded. Taking into account both cell resistance and cross-contamination, the effect of membrane properties (IEC, water uptake, chloride conductivity and thickness) on the corresponding cell performance (capacity utilization, coulombic efficiency, energy efficiency and power density) were discussed.

2. Experimental

2.1. Materials

All chemicals, if not specified otherwise, were used as received without further purification. Poly (2,6-dimethyl-1,4-phenylene oxide) (PPO) (M_n = 20,000, $Đ$ = 2.5) was purchased from Polysciences Inc. and dried under vacuum at 60 °C overnight before use. Methanol (99.9%), ethanol (99.9%) and chloroform (99.8%) were purchased from Fisher Scientific. N-Bromosuccinimide (NBS) (99%), 2,2'-azobis(2-methylpropionitrile) (AIBN) (98%), tetrahydrofuran (THF, ACS, >99%), diethyl ether (>99%), chloroform-d ($CDCl_3$-d, 99.9% D), Irgacure® 2959, D_2O (99.9 % D) and 1,2-dichloroethane (99.8%) were purchased from Sigma-Aldrich. Dimethyl sulfoxide-d$_6$ (DMSO-d$_6$, 99.9%), N-methyl-2-pyrrolidone (NMP, reagent grade) were supplied from Acros Organics. Chlorobenzene (ACS reagent, ≥ 99.5%), diallymethylamine (97%) and piperidine (≥99%) were bought from ABCR GmbH. Allyl bromide (98%) and allyl chloride (98%) were bought from Alfa Aesar. The electrolytes MV and TMA-TEMPO were provided by JenaBatteries. FAA-3-50® was purchased from Fumatech BWT GmbH (Bietigheim-Bissingen, Germany).

2.2. Polymer synthesis

Brominated PPO (PPO-Br): In order to introduce the N-spirocyclic QA cation, commercial PPO (M_n = 20,000, M_w/M_n = 2.5) was first functionalized by free-radical bromination, using NBS as a brominating agent and AIBN as initiator [34]. In a two-neck round bottom flask equipped with a condenser, PPO (6 g, 50 mmol repeating units) was dissolved chlorobenzene (60 mL) with stirring. Then NBS (2.07 g, 11.6 mmol) and AIBN (0.115 g, 0.7 mmol) were added. The reaction mixture was heated at 136 °C under reflux for 3 h, in order to ensure benzylic bromination [35]. Afterward, the mixture was poured into excess methanol (600 mL) to form a light-brown precipitate of brominated PPO (PPO-Br). The PPO-Br polymer was filtered, dried overnight in a vacuum oven at 60 °C and re-dissolved in chloroform (60 mL), followed by precipitation in 10-fold excess of ethanol. The precipitate was dried in a vacuum oven at 60 °C for 24 h before next use. The extent of bromination was calculated based on the ^{1}H NMR spectrum by comparing the integrals of the brominated methylene at 4.3 ppm and aromatic methyl group at 2.1 ppm.

Quaternized PPO (PPO-Q): The quaternized PPO (PPO-Q) polymer was prepared by reacting PPO-Br with diallylmethyllamine [31]. Diallylmethylamine (molar ratio diallylmethylamine to Br in PPO-Br = 2.5) was added to 10 wt.% PPO-Br dissolved in THF solution under argon at room temperature. A long reaction time (48 h) was used to assure the complete reaction. The quaternized product was precipitated in diethyl ether and dried in a vacuum oven at 35 °C for 48 h. The successful substitution of the Br atoms by diallylmethylamine and quaternization of the product was confirmed by ^{1}H NMR. The reaction protocol is summarized in scheme 1.

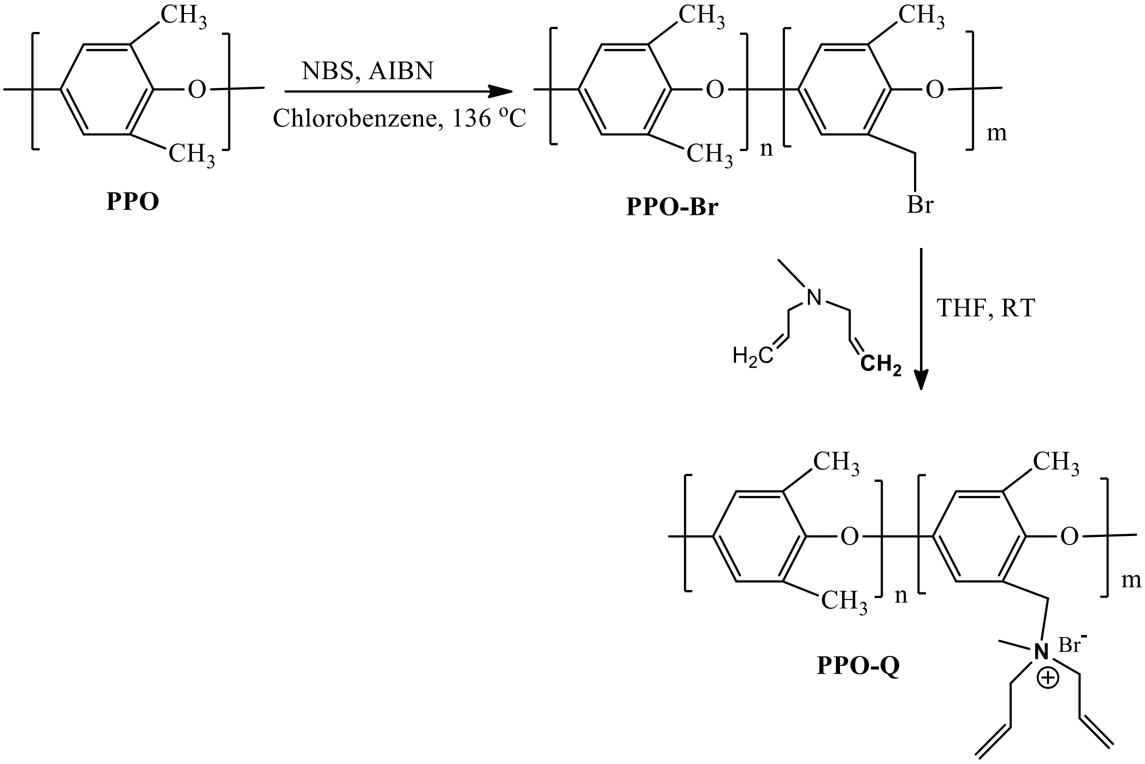

Scheme 1: Schematic representation of the preparation of PPO-Q polymer (m = 0.15 and n = 0.85).

2.3. *N,N*-Diallylpiperidinum chloride (DAPCl)

***N*-Allylpiperidine** [30]: In a 250 mL reaction flask, sodium hydroxide (14.5 g, 0.36 mol) was dissolved in deionized water (20 mL) at 0 °C and piperidine (30 mL, 0.30 mol) was added to the solution. Finally, allyl bromide (26.3 mL, 0.30 mol) was added dropwise (ca. 30 min). The temperature was raised to room temperature and the solution stirred for 6 h. The oil layer was collected using a separatory funnel and the remaining aqueous layer was extracted once with chloroform. The chloroform was removed via distillation. The product was washed with deionized water until pH = 7 was reached. Finally, the product was dried over $MgSO_4$ and filtered. The remaining colorless liquid (32.3 g, 86% yield) was collected.

***N,N*-Diallylpiperidinum chloride (DAPCl):** *N*-Allylpiperidine (32.3 g, 0.258 mol), allyl chloride (26.3 mL, 0.323 mol) and water (50 mL) were added to a reaction flask equipped with a magnetic stir bar (Scheme 2). The reaction flask was sealed with a rubber septum secured by Cu wire. The mixture was stirred at 65 °C for 48 h. The oil layer was collected using a separatory funnel and the remaining aqueous layer was extracted once with diethyl ether. After solvent evaporation, the viscous oil was precipitated in acetone. The solid product was washed several times using diethyl ether and precipitated in acetone to collect a white solid product by filtration (32.4 g, 62 % yield).

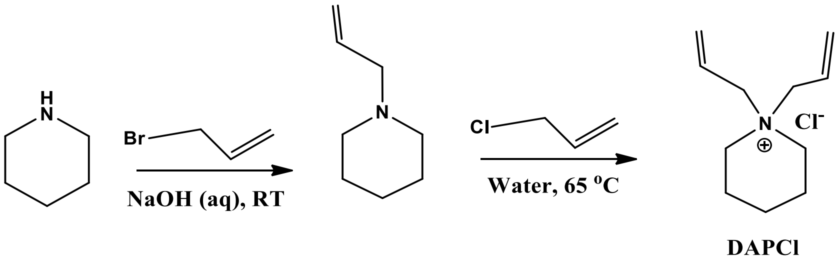

Scheme 2. Schematic representation of the synthesis of *N*-allylpiperidine and *N*, *N*-diallylpiperidinum chloride.

2.4. Membranes preparation

Five membranes with different expected IECs ranging from 1.96 to 3.25 mmol $Cl^- g^{-1}$ polymer were prepared and characterized. To manipulate the IEC, the DAPCl to PPO-Q ratio was tuned. In a typical example, a DAPCl to PPO-Q ratio of two (referred as ‘M1.7’) was used to prepare an AEM with a theoretical IEC of 2.23: a 0.075 g PPO-Q (0.076 mmol diallylmethylammonium), 0.0306 g DAPCl (0.152 mmol) and 0.01023 g (20% excess with respect to the diallylmethylammonium in the polymer) initiator (Irgacure® 2959) were dissolved in 1.2 mL of 1,2-dichloroethane (13 wt/v.%). After addition of 0.41 mL NMP (28.5 wt/v. %), the mixture was stirred for ten minutes.

The solution was filtered and poured into a petri dish with a 5 cm diameter. The glass petri dish was kept away from light to avoid decomposition of the initiator. After almost complete evaporation of the 1,2-dichloroethane under a fume hood at room temperature after ca. 30 minutes, the petri dish containing the viscous solution was put in a vacuum chamber (Figure 1) and degassed in order to remove oxygen. The film was then cross-linked using UV radiation (P300MT power supply, Fusion UV Systems) with a UV light exposure for 3 minutes. The obtained membrane was kept in a vacuum oven to evaporate the residual solvent at 60 °C for 24 h.

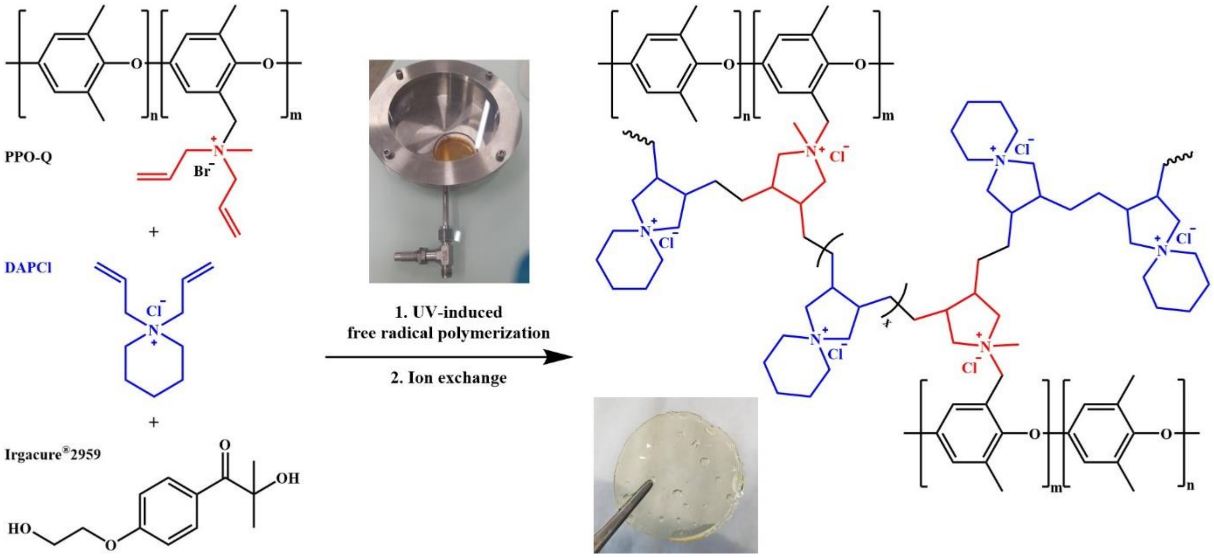

Figure 1: Schematic representation of the membrane preparation procedure.

2.5. Characterization

2.5.1. Structural characterization

The structure of the polymers and QA cation was determined by ^{1}H NMR spectroscopy. A Bruker AV 400 NMR spectrometer was used to record the ^{1}H NMR spectra. DMSO-d_6 (δ = 2.50 ppm) or $CDCl_3$ (δ = 7.26 ppm) or D_2O (δ = 4.79 ppm) were used as solvents.

2.5.2. Membrane chloride conductivity

The membranes were immersed in aqueous NaCl solution (1 M) at room temperature for 24 h to exchange bromide ions for chloride ions. Afterwards, they were immersed, and slowly stirred, in excess deionized water overnight to remove the excess of salts. Finally, they were rinsed with deionized water. The conductivity of the membranes was measured at room temperature via a through-plane impedance technique using a homemade measuring cell Figure 2 and a Hewlett Packard Model response analyser (HP Model 4192A LF Impedance Analyzer, Yokogawa Hewlett Packard, Japan) by two-point probe impedance method in the AC frequency range 13 MHz to 5 Hz. The membrane resistance is represented as the high-frequency intercept with the real impedance axis in Nyquist plot. The conductivity was calculated using equation (1):

$$\sigma = \frac{L}{R\ x\ A} \qquad (1)$$

Where σ is the ionic conductivity (S cm^{-1}), L (cm) is the distance between the electrodes (wet membrane thickness), R (Ω) is the resistance of the membrane obtained at high frequency, and A (cm^2) is the membrane area (0.0314 cm^2). The conductivity for each membrane was reported as the average of at least three measurements.

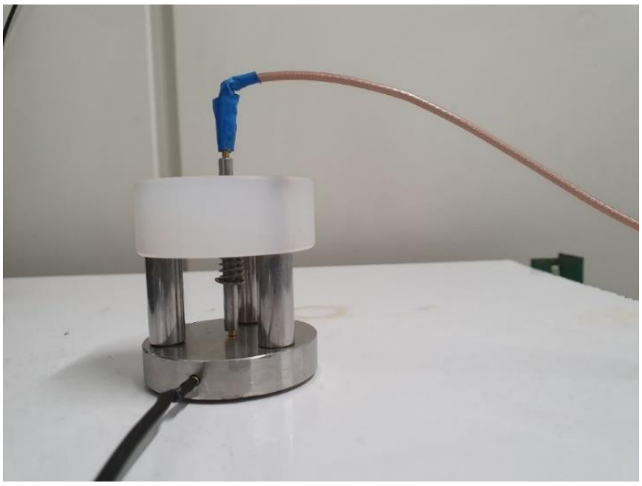

Figure 2: homemade membranes ion conductivity measuring cell.

2.5.3. Ionic exchange capacity and water uptake

The membranes were converted to Cl^- form by soaking in aqueous NaCl (1 M) solution for 48 h. Afterwards, excess salt was removed by washing the membranes about seven times with deionized water. The IEC, meaning the number of charged functional groups per gram of polymer was measured by Mohr titration method [36,37]. Membrane samples (~ 0.05 g) were dried in a vacuum oven at 50 °C for 24 h. The dry weight of the samples was recorded before immersion in 0.5 M aq. Na_2SO_4 (25 mL) for at least 48 h under stirring, thus replacing the Cl^- with SO_4^{2-}. Three samples of the resulting solution (containing released Cl^- ions) were titrated with 0.01 M aq. $AgNO_3$. K_2CrO_4 was used as an indicator. The IEC of the membranes was calculated using the following equation (2):

$$IEC\ (\mathrm{mmol\ g^{-1}}) = \frac{Volume\ of\ \mathrm{AgNO3\ (mL)}\ x\ Concentratio\ of\ \mathrm{AgNO3(mmol}\cdot mL^{-1})}{Weight\ of\ dry\ membrane\ \mathrm{(g)}} \tag{2}$$

Water uptake (WU) of the membrane after immersing in water at room temperature for 24 h was calculated using the weight of the dry and wet membrane samples. The WU of the membrane was calculated using equation (3):

$$WU(\%) = \frac{W_{wet} - W_{dry}}{m_{dry}}\ x\ 100 \tag{3}$$

The hydration number (or membrane water concentration) (λ), defined as the number of water molecules per (functional) ion-exchange group, is estimated as follow (equation 4):

$$\boldsymbol{\lambda} = \left(\frac{W_{wet} - W_{dry}}{18.01}\right)\left(\frac{1000}{IEC\ x\ W_{dry}}\right) = \frac{WU\ (\%)\ x\ 10}{IEC\ x\ 18.01} \tag{4}$$

The water uptake, IEC and hydration number for each membrane were reported as the average of at least three measurements.

2.5.4. Differential scanning calorimetry experiments

Differential scanning calorimetry (DSC) measurements were carried out using a Mettler-Toledo DSC1 instrument in order to determine the freezable (N_{free}) and non-freezable (N_{non}) water molecules in the membranes. Membrane samples were immersed in deionized water for at least a week to fully-hydrate them. The samples (about 10 mg) were surface-dried with tissue paper and quickly sealed in aluminum pans. They were analyzed on thermal cycles of cooling from 25 to -50 °C, following by stabilization at -50 °C for 10 min and successive heating up to room temperature under N_2 gas (50 mL min^{-1}) at a scan rate of 5 K min^{-1}. The amount of freezable (ratio of the mass of freezable water to the total mass of water in the membrane) and non-freezable water molecules was calculated using equations (5 and 6) [38,39]:

$$N_{free} = \frac{M_{free}}{M_{tot}} x\, \lambda = \frac{\Delta H_{free}/\Delta H_{ice}}{M_{tot}} \text{ x } \lambda \qquad (5)$$

Where M_{free} and M_{tot} are the masses of freezable and total water molecule absorbed in the membrane. ΔH_f is the enthalpy obtained by the integration of the DSC freezing peak and ΔH_{ice} is the enthalpy of fusion for water (334 J g^{-1}). The non-freezable bound water (N_{non}) was estimated by subtracting the freezable water content from the total hydration number.

$$N_{non} = \lambda - N_{free} \qquad (6)$$

2.5.5. Thermal analysis

The thermal stability of the monomer, polymer and membranes were measured by using a thermogravimetric analysis instruments TGA Q500 (Mettler-Toledo AG). Prior to analysis, the samples were dried at room temperature under vacuum for at least 24 h. The samples were preheated at 120 °C for 60 min in the TGA to remove traces of water. The measurement was performed under a N_2 atmosphere from 25 to 600 °C at a heating rate of 10 K min^{-1}.

2.5.6. Flow battery test

2.5.6.1. Charging/discharging tests

All cell tests carried out in this study were based on a lab scale single cell modified from the setup reported previously (JenaBatteries GmbH, Germany, active area: 5 cm^2) [40] using a VMP3 potentiostat/galvanostat (Bio-Logic, France). For each membrane type, three samples were tested. A representative protocol of the charging/discharging test is described as follows: Membranes were cut to squares of 3 cm × 3 cm and immersed in 0.5 M NaCl aqueous solution for 24 h before use. TMA-TEMPO (aq.) (10 mL, 1.12 mol L^{-1}) as catholyte and MV (aq.) (10 mL, 1.49 mol L^{-1}) as anolyte were used. Peristaltic pump (Heidolph Pumpdrive 5201, MASTERFLEX pump) was used for electrolyte circulation with a flow rate of 16 mL min^{-1} in an air-conditioned room of 22 °C. The first charge/discharge cycle was run at current density of 20 mA cm^{-2}. The cut-off voltages were 1.5 V and

0.9 V. Afterwards, it was charged/discharged at 80 mA cm^{-2} for consecutive 100 cycles. The final two cycles were performed at 20 mA cm^{-2}.

Resistance: An empty cell was manufactured with electrolytes while removing the membrane and the resistance was recorded as R_{empty} through electrochemical impedance spectroscopy (EIS) using the high-frequency real axis intercept in the Nyquist plot. The full cell resistances before and after the cycling tests were recorded by EIS and denoted as R_{cell}. The membrane resistance was calculated by R_{mem} (Ω cm^2) = ($R_{cell} - R_{empty}$) × active area.

Efficiency: The coulombic efficiency (CE), voltage efficiency (VE) and energy efficiency (EE) were calculated with the following equations:

$$\mathrm{CE} = \frac{\mathrm{t_d}}{\mathrm{t_c}}\ x\ 100\% \tag{7}$$

$$\mathrm{VE} = \frac{\mathrm{U_d}}{\mathrm{U_c}}\ x\ 100\% \tag{8}$$

$$\mathrm{EE} = \mathrm{CE}\ x\ \mathrm{VE} \tag{9}$$

Where t_d is the discharging time, t_c is the charging time, U_d is the average discharging voltage and U_c represents the average charging voltage. The same current was used for charging and discharging.

2.5.6.2. Cyclic voltammetry

After each charging/discharging experiment, the electrolyte solutions were characterized by cyclic voltammetry (CV) (VMP3 potentiostat/galvanostat Bio-Logic, France). The measurements were performed in 0.5 M NaCl (aq.) at room temperature via a three-electrode setup, where glassy carbon serves as working electrode, platinum wire as counter electrode, AgCl/Ag as reference electrode. The background was scanned first and then 100 µL of the investigated electrolyte solution was added into 4.6 mL NaCl (aq.) (0.5 M) under protective gas atmosphere. The potential was scanned six times within the range of -0.75 ~ 1.05 V at a scan rate of 200 mV s^{-1}. Background was subtracted and the fourth scan was chosen to prepare comparative graphs.

2.5.6.3. Polarization curve

Polarization curves were acquired directly after the cell cycling test without changing electrolytes. Following program was employed: The cell was fully charged at a constant current density of 50 mA cm^{-2} until it reached the upper limiting voltage of 1.5 V and then discharged at 10 mA cm^{-2} for 30 s. It was again charged at the same 50 mA cm^{-2} to 1.5 V, then discharged for 30s at 20 mA cm^{-2}. Every second cycle, the discharging current density was increased by 10 mA cm^{-2} until it reached 600 mA cm^{-2} or the lower limiting voltage of 0.2 V. The last point of each discharge curve was taken as the discharge cell voltage at the corresponding current density. The power density was calculated by multiplying the cell voltage by the current density.

2.5.7. Microscopy

The morphologies of the membranes before and after cell test were checked using microscopy (Carl Zeiss Microscopy GmbH) in order to detect potential morphological changes. The membrane samples were wetted with water and then placed under the camera lens. The studied area of the sample was roughly divided into five regions, four corners and the center. All regions were thoroughly examined.

3. Results and Discussion

3.1. Synthesis of the membrane

Commercial PPO was brominated in the benzylic position. The bromination degree was calculated by analysis of ^{1}H NMR spectrum from the ratio between the integrals of characteristic peak of protons of –CH_2Br at 4.3 ppm and the remaining unbrominated CH_3 groups (2.1 ppm) (Figure 3a). Moreover, the absence of a signal at 6.1 ppm indicated that no phenyl-brominated polymers were formed as side products. The bromination degree was calculated to be 15%, which corresponds to a bromination yield of 65%. In a second reaction step, the PPO-Br was reacted with diallylmethylamine to form quaternized PPO-diallylmethylamine bromide (PPO-Q). New signals corresponding to the protons of the diallylmethylammonium moiety appeared in the ^{1}H NMR spectrum (Figure 3b). The ratio between the integrals of the backbone and the substituent signals confirm the complete transformation of CH_2Br to quaternized ammonium group.

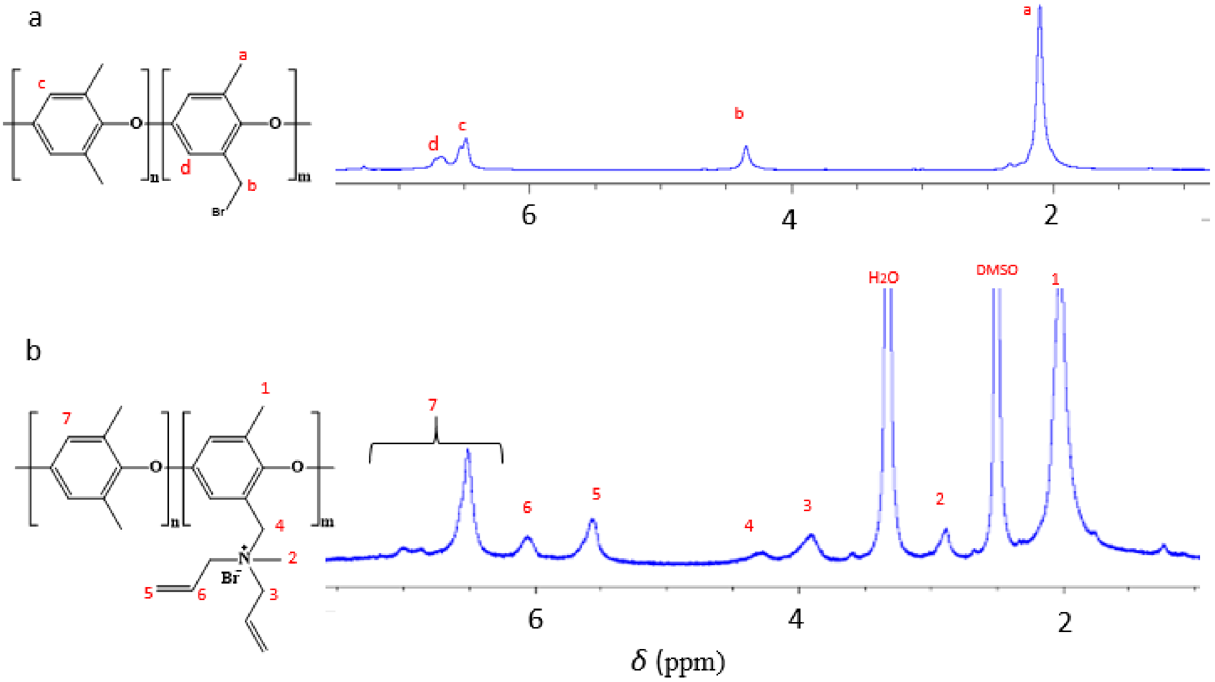

Figure 3: ^{1}H NMR spectra of PPO-Br (a) in $CDCl_3$ and PPO-Q (b) in DMSO-d_6.

DAPCl was prepared via a two-step process by a nucleophilic substitution reaction as outlined in Scheme 2 [30]. The structure and purity of the monomer were confirmed by ^{1}H NMR spectroscopy as well (Figure 4).

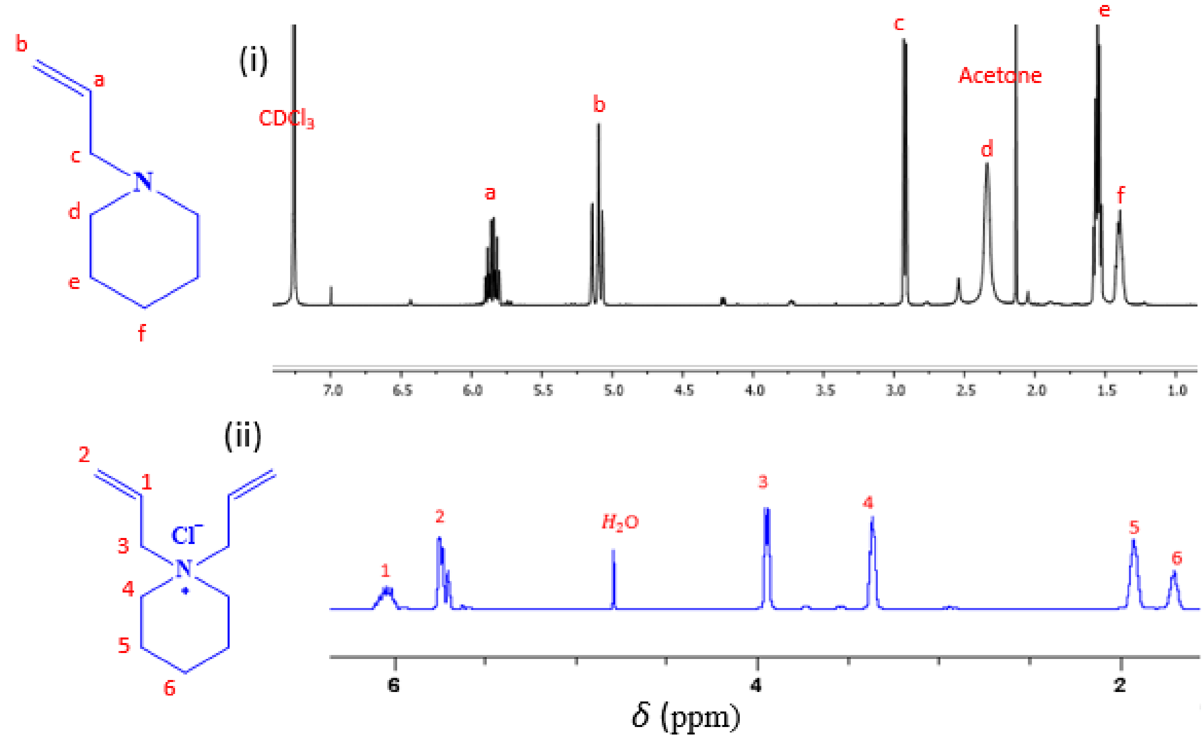

Figure 4: ^{1}H NMR (400 MHz) spectra of *N*-allylpiperidine in $CDCl_3$ (i) and of *N*,*N*-diallylpiperidinum chloride (DAPCl) in H_2O (ii).

Different amounts of DAPCl were copolymerized with the PPO-Q (Table 1) in order to vary the theoretical IEC between 1.96 and 3.3 mmol of $Cl^- g^{-1}$ and to study its impact on membrane properties and cell performance. The blend of PPO-Q polymer, DAPCl monomer and photoinitiator was cast from a solution of 1,2-dichloroethane and NMP (section 2.4). The photo-polymerization initiator Irgacure® 2959, a highly efficient non-yellowing radical Type I photoinitiator for UV curing systems [41,42], was used to initiate the reaction. Irgacure® 2959 was chosen as radical photoinitiator because of its solubility in 1,2-dichloroethane, good overlap of absorbance spectrum with the emission spectrum of the light source (visible light absorbance) and commercial availability. To assure a good yield of the crosslinking reaction, a good mobility of double bonds is required. Therefore, NMP was employed as a co-solvent ("plasticizer") during the irradiation as 1,2-dichloroethane is a highly volatile solvent.

The dried membranes were washed with water to remove the unreacted monomers, non-grafted oligomers, remaining initiator and NMP. Amounts corresponding to 10 to 20 wt.% of the total membrane dry weight were removed. The ^{1}H NMR spectra of the residues revealed the presence of a mixture of DAPCl and poly(DAPCl) in a molar ratio close to 50:50.

The experimental IECs were determined by titration and are summarized in Table 1. From these values and taking into account that only the DAPCl and poly(DAPCl) were removed from the cast membrane, the actual ratios between the polymer side chain and DAPCl monomer, which were converted by the crosslinking reaction, were calculated (Table 1). The DAPCl conversion varied between 46 and 66% and increased with the increase of IEC. This increase can be explained by the (i) lower viscosity and (ii) higher double bond concentration in the polymer/monomer blend before irradiation. Flexible and transparent membranes with thickness between 39 and 60 µm were obtained. Similarly, Strasser et al. [30] and Jannasch et al. [31] reported the preparation of water-insoluble, chemically stable and mechanically robust AEMs using poly(DAPCl) cation prepared via UV-initiated radical and reactive casting cyclo-polymerization, respectively.

Table 1. Chemical composition and membrane properties of the five prepared AEMs

Membrane	Thickness (µm)	DAPCl to PPO-Q molar ratio		DAPCl conversion (%)	IEC (mmol Cl^- g^{-1} polymer)	
		Feed ratio	Titration		Theoretical	Titration
M1.5	39 ± 3	1.4	0.65	46	1.96	1.52 ± 0.12
M1.7	45 ± 3	2	0.95	48	2.23	1.71 ± 0.11
M2.1	57 ± 3	3	1.7	56	2.58	2.08 ± 0.05
M2.5	58 ± 3	4	2.5	62	2.85	2.40 ± 0.07
M2.8	60 ± 3	6	4	66	3.3	2.84 ± 0.07

3.2. *Ex-situ* membrane characterization

Thermal stability: The thermal stability of the prepared polymers, cation and membrane (M2.8) was evaluated with thermogravimetric analysis (TGA) (Figure S1). The membrane reveals a high thermal stability, the weight loss associated with the degradation of M-2.8 membrane was registered to be above 250 °C corresponding to the degradation of benzylic quaternary amine side chains. The second thermal degradation step of the membrane occurred at 320 °C, in agreement with the poly(DAPCl) degradation temperature [31]. The last degradation step at about 440 °C corresponds to the PPO polymer backbone [43] and additional degradation of the poly(DAPCl) side chain. Similar two steps degradation of the poly(DAPCl) cation was reported elsewhere [31]. Therefore, the membranes have shown good thermal stability, which is far than what is needed in the battery, typically operated at a room-temperature.

Water uptake: Figure 5 shows the water uptake of the membranes (Cl^- form) at room temperature. At lower IEC values, the water uptake slightly increased between M1.5 and M1.7 membranes, an increase of only 5% is observed. Whereas, at higher IEC, a much sharper increase (more than 50%) in water uptake between M2.1 and M2.8 membranes was recorded. This sudden increase is due to (i) the increase of proportion of the hydrophilic ionic side chains in the membrane, i.e. the higher the IEC, the longer the lengths of poly(DAPCl) and (ii) the decrease of the crosslinking stiffness [44].

The **hydration number** values (λ, the number of absorbed water molecules per QA cation) of the membranes followed a similar trend. At relatively low IEC, λ is roughly the same in M1.5 and M1.7 membranes, averaging 11.6 and 11.8, respectively. As the IEC increases, the corresponding λ increased significantly (M2.1, ~14; M2.8, 21.5 water molecules). A similar hydration number increase with increase of IEC has been reported in the literature [45,46]. Based on our results, it can be assumed that for M1.5 and M1.7 membranes, the IEC drives the water uptake, by the interaction of water with the anions and cations, whereas in the other three membranes with higher IECs, the osmotic pressure becomes too high and water clusters are formed. It should be noted that the cation hydration [47] corresponds to the amount of water molecules directly interacting with the cation, whereas hydration shell indicates the number of water molecules surrounding the ion, but not necessarily directly interacting with it [48,49]. For instance, the cation hydration of a chloride ion was reported to be six in water solution [50,51]. Whereas, the cation hydration of poly(DAPCl) is not reported yet. However, the λ of a PPO-based AEM which has the same structure with ours, in OH^- form (2.34 mequiv g^{-1} IEC and 101% water uptake at 20 °C), was reported to be 25 [31].

To have more information about the state of water, i.e. in interaction with the ions or free water, we performed DSC measurements**.** Generally speaking, the water absorbed in the membrane can be classified into freezable and non-freezable water states [52]. The freezable or free state water has the physical characterization of as bulk water, including freezing temperature close to 0 °C. On the other hand, the non-freezable water is in strong interaction with the ionic function or polymer polar groups of the membrane. DSC measurements were done to investigate the water states in four of the prepared membranes. As shown in Table 2, there seems to be non-freezable water of about 11.4 – 14.5 molecules per ionic functions of the prepared membranes. There were no freezable water molecules in the case of M1.5 membrane. For the other membranes, the freezable amount of water was found to increase in line with their water uptakes.

For instance, the freezable water molecules within M2.8 membranes were found to be about 7 ± 0.8 per ionic function and were found to melt at about 0 °C, indicating the bulk water behavior of part of the absorbed water molecules, whereas for the other membranes, the melting occurs at lower temperature which can be associated with confinement or interaction effects. In conclusion, we expect that the membranes with higher amount of N_{free} to result in a higher degree of cross-contamination of TMA-TEMPO and MV compared to the membranes with low or no N_{free} as the N_{non} are mainly associated with the ionic functions, and less available for active species mobility.

Table 2: Amount of freezable and non-freezable water in the membranes, their enthalpy and melting temperature.

Membrane	Water hydration (λ)	ΔH_f DSC (J g^{-1} wet sample)[a]	ΔH_f DSC (J g^{-1} water)[b]	Freezable water (%) = $\Delta H_{f,DSC}/\Delta H_f$, pure water[c]	Freezable λ in the membrane[d]	Non-freezable λ in the membrane	T_m (K)[e]
M1.5	11.6 ± 1.4	0	0	0	0	11.6 ± 1.4	-
M1.7	11.8 ± 0.3	8 ± 3.1	30 ± 11	9 ± 3.5	0.4 ± 0.2	11.4 ± 0.2	255
M2.1	14.2 ± 0.7	15 ± 1.7	45 ± 5	14 ± 1.5	1 ± 0.1	13 ± 0.1	268
M2.8	21.5 ± 0.3	52 ± 6	98 ± 11	29 ± 3.3	7 ± 0.8	14.5 ± 0.8	273

a. Obtained from the DSC.

b. ΔH_f DSC (J g^{-1} water) = (ΔH_f DSC, J g^{-1} wet membrane) x (sample weight, g)/ (water weight in the sample, g).

c. Melting enthalpy of pure water is taken as 334 J g^{-1}.

d. Freezable λ in the membrane was calculated using equation (5).

e. T_m (K) is the melting temperature of the water absorbed in the membrane.

Conductivity: Similar to the water uptake, IEC has an impact on the conductivity of the membranes [53]. The conductivity is related to the number of charge carriers and their mobility, both of which are enhanced by IEC. Moreover, the charge carrier mobility increases with increasing water uptake as well as the connectivity between the ionic domains [54]. Figure 5 presents the conductivity of the membranes as function of their IECs. It is interesting to point out that the trend of the evolution of conductivity with IEC flattens at high IEC, thereby indicating a saturation effect. For the membrane with IEC between 1.5 and 2.1 mmol $Cl^- g^{-1}$, the conductivity increases linearly with factor of more than 2.5 while above 2.1 mmol $Cl^- g^{-1}$, the increase is much lower (less than 1.4) despite the much higher water uptake. Hence, for these high IEC membranes, where the presence of bulk water was evidenced, the impact of IEC on conductivity efficiency has a lower impact. The commercial reference membrane FAA-3-50® (thickness: 50 ± 5 µm; IEC: 1.85 mmol $Cl^- g^{-1}$ polymer; WU: 17 wt.%) was found to have a Cl^- ion conductivity of 1.57 ± 0.2 mS cm^{-1} in pure water at room temperature. By contrast, the conductivity value reported by the manufacturer is 3 - 8 mS cm^{-1} (0.5 M NaCl at 25 °C, through-plane measuring cell), higher than that found in this study. The method of measuring and the presence of free salt could be the main reason for the variation in the membrane conductivity [55].

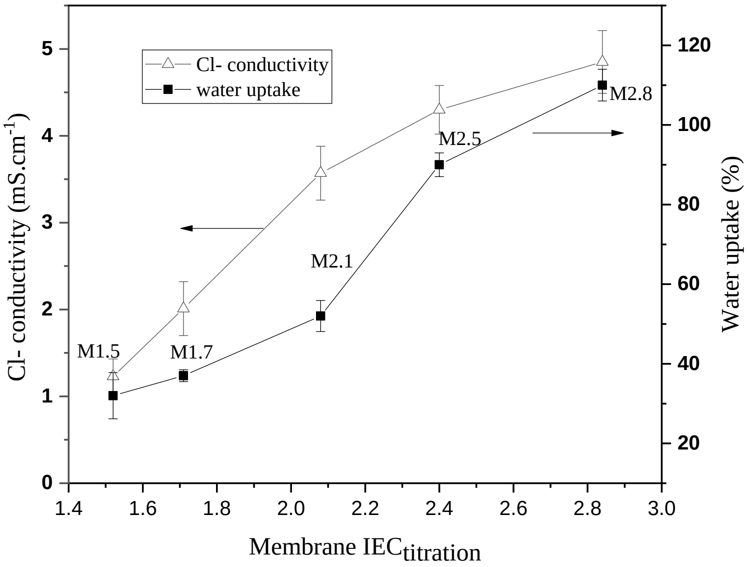

Figure 5: Water uptake and conductivity of the AEMs as function of IEC.

3.3. Cell performance and membrane stability

3.3.1. Charge/discharge tests

Four of the five prepared AEMs were investigated in a well-established TMA-TEMPO/MV based ORFB system. The test cells were primed at 20 mA cm^{-2} for one charging/discharging cycle and afterwards aged for 100 cycles at 80 mA cm^{-2}. Finally, the capacity retention was probed at 20 mA cm^{-2}

by two additional charging/discharging cycles. Table 3 presents the initial capacity of the cell measured at 20 mA cm^{-2} and the capacity retained after 103 charging/discharging cycles. This value indicates the capacity fade due to the cross-contamination of the redox-active species through the membrane [26,56,57]. In addition, the capacity that is accessible at 80 mA cm^{-2} is displayed. This value is typically lower since ohmic overpotentials limit the cell performance. It allows to evaluate the overall power capability of the membranes and provides an indication on their resistance. For each membrane type, three independent membrane samples were measured to avoid accidental error during membrane preparation. Membrane properties and cell performance of each independent sample are summarized in Table S1. For comparison, results of AEMs prepared in this study and a commercial reference membrane FAA-3-50® are shown.

In this work, it is reasonable to neglect the impacts of electrolyte degradation on the overall cell performance as the cycling stability of TMA-TEMPO/MV was evidenced in literature [12]. Thus, the evaluation of the cell performance is focused on the selectivity and retention capability of the membranes. The capacity fade is exclusively related to the crossover of the redox active species through the membrane, i.e. membrane ion selectivity. Using cyclic voltammetry, the crossover was evaluated.

Table 3: Summary of initial capacity and capacity retention of the prepared AEMs and commercial membrane FAA-3-50® at 20 and 80 mA cm^{-2}.

Membrane	Capacity 1st cycle at 20 mA cm^{-2} (mAh)	Accessible capacity at 80 mA cm^{-2} (mAh, retention (%)[a])	Capacity 103rd cycle at 20 mA cm^{-2} (mAh, retention (%)[b])
M1.5	283 ± 48	136 ± 18 (41 ± 4)	279 ± 48 (98.5 ± 0.5)
M1.7	297 ± 3	207 ± 8 (83.5 ± 0.5)	261 ± 2 (88 ± 0)
M2.1	218 ± 39	174 ± 45 (55 ± 16)	107 ± 24 (49 ± 4)
M2.8	216 ± 33	174 ± 22 (34 ± 8)	59 ± 8 (29 ± 5)
FAA-3-50®	301	244 (94)	288 (95)

[a]: Calculated by dividing the discharge capacity of 101st cycle by that of 2nd cycle.

[b]: Calculated by dividing the discharge capacity of 103th cycle by that of 1st cycle.

According to Table 3, the capacity retention of the four AEMs after 103 charging cycles has a negative correlation with their ion selectivity. Cyclic voltammetry was used as a tool to qualify the cross-contamination of the electrolytes after cell cycling test for each membrane. Electrolyte solutions of TMA-TEMPO and MV both before and after the cell tests were measured under the same condition. In principle, the degree of cross-contamination can be quantified through comparison of the redox peak intensities. In practice, however, the concentrations of the starting electrolyte solutions are unequal, which implies inevitably osmosis-induced water transfer during the cycling experiments. It means that the concentrations of TMA-TEMPO/MV solutions will change accordingly in some degree. For example, in Figure 6, the redox peak intensities of TMA-TEMPO with the M1.5 membranes are stronger than that before cell test, whereas in MV side, the trend reversed. This is because water was driven from TMA-TEMPO side to MV side by the osmosis pressure originated from the concentration difference. However, one can still tell from the curve whether crossover of electrolyte happens or not and to how large extent the crossover is. As a result, no crossover occurred for FAA-3-50® (Figure 7) and M1.5, small crossover for M1.7, middle crossover for M2.1 and strong crossover for M2.8. This is in agreement with the distinctly higher water uptake of the two membranes and the presence of bulk water.

More precisely, from M1.5 to M2.8, the capacity retention decreased from 98.5 ± 0.5% to 29 ± 5%. Correspondingly, increased peak intensity of MV was observed in the recorded cyclic voltammograms of the electrolyte solutions of the TMA-TEMPO half-cell (Figure 6a). Similarly, increasing amount of TMA-TEMPO occurred in the MV half-cell of the battery at the end of the charge/discharge tests (Figure 6b). Only in the post-cycling analysis of the M1.5 cell no additional peaks emerged, indicating that neither MV nor TMA-TEMPO crossed the membrane. As for the other three membranes, they displayed different levels of capacity fade with respect to their IECs and/or water uptake values. Compared to M1.7, both M2.1 and M2.8 display low capacity retention regardless of the current applied, which mainly resulted from the irreversible high level of cross-contamination.

Moreover, the initial capacity associated with the different membranes was found to be different. Especially membranes with high degree of crossover revealed a relatively low initial capacity. This can be associated with crossover already taking place during the first charging cycle.

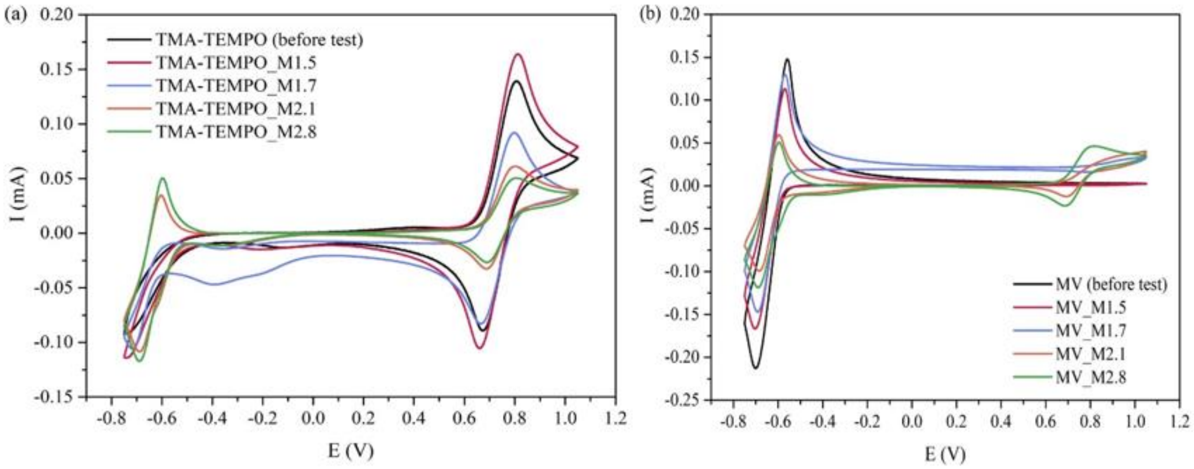

Figure 6. Cyclic voltammograms of TMA-TEMPO and MV solutions for each membrane before and after the cell cycling tests: (a) TMA-TEMPO half-cell, (b) MV half-cell. Scan rate: 200 mV s^{-1}.

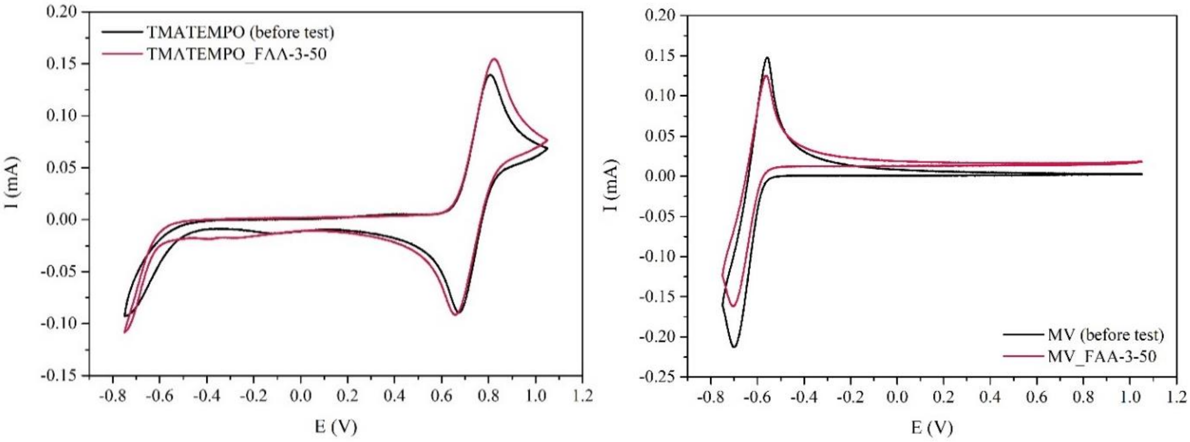

Figure 7: Cyclic voltammograms of TMA-TEMPO and MV solutions (100 µL in 4.6 mL 0.5 M NaCl (aq.)) for FAA-3-50® after the cell cycling test. Left: TMA-TEMPO, right: MV. Scan rate: 200 mV s^{-1}. Background subtracted before plotting; the fourth scan was chosen to prepare the comparative graphs.

For practical application, low cell resistance is essential for high current density operation [56] and high performance battery [5]. In this sense, charge/discharge cycling behavior was recorded at a relatively high current density of 80 mA cm^{-2}, when the cell resistance can have a large impact due to ohmic drop or ionic species diffusion limitation. To be more direct and comparative, all the cell resistances were corrected as membrane resistances by subtracting the cell resistance without membrane. Within expectation, both of the ex-situ and in-situ membrane resistances declined with the increasing chloride ion conductivity and hence, the IEC value, as plotted in Figure 8. The deviation between the in-situ and ex-situ membrane resistance for the more conductive membranes i.e. M2.1 and M2.8 could be attributed to the different electrolyte media, the ex-situ membrane resistance was measured in water while the in situ resistance was performed in the presence of redox active species (aq). In general, both thickness and ionic conductivity of the membrane affect the membrane resistance, i.e., higher thickness and lower ionic conductivity lead to higher membrane resistance [58]. However, in the current work, as the thickness of the membranes does not vary notably, the IEC is the main parameter defining the membrane resistance. Even though the thickness increased from about 39 µm (M1.5) to about 60 µm (M2.8), the corresponding membrane resistance dramatically fell from 3 to 0.7 Ω cm^2. The commercial FAA-3-50® membrane has 1.28 Ω cm^2 in-situ area resistance in the same conditions.

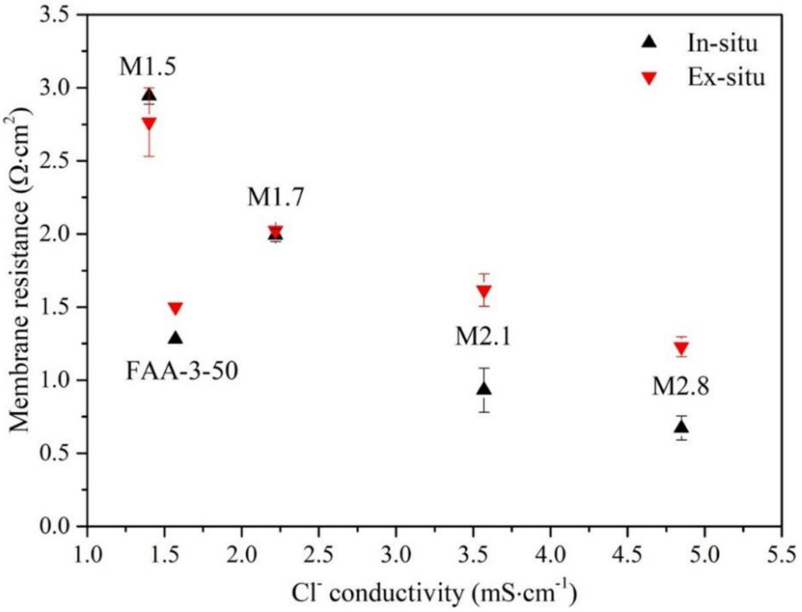

Figure 8: Membrane resistances compared to their chloride ion conductivity.

It becomes obvious that the membrane resistance has a strong influence on the overall cell performance, which reflects in the power capability of the test cells. When the current density is increased from 20 to 80 mA cm^{-2}, the capacity that remains accessible becomes increasingly limited as the ohmic drop gets higher. The starting charge/discharge cell voltage gets higher/lower and the cell reaches the cutoff voltages earlier than those that have lower ohmic resistance, i.e. less time is left to charge/discharge.

After priming at 20 mA cm^{-2}, all four AEMs were charged-discharged at 80 mA cm^{-2} for 100 cycles, as shown in Figure 9. In the case of M1.5 the ohmic overpotential elevated dramatically due to its rather high membrane area resistance (2.945 ± 0.055 Ω cm^{2}), limiting the accessible capacity at 80 mA cm^{-2} to 136 ± 18 mAh. M-1.5 that is exhibiting excellent capacity retention (98.5 ± 0.5) probed at 20 mA cm^{-2} after 103 cycles, which attributes to no crossover of TMA-TEMPO nor MV as detected by CV measurements (Figure 6), comes at the price of limited power capability. However, this failure to withdraw the full capacity is not irreversible capacity fade, instead, it will be available again when the charge/discharge current density drops back to 20 mA cm^{-2}. With lower membrane resistance than M1.5 and lower crossover than M2.1 or M2.8, M1.7 maintained a good balance between ion conductivity and selectivity of the membrane and, therefore, displayed the best capacity retention among the four membranes at 80 mA cm^{-2}.

As a reference, the commercial membrane FAA-3-50® has nearly no crossover like M1.5. Its low resistance; however, allows it to withdraw and store high capacity even at high current density (94%, 80 mA cm^{-2}). In fact, FAA-3-50® has a chloride conductivity close to the conductivity of M1.5, thickness between the thickness of M1.7 and M2.1, water uptake even lower than that of M1.5. Its membrane resistance; however, is much lower than that of M1.5 and comparable with that of M2.1.

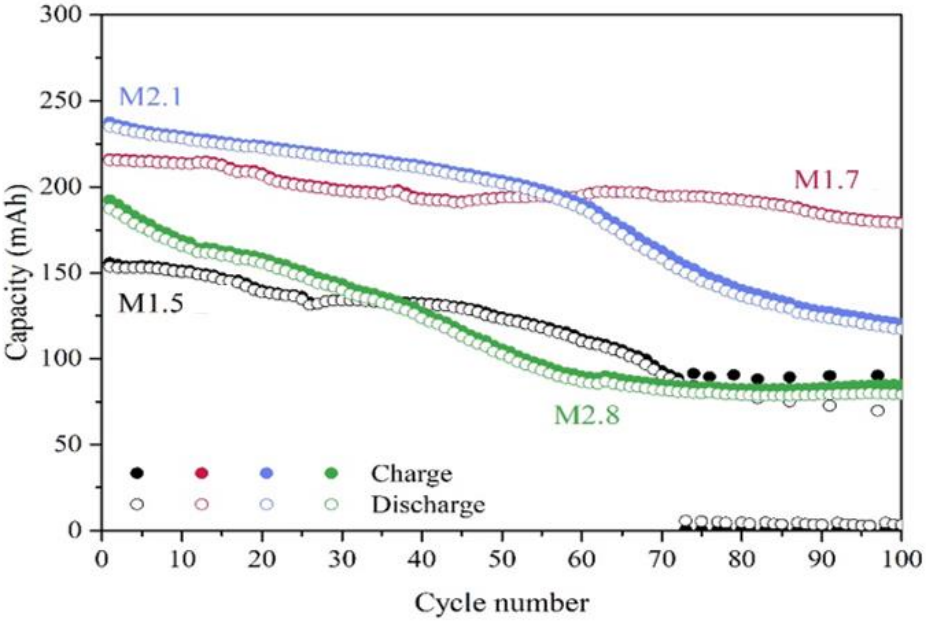

Figure 9: Charge/discharge capacity of the four AEMs at 80 mA cm^{-2} over 100 cycles in TMA-TEMPO/MV (1.12 M/1.49 M) based ORFB single cell. The cell was primed at 20 mA cm^{-2} for one cycle. Cutoff voltage: 0.9/1.5 V.

Coulombic efficiency (CE) and voltage efficiency (VE) are two additional parameters to evaluate the performance and reversibility of a battery system. As shown in Figure 10, the M1.5-based battery, using a membrane with high active material retention, exhibited an average CE of 99.1 ± 0.1%. Likewise, the cell employing M1.7, a membrane with slight crossover, was found to be above 99%. On the other hand, M2.1 and M2.8 displayed CE of 94.0 ± 5.3% and 93.9 ± 3.2%, respectively, which is an indication of the strong crossover of active species [5]. VE, on the other hand, is an indication of the internal resistance of the cell [59]. The test cells of M2.1 and M2.8, as expected, showed the highest VE (around 80% at 80 mA cm^{-2}) due to their low associated cell resistances. In contrast, the cell employing M1.5, membrane with highest resistance, showed the lowest VE (65.9 ± 1.7%) among the tested membranes.

Energy efficiency (EE) indicates the energy loss of a battery system. It is typically between 50 to 90% for RFBs depending on the material properties of the membrane, the active species used and applied current density [5]. Among the four tested membranes, M2.1 and M2.8 have the highest EE due to their higher VE (lower resistance) followed by M1.7 (Figure 10). The cell with M1.7 revealed an excellent CE of above 99% as that of FAA-3-50® does. However, its relatively high membrane resistance limited its EE. The same holds true for membrane M1.5.

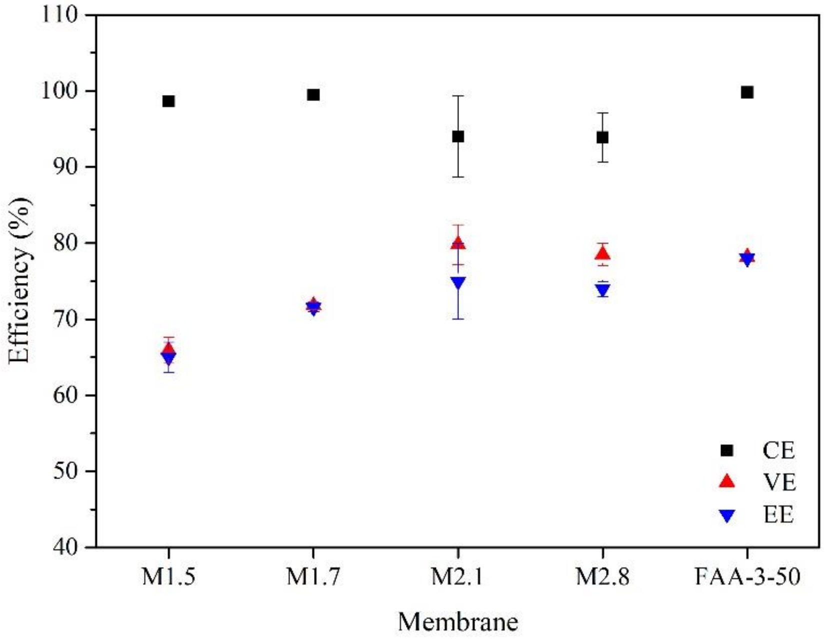

Figure 10: CE, VE and EE of the prepared AEMs and commercial membrane FAA-3-50® operated at 80 mA cm^{-2} for 100 cycles.

3.3.2. Polarization curve

With the best overall cell performance among the four AEMs, the discharging polarization curve of M1.7 in a single cell at 100% SOC was recorded in an effort to reveal the performance loss and evaluate its suitably for practical flow battery application. The cell was operated within the range of 10 to 600 mA cm^{-2} directly after the charge/discharge test, with the polarization curve of FAA-3-50® for comparison. As shown in Figure 11, the M1.7-based battery exhibited slightly higher peak power density than the commercial reference FAA-3-50® (258 vs. 254 mW cm^{2}) at about 360 mA cm^{-2} with a standard flow rate of 16 mL min^{-1}. The linear relation of voltage and current density at low current densities suggests low activation overpotentials at the electrodes [60]. The cell voltages of M1.7 and FAA-3-50® both started to deviate slightly from the linear trend at current densities above 350 mA cm^{-2}, which suggested the gradual shift from loss caused by internal resistance to that by mass transport of the redox-active molecules. Therefore, the electrolyte flow rate was elevated to 24 mL min^{-1} in order to investigate the influence of mass transport. Increasing the flow rate showed minor effects on the polarization behavior of the M1.7-based cell. While the maximum power density at 16 and 24 mL min^{-1} revealed similar values (258 and 257 mW cm^{2}), the trend of the polarization curve becomes fully linear. It follows Ohm's law well. Hence, the performance of the test cell is dominated by its internal resistance and the resulting ohmic over-potentials. As these values mainly originate in the membrane resistance, effects of mass transport can be neglected. A test cell employing the reference membrane FAA-3-50® displayed a 4% increase of retrievable power density at current densities above 350 mA cm^{-2} and a deviation from linear voltage-current behavior. In this setup, the depletion of redox-active species is compensated by an increased electrolyte flow. However, as both test cells are dominantly defined by their membrane resistance, future research needs to focus on the preparation of AEMs with high chloride ion conductivity to further increase the retrievable power.

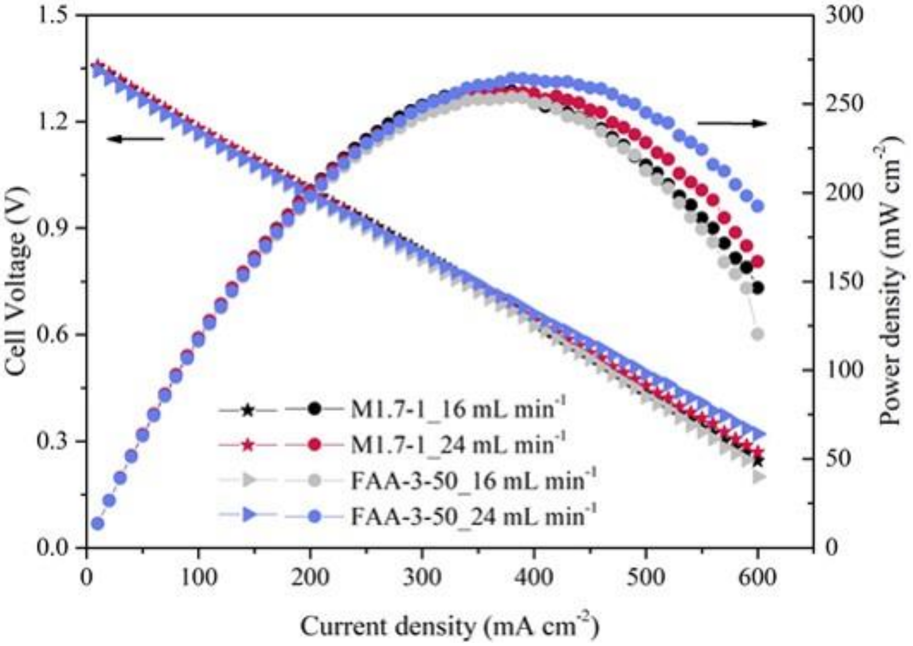

Figure 11: Discharging polarization curves and power densities of M1.7 and FAA-3-50® membranes over current density.

3.3.3. Membrane durability

To assess the long-term durability of the AEMs, the membrane resistances after the cell tests were recorded as a comparison to those before cell tests. As can be seen from Figure 12, the difference in the membrane resistance is small and remains within the error margin. This indicates the absence of membrane aging due to effects like a reduction of the IEC (due to ionic species loss), which would have caused an increase in resistance.

After cell disassembly, no observable breaks or holes appeared in all tested membranes. Morphology changes were further checked under the microscope. The mechanical deformation, which is visible on the surface of the membranes, is caused by the pressure applied on the membrane upon assembling the cell (Figure S2). The micrographs support the results found in the resistance measurement and suggest a good mechanical and chemical stability of the employed AEMs, benefiting from the noncorrosive nature of neutral electrolytes and the high chemical stability of the QA cations.

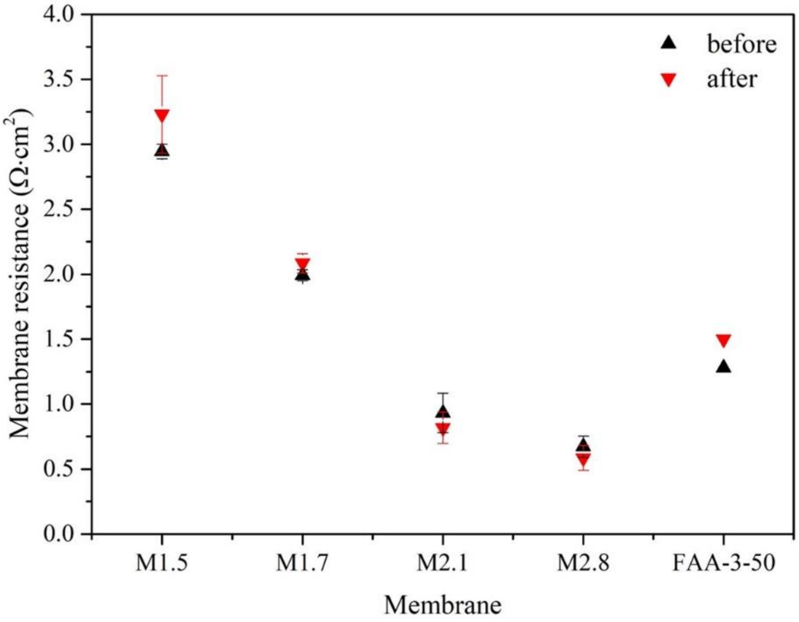

Figure 12: Membrane resistance of the four prepared AEMs and commercial membrane FAA-3-50® before and after the charge/discharge cycling tests.

4. Conclusions

In this study, five AEMs based on PPO grafted with various amounts of poly(DAPCl) cations were fabricated via a rapid UV-irradiation method and four of them were tested in a TMA-TEMPO/MV-based AORFB. Membranes with high IEC lead to higher water uptake, higher chloride mobility and lower membrane resistance. The membrane with low IEC and/or water uptake have been found to display low TMA-TEMPO/MV crossover and good capacity retention after 100 consecutive charging/discharging cycles. The M1.7 membranes with moderate membrane resistance and low crossover was found to display the best overall cell performance among the four tested membranes at high current density of 80 mA cm^{-2}, with highest capacity retention of 83.5 ± 0.5%, excellent CE of 99.5 ± 0.1% and moderate EE of 71.5 ± 0.5%. In this case, the IEC of M1.7 keeps a good balance of the chloride ion conductivity (2.22 ± 0.08 mS cm^{-1}) over water uptake (37 ± 1%), which are respectively related to membrane resistance and membrane crossover in cell performance. When all the results are comprehensively considered, the M1.7 membrane appears to have the highest applicability for AORFB because of having high power density and good retention capacity. Our results show quite a promising understanding on the correlations between the different membrane properties and their corresponding cell performance and stability. Therefore, further research efforts should be focused on preparing a more conductive or less resistant AEM with reduced electrolyte crossover, increased energy efficiency and increased power density.

References

[1] I.A.N. Whyte, P.R. Limited, Flow battery design, scale-up, and manufacture, in: 2018.

[2] Z.G. Yang, Status and Future Perspectives of Redox Flow Batteries, in: 2018.

[3] A.N. Colli, P. Peljo, H.H. Girault, High energy density MnO4-/MnO42- redox couple for alkaline redox flow batteries, Chem. Commun. 52 (2016) 14039–14042. doi:10.1039/c6cc08070g.

[4] S. Roe, C. Menictas, M. Skyllas-Kazacos, A High Energy Density Vanadium Redox Flow Battery with 3 M Vanadium Electrolyte, J. Electrochem. Soc. 163 (2016) A5023–A5028. doi:10.1149/2.0041601jes.

[5] J. Winsberg, T. Hagemann, T. Janoschka, M.D. Hager, U.S. Schubert, Redox-Flow Batteries: From Metals to Organic Redox-Active Materials, Angew. Chemie Int. Ed. 56 (2017) 686–711. doi:10.1002/anie.201604925.

[6] X. Wei, W. Pan, W. Duan, A. Hollas, Z. Yang, B. Li, Z. Nie, J. Liu, D. Reed, W. Wang, V. Sprenkle, Materials and Systems for Organic Redox Flow Batteries: Status and Challenges, ACS Energy Lett. 2 (2017) 2187–2204. doi:10.1021/acsenergylett.7b00650.

[7] S. Gentil, D. Reynard, H.H. Girault, Aqueous organic and redox-mediated redox flow batteries: a review, Curr. Opin. Electrochem. 21 (2020) 7–13. doi:10.1016/j.coelec.2019.12.006.

[8] S.R. Narayan, A. Nirmalchandar, A. Murali, B. Yang, L. Hoober-Burkhardt, S. Krishnamoorthy, G.K.S. Prakash, Next-generation aqueous flow battery chemistries, Curr. Opin. Electrochem. 18 (2019) 72–80. doi:10.1016/j.coelec.2019.10.010.

[9] V. Singh, S. Kim, J. Kang, H.R. Byon, Aqueous organic redox flow batteries, Nano Res. 12 (2019) 1988–2001. doi:10.1007/s12274-019-2355-2.

[10] J. Luo, B. Hu, M. Hu, Y. Zhao, T.L. Liu, Status and Prospects of Organic Redox Flow Batteries toward Sustainable Energy Storage, ACS Energy Lett. 4 (2019) 2220–2240. doi:10.1021/acsenergylett.9b01332.

[11] D.G. Kwabi, Y. Ji, M.J. Aziz, Electrolyte Lifetime in Aqueous Organic Redox Flow Batteries: A Critical Review, Chem. Rev. 120 (2020) 6467–6489. doi:10.1021/acs.chemrev.9b00599.

[12] T. Janoschka, N. Martin, M.D. Hager, U.S. Schubert, An Aqueous Redox-Flow Battery with High Capacity and Power: The TEMPTMA/MV System, Angew. Chemie Int. Ed. 55 (2016) 14427–14430. doi:10.1002/anie.201606472.

[13] G. Cong, Y. Zhou, Z. Li, Y.C. Lu, A highly concentrated catholyte enabled by a low-melting-point ferrocene derivative, ACS Energy Lett. 2 (2017) 869–875. doi:10.1021/acsenergylett.7b00115.

[14] H.S. Kim, T. Yoon, Y. Kim, S. Hwang, J.H. Ryu, S.M. Oh, Increase of both solubility and working voltage by acetyl substitution on ferrocene for non-aqueous flow battery, Electrochem. Commun. 69 (2016) 72–75. doi:10.1016/j.elecom.2016.06.002.

[15] H. Prifti, A. Parasuraman, S. Winardi, T.M. Lim, M. Skyllas-Kazacos, Membranes for Redox Flow Battery Applications, Membranes (Basel). 2 (2012) 275–306. doi:10.3390/membranes2020275.

[16] Y. Li, Y. Liu, Z. Xu, Z. Yang, Poly(phenylene oxide)-Based Ion-Exchange Membranes for Aqueous Organic Redox Flow Battery, Ind. Eng. Chem. Res. (2019). doi:10.1021/acs.iecr.9b01377.

[17] W. Zhou, W. Liu, M. Qin, Z. Chen, J. Xu, J. Cao, J. Li, Fundamental properties of TEMPO-based catholytes for aqueous redox flow batteries: effects of substituent groups and electrolytes on electrochemical properties, solubilities and battery performance, RSC Adv. 10 (2020) 21839–21844. doi:10.1039/D0RA03424J.

[18] K. Lin, Q. Chen, M.R. Gerhardt, L. Tong, S.B. Kim, L. Eisenach, A.W. Valle, D. Hardee, R.G. Gordon, M.J. Aziz, M.P. Marshak, Alkaline quinone flow battery, Science (80-.). 349 (2015) 1529–1532. doi:10.1126/science.aab3033.

[19] E.S. Beh, D. De Porcellinis, R.L. Gracia, K.T. Xia, R.G. Gordon, M.J. Aziz, A Neutral pH Aqueous Organic–Organometallic Redox Flow Battery with Extremely High Capacity Retention, ACS Energy Lett. 2 (2017) 639–644. doi:10.1021/acsenergylett.7b00019.

[20] B. Yang, A. Murali, A. Nirmalchandar, B. Jayathilake, G.K.S. Prakash, S.R. Narayanan, A Durable, Inexpensive and Scalable Redox Flow Battery Based on Iron Sulfate and Anthraquinone Disulfonic Acid, J. Electrochem. Soc. 167 (2020) 060520. doi:10.1149/1945-7111/ab84f8.

[21] Z. Yang, L. Tong, D.P. Tabor, E.S. Beh, M.-A. Goulet, D. De Porcellinis, A. Aspuru-Guzik, R.G. Gordon, M.J. Aziz, Alkaline Benzoquinone Aqueous Flow Battery for Large-Scale Storage of Electrical Energy, Adv. Energy Mater. 8 (2018) 1702056. doi:10.1002/aenm.201702056.

[22] T. Hagemann, J. Winsberg, M. Grube, I. Nischang, T. Janoschka, N. Martin, M.D. Hager, U.S. Schubert, An aqueous all-organic redox-flow battery employing a (2,2,6,6-tetramethylpiperidin-1-yl)oxyl-containing polymer as catholyte and dimethyl viologen dichloride as anolyte, J. Power Sources J. (2017). doi:10.1016/j.jpowsour.2017.09.007.

[23] R. Darling, K. Gallagher, W. Xie, L. Su, F. Brushett, Transport Property Requirements for Flow Battery Separators, J. Electrochem. Soc. 163 (2016) A5029–A5040. doi:10.1149/2.0051601jes.

[24] R.A. Potash, J.R. McKone, S. Conte, H.D. Abruña, On the Benefits of a Symmetric Redox Flow Battery, J. Electrochem. Soc. 163 (2016) A338–A344. doi:10.1149/2.0971602jes.

[25] B. Hu, C. Seefeldt, C. DeBruler, T.L. Liu, Boosting the energy efficiency and power performance of neutral aqueous organic redox flow batteries, J. Mater. Chem. A. 5 (2017) 22137–22145. doi:10.1039/C7TA06573F.

[26] L.J. Small, H.D. Pratt, T.M. Anderson, Crossover in Membranes for Aqueous Soluble Organic Redox Flow Batteries, J. Electrochem. Soc. 166 (2019) A2536–A2542. doi:10.1149/2.0681912jes.

[27] H.-S. Dang, E.A. Weiber, P. Jannasch, Poly(phenylene oxide) functionalized with quaternary ammonium groups via flexible alkyl spacers for high-performance anion exchange membranes, J. Mater. Chem. A. 3 (2015) 5280–5284. doi:10.1039/C5TA00350D.

[28] J. Ran, L. Wu, Y. Ru, M. Hu, L. Din, T. Xu, Anion exchange membranes (AEMs) based on poly(2,6-dimethyl-1,4-phenylene oxide) (PPO) and its derivatives, Polym. Chem. 6 (2015) 5809–5826. doi:10.1039/c4py01671h.

[29] M.G. Marino, K.D. Kreuer, Alkaline Stability of Quaternary Ammonium Cations for Alkaline Fuel Cell Membranes and Ionic Liquids, ChemSusChem. 8 (2015) 513–523. doi:10.1002/cssc.201403022.

[30] D.J. Strasser, B.J. Graziano, D.M. Knauss, Base stable poly(diallylpiperidinium hydroxide) multiblock copolymers for anion exchange membranes, J. Mater. Chem. A. 5 (2017) 9627–9640. doi:10.1039/c7ta00905d.

[31] J.S. Olsson, T.H. Pham, P. Jannasch, Poly(N,N-diallylazacycloalkane)s for Anion-Exchange Membranes Functionalized with N-Spirocyclic Quaternary Ammonium Cations, Macromolecules. 50 (2017) 2784–2793. doi:10.1021/acs.macromol.7b00168.

[32] L. Gu, H. Dong, Z. Sun, Y. Li, F. Yan, Spirocyclic quaternary ammonium cations for alkaline anion exchange membrane applications: An experimental and theoretical study, RSC Adv. 6 (2016) 94387–94398. doi:10.1039/c6ra22313c.

[33] T.H. Pham, P. Jannasch, Aromatic Polymers Incorporating Bis-N-spirocyclic Quaternary Ammonium Moieties for Anion-Exchange Membranes, ACS Macro Lett. 4 (2015) 1370–1375. doi:10.1021/acsmacrolett.5b00690.

[34] N. Li, T. Yan, Z. Li, T. Thurn-Albrecht, W.H. Binder, Comb-shaped polymers to enhance hydroxide transport in anion exchange membranes, Energy Environ. Sci. 5 (2012) 7888–7892. doi:10.1039/c2ee22050d.

[35] X. Tongwen, Y. Weihua, Fundamental studies of a new series of anion exchange membranes: Membrane preparation and characterization, J. Memb. Sci. 190 (2001) 159–166. doi:10.1016/S0376-7388(01)00434-3.

[36] H.W. Doughty, Mohr’s method for the determination of silver and halogens in other than neutral solutions, J. Am. Chem. Soc. 46 (1924) 2707–2709. doi:10.1021/ja01677a014.

[37] T. Xu, Z. Liu, Y. Li, W. Yang, Preparation and characterization of Type II anion exchange membranes from poly(2,6-dimethyl-1,4-phenylene oxide) (PPO), J. Memb. Sci. 320 (2008) 232–239. doi:10.1016/j.memsci.2008.04.006.

[38] L. Liu, G. Huang, P.A. Kohl, Anion conducting multiblock copolymers with multiple head-groups, J. Mater. Chem. A. 6 (2018) 9000–9008. doi:10.1039/C8TA00753E.

[39] A.L. Moster, B.S. Mitchell, Hydration and proton conduction in Nafion/ceramic nanocomposite membranes produced by solid-state processing of powders from mechanical attrition, J. Appl. Polym. Sci. 113 (2009) 243–250. doi:10.1002/app.30131.

[40] T. Janoschka, N. Martin, U. Martin, C. Friebe, S. Morgenstern, H. Hiller, M.D. Hager, U.S. Schubert, An aqueous, polymer-based redox-flow battery using non-corrosive, safe, and low-cost materials, Nature. (n.d.). http://www.nature.com/articles/nature15746 (accessed March 30, 2020).

[41] P. Coimbra, D. Fernandes, P. Ferreira, M.H. Gil, H.C. de Sousa, Solubility of Irgacure® 2959 photoinitiator in supercritical carbon dioxide: Experimental determination and correlation, J. Supercrit. Fluids. 45 (2008) 272–281. doi:10.1016/j.supflu.2008.01.014.

[42] B.D. Fairbanks, M.P. Schwartz, C.N. Bowman, K.S. Anseth, Photoinitiated polymerization of PEG-diacrylate with lithium phenyl-2,4,6-trimethylbenzoylphosphinate: polymerization rate and cytocompatibility, Biomaterials. 30 (2009) 6702–6707. doi:10.1016/j.biomaterials.2009.08.055.

[43] H.S. Dang, P. Jannasch, Alkali-stable and highly anion conducting poly(phenylene oxide)s carrying quaternary piperidinium cations, J. Mater. Chem. A. 4 (2016) 11924–11938. doi:10.1039/c6ta01905f.

[44] A.C. Tibbits, L.E. Mumper, C.J. Kloxin, Y.S. Yan, A Single-Step Monomeric Photo-Polymerization and Crosslinking via Thiol-Ene Reaction for Hydroxide Exchange Membrane Fabrication, J. Electrochem. Soc. 162 (2015) F1206–F1211. doi:10.1149/2.0321510jes.

[45] J. Han, L. Zhu, J. Pan, T.J. Zimudzi, Y. Wang, Y. Peng, M.A. Hickner, L. Zhuang, Elastic Long-Chain Multication Cross-Linked Anion Exchange Membranes, Macromolecules. 50 (2017) 3323–3332. doi:10.1021/acs.macromol.6b01140.

[46] J. Ran, L. Wu, B. Wei, Y. Chen, T. Xu, Simultaneous Enhancements of Conductivity and Stability for Anion Exchange Membranes (AEMs) through Precise Structure Design, Sci. Rep. 4 (2014) 1–5. doi:10.1038/srep06486.

[47] D. Bhowmik, N. Malikova, G. Mériguet, O. Bernard, J. Teixeira, P. Turq, Aqueous solutions of tetraalkylammonium halides: Ion hydration, dynamics and ion-ion interactions in light of steric effects, Phys. Chem. Chem. Phys. 16 (2014) 13447–13457. doi:10.1039/c4cp01164c.

[48] B. Hribar, N.T. Southall, V. Vlachy, K.A. Dill, How ions affect the structure of water, J. Am. Chem. Soc. 124 (2002) 12302–12311. doi:10.1021/ja026014h.

[49] M.T. Kwasny, L. Zhu, M.A. Hickner, G.N. Tew, Thermodynamics of Counterion Release Is Critical for Anion Exchange Membrane Conductivity, J. Am. Chem. Soc. 140 (2018) 7961–7969. doi:10.1021/jacs.8b03979.

[50] A. Montes-Rojas, J.A.Q. Rentería, N.B.J. Chávez, J.G. Ávila-Rodríguez, B.Y. Soto, Influence of anion hydration status on selective properties of a commercial anion exchange membrane electrochemically impregnated with polyaniline deposits, RSC Adv. 7 (2017) 25208–25219. doi:10.1039/c7ra03331a.

[51] P.-A. Bergstrom, J. Lindgren, O. Kristiansson, An IR Study of the Hydration of CI04", N03", Br, Cr, and S041 2" Anions In Aqueous Solution, 1991. https://pubs.acs.org/sharingguidelines (accessed April 27, 2020).

[52] S.J. Lue, S.-J. Shieh, Water States in Perfluorosulfonic Acid Membranes Using Differential Scanning Calorimetry, J. Macromol. Sci. Part B. 48 (2009) 114–127. doi:10.1080/00222340802561649.

[53] J.R. Varcoe, P. Atanassov, D.R. Dekel, A.M. Herring, M.A. Hickner, P.A. Kohl, A.R. Kucernak, W.E. Mustain, K. Nijmeijer, K. Scott, T. Xu, L. Zhuang, Anion-exchange membranes in electrochemical energy systems, Energy Environ. Sci. 7 (2014) 3135–3191. doi:10.1039/c4ee01303d.

[54] X. Luo, S. Rojas-Carbonell, Y. Yan, A. Kusoglu, Structure-transport relationships of poly(aryl piperidinium) anion-exchange membranes: Effect of anions and hydration, J. Memb. Sci. 598 (2020) 117680. doi:10.1016/j.memsci.2019.117680.

[55] J. Veerman, The Effect of the NaCl Bulk Concentration on the Resistance of Ion Exchange Membranes—Measuring and Modeling, Energies. 13 (2020) 1946. doi:10.3390/en13081946.

[56] R. Darling, K. Gallagher, W. Xie, L. Su, F. Brushett, Transport Property Requirements for Flow Battery Separators, J. Electrochem. Soc. 163 (2016) A5029–A5040. doi:10.1149/2.0051601jes.

[57] Q. Chen, L. Eisenach, M.J. Aziz, Cycling Analysis of a Quinone-Bromide Redox Flow Battery, J. Electrochem. Soc. 163 (2016) A5057–A5063. doi:10.1149/2.0081601jes.

[58] H. Chen, G. Cong, Y.-C. Lu, Recent progress in organic redox flow batteries: Active materials, electrolytes and membranes, J. Energy Chem. 27 (2018) 1304–1325. doi:10.1016/j.jechem.2018.02.009.

[59] D. Chen, M.A. Hickner, E. Agar, E.C. Kumbur, Optimizing membrane thickness for vanadium redox flow batteries, J. Memb. Sci. 437 (2013) 108–113. doi:10.1016/j.memsci.2013.02.007.

[60] D. Aaron, Z. Tang, A.B. Papandrew, T.A. Zawodzinski, Polarization curve analysis of all-vanadium redox flow batteries, J. Appl. Electrochem. 41 (2011) 1175–1182. doi:10.1007/s10800-011-0335-7.

Supplementary information

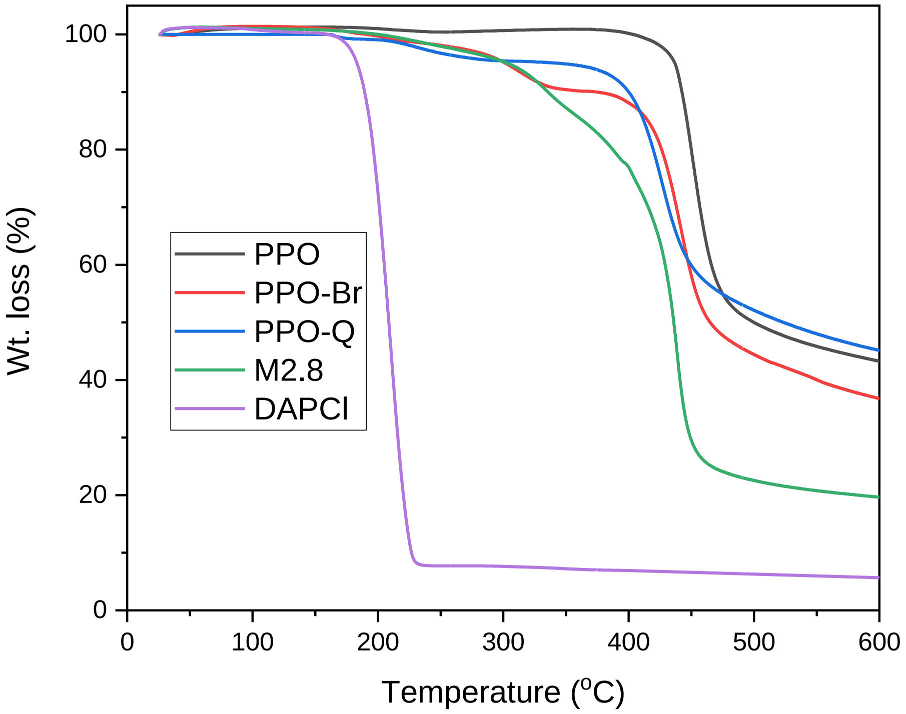

Figure S1: TGA curves of PPO, PPO-Br, PPO-Q, DAPCl and M2.8 measured under N_2 at 10 K min^{-1}.

Table S1: Summary of the membrane properties and cell performances of all tested AEMs.

Membrane	IEC	Thickness (μm)	Water uptake (%)	Cl^{-} conductivity (mS cm^{-1})	Membrane resistance (before/after, Ω·cm^{2})	CE (%)	EE (%)	Capacity (1st cycle, mAh at 20 mA cm^{2})	Accessible capacity (mAh, retention (%) at 80 mA cm^{-2})	Capacity (103rd cycle, mAh, retention (%) at 20 mA cm^{-2})
M1.5-1	1.58	39	30	1.30	3.000/3.630	99.0 [a]	63 [a]	331	119 (37)	327 (99)
M1.5-2	1.64	38	34	1.50	2.890/3.100	99.2 [a]	67 [a]	235	154 (45)	231 (98)
M1.7-1	1.84	46	38	2.30	1.950/2.160	99.4	71	294	199 (84)	259 (88)
M1.7-2	1.56	46	34	1.58	1.005/1.405	98.9	74	286	236 (31)	214 (75)
M1.7-3	1.72	44	36	2.15	2.035/2.010	99.6	72	300	215 (83)	263 (88)
M2.1-1	2.02	51	52	3.42	0.945/0.760	86.5	70	214	137 (77)	113 (53)
M2.1-2	1.98	58	48	3.30	1.110/0.985	97.1	74	173	148 (38)	76 (44)
M2.1-3	2.10	64	57	4.00	0.740/0.710	98.4	81	266	237 (49)	133 (50)
M2.8-1	2.78	56	106	4.42	0.730/x	96.5	75	255	190 (42)	69 (31)
M2.8-2	2.94	60	115	5.30	0.555/0.490	89.4	72	219	189 (23)	49 (22)
M2.8-3	2.81	62	110	4.82	0.730/0.680	95.8	74	174	142 (38)	60 (34)

M1.5-3 didn't cycle at 80 mA·cm^{-2} due to its high resistance.

x: not acquired. Hence, the average membrane resistance (0.585 ± 0.095 Ω cm^{2}) of M2.8 after the cell cycling test was calculated from M2.8-2 and M2.8-3.

[a]: Invalid data points, where capacities turned zero amid cycling, were removed from calculation of CE and EE of M1.5-1 and M1.5-2.

Micrographs of the AEMs

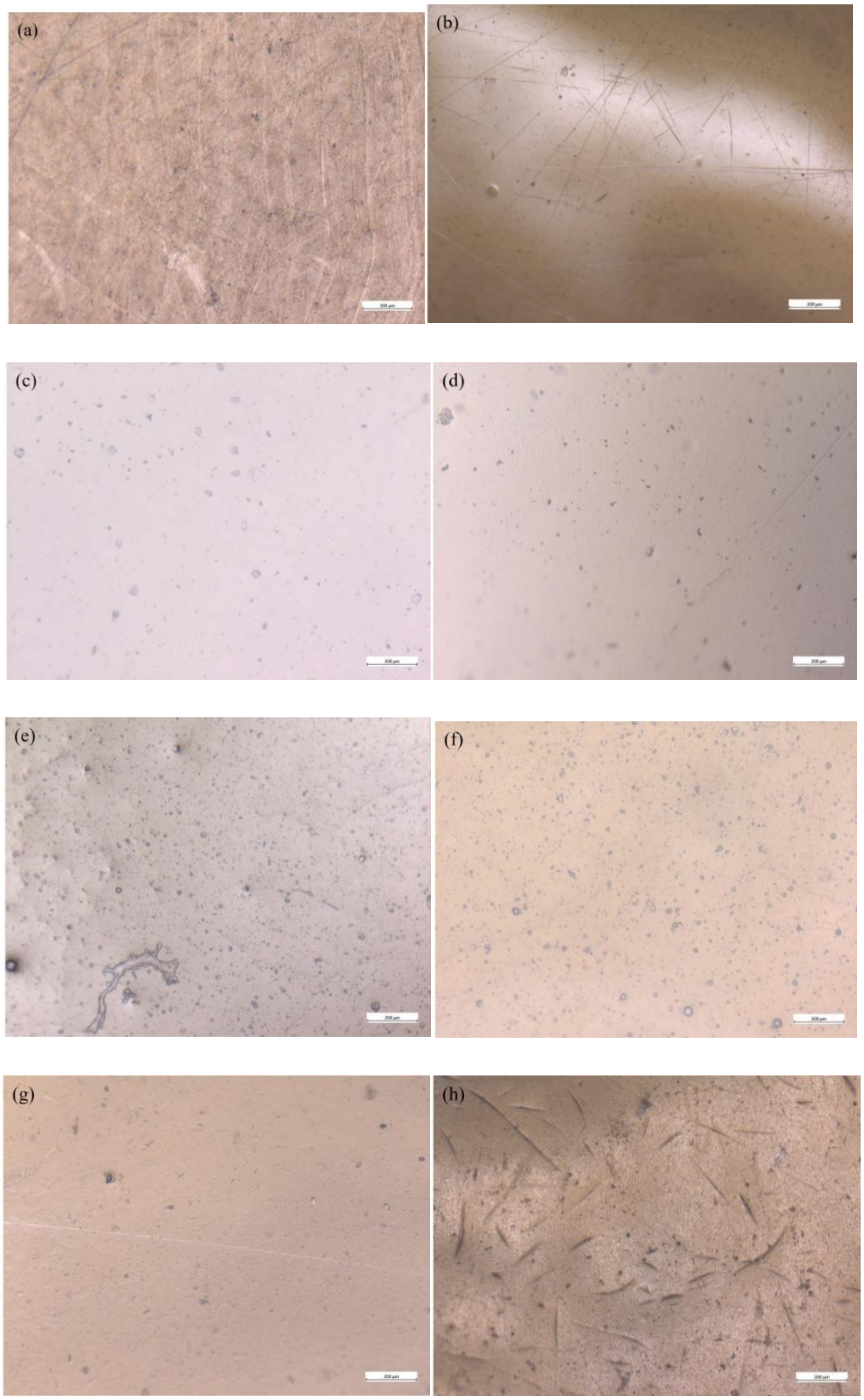

Figure S2: Micrographs of the AEMs before and after cell tests in wet form: (a) M1.5 before; (b) M1.5 after; (c) M1.7 before; (d) M1.7 after; (e) M2.1 before; (f) M2.1 after; (g) M2.8 before; (h) M2.8 after. Bar size: 200 µm.

Chapter 4: Anion exchange membranes with high power density and energy efficiency in neutral aqueous organic redox flow battery

1. Introduction

As discussed in the previous chapter, we investigated the detailed correlations between membrane properties and cell cycling performances by preparing series of AEMs containing the same chemical structure. The ion exchange capacity (IEC) of the membranes was varied to modulate the water uptake and ion conductivity of the membranes. Indeed, optimization of water uptake and chloride ion conductivity were key parameters for preparing AEM with a good battery efficiency and performance. Among the tested membranes, the membrane with a moderate membrane resistance and low crossover (named M1.7) exhibited excellent coulombic efficiency (>99%) and a power density that is similar with the well-performing commercial membrane (Fumatech® FAA-3-50)-based cell. The FAA-3-50®-based system permitted an energy efficiency and peak power density of 78% at 80 mA cm^{-2} and 258 mW cm^{-2}, respectively.

On the other hand, there are limited choice of commercially available AEMs that can be readily used in the system. Membranes designed for other applications, such as desalination and acid recovery are usually used [1–3]. Overall, synthesis of appropriate membrane at a low-cost combining high ionic conductivity and selectivity is utmost importance for widespread adoption and commercialization of high-performance, efficient and stable AORFBs [4]. However, in our previous study only the impact of IECs on the overall cell performance was studied, thus the impact of other key properties, such as crosslinking *vs* linear nature, chemical structure of side chain, type of cations and membrane thickness remains further investigation.

Inspired by our recent findings, we here envisioned a TMA-TEMPO/MV AORFB with high energy efficiency, peak power density and excellent coulombic efficiency by preparing and employing AEM with optimized water uptake and high chloride conductivity. Herein, a series of flexible AEMs composed of PPO with six carbon side chain spacer functionalized either with 1,4-diazabicyclo [2.2.2] octane (DABCO) or Trimethylamine (TMA) were fabricated and tested in the TMA-TEMPO/MV AORFB. Most of the prepared membranes involve a spacer between the polymer backbone and cation in order to provide a nanophase separated morphology with well-defined ionic channels [5] and increase the hydrophobicity of the membranes. Size of ionic channels and pore size determine the selectivity of ions transport in ion exchange membranes [6]. DABCO and TMA were chosen because of their commercial availability, easy incorporation onto the polymer backbone and the possibility of preparing cross-linked membranes when DABCO is used due to the presence of two tertiary amines in the DABCO cycles and possibility to control the crosslinking degree by the molar ratio between DABCO and brominate polymer side chain. Impact of various membrane composition and properties, such as IEC, polymer crosslinking degree, membrane thickness, cation type, presence/absence of a spacer and presence of tertiary amine on the overall performance and cycling stability of the TMA-TEMPO/MV AORFB were investigated in this work. For comparison purpose, the well-performing commercial FAA-3-50® membrane was used as a reference.

2. Experimental

2.1. Materials

Poly (2,6-dimethyl-1,4-phenylene oxide) (PPO) (Mn = 20,000 g mol^{-1}, Polydispersity = 2.5) was purchased from Polysciences Inc. Methanol (99.9%) was purchased from Fisher Scientific. *N*-Bromosuccinimide (NBS) (99%), 2,2'-azobis(2-methylpropionitrile) (AIBN) (98%), tetrahydrofuran (THF, ACS, >99%), 6-Bromohexanoyl chloride (97%), diethyl ether (99+ %), chloroform-d ($CDCl_3$-d, 99.9% D) and 1,4-diazabicyclo [2.2.2] octane (98%, DABCO) were purchased from Sigma-Aldrich. Dimethyl sulfoxide-d_6 (DMSO-d_6, 99.9%), $AlCl_3$ (98.5%, anhydrous), *N*, *N*-dimethylacetamide (DMAc, 99.0%) and *N*-Methyl-2-pyrrolidone (NMP, reagent grade) were supplied from Acros Organics. Chlorobenzene (ACS reagent, ≥ 99.5%) and Trimethylamine (TMA, 1 M soln. in THF) was bought from Alfa Aesar. MV and TMA-TEMPO were provided by JenaBatteries GmbH. All chemicals were used as received. The FAA-3-50® AEM was purchased from Fumatech GmbH.

2.2. Polymer synthesis

PPO-6CO-Br: In order to introduce the cation, commercial PPO (M_n = 20,000, M_w/M_n = 2.5) was first brominated either by the bromination of benzylic methyl resulting in bromomethylated PPO or by acylation resulting in bromohexanone PPO (a six-carbon pendant chain spacer). The synthesis of brominated PPO with a six-carbon spacer **(**PPO-6CO-Br), which was carried out based on a slight modification of the method described by Hibbs [7] and Parrondo et al. [8] is discussed first. PPO-6CO-Br polymers with 57, 33 and 15% degree of bromination were prepared. To prepare a PPO-6CO-Br with 33% degree of bromination, 5 g PPO (41.67 mmol polymer repeat units) was dissolved in 200 mL of chlorobenzene in a round bottom flask and flushed with argon. The reaction flask was chilled in an ice bath for about 30 min. Subsequently, 9.6 mL of 6- bromohexanoyl chloride (62.7 mmol) and 2.5 g of $AlCl_3$ (Lewis acid catalyst, 18.75 mmol) were added. Finally, the cold bath was removed, and the stirred reaction mixture was allowed to react at room temperature for 24 h. The PPO-6CO-Br polymer was precipitated in methanol (1 L). It was then dried under vacuum at 60 ˚C for 24 h. A white solid product was obtained (7.2 g, 97.3% yield). The polymer had approximately 0.33 mol of bromomethyl groups per polymer repeats unit. The followed protocol is summarized in Scheme 1. Similar protocol was followed to prepare the PPO-6CO-Br polymer with 57% and 15% degree of functionalization. More precisely, to prepare the PPO-6CO-Br with 57% degree of bromination, the same amounts of 6-bromohexanoyl chloride and $AlCl_3$ were used to brominate 2.5 g of PPO. Whereas, for the bromination of PPO-6CO-Br with 15% degree, 4.8 mL 6-bromohexanoyl chloride and 1.25 g $AlCl_3$ were used for 5 g PPO. The degree of bromination/functionalization was determined from the ^1H NMR peak areas.

PPO-Br: A brominated PPO polymer without spacer (PPO-Br) in which the Br was directly bonded in the benzylic position was also prepared following a protocol discussed in chapter 3. The PPO-Br prepared in the current work has a 26.5% degree of bromination.

2.3. Fabrication of membranes

In total, eight membranes were prepared and named from M1 to M8. Table 1 summarizes the composition and nomenclature of the membranes. For the cross-linked (M1 and M2) membranes, simultaneous quaternization and membrane preparation procedure was followed. The ratio between the quantity of bromomethyl groups in the PPO-6CO-Br polymer and DABCO was varied to prepare membranes with different degree of crosslinking. For instance, to prepare M1 using PPO-6CO-Br polymer with degree of functionalization of 57%, 0.15 g of PPO-6CO-Br (0.387 mmol Br units) was dissolved in 2 mL DMAc. Subsequently, 0.0135 g DABCO (0.12 mmol) (in solution of 1 mL DMAc) was added dropwise under stirring for 40 min at 80 °C to initiate and promote crosslinking. The prepared solution mixture was degassed under reduced pressure, poured onto a 5 cm diameter petri dish and kept in a 60 °C drying oven for 24 h to ensure the simultaneous cross-linking and quaternization reaction. In order to replace the remaining Br units, the dry membrane was then immersed in DI water containing (3% molar excess with respect to the Br units in PPO-6CO-Br) TMA for 24 h. A similar procedure was followed for the synthesis of M2 membrane, 0.125 molar excess of DABCO with respect to the Br units in the polymer was used.

Whereas, for the linear polymers DABCO-based membranes (M3 – M6), slightly different procedure was followed. In short, the PPO-6CO-Br polymer with 33%-degree bromination and the DABCO were dissolved in DMAc (7 wt./v%). The DABCO was added in excess (see Table 1) to avoid crosslinking. As discussed for the other membranes, the solution containing the polymer and DABCO was stirred for 24 h and poured onto a petri dish. It was kept in a 60 °C drying oven for 24 h to ensure the complete quaternization and solvent evaporation. To remove the excess amines and remaining solvents, the dried membranes were soaked in deionized water for 24 h. To prepare M5, dry M4 was re-dissolved in DMAc and an excess iodomethane was added to quaternize the free tertiary amine. Whereas for the M6, PPO-6CO-Br polymer with lower degree of bromination (15%) was used. For the TMA-based membranes (M7 and M8), the brominated polymers were first dissolved in the respective solvents (7 wt./v%); PPO-6CO-Br in DMAc and PPO-Br in NMP (as the polymer was not completely soluble in DMAc). For example, to prepare M7, 0.15 g of PPO-6CO-Br was dissolved in DMAc (7 wt./v%), and TMA (3% molar excess with respect to the Br units in the polymer) was added to the container. The procedure followed to prepare the membranes are schematically represented in Scheme 1.

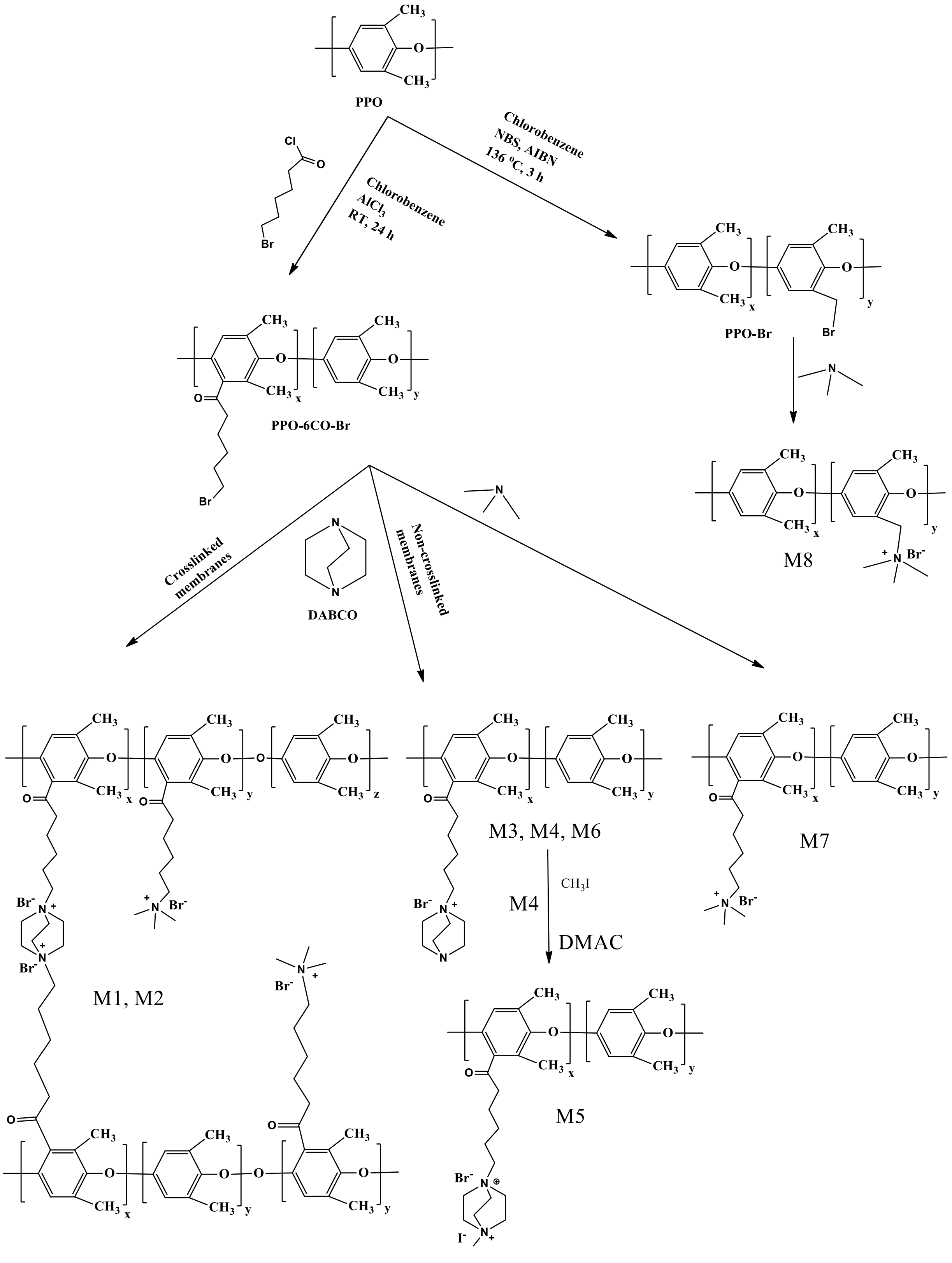

Scheme 1: Schematic representation of the syntheses of the different AEMs based on PPO-Br and PPO-6CO-Br polymers. Bromide and iodine ions in all membranes were replaced by chloride ions for further characterizations and cell tests.

Table 1: Composition and nomenclature of the AEM prepared.

Membrane	Polymer (degree of bromination)	Cation	(mol amine)/(mol Br units in the polymer)
M1	PPO-6CO-Br (57%)	DABCO + TMA	0.31 + (3x)*
M2	PPO-6CO-Br (57%)	DABCO + TMA	0.125 + (3x)*
M3	PPO-6CO-Br (33%)	DABCO	3x
M4	PPO-6CO-Br (33%)	DABCO	2x
M5	PPO-6CO-Br (33%)	DABCO	2x
M6	PPO-6CO-Br (15%)	DABCO	2x
M7	PPO-6CO-Br (33%)	TMA	3x
M8	PPO-Br (26%)	TMA	3x

*Values in brackets are amount of TMA used with respect to the Br units in the polymer

2.4. Characterizations

2.4.1. Structural characterization

^{1}H NMR spectroscopy was used to determine the structure of the polymers and membranes. A Bruker AV 400 NMR spectrometer was used to record the ^{1}H NMR spectra. DMSO-d_6 (δ = 2.50 ppm) or $CDCl_3$ (δ = 7.26 ppm) were used as NMR solvents.

2.4.2. Chloride ion conductivity, ionic exchange capacity and water uptake

The prepared membranes were converted to Cl^- form in a saturated NaCl (1 M) aqueous solution at room temperature for 48 h followed by immersing in excess deionized water overnight to remove the excess of salt. The Cl^- ion conductivity, IEC, water uptake and hydration number (λ) of the prepared membranes were measured as discussed in chapter 3. The values reported are an average of at least three measurements.

2.4.3. Degree of crosslinking

The degree of crosslinking of the M1 and M2 membranes was calculated from the feed DABCO (crosslinker) and brominated polymer using the following equation (1):

$$DC(\%) = \frac{mol_{DABCO}}{mol_{Br}/2}\ x\ 100 \qquad (1)$$

Where mol_{DABCO} and mol_{Br} are the amounts of DABCO (mol) added and bromine groups (mol) in the polymer, respectively.

2.4.4. Organic flow battery single cell tests

All membranes were investigated in a standard lab-scale flow battery single cell with an active area of 5 cm^2 (JenaBatteries GmbH), which was reported previously [9,10]. The charge-discharge cycling, polarization curve and cyclic voltammetry measurements were performed as discussed in chapter 3. In short, since current density directly affects the observed capacity, the first charge-discharge cycle of all cells was carried out at a current density (20 mA cm^{-2}) low enough to ensure that full capacity can be achieved. Then the current density was increased to 80 mA cm^{-2} and maintained for 100 consecutive charge-discharge cycles. Finally, the current density dropped back to 20 mA cm^{-2} and held for two cycles. This program will enable to differentiate the influence of resistance and crossover on capacity. The only difference in the current work was that during the polarization curve measurements the cycled membranes were assembled in a second cell with fresh electrolytes and ten charge-discharge cycles were performed utilizing the same protocol as described in the previous chapter to reach a well-compatible condition for measuring the polarization curve.

3. Results and discussion

3.1. Polymers and membranes preparation

The successful bromination and degree of functionalization of PPO brominated in the benzylic position (PPO-Br) was confirmed by analysis of ^{1}H NMR spectrum (Figure 1). The degree of functionalization was determined from the ratio of the integrals of characteristic peak of protons of $–CH_2Br$ at 4.3 ppm (Figure 1b, peak b) and the remaining unbrominated CH_3 groups (Figure 1b, peak a). The calculated bromination degree was 26.5%, which corresponds to a bromination yield of 65%. The functionalization of PPO with bromohexanone using 6-bromo-1-hexanoyl chloride in a Friedel–Crafts acylation was also determined by ^{1}H NMR (Figure 1c). Specifically, the peak at 3 ppm (peak i) represents the protons adjacent to the ketone group. Whereas, the protons in the bromomethyl group are shown in peak at 3.4 ppm (peak e). The degree of functionalization was found to be 33%. Similar method was used to determine the degree of functionalization in the other brominated polymers with 57 and 15% of degree of functionalization.

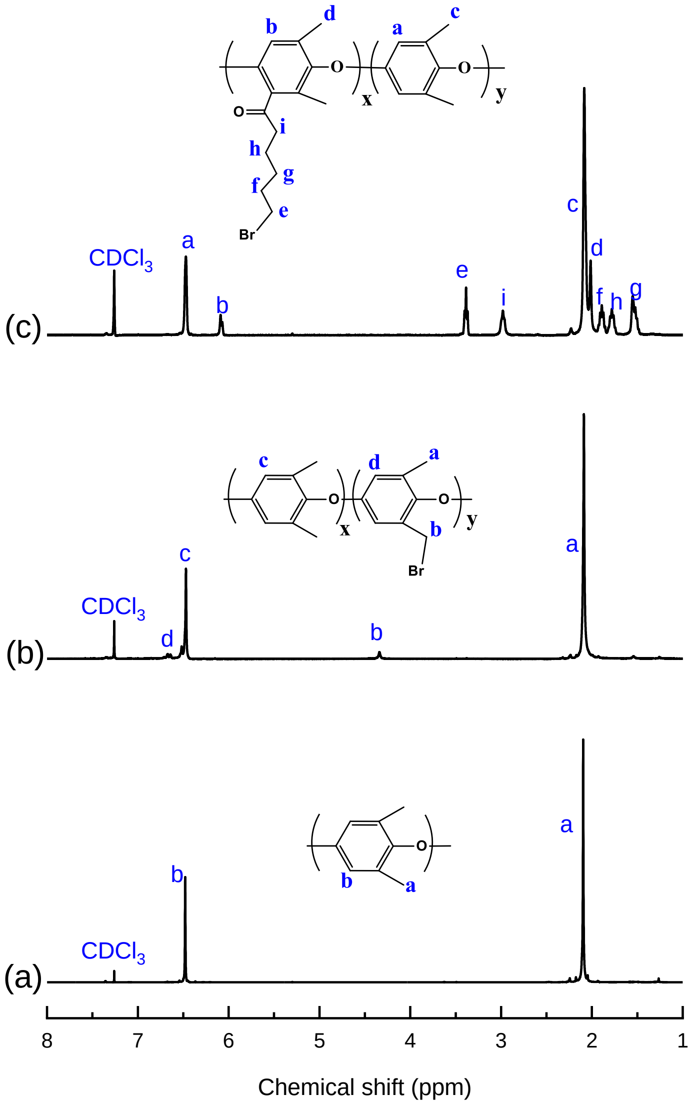

Figure 1: ^{1}H NMR spectra of (a) PPO, (b) PPO-Br (y = 0.265%) and (c) PPO-6CO-Br (x = 0.33) polymers.

The polymer bromination was followed by quaternization with DABCO or TMA. The complete substitution of the bromine units in the polymer by the quaternary ammonium groups and formation of the desired product was confirmed by the ^{1}H NMR for the non-cross-linked products. The ^{1}H NMR spectra of M4, M7 and M8 are shown in Figure 2 as representative of the membranes. In the case of M8 and M7 membranes, peaks corresponding to the methyl protons of the $–N^+(CH_3)_3$ quaternary ammonium groups appeared and are shown in peak d (Figure 2a) and j (Figure 2c), respectively. Similarly, the replacement of the Br units by DABCO was confirmed by ^{1}H NMR spectrum in the case of M4 (Figure 2b). The characteristic signal corresponding to DABCO appeared at 3.27 (peak j) and 2.99 ppm (peak k).

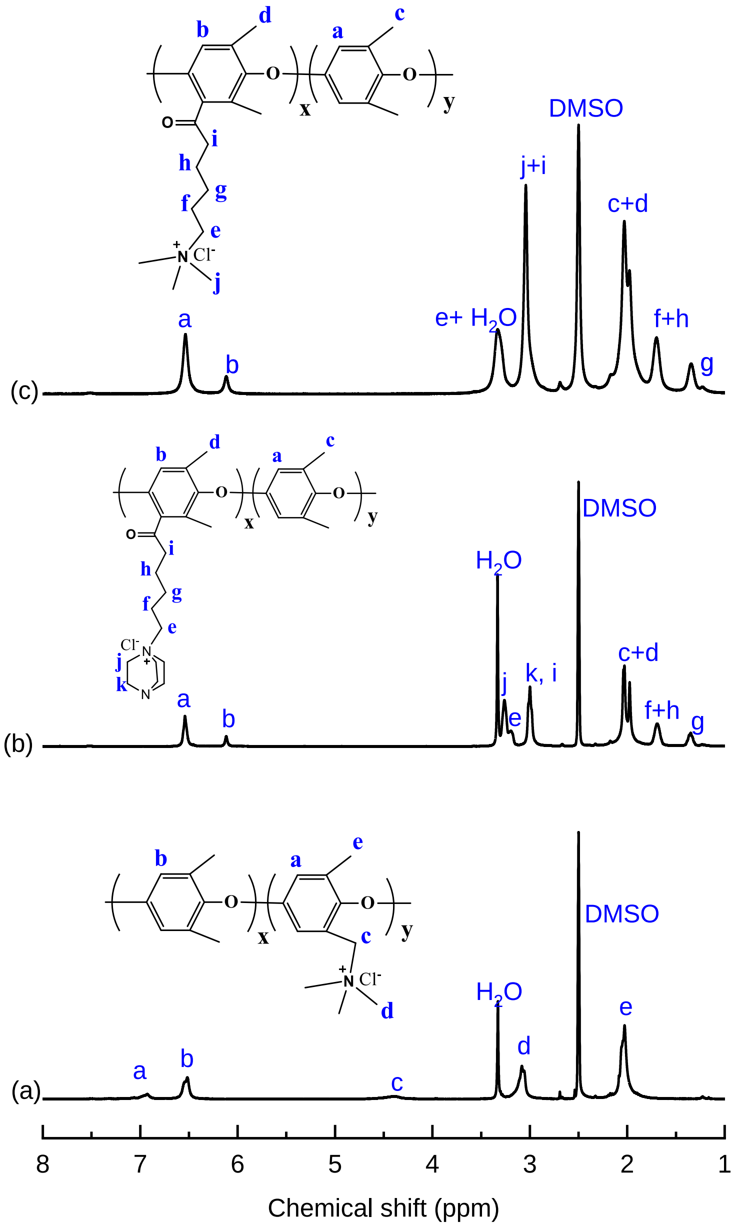

Figure 2: ^{1}H NMR spectra of membranes: (a) M8, (b) M4 and (c) M7 membranes.

3.2. Membranes *ex-situ* characterization

The eight self-standing prepared AEMs in Cl^- form were characterized in terms of their thickness, IEC, water uptake and ion conductivity and are summarized in Table 2. The values of IEC determined by titration were very close to those calculated from ^{1}H NMR, confirming the full quaternization of brominated PPO polymer precursors.

Water uptake is another key factor affecting the ion conductivity, the dimensional stability and cross contamination of redox active chemical species membranes [1]. In our previous work, we have shown that membranes with high water uptake were associated with high capacity fade in the TMA-TEMPO/MV AORFBs (see chapter 3). At the same time, an optimum water uptake play a significant role in formation of percolating conducting domain phase and enhancing the ion conductity of the membrane [11].

Table 2 : Membranes ex-situ characterizations: Thickness, IEC, water uptake and Cl^- ion conductivity

Membrane	Thickness (μm)	IEC (mmol Cl^- g^{-1})		Water uptake (wt. %)	Cl^- conductivity (mS cm^{-1})	Hydration number (λ)
		^{1}H NMR	Titration			
M1	82	2.50*	2.5	8	1	1.8
M2	28	2.49*	2.5	10	0.75	2.2
M3	130	1.65	1.63	64	6	22
M4	60	1.65	1.64	42	5	14
M5	60	3.05	3.0	95	30	17.6
M6	60	0.96	0.95	19	3	11
M7	60	1.8	1.79	25	4.3	8
M8	60	1.8	1.8	20	2.1	6
FAA-3-50®	50	1.6 - 2.1**	n.a.	17	1.7	5***

*Based on the degree of polymer bromination.

**Data taken from the technical datasheet provided by the manufacturer.

***The average value of IEC range (1.6 ~ 2.1) is 1.85 mmol Cl g^{-1}, which is used for calculating its hydration number (λ).

The wate uptake of the membranes (Table 2) seems to depend on the degree of crosslinking and IEC. Despite the high IECs of the M1 and M2 membranes, they exhibited low water uptakes which can be explained by the crosslinked structrue of the membranes. The theoretical degree of crosslinking of M1 and M2 membranes is estimated (equation 1) to be 31 and 12.5 %, respectively. As a result, the hydration numbers (λ) were found to be only about 2. As expected the water uptakes of linear DABCO-based membranes (M4, M5, M6) increased with their IECs. In M5 membrane, the two amines from DABCO are quaternized, thus it exhibited the highest IEC (3 mmol Cl^- g^{-1}) and water uptake (95%). Whereas the membrane with the lowest IEC (M6, 0.95 mmol Cl^- g^{-1}) displayed the lowest water uptake (19 wt.%). As a result, the λ of M6, M4 and M5 was found to be 11, 14 and 17.6.

As shown in Table 2, M4 reaches a bit lower water uptake and chloride ion conductivity than M3 with the same chemical structure and IEC, yet halves the thickness. This could be due to changes in the morphology of the membrane or potential formation of free volumes during the elaboration process due to the utilization of higher amount of DABCO that will be washed from the membrane. Indeed, the thickness might have influenced the homogeneity of the quaternization reaction in the depth of the membrane and the evaporation rate of the solvent during the drying process.

The TMA-based membranes with the same IEC, M7 and M8, exhibited water uptakes of 25 and 20 wt.%, respectively. The slight higher water uptake in the case of M7 could be due to the presence of 6-C side chain spacer that allow the formation of well-clustered ionic domains which promotes distinct water rich domains [12]. As a result, the λ of M7 (8 water molecules per ionic function) was higher than that of M8 (6 water molecules per ionic function). On the other hand, the commercial FAA-3-50® membrane displayed a low water uptake (17 wt.%) and λ (5 water molecules per ionic function). However, its chemical structure is not known, thus difficult to compare with the prepared membranes.

Membrane with high Cl^- ion conductivity is important for having an AORFB with high power density. The Cl^- ion conductivity of the memrbanes, measured at room temperature, are also summarized in Table 2. Among all the membranes, M5 recorded an outstanding Cl^- ion conductivity of 30 mS cm^{-1}. This extremely high value could be attributed to the very high IEC (since both amine units of DABCO are quaternized) and water uptake of the membrane. However, the membrane was brittle, especially in dry form. The high-water uptake induced swelling degree might have compromised the mechanical integrity of the membrane. M1 and M2 membranes have only about 1 mS cm^{-1} Cl^- ion conductivity due to their low water uptakes, only two water molecules per ionic function, which reduces both the ionic dissociation and the Cl^- ion mobility, in addition the crosslinked structure of the membranes constrains the dynamic of the system, thus the mobility of the ionic species [13]. Whereas, the conductivities of M4, M5 and M6 agreed with their IEC and water uptake. The Cl^- ion conductivity of M7 was two times higher than that of M8 membrane. This could be due to the presence of a spacer in the former membrane, which is known to promote hydrophilic-hydrophobic nanophase separation [13–15] and thus a more efficient ionic conductive channels. Similar increase of ionic conductivity by introducing a spacer between a polymer backbone and cation has been reported elsewhere [8]. On the other hand, the reference FAA-3-50® membrane had a lower Cl^- conductivity of 1.7 mS cm^{-1} at room temperature, due to its low water uptake and IEC.

3.3. Battery performance

All membranes listed in Table 2, except M5 which was brittle, were investigated in the TMA-TEMPO/MV based AORFB single cell. Tables S1 and S2 summarize the cell performance of the prepared AEMs and of the reference membrane FAA-3-50 characterized by initial capacity, capacity retention after long-term cycling, efficiencies (CE, VE, EE), resistance and peak power density; all of which are thoroughly discussed in the following sections.

3.3.1. Membranes resistance

The resistance of the membranes was investigated in the TMA-TEMPO/MV based AORFB single cell, both before and after the charge-discharge cycling test. The results are in agreement with the membrane properties and structures (IEC, crosslinking/linear and thickness).

For instance, M1 and M2 displayed a rather high membrane resistance because of their low chloride ion conductivity, which is assigned to their cross-linked structures. Despite having a similar IEC, M3 showed a higher resistance than M4 due to its higher thickness, but the ratio is lower than 2 (thickness ratio: 2.1) as the M3 membrane is more conductive that M4. Surprisingly, M6 showed almost same resistance with M4 before cycling despite its much lower conductivity and a similar thickness. Despite the similarity of the two membrane resistances before cycling, the resistance of M6 was higher by more than 30% than that of M4 after the cycling. This could be due to the different swelling behavior of the membranes with cycling and time.

M7 showed much lower resistance than that of M8, well in line with the ex-situ ion conductivity, owing to the presence of the six-carbon spacer to the polymer backbone in the former membrane. Moreover, with similar IEC but much higher chloride ion conductivity than the reference membrane, M7 exhibited the same membrane resistance as FAA-3-50®. Together with a low water uptake like FAA-3-50®, M7 is expected to reach similar cell performance.

Table 3. In-situ membrane resistance in the TMA-TEMPO/MV based AORFB single cell system (5 cm^2 active area).

Membrane	Membrane resistance(Ω cm^2)	
	Before cell test	After cell test
M1	7.2	7.05
M2	5.45	6.85
M3	2.2	1.8
M4	1.4	1.3
M6	1.4	1.7
M7	1.3	1.4
M8	2.65	2.9
FAA-3-50®	1.3	1.5

3.3.2. Capacity retention

The capacity accessible at high currents (i.e., power capability at high over potentials) and capacity retention/fade of a flow battery cell over long-term operation indicates the capability of the system to deploy energy, compatibility of the redox-active materials and membrane as well as the stability of both. Being two key components in a flow battery system, redox-active molecules and membranes contribute equally to the accessible capacity (i.e. power capability) and capacity retention. The long-term cycling stability of TMA-TEMPO and MV based AORFB system has already been evidenced at concentration of 2 M in aqueous solution [9], providing a steady system for assessing and comparing the cell performance of the prepared AEMs.

The discharge capacities as a function of cycle number for all tested membranes are shown in Figure 3. Membranes M1 and M2 reveal a relatively low accessible capacity at high current density (80 mA cm^{-2}). This effect is a result of the high membrane resistance (Table 3), i.e., low chloride ion conductivity, which causes high over potentials. Since the resistance is influenced by temperature, small day-to-night temperature changes (<2 K) in room temperature have a strong impact on the cell performance, causing a waving capacity curve. Both membranes share similar trend in capacity fade, yet have different causes as indicated by resistance measurements and cyclic voltammograms (CV) acquired of the electrolyte solutions taken from the anolyte and catholyte compartment after the cycling experiments. The CV for M2 suggests only minor cross-contamination of TMA-TEMPO and MV. Therefore, the speed-up decay in capacity of the cell after 30th cycle stems from the increasing membrane resistance from 5.45 Ω cm^2 to 6.85 Ω cm^2. For the cell with M1, the membrane resistance did not change considerably and no crossover of TMA-TEMPO/MV was observed (Figure 3 (A) and (B)). In Figure 3 (A), the redox peak intensities of TMA-TEMPO with M1 is stronger than that before cell test, whereas in MV half-cell, the trend reversed. This is because water migrated from the TMA-TEMPO half-cell to the MV side driven by the osmosis pressure difference and electroosmotic drag. This cell was aborted because a gradual external leakage occurred from 40th cycle and not repeated due to the poor overall performance.

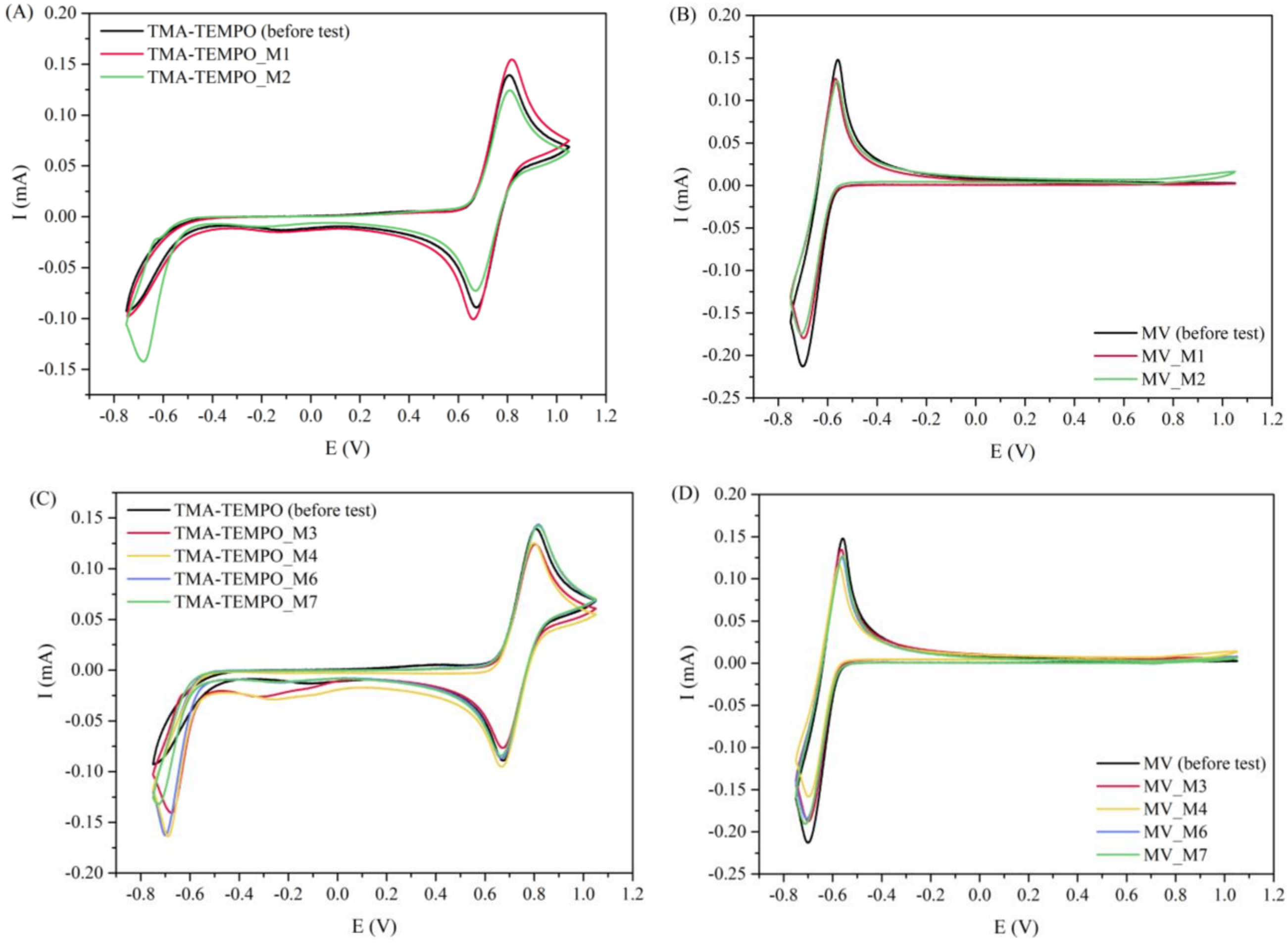

Figure 3: Cyclic voltammograms of the electrolyte solutions with the series of AEMs before and after the charge-discharge cycling tests: (A) TMA-TEMPO half-cell for membranes M1 and M2; (B) MV half-cell for membranes M1 and M2; (C) TMA-TEMPO half-cell for membranes M3, M4, M6 and M7; (D) MV half-cell for membranes M3, M4, M6 and M7. All samples were scanned within -0.75 and 1.05 V with a scan rate of 200 mV s^{-1}. Background signals were subtracted and the fourth scans were taken to prepare comparative graphs.

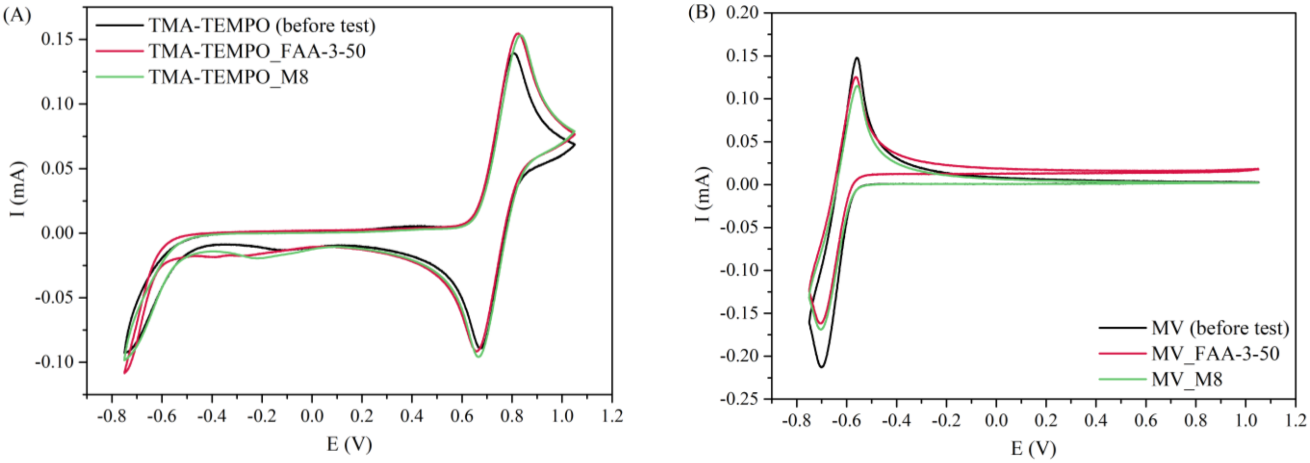

Figure 4: Cyclic voltammograms of the electrolyte solutions of a test cell using the reference FAA-3-50® and M8 membranes before and after the charge-discharge cycling tests: (A) TMA-TEMPO half-cell; (B) MV half-cell. All samples were scanned within -0.75 and 1.05 V with a scan rate of 200 mV s^{-1}. Background signals were subtracted and the fourth scans were taken to prepare comparative graphs.

After disassembling the test cells, M1 and M2 exhibited minor or no color change (Figure 6). In contrast, the active area of M3 was observed to be colored brown. The color change is probably attributed to the irreversible oxidation of the free tertiary amine groups of DABCO in M3 caused by the interaction with nitroxyl radical TMA-TEMPO [16–18]. The highly cross-linked membranes M1 and M2 bear nearly no free amine groups and are therefore protected from this oxidation process. M4 displayed an interesting capacity retention of 84% after 100 cycles at 80 mA cm^{-2}, whereas M3 exhibited only 74% partly because of the slightly higher membrane resistance. Compared to M3, the smaller number of free amines in M4 means that the polymer might have been less affected by the attack of the TMA-TEMPO redox couple.

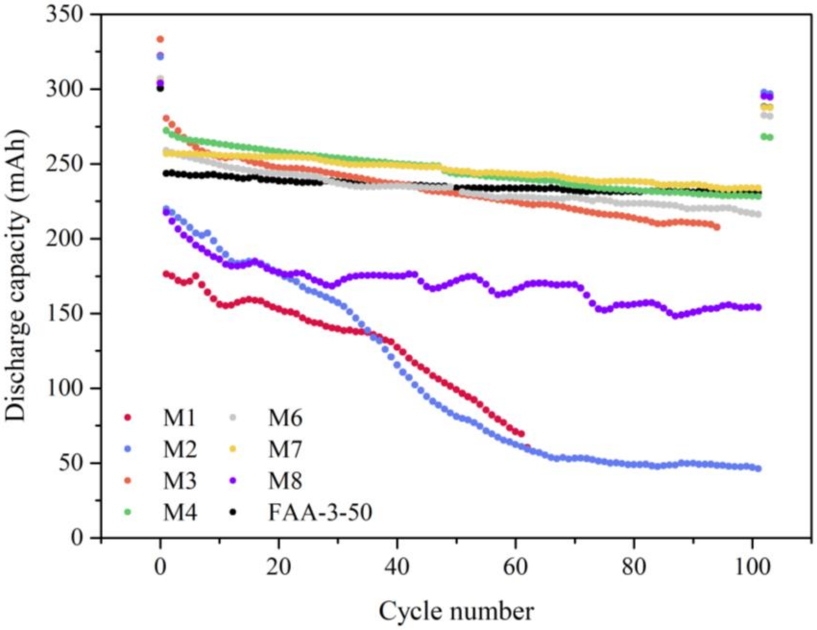

Figure 5: Discharge capacities of the TMA-TEMPO/MV based single cells with the series of prepared AEMs and the reference membrane FAA-3-50® over cycle number at different current densities. 10 mL 1.12 M TMA-TEMPO is used as the catholyte and 10 mL 1.49 M MV as the anolyte with flow rate of 16 mL min^{-1}. The first cycle was operated at 20 mA cm^{-2}, followed by 100 consecutive charge-discharge cycles at a constant current density of 80 mA cm^{-2}. The last two cycles were performed at 20 mA cm^{-2}.

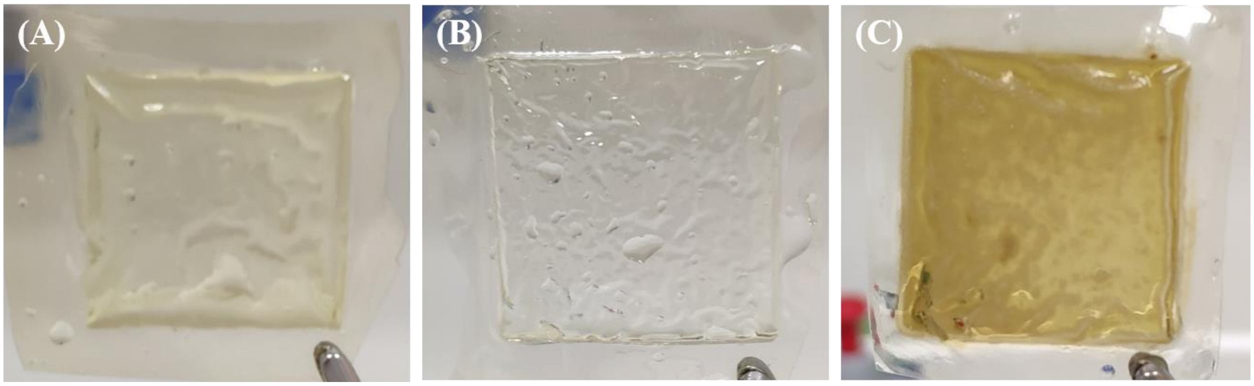

Figure 6: Photographs of membranes after the cell cycling tests. The protruding square is the tested area directly in contact with the electrodes and the electrolyte solutions: (A) M1, (B) M2 and (C) M3.

M3, M4, M6 and M7 all displayed good overall cell performance with low membrane resistance similar to the reference membrane and low water uptake to ensure low or no crossover. Among the four membranes, M3 shows the highest capacity fade upon long-term cycling. Small crossover of MV and TMA-TEMPO was observed, the main cause leading to the capacity fade is attributed to the irreversible reaction of the active species with the membrane. Yet, further evidence is needed to support this hypothesis.

Three membrane synthesis strategies were introduced to avoid the aging process: (i) M5 in which the free tertiary amines were fully quaternized on the basis of M4 and (ii) M6 with lower IEC in order to lower its water uptake and (iii) M7 with TMA replacing DABCO. Because of the mechanical instability, M5 was not tested in the cell. In the case of M6 membrane, the lower degree of functionalization of polymer backbone makes less free tertiary amine in the membrane exposed to TMA-TEMPO. Meanwhile, the good chloride ion conductivity and low water uptake of M6 guarantee its low membrane resistance (Table 3) and no cross-contamination (Figure 3(C) and (D)). Therefore, a high capacity retention (83%) at the current density of 80 mA cm^{-2} was observed for M6. It should be noted that this value is very close with the value obtained for M4. Therefore, lowering the IEC has not resulted in an improvement on the capacity retention.

As for M7 (third strategy used), when DABCO is replaced by TMA, it is not subjected to interaction with the nitroxy radical. The high ion conductivity of M7 resulted in low membrane resistance whereas its low water uptake maintains the selectivity for chloride ion. Therefore, the capacity and capacity retention of the cell with M7 at both low and high current densities preserved at the high level (over 90%). A capacity retention of 99.94%/cycle at 20 mA cm^{-2} was recorded, which is comparable to the best performing membranes (see chapter 2, Table 5). In other words, 94% of the capacity was available after the 100 cycles, which is a very promising result. Similarly, the commercial membrane FAA-3-50® also achieved high-level capacity retention at both current densities with low water uptake, yet a moderate chloride ion conductivity (1.70 mS cm^{-1}). As shown in Table S1, a capacity retention of 95% at 20 mA cm^{-2} was observed. As the exact polymer structure of FAA-3-50® is not publicly disclosed, it is hard to tell what exactly makes the difference, not to mention the complex nature of the microstructures of membranes.

With similar membrane properties as FAA-3-50®, M8 exhibited a higher capacity retention (97%) at 20 mA·cm^{-2}. However, the higher membrane resistance of M8, due to a low ionic conductivity, made it difficult to access the full capacity at a higher current density (80 mA cm^{-2}), only 71% of the capacity was available. The regular fluctuation in capacity is assigned to the waving temperature during summer time, as observed in an independent experiment with FAA-3-50® (Figure S1). Figure 4 shows the CVs of the electrolyte solutions of the test cell using FAA-3-50® and M8 membranes.

In summary, the best results for the TMA-TEMP/MV flow battery can be achieved when preventing membrane aging by quaternization of free amine groups, introducing a spacer to support the formation of water-rich domains and limiting the crosslinking to a moderate level. Capacity retention correlates strongly with the hydration number, the water uptake and chloride ion conductivity, suggesting aiming at membranes being well balanced between a good conductivity and sufficiently low water uptake.

3.3.3. Coulombic efficiency, voltage efficiency and energy efficiency

Coulombic efficiency (CE) indicates the degree of cross-contamination, which directly relates to the membrane ion selectivity. Voltage efficiency, expressed as mean discharging cell voltage divided by mean charging cell voltage at constant current, reflects the over potentials and resistance level of the system, which is strongly determined by the membrane resistance. As shown in Figure 7, all tested membranes exhibited excellent CE of over 99.3%, indicating a high membrane selectivity of chloride ion, which was further confirmed by the cyclic voltammograms of the electrolyte solutions taken from the test cell after the charge-discharge cycling tests (Figure 3).

As the CEs are almost identical for all the membranes (close to 100%), the voltage efficiencies (VEs) and energy efficiencies are close and mainly associated with the internal resistance, which in turn is dominated by the membrane resistance. The VEs of the cells with M1, M2, M3 and M8 reduced to different extent varying with the membrane area resistance (Table 3). M6 has a similar membrane resistance as FAA-3-50®, resulting in similar voltage efficiency. With slightly lower membrane resistance than FAA-3-50®, M4 and M7 displayed a bit higher voltage efficiency (80%) at 80 mA cm^{-2}. Therefore, the energy efficiency was enhanced to a certain level by further lowering the membrane resistance without sacrificing the membrane ion selectivity.

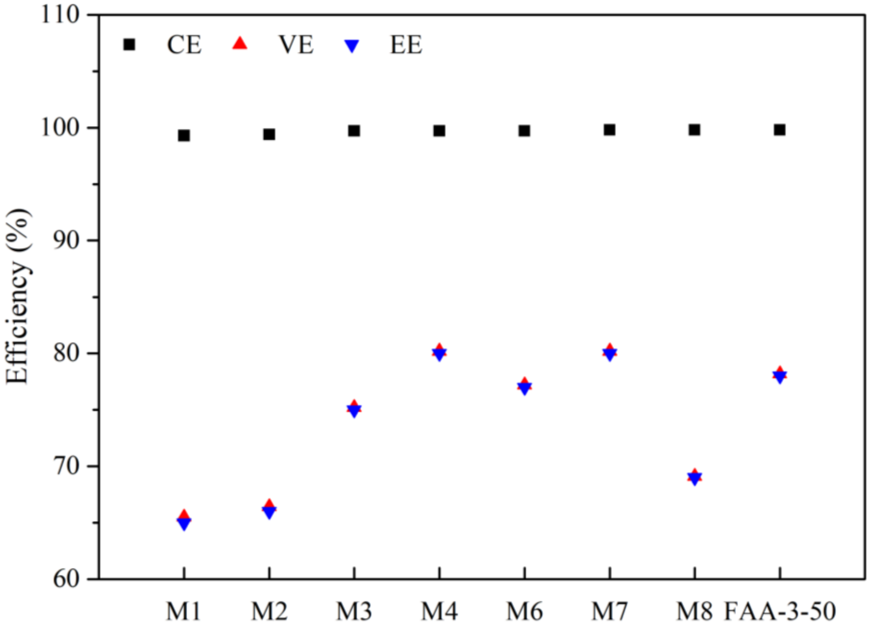

Figure 7: Mean coulombic efficiency (CE), voltage efficiency (VE) and energy efficiency (EE) of TMA-TEMPO/MV based single cells with the series of prepared AEMs and the reference membrane FAA-3-50® cycled over 100 cycles at a constant current density of 80 mA cm^{-2}.

3.3.4. Power density

Owing to their good battery performance, the power density of M3, M4, M6, M7, M8 and FAA-3-50® membranes were chosen for an in-depth study of their power capability. Therefore, polarization curves were acquired at two different flow rates (16 and 24 mL min^{-1}) after the cycling tests. Due to the well optimization of the system, unlike the Zn-air batteries, in the polarization curves of the AORFBs, the decrease of the potential is mainly due to the resistance of the cell, no other limitation associated with redox reaction and mass transport limitation in the range of the current density investigated.

As can be seen from Figure 5, the peak power densities of M3, M4, M6 and M7 were improved comparing to the reference membrane. Within the expectation, the peak power density of the tested membranes has a reverse relation to the corresponding membrane resistance (Table S2), except for M3, whose power density was probably influenced by the aging process upon interaction with the TMA-TEMPO redox couple. In a way to uncover the power density undisturbed from aging, the polarization curve of a freshly prepared M3 was recorded using fresh electrolytes. The peak power density of the cell with pristine M3 turned out to be 376 mW cm^{-2} at flow rate of 16 mL min^{-1}, promoted by 60% comparing to that of FAA-3-50®. As shown in Table S2, whereas, the aged M3 displayed a peak power density of 269 mW cm^{-2}.

With respect to the other membranes, the peak power densities were found to be in agreement with the ion conductivities (cell resistances since the membranes have same thickness) of the membranes. Accordingly, M4, M7, M6 and M8 delivered a maximum power density of 316, 293, 284 and 183 mW cm^{-2} at flow rate of 16 mL min^{-1}. While the order is expected, M8 membrane seems to be indeed affected by the absence of a flexible six-carbon spacer in its structure, it exhibited a low peak power in accordance to its lower ion conductivity (Table 2). The peak power density of cell with FAA-3-50® (235 mW cm^{-2}) is between that of M8 and M3 (aged), thus several of our membranes present better performances.

Finally, the influence of battery operating conditions was simulated by variation of the electrolyte flow. An increased mass transport is supposed to counteract the depletion of TMA-TEMPO and MV during the redox reaction. By increasing the flow rate from 16 to 24 mL min^{-1}, the peak power density of all tested membranes was raised by 1.4 to 4.7%. Hence, the cell with pristine M3 achieved the highest peak power density of 388 mW cm^{-2} at flow rate of 24 mL·min^{-1} for the TMA-TEMPO/MV system (Figure S2).

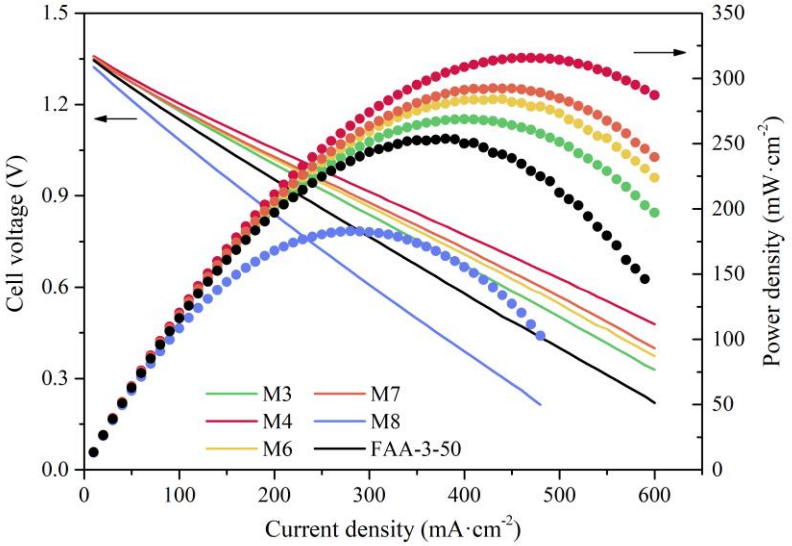

Figure 8: Power densities of the cells with membranes M3, M4, M6, M7, M8 and FAA-3-50® over different current densities at the flow rate of 16 mL·min^{-1} after the cycling tests.

Intended for practical application, we compared the highest peak power density value achieved in this work to those reported in different flow battery systems including the conventional vanadium system, semi-organic systems and all-organic systems. Technically, power density is determined by the cell voltage and the cell resistance including over potentials. Therefore, any factor in a battery that makes a difference to those two parameters can ultimately change the acquired power density. As the complex of methods and systems was involved in the literature, a comparison under the same condition is beyond possibility. Nevertheless, it allows us to assess the power capability achieved in this work for its practicability. To the best of our knowledge, the power density achieved with membranes M3 to M7 (except M5 is too brittle to test) is superior to the reported all-organic flow systems.

Comparing outside all-organic systems, the peak power density of 388 mW cm^{-2} in TMA-TEMPO/MV with M3 ranks in the middle in the listed systems. The main reason lies in the different nature of the membrane and the supporting electrolyte. While the system described above uses AEM and chloride ions, the literature examples employ highly conductive, but corrosive acid-based solutions (e.g. H_2SO_4) and cation exchange membranes. Hence, the results are within expectation and demonstrate that milder electrolyte solutions in combination with optimized membranes have become suitable for practical application.

Looking into detail, the extra high power density of 2780 mW cm^{-2} of VRFB system involved accumulated efforts on optimizing the flow field, electrode material, flow rate and membrane [19]. Similarly, in the semi-organic system employing 2,7-(anthraquinone-2,6-disulfonate) AQDS/Br_2, a peak power density of 1000 mW cm^{-2} was achieved in an optimized condition of electrolyte composition, electrode, membrane, flow rate and temperature. For instance, when the flow rate of VRFB system increased from 20 to 50 mL min^{-1}, the mass and ion transport was distinctly enhanced, which also significantly contributes to the ultimate power density [19]. By increasing from room temperature to 40 °C, the peak power density of the semi-organic system 2,7-$AQDSNa_2/Br_2$ could be elevated from 400 to 450 mW cm^{-2} [20]. In comparison, the peak power density achieved in this work is simply based on optimized membrane; other aforementioned parameters are beyond the scope of this work. Therefore, we are convinced that by further optimization of electrode, electrolyte composition, flow field design, flow rate and temperature, higher power density in TMA-TEMPO/MV based AORFB can be reached using the membranes presented here.

4. Conclusion

A series of eight AEMs based on PPO backbone varying the degree of functionalization, cation type and polymer architecture were prepared, followed by ex-situ membrane characterizations featured IEC, water uptake and chloride ion conductivity. M5, with high chloride ion conductivity of 30 $mS{\cdot}cm^{-1}$, turned out to be brittle, whose mechanical strength is expected to be compromised by its swelling degree. All other membranes were investigated in the TMA-TEMPO based ORFB single cell to probe how the cell performance is manipulated by polymer structure and the corresponding membrane properties. The partially crosslinked M1 and M2 membranes, despite the absence crossover of redox species, exhibited fast capacity fades with cycling and low energy efficiencies due to their high cell resistance. Whereas, the DABCO based linear membrane (with free tertiary amines) showed capacity fade following a permanent coloration of the membranes showing a possible interaction between the tertiary amine of M3 and the nitroxyl radical like TMA-TEMPO. M3 membrane with a high chloride ion conductivity (6 mS cm^{-1} at room temperature), thus when the 100 charge-discharge cycles were skipped, the measured peak power density of the membrane at 16 mL min^{-1} is extensively promoted by 60% as compared to the reference membrane FAA-3-50® (235 mW cm^{-2}), reaching a rather high power density of 376 mW cm^{-2}. When the aging issue is avoided or hindered by either lowering the degree of functionalization or replacing the DABCO cation, the resulting membranes M6 and M7 exhibited improved performance in capacity retention, energy efficiency as well as peak power density. Overall, the M7 membrane-cell achieved the best overall cell performance with appreciable high capacity retention (91% at current density of 80 mA cm^{-2} after 100 consecutive cycles) comparable with FAA-3-50®, delivered higher peak power density (293 mW cm^{-2} at 16 mL min^{-1}) and energy efficiency (80 vs 78%) than a well-performing commercial membrane FAA-3-50®. In addition, the production cost of M7 is estimated to be 4 € per 100 cm^2, which is much lower than that of FAA-3-50® (Table S3). These results will greatly contribute to the future market of ORFBs with competing low cost and high performance.

References

[1] L.J. Small, H.D. Pratt, T.M. Anderson, Crossover in Membranes for Aqueous Soluble Organic Redox Flow Batteries, J. Electrochem. Soc. 166 (2019) A2536–A2542. doi:10.1149/2.0681912jes.

[2] T. Hagemann, J. Winsberg, M. Grube, I. Nischang, T. Janoschka, N. Martin, M.D. Hager, U.S. Schubert, An aqueous all-organic redox-flow battery employing a (2,2,6,6-tetramethylpiperidin-1-yl)oxyl-containing polymer as catholyte and dimethyl viologen dichloride as anolyte, J. Power Sources. 378 (2018) 546–554. doi:10.1016/j.jpowsour.2017.09.007.

[3] B. Hu, C. Seefeldt, C. DeBruler, T.L. Liu, Boosting the energy efficiency and power performance of neutral aqueous organic redox flow batteries, J. Mater. Chem. A. 5 (2017) 22137–22145. doi:10.1039/C7TA06573F.

[4] X. Wei, W. Pan, W. Duan, A. Hollas, Z. Yang, B. Li, Z. Nie, J. Liu, D. Reed, W. Wang, V. Sprenkle, Materials and Systems for Organic Redox Flow Batteries: Status and Challenges, ACS Energy Lett. 2 (2017) 2187–2204. doi:10.1021/acsenergylett.7b00650.

[5] Y. Zhu, L. Ding, X. Liang, M.A. Shehzad, L. Wang, X. Ge, Y. He, L. Wu, J.R. Varcoe, T. Xu, Beneficial use of rotatable-spacer side-chains in alkaline anion exchange membranes for fuel cells, Energy Environ. Sci. 11 (2018) 3472–3479. doi:10.1039/C8EE02071J.

[6] I. Stenina, D. Golubenko, V. Nikonenko, A. Yaroslavtsev, Selectivity of Transport Processes in Ion-Exchange Membranes: Relationship with the Structure and Methods for Its Improvement, Int. J. Mol. Sci. 21 (2020) 5517. doi:10.3390/ijms21155517.

[7] M.R. Hibbs, Alkaline stability of poly(phenylene)-based anion exchange membranes with various cations, J. Polym. Sci. Part B Polym. Phys. 51 (2013) 1736–1742. doi:10.1002/polb.23149.

[8] J. Parrondo, M.J. Jung, Z. Wang, C.G. Arges, V. Ramani, Synthesis and Alkaline Stability of Solubilized Anion Exchange Membrane Binders Based on Poly(phenylene oxide) Functionalized with Quaternary Ammonium Groups via a Hexyl Spacer, J. Electrochem. Soc. 162 (2015) F1236–F1242. doi:10.1149/2.0891510jes.

[9] T. Janoschka, N. Martin, M.D. Hager, U.S. Schubert, An Aqueous Redox-Flow Battery with High Capacity and Power: The TEMPTMA/MV System, Angew. Chemie Int. Ed. 55 (2016) 14427–14430. doi:10.1002/anie.201606472.

[10] T. Janoschka, N. Martin, U. Martin, C. Friebe, S. Morgenstern, H. Hiller, M.D. Hager, U.S. Schubert, An aqueous, polymer-based redox-flow battery using non-corrosive, safe, and low-cost materials, Nature. 527 (2015) 78–81. doi:10.1038/nature15746.

[11] Q. Duan, S. Ge, C.-Y. Wang, Water uptake, ionic conductivity and swelling properties of anion-exchange membrane, J. Power Sources. 243 (2013) 773–778. doi:10.1016/j.jpowsour.2013.06.095.

[12] H.-S. Dang, E.A. Weiber, P. Jannasch, Poly(phenylene oxide) functionalized with quaternary ammonium groups via flexible alkyl spacers for high-performance anion exchange membranes, J. Mater. Chem. A. 3 (2015) 5280–5284. doi:10.1039/C5TA00350D.

[13] K. Yang, H. Ni, T. Shui, X. Chi, W. Chen, Q. Liu, J. Xu, Z. Wang, High conductivity and alkali-resistant stability of imidazole side chain crosslinked anion exchange membrane, Polymer (Guildf). 211 (2020) 123085. doi:10.1016/j.polymer.2020.123085.

[14] J. Liao, X. Yu, Q. Chen, X. Gao, H. Ruan, J. Shen, C. Gao, Monovalent anion selective anion-exchange membranes with imidazolium salt-terminated side-chains: Investigating the effect of hydrophobic alkyl spacer length, J. Memb. Sci. 599 (2020) 117818. doi:10.1016/j.memsci.2020.117818.

[15] C.X. Lin, X.L. Huang, D. Guo, Q.G. Zhang, A.M. Zhu, M.L. Ye, Q.L. Liu, Side-chain-type anion exchange membranes bearing pendant quaternary ammonium groups via flexible spacers for fuel cells, J. Mater. Chem. A. 4 (2016) 13938–13948. doi:10.1039/C6TA05090E.

[16] K. Sato, T. Ono, Y. Sasano, F. Sato, M. Kumano, K. Yoshida, T. Dairaku, Y. Iwabuchi, Y. Kashiwagi, Electrochemical Oxidation of Amines Using a Nitroxyl Radical Catalyst and the Electroanalysis of Lidocaine, Catalysts. 8 (2018) 649. doi:10.3390/catal8120649.

[17] A.L. Bartelson, K.M. Lambert, J.M. Bobbitt, W.F. Bailey, Recent Developments in the Nitroxide-Catalyzed Oxidation of Amines: Preparation of Imines and Nitriles, ChemCatChem. 8 (2016) 3421–3430. doi:10.1002/cctc.201600858.

[18] M.F. Semmelhack, C.R. Schmid, Nitroxyl-mediated electro-oxidation of amines to nitriles and carbonyl compounds, J. Am. Chem. Soc. 105 (1983) 6732–6734. doi:10.1021/ja00360a042.

[19] H.R. Jiang, J. Sun, L. Wei, M.C. Wu, W. Shyy, T.S. Zhao, A high power density and long cycle life vanadium redox flow battery, Energy Storage Mater. 24 (2020) 529–540. doi:10.1016/j.ensm.2019.07.005.

[20] A. Khataee, E. Dražević, J. Catalano, A. Bentien, Performance Optimization of Differential pH Quinone-Bromide Redox Flow Battery, J. Electrochem. Soc. 165 (2018) A3918–A3924. doi:10.1149/2.0681816jes.

Supplementary information

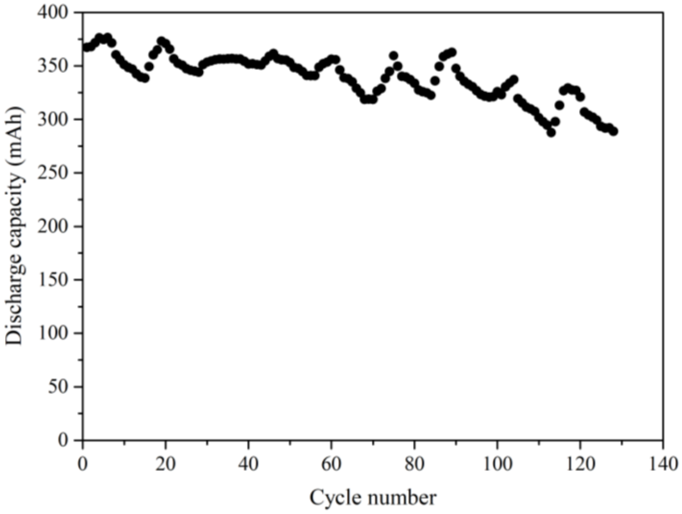

Figure S1: The discharge capacity of the cell with FAA-3-50® membrane over 128 consecutive charge-discharge cycles at 80 mA cm^{-2}. 20 mL of 1.12 M TMA-TEMPO is the catholyte and 20 mL of 1.49 M MV as the anolyte. The oscillation is caused by day-to-night temperature changes in a lab without temperature control in March.

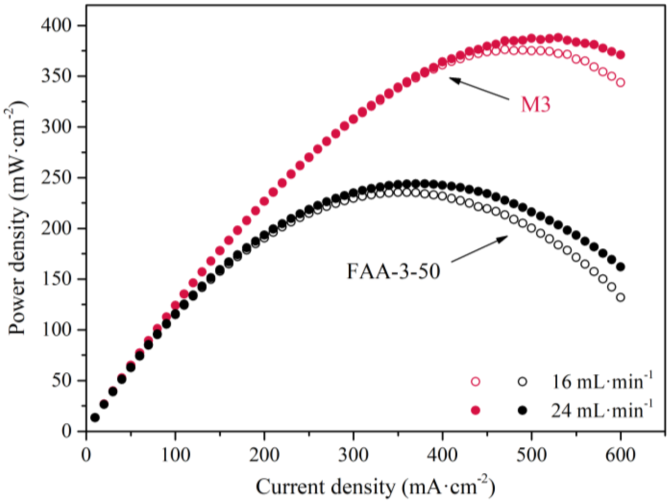

Figure S2: The power densities of the test cells employing membranes M3 and FAA-3-50® over different current densities at the flow rate of 16 and 24 mL min^{-1}. The cell was assembled with a fresh membrane and fresh electrolytes, cycled at 80 mA cm^{-2} for 10 times, followed by the polarization curve measurement.

Table S1: Cell performance of the series of the prepared AEMs and the reference membrane FAA-3-50® in the TMA-TEMPO/MV based organic flow battery single cell system.

Membrane	Membrane resistance (Ω) before/after	Capacity (mAh, 1st cycle, 20 mA cm^{-2})	Accessible capacity (mAh, 2nd cycle, 80 mA cm^{-2} (retention/%))	Capacity (mAh, 103rd cycle, 20 mA cm^{-2} (retention/%))	CE/%	EE/%
M1	1.437/1.413	322	177 (39)[a]	n.a.	99.3	65
M2	1.087/1.370	322	220 (21)	297 (92)	99.4	66
M3	0.437/0.362	333	280 (74)[b]	n.a.	99.7	75
M4	0.280/0.262	307	272 (84)	268 (87)	99.7	80
M6	0.284/0.335	307	259 (83)	282 (92)	99.7	77
M7	0.257/0.276	305	257 (91)	288 (94)	99.8	80
M8	0.528/0.579	304	217 (71)	295 (97)	99.8	69
FAA-3-50®	0.256/0.300	301	244 (94)	288 (95)	99.8	78

[a]: Apparent external leakage happened from 62th charge/discharge cycle, leading to immediate irreversible capacity fade. Hence, the capacity retention of this sample at 20 mA cm^{-2} is not available and the cycles after 62th are excluded from calculating the capacity retention, coulombic efficiency and energy efficiency at 80 mA·cm^{-2}.

[b]: Apparent external leakage happened from 94th charge/discharge cycle, leading to immediate irreversible capacity fade. Hence, the capacity retention of this sample at 20 mA cm^{-2} is not available and the cycles after 94th are excluded from calculating the capacity retention, coulombic efficiency and energy efficiency at 80 mA cm^{-2}.

Table S2: List of membrane chloride ion conductivity, membrane resistance and the power density at 16 and 24 mL min^{-1}.

Membrane	Chloride ion conductivity (mS cm^{-1})	Membrane resistance (Ω)	Power density (mW cm^{-2})* 16 mL min^{-1}	24 mL min^{-1}
M4	5.0	0.22	316	331
M7	4.3	0.28	293	297
M6	3.0	0.31	284	295
M3	6.0	0.28	269	277
M8	2.1	0.48	183	n.a.
FAA-3-50®	1.7	0.30	254	264

*: The standard protocol for measuring the polarization curve is described as 100c-10c-pc. It means that the cell was first cycled at 80 mA cm^{-2} for 100 times, disassembled and re-assembled with the tested membrane using fresh electrolytes. Before acquiring the polarization curve, the cell was cycled at 80 mA·cm^{-2} with the fresh electrolytes to initialize the system, followed by the polarization curve measurement at different current densities from 10 to 600 mA cm^{-2}.

Membrane cost

The cost of M7 with the best overall battery performance is listed in Table 4. PPO (5 g) was dissolved in chlorobenzene and then $AlCl_3$ and 6-bromo-1-hexanoyl chloride were added. The product was precipitated in methanol and dried in vacuum oven. The brominated product (7.2 g), dissolved in DMAC and quaternized with TMA. The final cost of the membrane was estimated to be 2.5 € for a 5 cm diameter membrane (19.63 cm^2). However, the purchase of the raw chemical was done at a lab-scale. Usually, the final cost is divided by about three as it is less expensive to purchase large amount of solvents and polymers. Therefore, the final cost of M7 could be estimated to be about 0.8 €/19.63 cm^2, which equals 4 €/100 cm^2. In contrast, the price for purchasing a 100 cm^2 of FAA-3-50® as acquired from the official website of Fumatech GmbH is 13.8 € (17 $). Therefore, M7 is a promising alternative for large production in terms of its good cell performance and low production cost.

Table S3: Cost estimation of M7 membrane in small scale.

Chemical	PPO	Chlorobenzene	6-Bromohexanoyl chloride	$AlCl_3$	Methanol	DMAC	TMA
Amount purchsed	100 g	200 mL	100 g	100 g	1 L	1 L	100 mL
Price/ €*	102.5	58.8	282.5	23.5	49.2	139	75.8
Amount used	5 g	200 mL	9.6 mL	2.5 g	1 L	103 mL	3.5 mL
Total price/ €			121 € **				

* 1 € = $1.23 conversion rate was used.

** Price for preparing 48 membranes (60 µm thickness) of 5 cm diameter, thus = 2.5 €/19.63 cm^2.

Part-II: Membranes for Zinc Slurry-air Flow Batteries

Chapter 5: Membranes for zinc-air batteries: Recent progress, challenges and perspectives

1. Introduction

The ever-increasing global concerns over environmental and energy issues, such as air pollution, climate change and fossil fuel depletion has triggered substantial development of renewable energy technologies, including wind energy, solar, tidal/ocean currents, wave energy, bioenergy, geothermal and hydropower [1–3]. Replacement of fossil fuels by renewable sources of energy is one of the major challenges, which humanity has been facing during the last years. On the bright side, it is estimated that the world could possibly reach 100% renewable electricity by 2032 if the current installation rate of photovoltaic cells and wind power is maintained [4].

However, the intermittent nature of these sources has a significant impact on the operation, making the match between energy supply and demand difficult. To address these problems, low-cost, energy-efficient, safe and large-scale energy storage systems are needed [3,5]. It is essential to level off the variation in the grid and securing a reliable, steady and efficient energy supply [6–8].

Various types of electrochemical energy storage technologies, including, Li-ion batteries [9–12], Pb-acid batteries [13–20], metal-air batteries [21–25], RFBs [5,26–30], fuel cells [31–36] and supercapacitors [37–42] have been developed. Nowadays, Li-ion battery is widely used; however, because of its low energy density and concerns over safety, researchers have been seeking for better replacements [9]. In this regard, metal-air batteries have drawn great attention due to their several advantages, such as low-cost, high theoretical energy densities and for some due to environmental benefits [43]. Various metals, such as Zn, Mg, Al, K, Na and Li can be used to fabricate rechargeable metal-air batteries. The theoretical energy density, voltage, specific capacity and electrolyte of the various metal-air batteries are summarized in Table 1.

Table 1: Comparison of different metal-air batteries [43,44].

Battery systems	**Li-air**	**Na-air**	**Mg-air**	**Al-air**	**Zn-air**	**K-air**	**Fe-air**
Theoretical cell voltage (E^{o}_{cell}) (V)	2.96	2.27	3.09	2.71	1.65	2.48	1.28
Cost of metals (US $ kg^{-1})	20	2.5	2.3	1.9	2.6	1.0	0.5
Theoretical energy density (Wh kg^{-1})*	3458	1106	2840	2796	1087	935	763
Specific capacity (mAh g^{-1})	3861	1166	3833	2980	820	377	2974
Electrolyte for practical batteries	Aprotic	Aprotic	Aprotic	Alkaline/ saline	Alkaline	Aprotic	Alkaline
Year invented	1996	2012	1966	1962	1878	2013	1968

*Oxygen inclusive.

Metal-air batteries have drawn special attention, because of their half-opened nature that uses inexhaustible oxygen from the air as oxidant, resulting in a high theoretical energy density [45]. Among them, the Zn-air batteries have so far received increasing attention because of their reasonable energy density in combination with a relatively low cost [46] and environmental friendliness as Zn is a nontoxic element. A typical Zn-air battery consists of four main components: an air electrode, membrane, an alkaline (concentrated KOH [47], NaOH [48] or LiOH [49]) electrolyte and a Zn negative electrode (Figure 1). It has a theoretical maximum output voltage of 1.65 V based on the electrochemical reactions of oxygen reduction at the cathode and Zn oxidation at the anode under alkaline condition. The electrode reaction equations and their standard potential are shown below (R1-R4) [48,50,51].

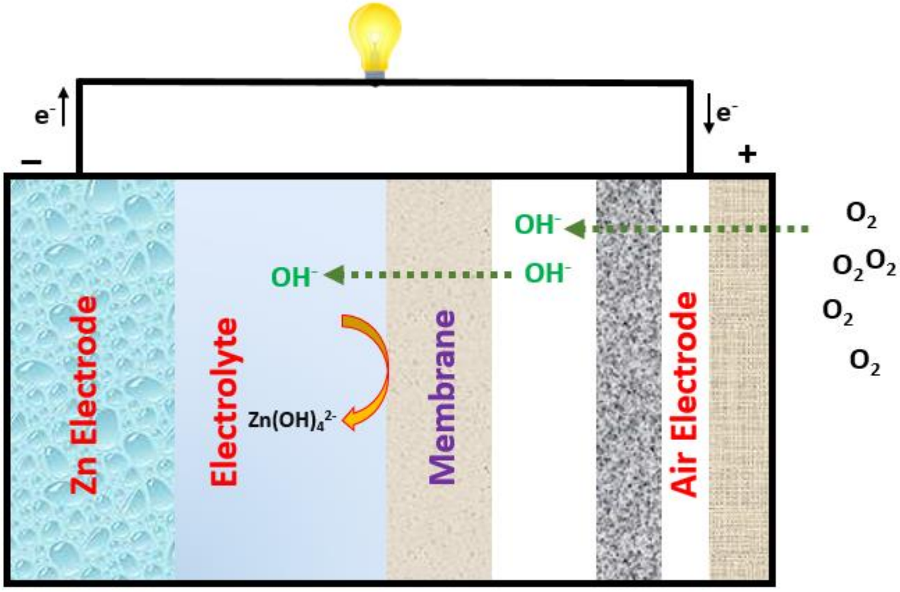

Figure 1: A schematic diagram of alkaline Zn-air battery in discharge.

Positive electrode: $O_2 + 2H_2O + 4e^- \leftrightarrow 4OH^-$ ($E^0 = +0.4$ V vs. SHE) (R1)

Negative electrode: $Zn + 4OH^- \leftrightarrow Zn(OH)_4^{2-} + 2e^-$ ($E^0 = -1.25$ V vs. SHE) (R2)

$Zn(OH)_4^{2-} \leftrightarrow ZnO + H_2O + 2OH^-$ (in the electrolyte) (R3)

Overall reaction: $2Zn + O_2 \leftrightarrow 2ZnO$ ($E_{cell} = E^o_{cathode} - E^o_{anode} = +1.65$ V) (R4)

The Zn-air system started to be commercialized in 1932 for hearing aids [52]. Mechanically rechargeable Zn-air systems showed significant progress in the 1990s. However, after about 50 years of intensive research, rechargeable Zn-air batteries are still in an early stage of commercialization because of various challenges, such as water evaporation, dendrite formation, atmospheric CO_2 reaction with OH^- ions and resulting in carbonate precipitation, lack of bifunctional air cathode (allowing both oxygen reduction and evolution reaction) and appropriate selective membrane [53]. Regarding the CO_2 contamination, it can have a large impact on battery performance. For example, the stability of bifunctional La0.6Ca0.4CoO_3 oxygen electrodes for rechargeable Zn-air battery as a function of the CO_2 concentration in the feed gas has been investigated by Drillet et al. [54]. When air containing up to 1000 ppm was used as a feed gas, the oxygen reduction reaction (ORR) became life-limiting and run for only about 270 h (2500 h when pure oxygen as feed gas was used) due to pore clogging by carbonate precipitation. Similarly, 1% CO_2 in oxygen stream caused a drop in Ag/PTFE ORR electrode current density with time due to the formation of K_2CO_3 in the micropores [55]. To address these issues and endure the life and performance of Zn-air batteries, various strategies, such as passing the inlet air through a scrubber of alkaline filter materials or amines [56], replacing electrolyte to remove any accumulated carbonate [57], operating at higher temperatures to increase the solubility of carbonates and slow down its precipitation [44] and/or ionic liquids electrolytes which are CO_2-tolerant [58] have been suggested. However, it must be noted that most of these strategies result in much poorer battery performance. Moreover, the impact of CO_2 on AEM fuel cell performance has been reported to significantly decrease when operating the cell at high current densities (above 1000 mA cm^{-2}) [59]. When a high current density was applied on the operating fuel cell, the OH^- ions formation at the cathode was increased. The OH^- ions are transported through the membrane, thus diluting the carbonate anions and consuming more CO_2 in the membrane. Similar high current densities operation technique might be used to avoid CO_2 effects in Zn-air batteries.

Recently, a number of research groups have been working to address these issues in order to realize rechargeable Zn-air flow batteries. This is clearly visible by the number of published papers in recent years (Figure 2). The number of scientific publications in this field has revealed steady growth in the last 10 years, which points out that the Zn-air battery technology for energy storage is indeed a potential candidate attracting wide interest. The increasing attention to these batteries is attributable to the abundance and low cost of Zn [60] in combination with a relatively high energy density (theoretically 1087 Wh kg^{-1}, including the weight of oxygen in the capacity calculation), high safety and environmental friendliness [61]. Moreover, the battery generally exhibits a flat, constant discharge voltage and low equilibrium potential, which is an additional reason why it has received great attention [51]. Furthermore, Zn can be easily recycled using current recycling technologies [62].

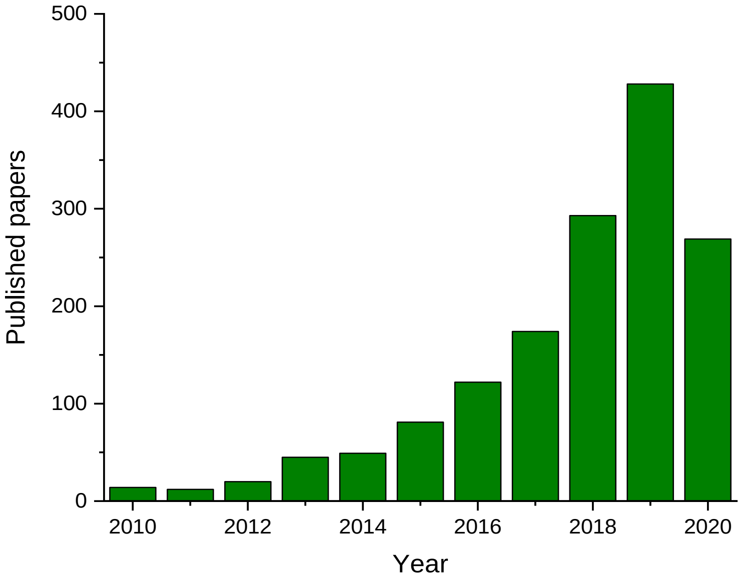

Figure 2: Number of publications per year from 2010 to 2020 mentioning the term “Zinc/Zn-air battery” as derived from Web of Science database (accessed on June 22, 2020).

Excellent reviews on the overall status and recent progress of Zn-air batteries exist in the literature [43,44,50,51,63–66], with the vast majority of research focused on the electrode materials and electrolyte (alkaline, acidic and neutral) components. In these studies, different air catalysts configurations, such as unifunctional ORR electrocatalyst, bifunctional air electrocatalysts and three-electrode configuration have been investigated. Moreover, the various groups of bifunctional catalysts, namely transition metal oxides, transition metals, carbon-based materials and precious metals/alloys, which are used in primary/secondary Zn-air batteries have been reviewed elsewhere [67].

Due to the intense research efforts on the cathode electrocatalysts, the performance of Zn–air batteries is no longer limited by electrocatalysts and air electrode [68]. Various researchers have bypassed the cycling stability issue by adapting a three-electrode configuration, in which the oxygen evolution reaction (OER) and ORR electrodes are decoupled [69,70]. Therefore, a shift in a research direction from cathode electrocatalysts to the Zn negative electrodes has been suggested to truly commercialize this a century-old technology. However, in comparison to the other parts of the battery [71–77], the membrane has not yet received its deserved attention [78]. Therefore, the present review is focused on the membrane, which is a critical component of the Zn-air battery system. The main role of the membrane is to separate the electrodes, thus avoiding electrical short circuits, and to selectively conducting hydroxide (OH^-) ions from the air electrode to the Zn electrode and *vice versa* [79]. Additionally, it is very important to design a membrane that exhibits high structural resistance to avoid possible perforation by Zn-dendrites in order to assure the safety and long-term reliability of the battery [44,80]. Zn-dendrites growth retarding membranes are discussed in section 4.

There are several partially contradicting requirements for an appropriate membrane to be used in rechargeable Zn-air batteries. The membrane should exhibit high chemical and electrochemical stabilities in an oxidative medium [81,82], a high ionic conductivity and should be able to swell in the electrolyte [51,81] without compromising its mechanical robustness. The membrane should also reduce the crossover of zincate ($(Zn(OH)_4^{2-}$) ions [83–85]. Moreover, the membranes should be manufactured at an acceptable cost. The key requirements of membranes to be applied in high-performance Zn-air battery systems are discussed in detail in section 2.

Most of the membranes currently used in Zn-air batteries i.e., porous membranes, have been adapted from Li-ion and nickel batteries. Despite the relatively good chemical stability and low costs of these commercial membranes, such as Celgard® 4560 and Celgard® 5550 (Celgard LLC), a crossover of significant amounts of $Zn(OH)_4^{2-}$ species from the Zn electrode to the air one has been reported to increase cell polarization and resulting in capacity fading of the battery (section 2.3) [83,86,87]. This indicates the need for designing and developing dedicated membranes that can block zincate permeation in order to achieve a highly-effective rechargeable Zn-air flow battery [83,84,86].

To address this challenge, various types of membrane chemistries, including anion or cation-exchange membranes (AEM/CEMs), composite membranes and electrospun nanofiber membranes have been explored. Each of these membranes has different sets of advantages and drawbacks, which influence the performance of Zn-air batteries. In conventional batteries, the term “separator” is often used to refer to a porous membrane, which mechanically separates two compartments without functionality, imbibed with electrolytes [88]. Moreover, in the literature, the terms membrane, separator and membrane separator have been used interchangeably. To avoid a possible misinterpretation, the basic definition and classification of the term “membrane” is revised more closely here. A membrane can be defined as a permselective barrier material between two phases [89] that allows some species to pass while preventing others on application of a transmembrane driving force [90,91], which could be a hydrostatic pressure gradient, vapor pressure gradient, electrical potential gradient or concentration gradient [92]. Based on their morphology, membranes can be classified into two main categories of porous and non-porous (dense) membranes [93]. Porous membranes, which are made up of a solid matrix with defined pore sizes varying from 0.2 nm to about 20 μm [94] separate target solutes mechanically by their size exclusion, whereas in non-porous membranes transport occurs by a solution-diffusion mechanism [95] inside the membrane. Porous membranes can be further referred to macroporous (average pore diameters larger than 50 nm), mesoporous (average pore diameters between 50 and 2 nm) and microporous (average pore diameters between 2 and 0.2 nm) according to the classification adopted by the IUPAC [96].

For this reason and to avoid confusion, only the term membrane will be used throughout the present treatise, which, to the best of our knowledge, is the first review on the state-of-the-art membranes used in Zn-air batteries. The properties and performance of seven types of membranes used in Zn-air batteries (following a classification done on the basis of their composition and structure), namely porous polymeric membranes prepared by phase inversion and electrospinning, modified porous membranes, ion solvating membranes, AEMs, CEMs and inorganic membranes are discussed and compared. The existing research gaps and strategies proposed to solve the problems associated with the currently used membranes are also discussed.

2. Performance determining properties of membranes in zinc-air batteries

2.1. Chemical and electrochemical stability

The most commonly used electrolytes in Zn-air batteries are aqueous alkaline (KOH or NaOH) solutions because of the higher stability of Zn in alkaline media and the use of non-noble catalyst in air electrodes. Usually, KOH has been used as the electrolyte in Zn-air batteries because of its higher ionic conductivity, higher oxygen diffusion coefficients, and lower viscosity compared to that of NaOH [97]. The specific conductivity of an aqueous KOH electrolyte depends on its concentration and temperature. Generally, the conductivity of the electrolyte increases up to a certain concentration and then it decreases due to an increase of viscosity and lower dissociation due to lack of water and formation of ion pairs, precipitates, etc. An increase in viscosity decreases the mass transport rate of OH^- ions [98–100]. For this reason, 6 M KOH solution is most commonly used to provide both an appropriate ionic conductivity and viscosity [100,101].

The chemical stability of membranes in such a highly alkaline harsh environment is critical since the OH^- ions, which are strong nucleophilic bases, could degrade the membrane. In a study done by Sapkota and Kim [79], microporous synthetic resin filters (Yumicron MF-250), cotton cloths, polyimide-based nylon net filter and polypropylene resin membrane were tested in a Zn-air fuel cell. Despite the known resistance of the cotton cloths and Yumicron MF-250 to alkalis, the membranes were reported to be stiffened and easily fractured, whereas the polypropylene resin membrane and Nylon net filter showed a good stability. However, the mechanisms responsible for the degradation of the membranes used were not identified.

The alkaline stability of a membrane is usually determined by comparing its chemical structure, mechanical properties and/or performance (e.g., conductivity) before and after immersing into an alkaline media (e.g., 2 M KOH solution at 60 °C), for defined time. A decrease in ionic conductivity and/or ion-exchange capacity with immersion time indicates degradation of functional groups.

The alkaline stability issue is more critical when AEMs are used since most of their functional groups are prone to a nucleophilic attack. The alkaline stability/degradation of AEMs is well-reviewed in the literature [102–107]. Operations under electrical current flowing conditions make the chemical stability problem more complicated as a result of a possible formation of free radicals. Therefore, a membrane with a high stability in the alkaline solution, which withstands during electrochemical operations is required [79]. For instance, commercial porous membranes based on polyolefins (e.g., polypropylene, polyethylene), such as Celgard®3501 and 5550, and inorganic membranes are known for their good alkaline chemical stability. Similarly, the commercial CEMs based on a perfluorosulfonic acid polymer i.e. Nafion® has a good chemical stability.

2.2. Conductivity

Hydroxide conductivity has a major influence on the performance of Zn-air batteries. A membrane with a high OH^- conductivity is desirable since a low resistive OH^- ion transport allows high conversion rate of the electrochemical reaction. As the OH^- mobility through the membrane must be as high as possible, the formation of swelling nanochannels in the membrane thickness is very important. Due to the larger size (1.6 x) and, thus, lower diffusivity of OH^- ions compared to that of H^+ ions, the rate of OH^- transport is expectedly lower than that of H^+. However, it must be noted that the transport easiness of OH^- is not only associated with its size, which is important for diffusion process, but also with its transport via Grotthuss mechanism [108–110].

Understanding the transport mechanism of $OH^−$ ions is important in order to increase the $OH^−$ ion conductivity. The transport mechanisms of hydrated $OH^−$ ions in aqueous solution have been discussed elsewhere [111,112]. It is considered that $OH^-(aq)$ exhibits a nonclassical, hypercoordinated solvation structure. The main transport mechanisms of $OH^−$ ions through AEMs that have been proposed in the literature are schematically shown in Scheme I. Similar to the transport of protons in proton exchange membranes, Grotthuss and vehicle mechanisms are believed to be the dominant $OH^−$ transport mechanisms through membranes [110,113]. In Grotthuss mechanism, the $OH^−$ ions transports from one water molecule to the next via hydrogen-bonding [111,112,114,115]. In addition to the membrane properties, the operating conditions, such as temperature and relative humidity, affect the OH^- mobility through a membrane. The $OH^−$ ion conductivity increases with increasing temperature and relative humidity. The increment in ionic conductivity of the membrane with the temperature increasing can be explained for two reasons: The trend can be explained by faster OH^- ions motion [116] and wider ion transport channels [117] at an elevated temperature.

Surface site hopping is another mechanism discussed in the literature as a possible OH^- ion transport in the membrane. It involves the movement of hydroxide ion by hopping between strongly interacting groups in the polymer chain [105,110,118]. In this mechanism, the $–N^+ OH^−$ grafted functional group is solvated and dissociated by water molecules. Subsequently, the $OH^−$ ion is attracted by the adjacent cationic chain, then the process repeats. The distance between the neighboring functional fixed groups and the ion exchange capacity influence the transport rate of $OH^−$ ions via the surface site hopping mechanism.

On the other hand, the conductivity of non-functionalized porous membranes depends on their electrolyte wettability. The wettability of porous membranes depends on the polarity and tortuosity of the membrane porous structure. For instance, some Celgard® membranes are treated with a (cationic/nonionic) surfactant to increase their hydrophilicity leading to higher electrolyte uptake. This has been discussed in section 3.1.3.2.

Ionic conductivity of gel-polymer electrolyte membranes is achieved by the transport of salt ions through the water [119]. In other words, the conductivity is mainly related to the water diffusive motion across the membrane. In such membranes, ions motion paths can be eventually blocked by the ions aggregation unless the salt concentration is optimized [120]. Another challenge associated with gel-polymer electrolyte membranes is the progressive loss of electrolyte, which leads to an increasing ohmic resistance and decline of the battery performance [121]. One option to address this issue is to fix the functional charged groups functions on the polymer backbone, as it is done in ion-exchange membranes.

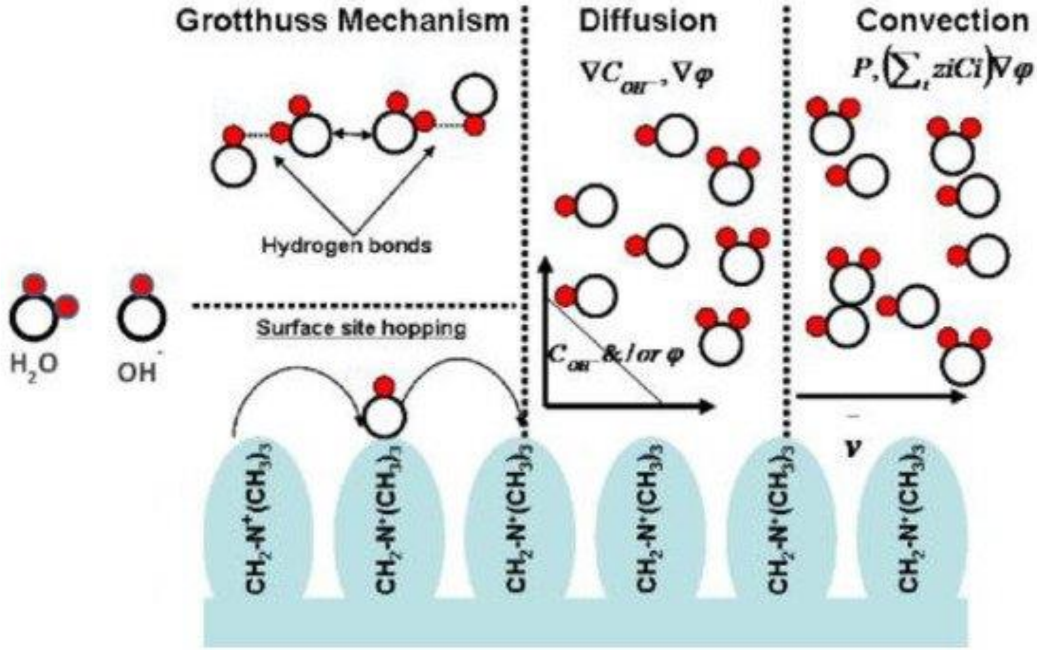

Scheme I: Dominant transport mechanisms for hydroxide ions in AEMs. Reproduced with permission from Ref [110]. Copyright 2010, The Electrochemical Society.

The OH^- conductivity (σ) of a membrane can be measured by impedance spectroscopy [117,122]. Usually, fully hydrated membranes (in OH^- form) are sandwiched in a Teflon cell equipped with Pt foil contacts. The in-plane ionic conductivity, in mS cm^{-1}, of a sample is calculated from equation (1):

$$\sigma = \frac{L}{R \text{ x } A} \tag{1}$$

where L (cm) is the distance between electrodes (thickness of the membrane), R is the resistance of the membrane (Ω) and A is the cross-sectional area of the sample (cm^2).

2.3. Selectivity and permselectivity

Another important membrane requirement for rechargeable Zn-air batteries is its selectivity. In strong alkaline solutions, OH^- reacts with Zn^{2+} and forms $Zn(OH)_4^{2-}$ [44,50] via a number of elementary first-order reactions [123,124] (Equations R5-R6). The membranes need to be selective for OH^- ions, without any crossover of $Zn(OH)_4^{2-}$ formed in the Zn electrode compartment [44,51]. In practice, $Zn(OH)_4^{2-}$ crossover is a common problem as it is able to cross due to the concentration gradient, especially when porous membranes are used. Therefore, to address the crossover of $Zn(OH)_4^2$ ions issues, a membrane that is able to block the transportation of $Zn(OH)_4^{2-}$ ions without significantly affecting the OH^- ions transportation would be one major requirement to achieve a long cycle life.

$Zn + OH^- \leftrightarrow Zn(OH) + e^-$ (R5)

$Zn(OH) + OH^- \leftrightarrow Zn(OH)_2^-$ (R6)

$Zn(OH)_2^- + OH^- \leftrightarrow Zn(OH)_3^- + e^-$ (R7)

$Zn(OH)_3^- + OH^- \leftrightarrow Zn(OH)_4^{2-}$ R8)

Due to the low solubility of ZnO at the air electrode, the $Zn(OH)_4^{2-}$ to ZnO conversion ($Zn(OH)_4^{2-} \rightarrow ZnO (s) + H_2O + 2OH^-$) is accelerated, resulting in the formation of resistive ZnO layers. This leads to a loss of battery capacity with cycling [85]. Moreover, ZnO powders could clog the porous air electrode, resulting in large cell polarization [125]. Thus, $Zn(OH)_4^{2-}$ crossover could affect the durability of the battery by decreasing its lifespan. This indicates the substantial need for avoiding $Zn(OH)_4^{2-}$ ions crossover [83]. One possible way is by using a porous membrane with a proper pore size and porosity. Another method that has been widely proposed to solve the problem is to use an AEM that has well-defined and controlled ionic nanochannels [44,63]. Moreover, different membrane surface modification techniques could also be performed to minimize the permeation of $Zn(OH)_4^{2-}$ ions.

On the other hand, the size of the $Zn(OH)_4^{2-}$ anionic complex consisting of four OH^- groups and a Zn^{2+} cation is far larger than that of a single OH^- anion. The solvodynamic radius of the $Zn(OH)_4^{2-}$ ion in 4 M NaOH and at 25 ˚C was reported to be 3.41 Å [126]. The Stokes radii were reported to decrease with increasing alkali concentration, due to the competition between solvation of $Zn(OH)_4^{2-}$, Na^+, and OH^- ions by water molecules. Here, the ionic radius of $Zn(OH)_4^{2-}$ is assumed to be the same as the ionic radius of Zn^{2+} [90,91] i.e., much higher than that of OH^-. The relative diffusivity easiness of OH^- ion compared to that of the $Zn(OH)_4^{2-}$ ion is favoring the OH^- transport across the membrane [83]. Table 2 presents the ionic Stokes radii of the different species involved (OH^-, Zn^{2+} and $Zn(OH)_4^{2-}$) and their diffusion coefficients at infinite dilution at 25 ˚C. Depending on the electrolyte used (KOH or NaOH), K^+ or Na^+ will be present, whereas CO_3^{2-} is due to the possible carbonation unless the CO_2 is removed, as the air electrode is open to the air.

Table 2: Ionic Stokes radii and diffusion coefficient (D) of species involved in Zn-air battery at 25 ºC.

Species	Ionic Stokes radii (Å) [127]	D (10^{-9} m^2 s^{-1}) in water [128–130]
OH^-	0.46	5.27
K^+	1.25	1.96
Na^+	1.84	1.33
CO_3^{2-}	2.66	0.96
Zn^{2+}	3.49	0.72

A simple diffusion cell composed of two chambers, separated by a membrane, filled one side with a KOH electrolyte solution (a typical example is, 6 M, 100 mL) and $Zn(OH)_2$ and a second side with only a KOH (6 M, 100 mL) solution is usually used to determine the diffusion coefficient of $Zn(OH)_4^{2-}$ ions through the membrane. This is similar to the method employed to determine the vanadium ion crossover in Vanadium RFB [131–133]. However, it should be noted that this procedure does not compensate for ionic strength. Best practice procedure would be to use a non-active ion (e.g., $Mg(SO_4)$ in the case of Vanadium) to compensate for the loss in ionic strength and to exclude osmotic pressure as an additional driving force. The change of concentration of $Zn(OH)_4^{2-}$ ions with time is usually monitored using elemental analysis methods, such as inductively coupled plasma atomic emission spectrometry (ICP-OES) [83,85,86], ICP-mass spectroscopy (ICP-MS) [134], polarographic response [135], or complexometric titrations [136]. To avoid a long experimental period and sample post-processing steps associated with ICP-MS analyses, an anodic stripping voltammetry (ASV) sensing platform which provides real-time concentrations of $Zn(OH)_4^{2-}$ crossing the membrane has been reported [136]. The diffusion coefficient (D, m^2 s^{-1}) of $Zn(OH)_4^{2-}$ ions can be calculated using a mass balance equation:

$$V_B \frac{dC_B(t)}{dt} = \frac{DA}{L}\left(C_A - C_B(t)\right) \qquad (2)$$

which after integration (by assuming V_B to be constant) can be rearranged as:

$$ln\left(\frac{C_A}{C_A - C_B}\right) = \frac{DA}{V_B L} t \qquad (3)$$

where A and L are the effective area (m^2) and thickness (m) of the membrane, respectively; V_B is the volume of the depleted side and t is the elapsed time (s). C_A (mol L^{-1}) and C_B (mol L^{-1}) are the concentrations of $Zn(OH)_4^{2-}$ in the enriched and depleted chambers, respectively. As an example, the dependence of the $Zn(OH)_4^{2-}$ ion diffusion coefficient on NaOH concentration (1-4 M) and temperature has been reported elsewhere [126].

Another important parameter which should be taken into consideration is the permselectivity (S cm s^{-1}) of the membrane, which can be calculated as the ratio of hydroxide conductivity (σ (OH^-), mS cm^{-1}) to $Zn(OH)_4^{2-}$ diffusion coefficient (D ($Zn(OH)_4^{2-}$), cm^2 s^{-1}) [85]. Permselectivity indicates the preference of the membrane for OH^- ions over $Zn(OH)_4^{2-}$ ions. Therefore, in practice, this parameter should be taken into consideration when selecting a suitable membrane for a specific application. For instance, a porous membrane, such as Celgard® 3501, might have a high hydroxide ion conductivity but exhibits also a high crossover of zincate ions. On the other hand, an AEM could have a comparably acceptable hydroxide ion conductivity, but offer much better zincate ions retention. In this case, the membrane permselectivity can be used as the final decision factor to select the most appropriate membrane.

2.4. Mechanical strength

The membranes must be mechanically robust to withstand the tension of winding operation and stacking stress during continuous cell assembly. For a stable and long battery lifespan, an optimal and uniform membrane thickness is required [137]. Usually, thin membranes have lower internal resistance, but a small thickness can have a negative impact on the mechanical strength. On the other hand, thicker membranes are generally less prone to fail mechanically, which improves better battery safety. However, the internal resistance increases with increasing thickness, and the mechanical robustness on one hand must therefore be balanced against the ohmic resistance on the other. The typical thickness of membranes used for rechargeable batteries is reported to lie between 20 and 50 µm [138].

Mechanical properties of a polymeric membrane are dependent of its elastic modulus, tensile strength and ductility [139]. Typical mechanical strength values of commercial Celgard® membranes have been summarized in [140,141]. The minimum requirement of puncture (i.e., the maximum load required for a given needle to puncture a membrane) and mechanical strengths for a 25 μm thick membrane is 300 g and 1000 kg cm^{-2}, respectively. Trilayer structured (PP/PE/PP) Celgard® membranes display exceptional puncture strength, whereas AGM membranes exhibit a low puncture resistance [141].

2.5. Water uptake and anisotropic swelling ratio

The membrane should possess optimized water retention capacity in order to facilitate the mobility of OH^- ions and to avoid drying out by evaporation since the air electrode is exposed to the atmosphere [142]. Compared to other types of aqueous batteries, in which in general both sides of the membranes are in contact with aqueous electrolytes, Zn-air batteries are usually half-closed system, in which only one side of the membrane is in contact (immersed) in the aqueous alkaline solution, whereas the other side of the membrane is contacted to a gas-diffusion electrode, the system is therefore asymmetric. The air electrode has to maintain its hydration even during the discharge process and water consumption associated with O_2 reduction.

The water consumption due to both electrochemical reactions and electro-osmosis can induce electrode or/and AEM drying out, membrane shrinking and lead to a shortened battery lifespan. Moreover, the membrane may undergo mechanical stress and deformation from the volume expansion of the Zn electrode due to the formation of oxidized Zn species. This can lead to ineffective interfacial contact between the electrode and electrolyte. Thus, the active materials become less accessible to the ionic species. Accordingly, the anisotropic swelling ratio of the membrane is another crucial parameter that affects the Zn-air battery cycling performance [142–145]. An anisotropic swelling degree is defined as the ratio of through-plane swelling to in-plane swelling of the membrane [146]. A membrane with a low anisotropic swelling degree, combined with high water retention and OH^- conductivity is expected to improve the specific capacity and the cyclic stability of the battery [142]. On the other hand, membrane with high anisotropic swelling degree, for instance, the A201®-based Zn-air batteries exhibited a rapid voltage and capacity loss after some cycles, which was attributed to the progressive loss of water and ionic conductivity in the membrane during the constant current conditions applied [142–145].

3. Classification of membranes used in zinc-air batteries

The membranes used in Zn-air batteries can be classified into seven major types: (a) phase inversion polymeric porous membranes, (b) electrospun nanofiber membranes, (c) modified porous membranes, (d) inorganic membranes, (e) AEM, (f) CEM and (g) ion solvating membranes (also called gel polymer electrolyte membranes) depending on their composition and structure (Scheme II). The first sub-section (3.1.1) is devoted to polymeric porous membranes prepared by the phase inversion method, since they are the most commonly used ones. On the other hand, the nanofiber membrane is another group of porous membranes prepared by an electrospinning technique presented in sub-section 3.1.2. The next sub-section (3.1.3) focuses on modified porous membranes. In this section, strategies followed to improve the properties of porous membranes are discussed. A brief discussion on inorganic membranes is presented in section 3.1.4. Finally, in section 3.2, dedicated to polymer electrolyte membranes, AEMs, CEMs and ion solvating membranes are discussed in sub-sections 3.2.1, 3.2.2 and 3.2.3, respectively.

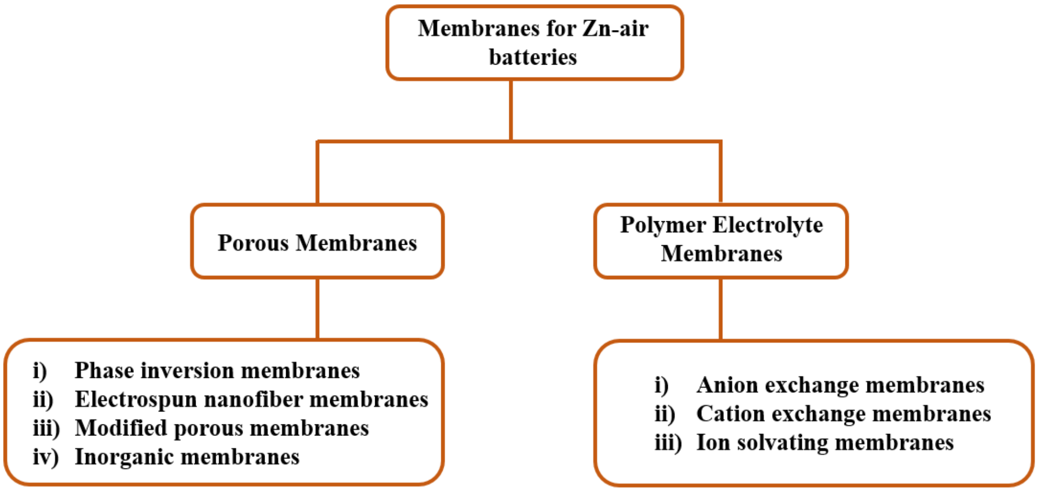

Scheme II: Classification of membranes used in Zn-air batteries based on their composition and structure.

3.1. Porous membranes

3.1.1. Phase inversion membranes

The early development of Zn-air batteries was limited by the lack of suitable membranes. As a result, inorganic filter paper (Whatman) impregnated with poly(vinyl acetate) (PVAc) aqueous solution (24 wt.%) [147,148] and porous membranes [79] developed for other applications were used. In the latter work, the performance of various porous membranes was compared in a Zn-air fuel cell. An Yumicron MF-40 (pore size of 0.4 μm) membrane was reported to have lower performance in terms of cell voltage than Yumicron MF-250 (pore size of 2.5 μm).

Later on, nonwoven porous membranes made of polyethylene (PE), poly(vinyl alcohol) (PVA), polyamide, poly(etherimide) (PEI), poly(acrylic acid) (PAA) and polypropylene (PP) have been commonly used in Zn-air batteries [48,84,149]. Nowadays, commercial membranes with a well-defined porous structure, such as Celgard® 5550 [149], which has a PP/PE/PP trilayer structure are commonly used in Zn-air batteries. The PP is used to maintain the integrity, providing mechanical support to avoid internal shorting, whereas the core PE due to its low melting point is able to shut down when the battery is overheated [149] since the PE layer melts and closes the film pores, thus blocking ions migration [150]. These laminated porous membranes are prepared via a dry process i.e., the polyolefin is melted, thermally annealed to increase the size and amount of lamella crystallites, and then precisely stretched to form tightly ordered meso-pores, which are usually coated with surfactants to increase water-based electrolyte wettability [140,149]. The closely ordered nature of the meso-pores of these membranes allows them to be highly OH^- ion conductive [44,149,151]. For instance, Celgard® 3501 was reported to have an OH^- conductivity of 12.8 mS cm^{-1} and 80.1 wt.% KOH solution (6 M) uptake at room temperature [86].

The porous membranes commonly used (PP-based) in rechargeable batteries have an average pore size which is much larger than the size of solvated zincate ions, which results in their crossover. For example, Celgard® 5550 has an average pore size of 100 nm [152], 64 nm [153] (according to Manufacturer's datasheet), which is much larger than the size of zincate ions. Therefore, the $Zn(OH)_4^{2-}$ species are able to diffuse across them to the air electrode [83,154]. Significant zincate ions crossover has been reported in a number of studies when such porous membranes were used [83,85,86,155]. The diffusion coefficient of zincate ions through Celgard® 3501 and Celgard® 5550 was reported to be 3.2×10^{-11} [85] and 1.1×10^{-5} m^2 s^{-1} [83], respectively. This is a very large difference in the zincate ions diffusion coefficient value despite the fact that both membranes have exactly the same porosity (55%) and pore size (64 nm) [153]. The notable difference between the two membranes, which might explain the large difference in zincate ion diffusion, is that Celgard® 3501 is only coated, whereas Celgard® 5550 is laminated and coated membrane [153]. The use of two Celgard® 3401 membranes (50 nm pore size) together was reported to have a lower zincate ions diffusion coefficient (6.9×10^{-12} m^2 s^{-1}) [156]. To improve the performances and avoid the crossover of $Zn(OH)_4^{2-}$ ions, a membrane with pores that are large enough to permit the OH^- ions but small enough to prevent the permeation of $Zn(OH)_4^{2-}$ ions is required [51].

Other membrane materials, including cellulosic films, such as cellophane, have also been investigated in Zn-air batteries [157,158]. The diffusion coefficient of zincate ions for cellophane® 350PØØ membranes (unsoften cellulose film) (Innovia Films Company), wet ionic resistance of > 96.8 mΩ cm^2 using 40% KOH [159], was measured using anodic stripping voltammetry (ASV) [136]. The cellophane membrane (6.7×10^{-12} m^2 s^{-1}) was found to have a lower zincate crossover than that of Celgard® 3501. The diffusion coefficient of $Zn(OH)_4^{2-}$ through Celgard® 3501 reported in this study was coherent with the value discussed previously in [85]. The cellophane membrane's diffusivity to $Zn(OH)_4^{2-}$ was reported to be similar (3.7×10^{-12} m^2 s^{-1}) in another study [157]. It should be noted that cellophane typically has a less porous (about 3-10 nm [160]) structure and is more negatively charged than that of Celgard® 3501 [161]. Thus, the smaller and (negatively) charged pores of the cellophane were thought to be more selective in excluding the negatively charged $Zn(OH)_4^{2-}$ ions. A contradictory result was reported in another study, in which a cellophane membrane was reported to show no zincate blocking effect at all when used in Zn/MnO_2 cell [162].

In addition to commercial porous membranes, various composite porous membranes have been reported in the literature. Phase inversion is a process, in which a homogeneous polymer solution (polymer and solvent) casted on a suitable support is immersed in a coagulation bath containing a nonsolvent (usually water) and is converted into two phases (polymer-rich and liquid-rich phases) [163–165]. Phase inversion has been so far the most commonly used method to prepare (porous) membranes due to its simple processing and flexible production scales [166,167]. Porous membranes used so far in Zn-air batteries are presented in Table 3.

Wu et al. [168] prepared PVA/ poly(vinyl chloride) (PVC) porous membrane and studied its potential electrochemical performance on a secondary Zn battery. The PVA and PVC polymers were dissolved in water, and the dried composite PVA/PVC film was immersed in THF in order to form a macroporous structure (pore size range of 60–180 nm) via a partial dissolution process. This allowed a high KOH electrolyte uptake by the membrane. The membrane pore size and its distribution were controlled by varying the amount of PVC, the partial dissolution time and the etching temperature. The PVA/PVC-based secondary Zn battery exhibited a stable charge potential. This was claimed to be due to the high ionic conductivity (37.1 mS cm^{-1} at 30 °C for PVA/10 wt.% PVC) and macroporous structure of the membrane. As a result, the cell potential during the charge period was much less polarized; thus, the current efficiency (70–80%) and the life-span (50 cycles) of the battery were improved.

Moreover, solid PVA/PAA membranes with a uniform structure were prepared via a solution casting method [169]. The room temperature ionic conductivity of these membranes reached 140-300 mS cm^{-1} depending on the ratio of PVA to PAA. The ionic conductivity of membranes was reported to increase with the increase of PAA content. The percent utilization of the Zn-air cell capacity was as high as 90% when the PVA/PAA (10:7.5) membrane was used and the cell was discharged at a C/10 rate. The power density was reported to reach 50 mW cm^{-2}.

Table 3: Performance of porous polymeric phase inversion membranes used in Zn-air batteries.

Membrane	**Preparation method**	**Characteristics**	**Cell type and conditions**	**Electrodes**	**Electrolyte**	**Performance**	**Ref.**
Celgard® 3501	Commercial (Celgard LLC)	Porosity* = 55%, pore size* = 64 nm Thickness : 24 µm	Rechargeable Zn–air battery	Zn electrode: Zn-based gel (Zn powder, PAA and 6 M KOH electrolyte solution) Ni foil : current collector Air electrode: commerciale (ADE75 (catalyst = Co_3O_4), MEET)	6 M KOH electrolyte solution	-Discharge capacity (2nd cycle) ~34 mAh g_{Zn}^{-1} -Pinwheel connected to Zn–air cell stopped after about18 min	[85]
Celgard® 5550	Commercial (Celgard LLC)	Porosity* = 55%, pore size* = 64 nm Thickness: 25 µm	Rechargeable Zn–air battery	Zn electrode: pure Zn plate Air electrode : Pt and Ir carbon composite	6 M KOH aqueous solution	-Initial (59.4%) and final (51.2%) energy efficiencies -Coulombic efficiency (99.8%). -37 cycles	[83]
Celgard® 3401	Commercial (Celgard LLC)	Porosity* = 41%, pore size* = 43 nm Thickness*: 25 µm	Zn-air fuel cell	Zn electrode: Zn powder Air electrode : MnO_2 powders was used as the catalytic material.	carboxymethyl cellulose with 8M KOH solution.	-Discharge current (mA) = 500 mA, at constant 0.7 V for 40 minutes using flowing KOH solution.	[170]
PVA/PVC	Solution casting method and a partial dissolution process	Pore size: 60–180 nm Thickness : 150 - 200 µm	Rechargeable Zn electrodes Galvanostatic charge/discharge measurements were carried out at a C/10 charge rate and a C/5 discharge rate.	Zn electrode: ZnO and $Ca(OH)_2$ 2 wt.% of Cu conductive nanopowders	8 M KOH aqueous solution.	-Specific discharge capacity: 353 mAh g_{Zn}^{-1} for 45 cycles -Coulombic efficiency: 70–80% -Effectively prevented any Zn dendritic formation. -Life cycle reached over 50 cycles	[168]

PVA/PAA	Solution casting method	ionic conductivity 301 mS/cm room temperature and 32 wt% KOH solution (PVA:PAA = 10:7.5 sample)	Zn-air cell BAT 778 model charge/discharge unit The discharge curves : C/10 discharge rate at 25 ◦C	Zn powder gel: Zn powder, carbopol 940, 32 wt% KOH and additives Ni-foam current collector GDL: carbon slurry	32 wt% KOH	PVA/PAA (10:7.5) membrane: -Discharge current (mA) = 150, 8.98 discharge h and -Utilization (%) = 89.8 -Power density: 50 mW cm^{-2}	[169]
PEO/PVA	Solution-cast technique	Average pore size (175 nm) ionic conductivity :153 mS cm^{-1} tensile strength 0.76 MPa.	Zn-air battery discharged at room temperature with the *C*/10 rate	Zn electrode: mix of Zn powder and Polyvinylidene fluoride (PVDF) Air electrode: -carbon slurry for the active layer of the air electrode was prepared by mixing of acetylene black, $KMnO_4$, Carbon black (Vulcan XC-72R), Na_2SO_4 and PVDF	KOH	Discharge curve: 0- 25 min: the voltage falls abruptly to an OCV (1.10 V). 25–510 min: voltage drops to 0.55 V. 510–560 min: the rate of discharge starts accelerating (voltage decline to 0.3 V)	[82]
PVA / poly(epichlorohydrin) (PECH)	Solution-cast technique	Ionic conductivity : 10^{-2} - 10^{-3} S cm^{-1} at room temperature when the blend ratio is varied from 1:0.2 to 1:1.	Solid-state Zn–air battery discharged at the C/10 rate at 25 °C	Zn powder gels: Zn powder, Carbopol 940 gelling agent, 32 wt.% KOH and some metal additives Carbon slurry for the gas-diffusion acetylene black and 30 wt.% PTFE (teflon-30 suspension) as a binder Ni-foam current-collector	32 wt.% KOH	PVA/PECH (1:0.2) membrane: -Cell utilization 86% -C/10, 150 mA, 8.59 h	[171]

*Manufacturer datasheet [153].

3.1.2. Electrospun nanofiber-based membranes

Electrospinning is a versatile membrane preparation technique widely used to produce membranes with large specific surface area and small fiber diameter and pore size [172–174]. Membranes prepared by this method are referred to as electrospun nanofiber membranes [175]. The entangled fibers provide integrity and mechanical strength to these membranes. Non-woven mat membranes are commonly used in Li-ion [176,177], lead-acid [178] and in some types of alkaline [149] batteries. High electrochemical performances [172] and oxidation stability [173] were reported in Li-ion polymer batteries using such membranes. Recently, few electrospun-based nanofibrous membranes have been reported in the literature and have been tested in Zn-air battery applications.

Membrane-based on syndiotactic polypropylene (syn-PP) nanofibers were prepared using electrospinning [179]. Granular syn-PP was dissolved in a mixture of decalin, acetone and DMF and the resulting solution (7.5 wt%) was electrospun (Potential 10.5 kV; distance 15 cm; flow rate 0.8 mL h^{-1}). The syn-PP nanofibers (coated with PVAc glue)-based Zn-air battery was found to exhibit more than 40% discharge capacity improvement compared to the Whatman filter paper-based battery. The improvement in the performance of the batteries was attributed to the membrane non-ordered and layered-fibrous structures.

A promising electrospun nanofiber mat-reinforced composite membrane (ERC) for Zn-air battery was reported by Lee et al. [85]. The membrane was fabricated by impregnating KOH liquid electrolyte-swollen PVA into PEI nanofiber mats (referred to ERC membrane, with a thickness of 27 ±5 μm). Figure 3 represents the electrospun PEI nanomat (a) and impregnation of PEI nanomat with PVA (b), respectively. Here, the PEI nanofiber provides a mechanical strength and dimensional stability, whereas the relatively entangled electrolyte swollen PVA is believed to allow the small-sized OH^- and prevent the bulky zincate ions passage. This unusual OH^- permselective transport behavior of the electrospun composite membrane is illustrated schematically in Figure 3 (c and d).

The prepared composite membrane and reference membranes (PVA film and Celgard®3501) used were compared in terms of OH^- ions conductivity, $Zn(OH)_4^{2-}$ ions crossover (in mol min^{-1}) and permselectivity. The $Zn(OH)_4^{2-}$ ions diffusion coefficient of the ERC membrane was four times lower than that of Celgard® 3501 membrane (Figure 3e and 3f), which induced a better permselectivity of OH^- ions over $Zn(OH)_4^{2-}$ ions (1.7×10^{11} vs. 6×10^9 S.s m^{-3}). This better permselectivity improved the cycle capacity retention of Zn-air batteries, since the 2nd discharge capacity of the ERC-based cell was about 7 times higher than that of the Celgard® 3501 membrane (~213 vs. ~34 mA h g^{-1}).

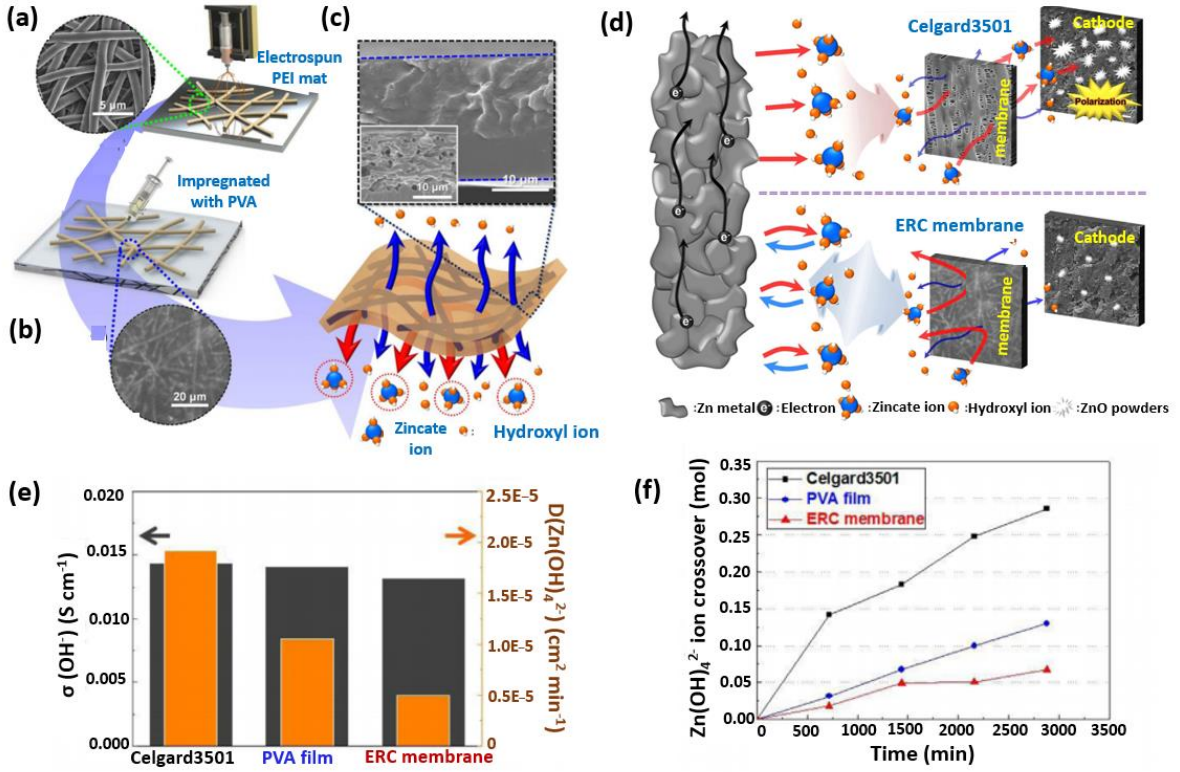

Figure 3: Preparation of ERC membrane and characterization of Celgard®3501, Pristine PVA film and ERC membrane: (a) electrospun PEI nanomat; (b) impregnation of PEI nanomat with PVA; (c) Cross-sectional SEM of ERC membrane and an illustration showing its permselective transport behavior; (d) illustration of permselectivity of ERC and Celgard®3501 membranes; (e) OH^- conductivity ($\sigma(OH^-)$) and ($D(Zn(OH)_4^{2-})$); (f) $Zn(OH)_4^{2-}$ ions across the membranes (mol). Reproduced with permission [85]. Copyright Elsevier 2015.

3.1.3. Modified porous membranes

To prevent the permeation of $Zn(OH)_4^{2-}$ ions through porous polymeric membranes, further optimization of these membranes have been achieved through surface modification approaches, which can be classified into two broad categories as nanoparticle-filled (composite) membranes and ion selective polymer-coated membranes.

3.1.3.1. Composite membranes

One possible method to minimize the crossover of $Zn(OH)_4^{2-}$ species is by plugging the pores of the porous membranes using inorganic particles. The preparation of composite membranes can involve incorporation of inorganic nanoparticles into the polymeric matrix during the fabrication process or filling/coating of a porous membrane with particles once the membrane is prepared. In both cases the aim is to prevent passage of zincate ions [180]. These techniques have been extensively investigated also for other batteries, such as Li-ion batteries. Similarly, pore filling with inorganic salt containing fluoride ions has been employed in cross-linked PVA-based membranes and used for a silver-Zn battery [181]. The fluoride salt due to its relative insolubility is expected to remain in the polymer gel.

On the other hand, despite the potential role of nanoparticle-filled composite membranes in minimizing the crossover of $Zn(OH)_4^{2-}$ ions, few studies are reported in the literature. ZIRFON® PERL (Agfa Specialty Products) membrane (pore size of 130 nm) that consists of a polysulfone network and zirconium oxide [182–184] has been used in Zn-air flow battery [185]. The ZIRFON® PERL-based battery exhibited above 50% round trip efficiency and the performance was not altered after l00 h of cycling at 25 mA cm^{-2}. Kiros [156] modified Celgard® 3401 (50 nm pore size, electrical resistance of 0.1 $\Omega.cm^2$ at room temperature and in a 6 M KOH solution) using insoluble inorganic compounds, such as $Al(OH)_3$, CaF_2, $Mg(OH)_2$ and $Mn(OH)_2$. Since they possess a very low solubility, after gelation/precipitation, they were sandwich between two Celgard® 3401 membranes, as schematically shown in Fig. 4a. Coating the membrane with $Mn(OH)_2$ produced the highest $Zn(OH)_4^{2-}$ ion-separation capacity, with no crossover of $Zn(OH)_4^{2-}$ ions. Coating of the membrane (10 cm^2) with 0.3 g of $Mn(OH)_2$ almost completely blocked the $Zn(OH)_4^{2-}$ permeation (only 0.03 mg/h of $Zn(OH)_4^{2-}$ ions crossover occurred). On the other hand, the use of two Celgard® 3401 membranes together (Figure 4a) resulted in $Zn(OH)_4^{2-}$ crossover of 28.46 mg h^{-1} (close to 1000 times higher).

Nevertheless, the ohmic resistance of the membrane was dramatically increased especially with a higher amount of $Mn(OH)_2$ coating due to the plugging of the pores of the membrane by the fine colloidal particles (Figure 4b). The electrical resistance of the Celgard® 3401 increased from 0.1 to about 150 Ω cm^2 (factor of 1500) when 0.3 g of $Mn(OH)_2$ were coated on the membrane in a 6 M KOH solution at room temperature. This has a negative impact on the OH^- ion conductivity and, thus on the overall performance of the battery. Therefore, the coating of porous membranes with an optimized amount of insoluble particles without a significant increase in their resistance is required in order to justify their use in Zn-air batteries.

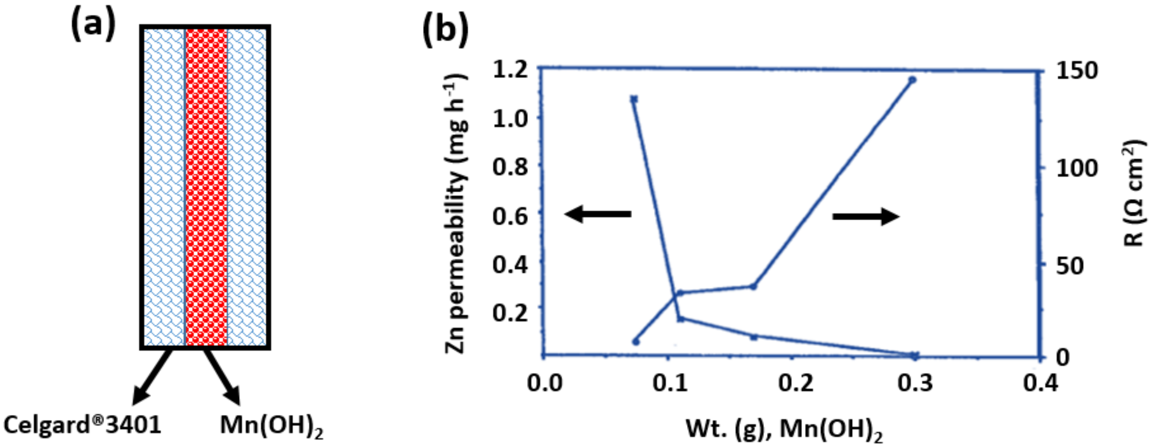

Figure 4: Schematic representation of a composite membrane (a) and Zn permeability and resistance as a function of amount of $Mn(OH)_2$ (g) coated on the Celgard® 3401 (b). Figure 4b is adapted with permission from [156]. Copyright Elsevier 1996.

3.1.3.2. Coating porous membranes with ion-selective polymers

Another method to minimize the crossover of zincate ions is coating the porous membranes with an ion-selective layer. The coat is expected to allow OH^- transfer through the membrane and to minimize the migration of zincate ions to the cathode compartment without significantly affecting the ionic conductivity. Moreover, the porous part of the membrane can serve as a mechanical support and an additional barrier to the zincate ions passage based on their size exclusion effect. Various layer support options are available commercially, such as cellophane 350PØØ and Celgard®5550 and 3501 etc.

On the other hand, there is still a need for developing alkaline stable, water-insoluble anionic-exchange polymers. Polymerized ionic liquids (PILs) are one promising class of candidates for tuning the membrane permselectivity to OH^-. Hwang et al. [83] coated a Celgard® 5550 membrane with PIL to prepare bilayer membranes for a rechargeable Zn-air battery. The anion exchange polymer (PEBIH-PBMA) coating layer was prepared via free radical polymerization, i.e., by copolymerization of two monomers: 1-[(4-ethenylphenyl) methyl] -3- butylimidazolium hydroxide (EBIH) and butyl methacrylate (BMA).

The surface and cross-sectional FE-SEM images of the Celgard® 5550 and PEBIH-PBMA coated Celgard® 5550 membranes are shown in Figure 5a and Figure 5b, respectively. However, no thickness increase is seen by the SEM images after coating compared to the original thickness of the Celgard® 5550 (25 μm), thus indicating a possible penetration of the viscous anionic-polymer solution onto the porous structure of the support layer despite the use of a highly viscous solution (20 wt.% of polymer in ethanol). Over 96% reduction in the transport of $Zn(OH)_4^{2-}$ ions through the membrane to the cathode compartment was achieved. Compared to the Celgard® 5550 membrane, the modified membrane has over 2 magnitudes of $Zn(OH)_4^{2-}$ ions diffusion coefficient. Figure 5c presents $Zn(OH)_4^{2-}$ concentration levels of the cathode electrolyte versus cycle number. The high selectivity is explained by the lower mobility $Zn(OH)_4^{2-}$ ion associated with their size exclusion. This was reported to enhance the durability of the battery as its life-span was increased by about 300% compared to the same battery using a non-modified membrane (37 vs 104 cycles).

Besides this three-fold improvement in lifetime of the battery, the modified membrane-based battery exhibited comparable initial energy efficiency with the Celgard® 5550-based one (60.8 vs 59.4 %). On the other hand, the Celgard® 5550-based battery displayed higher final energy efficiency than the coated-ones (51.2 vs 41.8 %), suggesting that the Celgard® 5550-based battery has prematurely deceased due to the $Zn(OH)_4^{2-}$ ions rather than degradation of the air-electrode catalyst. The modified membrane displayed a similar overpotential increase during both the discharge and charge steps, whereas, the Celgard® 5550 membrane did not. The ORR characteristics was found to remain unchanged, whereas the OER process exhibited difficulties manifested as overpotential growth, which resulted in a higher final voltage. The OER catalyst is expected to be more sensitive toward $Zn(OH)_4^{2-}$ exposure. The energy efficiency plot of PEBIH-PBMA coated membrane is presented in Figure 5d.

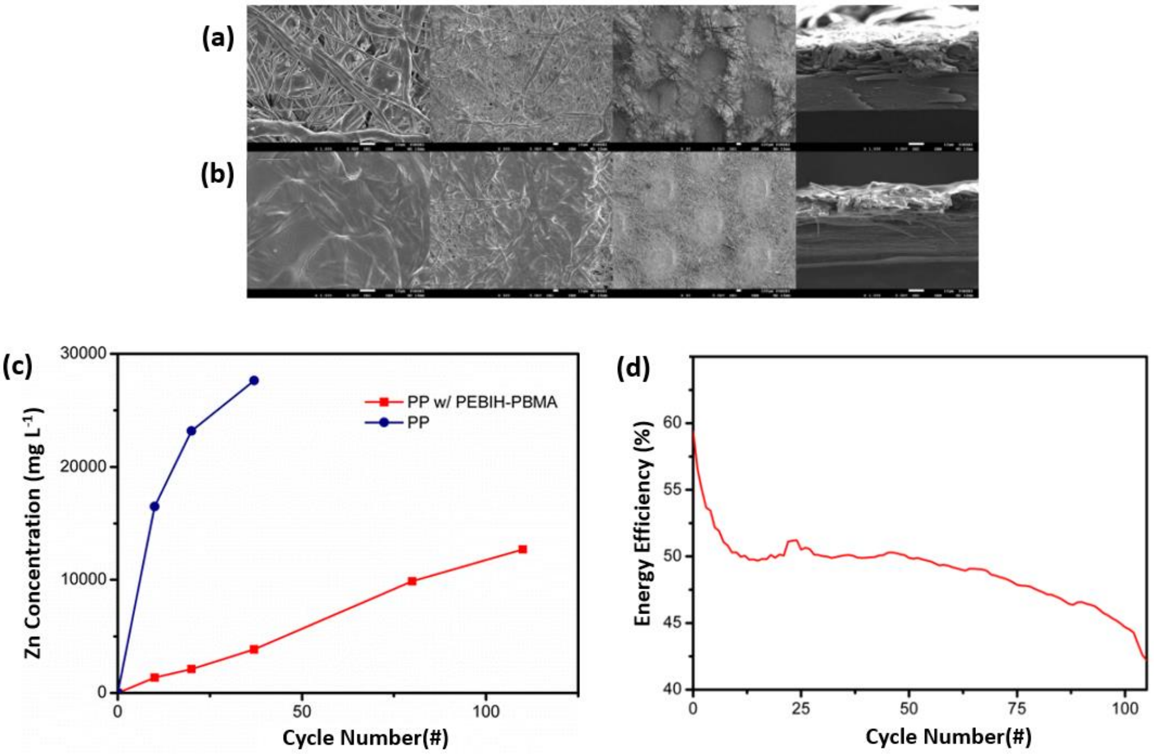

Figure 5: SEM images of Celgard®5550 (a) and Celgard®5550 coated with PEBIH-PBMA (b), Zn concentration with cycle number (c) and Energy efficiency for Celgard®5550 coated with PEBIH-PBMA under the constant current mode at 10 mA cm^{-2} (d). Reprinted with permission from [83]. Copyright © 2016 American Chemical Society.

Nafion®117 (CEM) has been reported to improve the selectivity of Celgard®3401 and Celgard®3501 membranes [135]. Celgard® membranes are usually hydrophilized by treatment with a (cationic/nonionic) surfactant. In this work, to prepare hydrophobic membranes, the surfactant was removed by washing it out several times with methanol. The Celgard® membranes (with and without surfactant) were coated with a solution of Nafion® 117 (from its alcoholic or aqueous dispersions of various concentrations) using several techniques. When the Celgard® 3401 without surfactant was coated with a 1% Nafion® solution, no zincate ion transport during 5 h was reported. However, a high resistance was obtained (186 Ω cm^2 at 50 kHz) due to the hydrophobization of the membrane. The hydrophobic pores of the membrane have probably excluded the Nafion® solution and remained filled with trapped air (rendering low conductivity). An increase in both conductivity and zincate ion flux through the membrane was observed when a membrane with surfactant was used (Table 4). Moreover, higher zincate crossover and ionic conductivity were observed with an increase in the amount of Nafion® coated on Celgard® 3501 without surfactant. For example, the $Zn(OH)_4^{2-}$ ion diffusion coefficient for the Celgard® 3501 coated with 0.047 mg cm^{-2} of Nafion® was 1.1×10^{-12} m^2 s^{-1} and with 0.079 mg cm^{-2} of Nafion®, it was much higher: 8.3×10^{-12} m^2 s^{-1}. Based on this study, coating with Nafion® seems to be not an efficient method to improve permselectivity of the membranes.

3.1.3.3. Sulfonated porous membranes

A limitation associated with the use of some commercial porous membranes is their hydrophobicity, which could decrease the pore wettability with KOH aqueous solution. A common strategy to enhance the hydrophilicity is by membrane surface modification. Sulfonation is a unique chemical treatment that can increase polymer hydrophilicity by incorporating sulfonic acid functional group on the surface of polymer [186]. Wu et al. [187] prepared sulfonated membranes with a high ionic conductivity and evaluated their performance in a Zn-air battery. These membranes were prepared by sulfonation of commercial non-woven PP/PE membranes (thickness = 0.2 mm, porosity = 60-70%) using concentrated sulfuric acid (Figure 6a). The sulfonation reaction took place by immersing the PP/PE membranes in a 98 wt.% sulfuric acid at 90 ^{o}C and atmospheric pressure for 3 to 128 h. The highly sulfonated s-PP/PE membrane (sulfonation time 128 h) is shown in Figure 6b. As shown by the infrared spectra of the membranes (before and after the sulfonation treatment) in Figure 6c, the peaks at around the wavenumbers of 1150–1200 and 550–585 cm^{-1} can be attributed to the asymmetric SO_3^- stretching modes and deformation of the S–O bonds, respectively, showing successful incorporation of sulfonic acid groups to the polymer membrane. However, after sulfonation, many of the filaments (originally, 10–20 μm) showed a reduced diameter indicating that part of the polymer had been degraded or/and dissolved by the sulfuric acid.

The water contact angles decreased from 58^{o} (commercial PP/PE membrane) to 18^{o} after 128 h of sulfonation, showing the effectiveness of the sulfonation in increasing surface hydrophilicity. The sulfonated membrane exhibited a higher ionic conductivity than that of the unsulfonated with 17.5 mS cm^{-1} vs 8.8 mS cm^{-1} at 25 °C (32 wt.% KOH solution) and, thus, a higher power density of 38 mW cm^{-2} vs 20 mW cm^{-2} (Figure 6d). However, compared to the pristine membrane, the sulfonated membrane showed a decrease in both tensile strength (21%) and thermal resistance (4%). The decrease in mechanical strength can be attributed to the surface etching effect of sulfuric acid, leading to decrease filaments diameter and, probably lower polymer molecular weight.

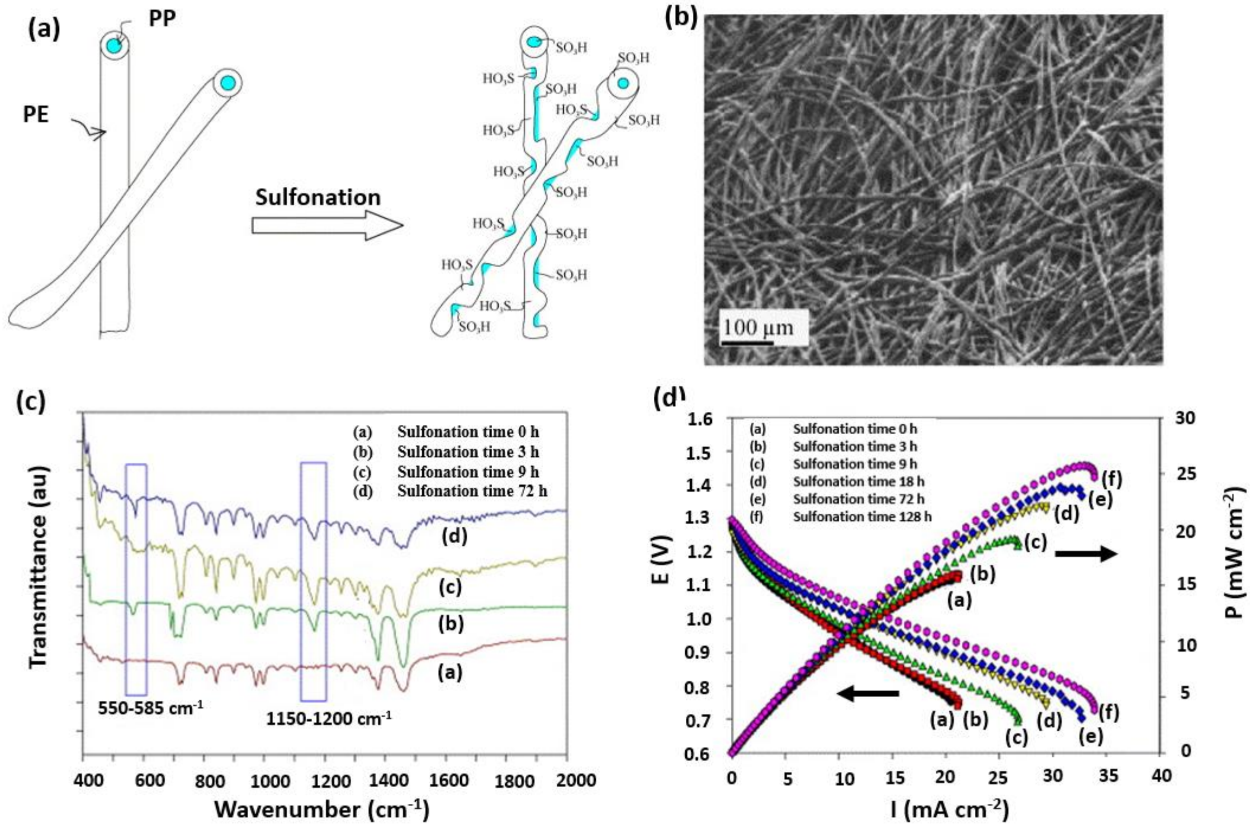

Figure 6. Schematic illustrations of the non-woven membrane structures before and after the sulfonation treatment (a), SEM micrographs of the sulfonated s-PP/PE membrane (sulfonation time 128 h) (b), IR spectra of the different membrane samples (c) and the cell potential and power density curves of the solid-state zinc-air batteries as functions of discharge current density (d). Adapted with permission from [187]. Copyright © 2006 Elsevier.

3.1.4. Inorganic membranes

Inorganic membranes refer to membranes which are made from materials such as ceramic, magnesia, alumina and titania. Inorganic membranes are known for their high chemical and thermal stabilities. These membranes are interesting as potential candidates for Zn-air batteries because of their good alkaline chemical stability [188]. Additionally, hydrotalcite clay is an interesting alkaline AEM material [189], but has never been exploited for Zn-air batteries. A ceramic membrane could provide the required dimensional rigidity that could be effective in avoiding internal short circuit problem. Moreover, ceramic membranes are known to have better chemical stability (against oxidative agents) compared to polymeric membranes [190,191]. However, despite the excellent alkaline stability, almost no attention has been given to the preparation of such membranes for Zn-air flow batteries. This could be due to the fact that inorganic porous membranes are usually fragile [192,193]. Therefore, it is difficult and expensive to fabricate large inorganic membranes [87].

Ceramic membranes which are impermeable to $Zn(OH)_4^{2-}$ has been evaluated in rechargeable alkaline Zn/MnO_2 batteries [134]. In this study, a commercial sodium super-ion conducting ceramic membrane (NaSICON) was used. Here, the Na^+ cation is the charge carrier, rather than the OH^- ion. Due to its inherent property (cation conductor) and solid-state nature of the membrane, no $Zn(OH)_4^{2-}$ crossover was detected. Nevertheless, the membrane (1.17 cm^2) had high resistance values: 26 Ω for the 1.0 mm thick and 11 Ω for the 0.5 mm thick NaSICON membrane, strongly suggesting that a decrease in membrane thickness is required. However, such strategy will probably result in a brittle membrane.

Saputra et al. [172] prepared microporous MCM-41 membrane by a facile, dip-coating technique from a solution consisting of cethyltrimethylammonium bromide (CTAB), hydrochloric acid, DI water, ethanol and tetraethylorthosilicate (TEOS). MCM-41 membrane (thickness ca. 5 µm and average pore size 2.2 nm) with hexagonally ordered, narrow, pore structure formation was verified using X-ray diffraction. The membranes tested in Zn/MCM-41/air cell using KOH electrolyte displaying a good performance: a maximum power density of 32 mW cm^{-2} and energy density of 300 Wh L^{-1}, which was comparable to that of commercial Zn-air button cells of equivalent size was reported.

Table 4 presents the diffusion coefficients of $Zn(OH)_4^{2-}$ ions through the pristine and porous polymeric membranes. The porous Celgard® membranes are included in the table for comparison purpose.

Table 4: Zincate crossover through pristine and modified porous membranes.

Membrane		Analysis method	Flux of $Zn(OH)_4^{2-}$ ($\times 10^{-6}$ mol m^{-2} s^{-1})	Diffusion coefficient of $Zn(OH)_4^{2-}$ (m^2 s^{-1})***	Ref.
Two Celgard® 3401		Electrogravimetric	120.8	6.9×10^{-12}	[156]
Two Celgard® 3401 coated with inorganic molecules	$Al(OH)_2$ + Teflon		21.2	8.5×10^{-12}	
	CaF_2		15.6	1.8×10^{-12}	
	$Mg(OH)_2$		0.31	5.1×10^{-14}	
	$Mn(OH)_2$		0.14	6.0×10^{-15}	
Celgard® 5550		ICP-OES	-	1.1×10^{-5}	[83]
Celgard® 5550 coated with PIL (PEBIH−PBMA)			-	5.0×10^{-7}	
Celgard® 3501 with surfactant (hydrophilic)		Polarography measurement	94.4	2.4×10^{-11}	[135]
Celgard® 3501 without surfactant (hydrophobic)			0**	0	
Celgard® 3501 coated with Nafion®117*	0.024 mg cm^{-2} Nafion®117		1	2.5×10^{-13}	
	0.047 mg cm^{-2} Nafion®117		4.4	1.1×10^{-12}	
	0.079 mg cm^{-2} Nafion®117		33.3	8.3×10^{-12}	
Celgard® 3401 coated with Coated with 1% Nafion®117*	Without surfactant		0	0	
	With surfactant		45.6	5.8×10^{-13}	

Electrospun nanofiber membrane	Electrospun nanofibre mat-reinforced composite polymer (ERC) membranes	ICP-OES	-	8.33×10^{-12}	[85]
Inorganic membrane	NaSICON membrane	ASV analysis	-	8.5×10^{-15}	[134]

*Diffusion coefficient calculated (using Fick's law) based on the provided flux data.

**Not detected during the first 5 h of operation.

*** Diffusion coefficient of $Zn(OH)_4^{2-}$ performed at room temperature.

3.2. Polymer electrolyte membranes (ion-conducting membranes)

3.2.1. Anion exchange membranes

An AEM consists of polymer chains functionalized with a number of cationic groups. Most AEMs are made from hydrocarbon polymer backbones with covalently attached quaternary ammonium (QA) groups. The use of AEMs in Zn-air batteries have been widely proposed [65] since a typical AEM exhibit only a 10% loss in performance after 1000 h [44]. This performance is more than satisfactory for meeting the required shelf life and cycle life of the battery. However, no information has been provided regarding the AEM type and battery testing conditions. The prospects for AEMs in Zn-air batteries, including the major recent developments and strategies to overcome the remaining challenges has been reviewed recently [194]. Indeed, the performance and cyclability of the batteries have been found to be dependent on the properties of the AEMs (such as water uptake, anisotropic swelling ratio and hydroxide conductivity). Additionally, the common AEMs chemical degradation ways and their mitigation strategies have been discussed.

A commercial AEM A201® (Tokuyama Soda, Japan) has been tested in Zn-air batteries. The A201®-based battery showed a rapid voltage and capacity loss after some cycles. This was attributed to the continuous loss of membrane water content and ionic conductivity during the constant current operation [142–145]. To solve this issue, AEMs following different synthesis strategies have been prepared and tested in Zn-air batteries [142–145]. The prepared AEMs which exhibit superior OH^- ion conductive properties, water retention and low anisotropic swelling were reported to boost the specific capacity and improved the cycling stability of the battery compared to that of A201®-based battery (Table 5). However, the effect of zincate ions crossover was not investigated in these studies.

Dewi et al. [84] synthesized AEM by using polysulfonium cation (poly(methylsulfonio-1,4-phenylenethio-1,4-phenylene trifluoromethanesul-fonate). The prepared polysulfonium-based membrane was effective in preventing zincate ions crossover from the negative to the positive electrode, leading to a more than 6-fold discharge capacity increase of the cell compared to the case of using a

Celgard® 5550 membrane. It was assumed that Zn (II) species in the electrolyte are able to cross through the membrane to the air electrode in the form of Zn^{2+}. However, in a strongly alkaline solution, the Zn^{2+} ions combine with OH^- ions, instantly forming $Zn(OH)_4^{2-}$ ions.

Fu et al. [142] prepared a flexible, highly conductive (21 mS cm^{-1} at 30 °C) nanoporous membrane from natural cellulose nanofibers with very high water retention (96.5%) and low anisotropic swelling degree (1.1). The membrane was prepared via functionalization of the cellulose fibers using dimethyloctadecyl[3-(trimethoxysilyl)propyl] ammonium chloride (DMOAP) (in methanol) as a precursor. The mixture of DMOAP and cellulose fibers was stirred (12 h at room temperature), centrifuged and washed (with ethanol and distilled deionized water) to remove unreacted traces of DMOAP. The QA-functionalized cellulose (QAFC) membrane was prepared by vacuum filtration, followed by drying and crosslinking. The reference A201® membrane exhibited an anisotropic swelling degree of 4.4 and water uptake of 44.3%. As a result, the 2-QAFC (cellulose nanofibers modified with 200 mol. % concentration of DMOAP with respect to the cellulose repeating glucose unit) membrane-based battery was reported to have a higher discharge capacity with a more stable voltage compared to the A201®-based battery.

Zhang et al. [143] prepared a laminated, cross-linked nanocellulose/graphene oxide membrane functionalized with QA for a flexible rechargeable Zn-air battery. Here, Graphene oxide (GO) was incorporated in order to enhance the ionic conductivity since it has abundant oxygen-containing groups which can be easily functionalized. Cellulose fibers are used as interconnected framework to integrate GO into a flexible membrane with a high water content, which can be cross-linked to achieve the required structural stability and (low) anisotropic swelling degree. Figure 7a shows the procedure followed for the preparation of the 2-QAFGO membrane. The QA-functionalized nanocellulose/GO (QAFCGO) membrane showed superior OH^- conductivity of 33 mS cm^{-1} at room temperature. The QAFCGO-based battery was reported to show higher performance compared to the A201®-based battery, with smaller over potentials for both discharge and charge processes. At current densities above 20 mA cm^{-2}, the QAFCGO-based battery remarkably outperformed the A201®-based battery (Figure 7b). The former battery had a better cycling stability performance than the latter one (Figure 7c). Moreover, the QAFCGO-based battery reached a higher peak power density (44 mW cm^{-2}) than the A201®-based one (33 mW cm^{-2}) (Figure 7d).

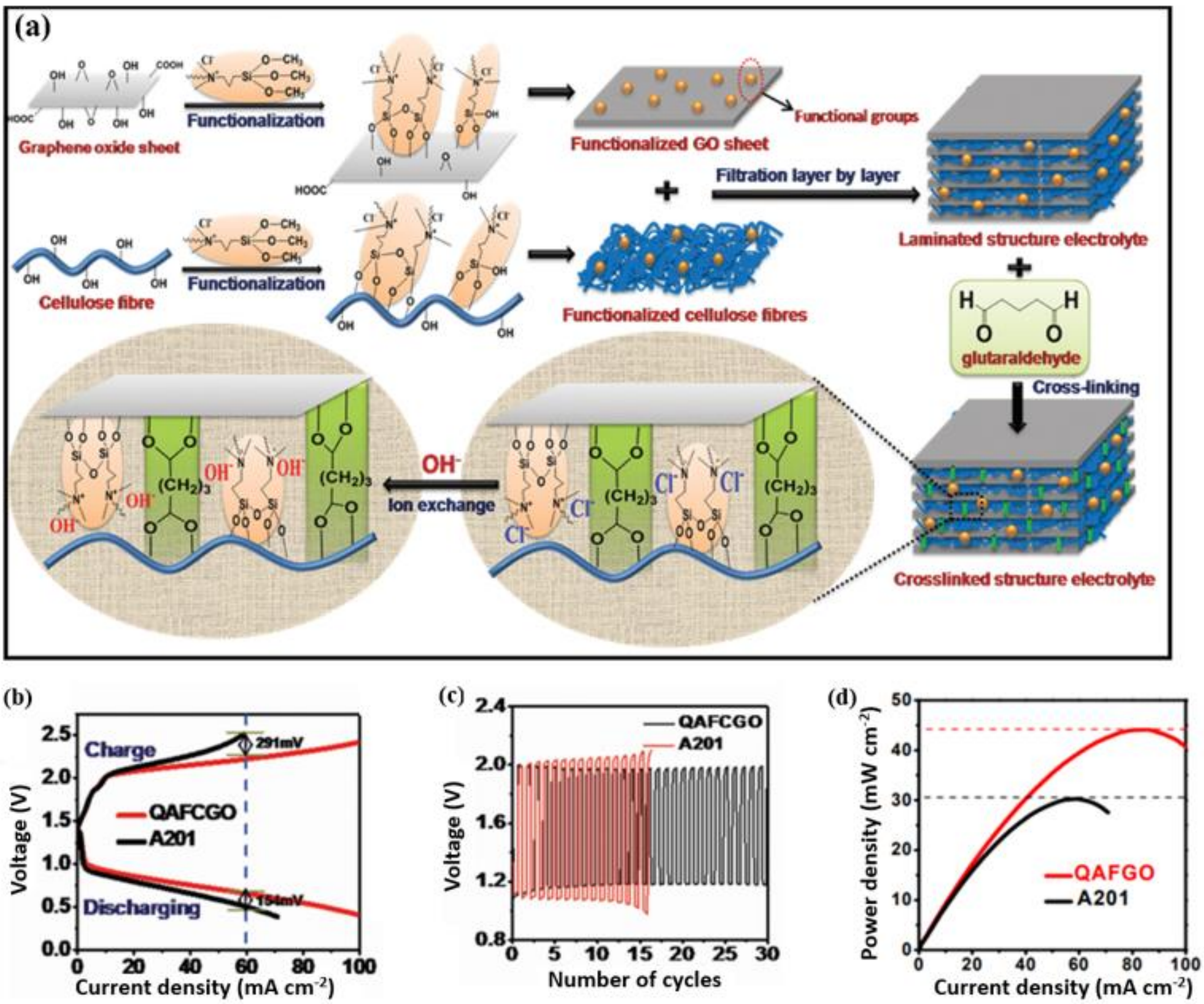

Figure 7: QAFCGO and A201® membranes-based Zn-air batteries: Schematic diagram of the chemical structure evolution of the nanocellulose membrane by functionalization, cross-linking and hydroxide-exchange (a), charge and discharge polarization curves (b), galvanostatic charge and discharge cycling at a current density of 1 mA cm^{-2} with a 20 min per cycle period (10 min discharge followed by 10 min charge) (c) and the power density plots at a current density of 1 mA cm^{-2} (d). Reproduced with permission from [143] . Copyright 2016, Wiley-VCH.

Furthermore, Abbasi et al. [155] prepared three AEMs using poly (p-phenylene oxide) (PPO) as polymer backbone and three different cations - trimethylamine (TMA), 1-methylpyrolidine (MPY), and 1-methylimidazole (MIM). PPO was chosen as a polymer backbone due to its commercial availability, high thermal, mechanical, and acceptable chemical stability and facile postfunctionalization [195,196]. The cations were directly attached on the PPO backbone. The PPO-TMA membrane was reported to have OH$^-$ ion conductivity equal to 17 mS cm^{-1}, 89 wt.% water uptake at room temperature and to prevent the crossover of $Zn(OH)_4^{2-}$ ions (Table 6). Moreover, the membrane showed excellent alkaline stability for at least 150 h in an alkaline solution commonly used in Zn–air batteries (7 M KOH solution at 30 °C). The PPO-TMA–based Zn-air battery exhibited low zincate diffusion coefficients (1.9 ×10^{-14}

m^2 s^{-1}) and high specific discharge capacity (~800 mAh g_{Zn}^{-1}). The low zincate diffusion coefficient of the PPO-based membrane was ascribed to the formation of ionic channels in the polymer structure through hydrophilic/hydrophobic microphase separation. However, no experimental evidence was provided for the formation of such a hydrophilic/hydrophobic microphase separation structure.

Well-defined hydrophilic-hydrophobic phase separation is crucial for enhancing ionic conductivity of AEMs [197]. However, not all AEMs develop a phase separation structure. Different strategies, such as block copolymers [198] and cation functionalization via a long-spacer-chain [199] have been used to design an AEM with a phase separation structure. AEMs composed of PVA/guar hydroxypropyltrimonium chloride (PGG-GP) displaying a hydrophilic-hydrophobic microphase separation structure and large ionic clusters was developed by using GA and pyrrole-2-carboxaldehyde as binary cross-linking agents. The prepared PGG-GP membrane exhibited a high OH^- ion conductivity (123 mS cm^{-1} at room temperature) and an excellent dimensional stability. The PGG-GP-based, flexible, all-solid-state Zn–air battery displayed a peak power density of 50.2 mW cm^{-2} at 48 mA cm^{-2} and a promising cycling stability (9 h at 2 mA cm^{-2}) [121]. On the other hand, formation of ionic channels with appropriate sizes in the two domains is required to develop AEMs with high selectivity [194].

Recently, an interesting investigation of effect of microdomain morphology on selective $Zn(OH)_4^{2-}$ and OH^- ions transport was performed [200]. PILs-based liquid-crystalline AEM with inverse bicontinuous cubic ($Ia\bar{3}d$) structure was prepared through a one-step chemical synthesis. The AEM-$Ia\bar{3}d$, with IEC of 0.76 mmol/g, had an OH^- conductivity of 12.6 mS cm^{-1} at 30 °C. Whereas, the crossover of hydrated $Zn(OH)_4^{2-}$ was found to be hindered ($Zn(OH)_4^{2-}$ diffusion coefficient of 1.6×10^{-13} m^2 s^{-1}). This well-defined 3D-interconnected ionic channels and the size-exclusion effect played a role to enhance the OH^- permselectivity of the membrane.

Table 5: Anion exchange membranes used in Zn-air batteries.

Membrane	Preparation method	properties	Battery type and operation conditions	Electrodes	Electrolyte	Performance	Ref
FAA®-3-based AEM	Commercial FAA®-3-SOLUT-10 in NMP, Fumatech BWT GmbH) Solution casting method.	QA cation	Bendable rechargeable Zn–air battery	Zn electrode: stainless-steel mesh coat with Zn species Air electrode: cobalt oxide based commercial	6 mol KOH PAA gel	Maximum power density of 9.8 mW cm^{-2}. Cells stable for at least 100 cycles. Specific capacity ~700 mAh g_{Zn}^{-1} under 1 mA cm^{-2} and discharging conditions.	[201]
A201® membrane	Commercial (Tokuyama Corporation, Japan)	28 µm thickness	Solid state rechargeable Zn-air battery	Zn electrode: Zn powder, carbon nanofiber, carbon black and poly (vinylidene fluoride-co -hexafluoropropene) polymer binder. Air electrode: Co_3O_4 nano-particles (<50 nm particle size) Gas diffusion layer: (catalyst loading of 1.0 mg cm^{-2})	-	A201-based battery membrane deteriorated noticeably after 720 min - The rapid voltage and capacity loss due to water loss	[142]

Polysulfonium-based membrane	Solution casting method	Transparent, 30 µm thickness	Zn-air cell, The cells were discharged at 1 mA at room temperature	Zn electrode: Zn powder (99.9% grade) (1 g) Air electrode: Carbon paste that contained MnO_2 catalyst	1 M KOH	-Capacities of discharge cell: 0.6 V, 124.8 h, 86 mAh g_{Zn}^{-1}	[84]
PPO-based AEM	Solution casting method	uniform and flexible films, 50 µm thickness	Primary Zn-air battery effective membrane and electrode area of 1.77 cm^2 The cell was discharged at a constant discharge current in the range of 2.5 to 15 mA cm^{-2} All experiments, the cut-off voltage was 0.9 V.	Zn electrode: anode was a 1 × 1 cm^2 pure zinc plate Cathode electrode: Ni-foam used as the current collector and gas diffusion layer. Mixture of MnO_2 and VXC-72 was used to prepare catalyst.	7 M KOH solution	PPO–MPY based cells: -maximum discharge current density of 117 mA/cm^2 with a maximum power density of 70 mW cm^{-2}. -Specific capacity: 772 mAh g_{Zn}^{-1} at 2.5 mA cm^{-2} -Power of the cell was 996 mWh g_{Zn}^{-1} for 2.5 mA cm^{-2} discharge current density.	[155]

Porous AEM based on QA and nanocellulose	Functionalization, followed by crosslinking.	High flexible, thickness of 30 µm	Solid state rechargeable Zn-air battery	Zn electrode (40 mg): Zn powder, carbon nanofiber, carbon black and poly (vinylidene fluoride-co -hexafluoropropene) polymer binder. Air electrode: Co_3O_4 nano-particles (<50 nm particle size) Gas diffusion layer: (catalyst loading of 1.0 mg/cm^2) Catalyst ink consisted of Co_3O_4, ionomer (AS-4, Tokuyama Inc.) and 1-propanol was sprayed onto a carbon cloth	-	2-QAFC battery - Specific capacity of was 492 mA h g_{Zn}^{-1}. - High power density of 2362 mW g_{Zn}^{-1} at a large current density of 4650 mA g_{Zn}^{-1} -Cycling stability over 2100 min.	[142]
Laminated cross-linked nanocellulose/GO	Vacuum filtration, followed by cross-linking	Thickness = 30 –50 µm	Flexible rechargeable Zn–air battery	Zn electrode: Zn film (zinc powder, carbon nanofiber, carbon black, and poly(vinylidene fluoride-co-hexafluoropropene) polymer binder) Air electrode: Co_3O_4 nanoparticles (<50 nm particle size) spayed onto a carbon cloth	-	QAFCGO-based battery: -Power density 44 mW cm^{-2}. -Stable output power within current density of 60 mA cm^{-2} under stressed conditions	[143]

GO membrane functionalized with imidazolium (1-hexyl-3-methylimidazolium chloride, HMIM)	Solution casting/vacuum filtration method	27 µm thickness, flexible and tough	Fully solid-state, thin, flexible Zn–air battery active surface area of 1.13 cm^2	Zn pellet electrode Gas-diffusion layer : active material and carbon black in isopropyl alcohol with binder (AS-4 ionomer, Tokuyama Inc.) A bifunctional Co_3O_4 Loading of the active material on the air electrode was 1.0 mg cm^{-2}	-	The 5-HMIM/G (5 = HMIM/GO)-battery: -Stable charge/discharge performance for 60 cycles -Specific energy density dropped only 16.6 Wh kg_{zn}^{-1} as the specific power density increase from 120 to 360 W kg_{zn}^{-1}	[144]
Cross-linked chitosan (CS) and poly (diallyldimethyl ammonium chloride) (PDDA)	Solution casting method	Anisotropic swelling (1.7) degree and water uptake (1.59 g g^{-1})	Solid-state Zn–air battery	Zn electrode: Zn metal Air electrode: 20 wt% Pt/C and IrO_2 (Ir = 85.7%) Catalyst ink consisted of 40 mg catalyst, 80 µL of 5 wt% Nafion and 10 mL ethanol.	-	The CS-PDDA-based battery: -High open-circuit voltage (1.3 V) -High power density (48.9 mW cm^{-2}) at 100 mA cm^{-2} but a limited cycle life of 2.5 h.	[145]
AEM composed of PVA/guar hydroxypropyltrimonium chloride (PGG-GP)	Solution casting, followed by cross-linking	1.52 mequiv/g IEC, anisotropic swelling degree (1.5) Thickness: 30-40 µm	All-solid-state Zn–air battery	Zn electrode: polished Zn foil Air electrode: IrO_2 and 40 wt% Pt/C Catalyst ink consisted of IrO_2/ Pt/C (1:1 by mass), 5 wt % Nafion and ethanol	-	-Peak power density of 50 mW cm^{-2} at 48 mA cm^{-2} -Cycling stability of 9 h at 2 mA cm^{-2}.	[121]

* It should be noted that the theoretical specific capacity of Zn is 820 mAh g_{Zn}^{-1}.

3.2.2. Cation exchange membranes

Nafion®, composed of a perfluorinated polymer backbone with pendant perfluoro ether terminated sulfonic acid side chains (PFSA), is the most frequently used material as a proton exchange membrane in fuel cells. It is chemically stable and has a high phase-separated morphology which makes it of possible interest for Zn-air battery applications. The water domains in PFSA membranes have been reported to be organized as locally flat and narrow (around 1 nm) channels [202]. This agrees with the finding of cryo-TEM tomographs of hydrated Nafion® membrane [203]. However, the hydrophilic negatively-charged sulfonate group in the Nafion® film allows the transportation of positively charged species while blocking negatively charged species, such as OH^- and $Zn(OH)_4^{2-}$ ions.

Therefore, when Nafion® is used in Zn-air battery, both $Zn(OH)_4^{2-}$ and OH^- ions will be repulsed by the Donnan exclusion mechanism; however, some OH^- ions (co-ions) can still permeate through the hydrophilic phase since the Nafion® membrane swelling is high in aqueous media [204] and especially in electrolyte solutions of the high ionic strength [205]. Indeed, the diffusion coefficient of $Zn(OH)_4^{2-}$ ion of Nafion® 521 film tested in a Zn-air battery was reported to be very low, 6.67×10^{-14} m^2 s^{-1} [86]. However, the Nafion® 521 film showed also a rather low $OH^–$ transference number of 0.14 [86] since as expected the protons conductivity was favored resulting in extremely low (0.8 mS/cm) $OH^–$ ion conductivity at room temperature. As a result, the Nafion® film-based Zn–air battery showed considerably large discharge/charge polarization, resulting in a very poor cyclic stability. Similarly, in another study, Nafion®117-based Zn-air fuel cell was reported to exhibit a poor performance (0.4 V at 1.3 mA cm^{-2}) [79].

Overall, Nafion® membranes afford a low voltage efficiency, even at low working current densities, in batteries using alkaline electrolytes. Therefore, given its low performance and high cost, it can be concluded that Nafion® membranes are not suitable for alkaline electrolyte-based batteries [204].

On the other hand, since Nafion® film has negative fixed charged groups that prevent the passage of $Zn(OH)_4^{2-}$ ions, it can be used to improve the selectivity of the membranes in Zn-air batteries. For example, Kim et al. [86] fabricated polymer blend electrolyte membranes (PBE membranes) (24 µm thick) by impregnating Nafion® films into an electrospun PVA/PAA nanofiber mat for rechargeable Zn-air battery. The Nafion® acts as an anion-repelling continuous polymeric phase. This was reported to effectively block $Zn(OH)_4^{2-}$ ions crossover with only slightly reducing the OH^- conduction. As a result, the PBE membranes had better cyclic stability compared to Celgard® 3501 membrane (over 2500 min vs. 900 min).

A summary of zincate permeation through AEMs and CEMs is presented in Table 6. Porous membranes are also included in the table for the sake of comparison. Evidently, the reported $Zn(OH)_4^{2-}$ diffusion coefficients for AEMs are quite similar to that for the Nafion®521 membrane. They were a much lower than those for the porous membranes and Nafion® bearing electrospun PVA/PAA mat (PBE membrane). For instance, the PPO-TMA membrane had a selectivity which is three order of magnitude higher than that of the Celgard® 3501 membrane. As stated in the previous section, this could be due to the formation of proper hydrophilic ions-conducting channels forming a hydrophilic-hydrophobic phase separation. The order of effectiveness in hindering zincate crossover of the membranes is: PPO–MPY > PPO–TMA > Nafion® 521 > AEM-Ia$\bar{3}$d > PBE > Celgard® 3501.

Table 6: Zincate crossover through ion-conducting membranes.

Membrane		$Zn(OH)_4^{2-}$ diffusion coefficient (D) ($m^2\ s^{-1}$)	OH^- ions conductivity (σ) in water ($mS\ cm^{-1}$) (at room temperature)	Permselectivity (σ/ D) ($S.s\ m^{-3}$)	Ref.
AEM	PPO–TMA	1.9×10^{-14}	17.4	9.2×10^{13}	[155]
	PPO–MPY	4.7×10^{-15}	16.3	3.5×10^{14}	
	AEM-Ia$\bar{3}$d	1.6×10^{-13}	12.6	7.9×10^{12}	[200]
CEM	Nafion® 521 film	6.7×10^{-14}	0.8	1.2×10^{12}	[86]
	Nafion® bearing electrospun PVA/PAA mat (PBE)	6.8×10^{-13}	6.6	9.7×10^{11}	[85]
Porous (reference)	Celgard® 3501	3.20×10^{-11}	13.7	4.3×10^{10}	

In most studies, only the observed decrease in zincate ions crossover is reported as an improvement. However, usually, this comes at the cost of a reduced OH^- ions conductivity. For instance, as shown in Table 6, Nafion® membrane has a quite low zincate ions crossover. Nevertheless, its OH^- conductivity was reported to be low as well. On the other hand, the AEMs displayed low diffusion coefficients of $Zn(OH)_4^{2-}$ and high OH^- conductivities, showing their superior degree of selectivities. Therefore, a concept rarely used, permselectivity, should be considered for comparing the membranes. The order of the membranes in terms of permselectivity is: PPO–MPY > PPO–TMA > AEM-Ia$\bar{3}$d > Nafion® 521 > PBE membrane > Celgard® 3501.

It is worth noting that the comparison is dependent of the zincate ion crossover testing conditions and measurement techniques. For instance, the electrolyte used has been reported to have an effect on the degree of crossover. For the same membrane, a higher zincate diffusion coefficient was reported when KOH was used instead of NaOH. This was attributed to the larger conductivity of (35 wt.%) KOH (620 mS cm^{-1}) [98] over (30 wt.%) NaOH (190 mS cm^{-1}) [206]. Therefore, it is difficult to compare the membranes performance when the same electrolyte is not used. This requires further investigation for developing reliable standard membrane performance protocols.

Last but not least, it is worth identifying the zincate concentration at which a detrimental effect is seen in the air electrode activity and cell capacity. For example, in alkaline Zn/MnO_2 batteries, detrimental effects of $Zn(OH)_4^{2-}$ ions on the positive electrode have been reported to occur at concentrations ≥ 0.1 M $Zn(OH)_4^{2-}$ [207]. Besides, a study correlating AEM properties (mainly ion exchange capacity, nanochannel size and degree of zincate ions crossover) with cell performance and cyclic stability is missing.

3.2.3. Ion solvating membranes (gel-polymer electrolyte membranes)

Ion solvating membranes (gel-polymer electrolyte membranes) are usually used as membrane. Conventional aqueous electrolytes cannot maintain a steady form and, thus cannot effectively separate the electrodes to prevent a short circuit [208]. On the other hand, gel polymer electrolytes, composed of one or more polymers gelled by an aqueous electrolyte, have been widely employed in flexible Zn-based batteries as a membrane [209]. Ion solvating membranes rely on the aqueous alkaline electrolyte (typically, KOH in water) to provide their ionic conductivity and when swelled with the KOH solution, they tend to form a homogenous ternary polymer/water/KOH system [210]. The performance of these membranes greatly depends on the choice of polymer matrix and the proportion of each ingredient. Usually, vinyl polymers and cellulose derivatives are used as matrices since they swell well upon exposure to an alkaline aqueous solution [63].

Mostly, composite polymeric membranes with high swelling degree are used in Zn-air batteries. For instance, a cross-linked PAA/ PVA gel polymer electrolyte (thickness = 28 µm) was prepared by thermal crosslinking (heat treatment: 140 ^{o}C for 3 h) method and used in a Zn-air cell [211]. The crossover of $Zn(OH)_4^{2–}$ ions through the crosslinked PVA/PAA (about 0.1 mmol) was significantly reduced compared with that of the Celgard® 3501 membrane (0.25 mmol) within 35 h of operation. More recently, Kim et al. [86] also prepared cross-linked PVA/PAA gel polymer electrolyte membrane (thickness, 24 µm) via thermal treatment of PVA and PAA mixture. Compared to the Zn-air cell with Celgard® 3501 membrane, the cell with the PVA/PAA electrolyte membrane showed a better OH^- permselectivity and electrochemical properties. The membrane was effective (lowered by about a half), the $Zn(OH)_4^{2-}$ ions crossover compared to that of the Celgard® 3501 membrane.

Yang *et al.* [212] reported the synthesis of a PVA-based gel polymer electrolyte that was doped with KOH. The PVA/KOH/H_2O electrolyte membrane exhibited a high ionic conductivity (47 mS cm^{-1} at room temperature) and good electrochemical performance. They also measured the anionic transport number ($t^–$) for PVA, PVA/PECH, and PVA/tetraethyl ammonium chloride (TEAC) polymer electrolytes using the Hittorf's method at 25 °C. The $t^–$ (varying between 0.82 and 0.99) was found to be dependent on the types of alkali metal salts and the chemical compositions of polymer electrolytes [213]. The PVA/TEAC (50/50 wt.%) blend membranes displayed an ionic conductivity of 23 mS cm^{-1} at room temperature.

A porous PVA-gelled polymer electrolyte prepared by a phase inversion method was used in rechargeable Zn–air battery [214]. After the phase inversion, the PVA membrane was cross-linked using a solution of 10 wt% glutaraldehyde (GA) in acetone at 30 °C for 10 min and immersed in a solution of KOH/PVA (35/2 wt%) for 24 h. The battery employing the PVA-gelled electrolyte membrane (20–50 μm) and highly flexible electrodes exhibited an excellent cycle stability over 120 cycles (at a volumetric charge-discharge rate of 250 A L^{-1}). The battery also demonstrated high volumetric (2905 Wh L^{-1}) and gravimetric (581 Wh kg^{-1}) energy densities. Furthermore, Peng et al. [215] reported a flexible, stretchable and rechargeable Zn-air battery using a PVA/poly(ethylene oxide) (PEO)–based alkaline polymer electrolyte. The discharge current density reached 1 A g^{-1} maintained for 30 discharge/charge cycles at a voltage plateau of 1.0 V. The influence of various properties of gel polymer electrolyte membranes, such as ionic conductivities, chemical stability, electrochemical windows and mechanical properties on the performance of rechargeable Zn–air batteries have been investigated elsewhere [216]. An inverse relationship between ionic conductivity and mechanical stiffness of the gel-polymer electrolytes was noticed. PAA6M-based battery exhibited the highest initial charge- discharge efficiency of 79% at 0.5 mA cm^{-2}. The performance was reported to be enhanced by reducing the gel polymer electrolyte thickness.

Modified gel-polymer electrolyte membranes have been also tested in Zn-air batteries. PEO-PVA-glass-fiber-mat (thickness controlled between 0.30 and 0.60 mm) with a high ionic conductivity (10 mS cm^{-1}) at room temperature has been prepared and employed in solid-state primary Zn–air cells by Yang and Lin [217]. The PEO–PVA polymer electrolyte showed a broad electrochemical stability window of 2.4 V (±1.2 V). The PEO–PVA-based Zn-air cell displayed a 1305 mA h capacity, thus with utilization of Zn 84% (since the theoretical capacity is 1560 mA h) at the C/10 rate at room temperature. On the other hand, the cell based on PE/PP's utilization was only 75%. The higher capacity and utilization of the cell employing the modified gel-polymer electrolyte membrane were attributed to its much smaller (0.1–0.2 μm) pores size compared with that of a PE/PP membrane (about 10–20 μm). On the other hand, the cell based on the PE/PP membrane was reported to be easily short-circuited when it is under a high discharge rate due to its larger pore size and non-uniform pore size distribution. Similarly, a gel polymer electrolyte consists of porous PVA and silica has been tested in Zn-air battery [218]. It was reported to show a high ionic conductivity (57 mS cm^{-1}) and a superior electrolyte retention capability out-performing that of the conventional PVA-KOH gel polymer electrolyte system.

4. Zinc-dendrites growth suppressing membranes

One of the main challenges related to the presence of the Zn-electrode of rechargeable Zn-air batteries is the formation of Zn-dendrites [219]. During the reduction of ZnO to Zn metal, the $Zn(OH)_4^{2-}$ ions close to the Zn electrode surface are first depleted and most of the remaining are retained by the membrane (inside and/or its surface) or at the exterior of the electrolyte, thus resulting in an uneven distribution of $Zn(OH)_4^{2-}$ ions (severe concentration polarization) [80]. Zn-dendrites are formed as a result of the inhomogeneities in the electrode surface morphology and the electric field strength distribution across the Zn electrode, caused by the free diffusion of Zn ions in the vicinity of the electrode surface [80,220,221]. In other words, the diffusion-controlled Zn deposition process is influenced by both electric field and concentration gradients [222] and the inhomogeneity on the electrode surface brings about its formation since there is faster mass transport due to a non-planar Zn ions diffusion. Moreover, Zn-dendrites tend to develop at high current densities, which lead to a rapid Zn deposition, due to the resulting non-uniform concentration gradients [223]. This is similar to the dendritic growth mechanism model proposed for copper and lithium metallic electrodes [224–226].

The usually sharp-structured dendrites can puncture the membrane [227], especially when the amount of dendrites is increased. This can lead to an electrical short-circuit of the cell during the charging process and result in battery failure [227]. Therefore, reinforcement of the membranes is necessary in addition to the efforts to avoid the formation of dendrites.

To reduce/avoid the continuous formation and growth of Zn-dendrites, thus extending the battery life-span as much as possible, several strategies including addition of additives into electrolytes [228] and electrodes [229], modification of Zn-electrode structure [230], optimization of electrolyte properties and selection of appropriate membranes [168,231,232] have been so far employed. However, despite the important role of membranes in retarding Zn-dendrite formation, there are only few reported studies focusing on their effects [231,233].

The use of an ion-conductive and/or optimized porous membrane is believed to improve the cycling stability of the battery by suppressing dendrite formations [234,235]. This is due to the fact that (i) membrane can regulate ion transport and avoid ion concentration gradient, which is the main cause of dendrite growth and (ii) the nanochannels in the membranes can greatly enhance the uniformity of current distribution resulting in a uniform Zn deposition [231]. For instance, prevention of Zn-dendrites formation has been observed when a membrane with a proper pore size and pore size distribution was used [168]. In this work, the microstructures of PVA/PVC membrane with pore size in the range of 60 – 120 nm were reported to effectively prevent any Zn dendritic formation during the overcharge period. As a result, over 50 cycles were attained for the rechargeable Zn electrode.

Moreover, Lee et al. [231] prepared a mechanically robust CEM for a Zn/Zn symmetric cell by cross-linking polyacrylonitrile (PAN) with lithium polysulfide (equivalent Li_2S_3), simultaneously leading to the formation of sulfur-containing functional fixed groups. This was then followed by hydrolysis, which resulted in the formation of a PAN-S membrane that achieved selective cationic transport (due to the sulfonic functional groups) and a homogeneous ionic flux distribution. As a result, the PAN-S membrane, with a high Young's modulus of 391 MPa, was found to suppress dendrite growth, exhibit a small polarization (<40 mV) and a long cyclic stability (>350 cycles) when tested in the Zn/Zn battery cell.

Another promising method to minimize/avoid the growth of dendrite is to fill the pores of the membranes with chemical compounds that can react with the Zn dendrites and dissolve them. Recently, Xie et al. [232] utilized a 900-µm thick elastomer porous polyolefin membrane (0.1 µm pore size, 58% ±7.5% porosity) in a Zn-iodine flow battery aiming at overcoming the negative impacts of Zn dendrites. Different compositions of KI, $ZnBr_2$, and KCl were used as electrolytes, thus I^-/I_2 and Zn^{2+}/Zn are the positive and negative redox couples, respectively. The reaction rate of the I_3^-/ I^- redox couple was found to be diffusion-limited. The pores of the membranes are believed to be filled with the solution of oxidized I_3^- ions. In this way, the oxidized I_3^- ions are able to oxidize the growing Zn dendrites when entered into the pores and make them soluble again ($Zn + I_3^- \leftrightarrow 3I^- + Zn^{2+}$). The problem with this system is that I_3^- can diffuse through the membrane and leading to a self-discharge and decrease in coulombic efficiency. Therefore, it is essential to develop and employ a membrane with a proper pore size and/or covered by a thin Nafion® layer faced to the battery positive side [236]. Similar membrane pores functionalization/filling techniques can be considered in Zn-air batteries in order to overcome the adverse effects of Zn-dendrites formation.

5. Summary, outlook and thesis work plan

5.1. Summary and outlook

Because of the growing demands for grid-scale electrical energy storage and the inherent attractive attributes of rechargeable Zn-air batteries, such as high theoretical specific energy, high safety, economic feasibility and environmental friendliness, they are considered feasible devices for large-scale electricity storage. The high number of scientific papers published and projects funded so far focused on Zn-air batteries indicates their promising future as next-generation energy storage devices. Membranes have been known to be a critical component of Zn-air batteries as they must selectively transport OH^- ions. Additionally, properly designed membranes should restrict/minimize Zn dendrites formation and growth. This can be achieved by preparing dedicated membranes with an optimal morphology to regulate the ions transport and appropriate chemical modifications to interact and solubilize the dendrites. However, it must be noted that the role of membrane in suppressing Zn-dendrite formations in Zn-air batteries has not been extensively investigated and explored. Therefore, more works on membrane design and investigation of its impact on suppression of dendrite formation and growth are required.

In this review, we have presented and discussed the recent developments in membranes used in Zn-air batteries. The commonly used porous membranes have not been primarily designed for this application, instead, they are adapted from other battery applications. Despite their acceptable OH^- conductivities and chemical stabilities, the crossover of $Zn(OH)_4^{2-}$ ions restricts their widespread usage. Therefore, further research efforts from both researchers and industries on design, fabrication and characterization of high-performance membranes for Zn-air battery are of utmost importance in order to fully commercialize the battery.

One of the strategies used to minimize the crossover of $Zn(OH)_4^{2-}$ ions is the use of properly designed porous membranes specific for Zn-air battery. A porous membrane with an average pore size larger than the hydrated ionic radius of OH^- ions but smaller than that of the $Zn(OH)_4^{2-}$ is needed. Recently, the use of electrospun nanofiber-based porous membranes for rechargeable Zn-air batteries has been introduced in order to improve the membrane integrity. The nanofibers materials fabricated using electrospinning technology have a large surface area, large porosity and favorable molecular orientation along the fiber axis. A promising performance has been reported in the literature.

Another way to inhibit $Zn(OH)_4^{2-}$ ions crossover is by surface modification of porous membranes. The membrane pore size can be decreased by filling the pores with inorganic particles. Membrane coating with inorganic particles has been shown to minimize the $Zn(OH)_4^{2-}$ ions crossover; however, deposition of inorganic particles was reported to also increase the resistance of the membranes. As a result, such membranes have not been commercialized at industrial scale. Hence, an optimum content of inorganic particles not significantly reducing the conductivity of the membrane is required. Coating/filling of porous membranes with ion selective polymers, such as PILs is another promising way to improve their selectivity. This has been reported to block $Zn(OH)_4^{2-}$ crossover from the Zn to the air electrode. However, the high cost of PILs might limit their practical applications. At the same time, this is not well-investigated topic. Hence, more research is needed to explore its potential for practical implementation.

Last but not least, arguably, the most promising approach to reduce $Zn(OH)_4^{2-}$ ions crossover seems to be using ion-selective membranes. Such membranes are able to permeate the OH^- ions while blocking the passage of the larger size $Zn(OH)_4^{2-}$ ions. For instance, the alkaline stable Nafion®, a typical CEM, has been used in Zn-air battery. However, it was reported to exhibit poor performance due to the low $OH^–$ ion conductivity of the membrane. Moreover, it is a well-known that Nafion® is a high cost membrane. Therefore, a CEM with an acceptable conductivity and cost should be considered as an alternative. On the other hand, Nafion® films can be incorporated/coated onto porous membranes to further improve the selectivity of these membranes.

AEMs have been widely proposed to replace the porous membranes used in Zn-air battery applications. It must be noted that since both OH^- and hydrated zincate ions have the same charge, controlling the membrane nanochannels size in a way allowing only OH^- transport is required. The main challenge associated with the use of these membranes is their relatively low alkaline stability. However, this problem is less severe compared to the application of AEMs in high-temperature and low relative humidity fuel cells. Considering the impressive progress nowadays, a promising potential can be foreseen towards the development of low-cost and stable AEMs for the Zn-air battery.

One of the main reasons why Zn-air batteries are considered to be promising energy storage is due to their high specific energy density at a relatively low cost. The material costs of such batteries can be relatively low because Zn is one of the most widely abundant elements and O_2 is merely obtained from air. However, to realize a feasible rechargeable Zn-air battery, reduced cost of the membrane as well as the remaining components of the battery are quite important. The final cost of the membrane highly depends on the raw materials and preparation process.

5.2. Thesis work plan

Following the critical review of the state-of-the-art studies on membranes for Zn-air batteries, two membrane synthesis strategies were used to prepare appropriate membranes for Zn-air batteries and address the problems of zincate ions crossover, alkaline stability and hydroxide conductivity. We have investigated the performance of porous, modified porous membranes and anion-exchange membranes in a Zn slurry-air flow battery, a type of Zn-air battery.

In our first work, which is presented in chapter 6, we first tested six commercial porous membranes and investigated the relationship between their structure and properties (electrolyte uptake and zincate ions crossover) and corresponding single cell performance (cell resistance and power densities). However, as expected, a significant amount of zincate ions crossover was observed which makes their application in rechargeable Zn slurry-air flow batteries in question. To minimize the zincate ions crossover, one of the porous membranes was coated with prepared and commercial ionomers, ex-situ characterized and tested them in the same battery.

In the second work, which is presented in chapter 7, a series of AEMs with good stability in alkaline medium were prepared. In this work, similar to the high-performing AEMs in the AORFBs, to improve the stability of the cationic groups, we attached the N-spiro QA cation i.e., poly(DAPCl), via a long alkyl side chain into the PPO polymer backbone. Different from our previous work, herein, the ketone group C=O in the spacer was reduced to CH_2 since the protons in the α-position are acidic, they can form enolate anions that are powerful nucleophiles. The prepared membranes were characterized in terms of hydroxide conductivity, zincate ions crossover, alkaline stability and battery performance.

References

[1] H. Prifti, A. Parasuraman, S. Winardi, T.M. Lim, M. Skyllas-Kazacos, H. Prifti, A. Parasuraman, S. Winardi, T.M. Lim, M. Skyllas-Kazacos, Membranes for redox flow battery applications, Membranes (Basel). 2 (2012) 275–306. doi:10.3390/membranes2020275.

[2] B. Dunn, H. Kamath, J.-M. Tarascon, Electrical energy storage for the grid: a battery of choices., Science. 334 (2011) 928–35. doi:10.1126/science.1212741.

[3] G.L. Soloveichik, Flow batteries: current status and trends, Chem. Rev. 115 (2015) 11533–11558. doi:10.1021/cr500720t.

[4] A. Blakers, M. Stocks, B. Lu, C. Cheng, R. Stocks, Pathway to 100% renewable electricity, IEEE J. Photovoltaics. 9 (2019) 1828–1833. doi:10.1109/JPHOTOV.2019.2938882.

[5] W. Wang, Q. Luo, B. Li, X. Wei, L. Li, Z. Yang, Recent progress in redox flow battery research and development, Adv. Funct. Mater. 23 (2013) 970–986. doi:10.1002/adfm.201200694.

[6] M. Aneke, M. Wang, Energy storage technologies and real life applications – A state of the art review, Appl. Energy. 179 (2016) 350–377. doi:10.1016/J.APENERGY.2016.06.097.

[7] C.W. Chan, J. Ling-Chin, A.P. Roskilly, A review of chemical heat pumps, thermodynamic cycles and thermal energy storage technologies for low grade heat utilisation, Appl. Therm. Eng. 53 (2013) 160–176. doi:10.1016/J.APPLTHERMALENG.2013.02.030.

[8] P. Pardo, A. Deydier, Z. Anxionnaz-Minvielle, S. Rougé, M. Cabassud, P. Cognet, A review on high temperature thermochemical heat energy storage, Renew. Sustain. Energy Rev. 32 (2014) 591–610. doi:10.1016/J.RSER.2013.12.014.

[9] J.-M.M. Tarascon, M. Armand, Issues and challenges facing rechargeable lithium batteries, Nature Publishing Group, 2001. doi:10.1038/35104644.

[10] S. Leuthner, Lithium-ion battery overview, in: Lithium-Ion Batter. Basics Appl., Springer Berlin Heidelberg, 2018: pp. 13–19. doi:10.1007/978-3-662-53071-9_2.

[11] L. Lu, X. Han, J. Li, J. Hua, M. Ouyang, A review on the key issues for lithium-ion battery management in electric vehicles, J. Power Sources. 226 (2013) 272–288. doi:10.1016/j.jpowsour.2012.10.060.

[12] B. Scrosati, J. Hassoun, Y.K. Sun, Lithium-ion batteries. A look into the future, Energy Environ. Sci. 4 (2011) 3287–3295. doi:10.1039/c1ee01388b.

[13] G.J. May, A. Davidson, B. Monahov, Lead batteries for utility energy storage: A review, J. Energy Storage. 15 (2018) 145–157. doi:10.1016/j.est.2017.11.008.

[14] L. Gaines, J. Sullivan, A. Burnham, I. Belharouak, Life-cycle analysis of production and recycling of lithium ion batteries, Transp. Res. Rec. (2011) 57–65. doi:10.3141/2252-08.

[15] Ramasamy Kulandaivel Saminathan, Lead acid battery. Attacking sulphate passivation and cyclability problems, 2006. http://www.grin.com/en/e-book/373853/lead-acid-battery-attacking-sulphate-pas- (accessed May 4, 2020).

[16] R. Ahuja, A. Blomqvist, P. Larsson, P. Pyykkö, P. Zaleski-Ejgierd, Relativity and the lead-acid battery, Phys. Rev. Lett. 106 (2011) 18301. doi:10.1103/PhysRevLett.106.018301.

[17] P. Ruetschi, Aging mechanisms and service life of lead-acid batteries, in: J. Power Sources, Elsevier, 2004: pp. 33–44. doi:10.1016/j.jpowsour.2003.09.052.

[18] D. Pavlov, Lead-acid batteries: Science and technology a handbook of lead-acid battery technology and its influence on the product, Elsevier, 2017. doi:10.1016/C2012-0-00146-9.

[19] D.A.J. Rand, P.T. Moseley, Energy storage with lead-acid batteries, in: Electrochem. Energy Storage Renew. Sources Grid Balanc., Elsevier Inc., 2015: pp. 201–222. doi:10.1016/B978-0-444-62616-5.00013-9.

[20] G. May, Secondary batteries –Lead-acid systems: Stationary batteries, Encycl. Electrochem. Power Sources. 5 (2009) 693–704.

[21] S. Trocino, M. Lo Faro, S.C. Zignani, V. Antonucci, A.S. Aricò, High performance solid-state iron-air rechargeable ceramic battery operating at intermediate temperatures (500–650 °C), Appl. Energy. 233–234 (2019) 386–394. doi:10.1016/j.apenergy.2018.10.022.

[22] D. Gelman, B. Shvartsev, Y. Ein-Eli, Aluminum-air battery based on an ionic liquid electrolyte, J. Mater. Chem. A. 2 (2014) 20237–20242. doi:10.1039/c4ta04721d.

[23] R. Cao, J.-S. Lee, M. Liu, J. Cho, Recent progress in non-precious catalysts for metal-air batteries, Adv. Energy Mater. 2 (2012) 816–829. doi:10.1002/aenm.201200013.

[24] K.F. Blurton, A.F. Sammells, Metal/air batteries: Their status and potential - a review, J. Power Sources. 4 (1979) 263–279. doi:10.1016/0378-7753(79)80001-4.

[25] Z.L. Wang, D. Xu, J.J. Xu, X.B. Zhang, Oxygen electrocatalysts in metal-air batteries: From aqueous to nonaqueous electrolytes, Chem. Soc. Rev. 43 (2014) 7746–7786. doi:10.1039/c3cs60248f.

[26] A.Z. Weber, M.M. Mench, J.P. Meyers, P.N. Ross, J.T. Gostick, Q. Liu, Redox flow batteries: A review, J. Appl. Electrochem. 41 (2011) 1137–1164. doi:10.1007/s10800-011-0348-2.

[27] B. Hu, C. DeBruler, Z. Rhodes, T.L. Liu, Long-cycling aqueous organic redox flow battery (AORFB) toward sustainable and safe energy storage, J. Am. Chem. Soc. 139 (2017) 1207–1214. doi:10.1021/jacs.6b10984.

[28] A. Parasuraman, T.M. Lim, C. Menictas, M. Skyllas-Kazacos, Review of material research and development for vanadium redox flow battery applications, Electrochim. Acta. 101 (2013) 27–40. doi:10.1016/j.electacta.2012.09.067.

[29] X. Li, H. Zhang, Z. Mai, H. Zhang, I. Vankelecom, Ion exchange membranes for vanadium redox flow battery (VRB) applications, Energy Environ. Sci. 4 (2011) 1147–1160. doi:10.1039/c0ee00770f.

[30] K. Lin, R. Gómez-Bombarelli, E.S. Beh, L. Tong, Q. Chen, A. Valle, A. Aspuru-Guzik, M.J. Aziz, R.G. Gordon, A redox-flow battery with an alloxazine-based organic electrolyte, Nat. Energy. 1 (2016) 1–8. doi:10.1038/nenergy.2016.102.

[31] W. Smith, Role of fuel cells in energy storage, J. Power Sources. 86 (2000) 74–83. doi:10.1016/S0378-7753(99)00485-1.

[32] B. Peng, J. Chen, Functional materials with high-efficiency energy storage and conversion for batteries and fuel cells, Coord. Chem. Rev. 253 (2009) 2805–2813. doi:10.1016/j.ccr.2009.04.008.

[33] J. Bowers, Center for energy efficient materials (CEEM) (final technical report), Argonne, IL (United States), 2014. doi:10.2172/1169473.

[34] N. Mahmood, C. Zhang, H. Yin, Y. Hou, Graphene-based nanocomposites for energy storage and conversion in lithium batteries, supercapacitors and fuel cells, J. Mater. Chem. A. 2 (2014) 15–32. doi:10.1039/c3ta13033a.

[35] S. Dong, X. Chen, X. Zhang, G. Cui, Nanostructured transition metal nitrides for energy storage and fuel cells, Coord. Chem. Rev. 257 (2013) 1946–1956. doi:10.1016/j.ccr.2012.12.012.

[36] W. Vielstich, A. Lamm, H.A. (Hubert A. Gasteiger, H. Yokokawa, Handbook of fuel cells : fundamentals, technology, and applications, Wiley, 2003.

[37] C. Abbey, G. Joos, Supercapacitor energy storage for wind energy applications, IEEE Trans. Ind. Appl. 43 (2007) 769–776. doi:10.1109/TIA.2007.895768.

[38] L. Qu, W. Qiao, Constant power control of DFIG wind turbines with supercapacitor energy storage, IEEE Trans. Ind. Appl. 47 (2011) 359–367. doi:10.1109/TIA.2010.2090932.

[39] W. Li, G. Joós, J. Bélanger, Real-time simulation of a wind turbine generator coupled with a battery supercapacitor energy storage system, IEEE Trans. Ind. Electron. 57 (2010) 1137–1145. doi:10.1109/TIE.2009.2037103.

[40] B.E. Conway, Transition from “supercapacitor” to “battery” behavior in electrochemical energy storage, J. Electrochem. Soc. 138 (1991) 1539. doi:10.1149/1.2085829.

[41] T. Ma, H. Yang, L. Lu, Development of hybrid battery-supercapacitor energy storage for remote area renewable energy systems, Appl. Energy. 153 (2015) 56–62. doi:10.1016/j.apenergy.2014.12.008.

[42] D.P. Dubal, O. Ayyad, V. Ruiz, P. Gómez-Romero, Hybrid energy storage: The merging of battery and supercapacitor chemistries, Chem. Soc. Rev. 44 (2015) 1777–1790. doi:10.1039/c4cs00266k.

[43] J. Yi, P. Liang, X. Liu, K. Wu, Y. Liu, Y. Wang, Y. Xia, J. Zhang, Challenges, mitigation strategies and perspectives in development of zinc-electrode materials and fabrication for rechargeable zinc–air batteries, Energy Environ. Sci. 11 (2018) 3075–3095. doi:10.1039/C8EE01991F.

[44] Y. Li, H. Dai, Recent advances in zinc–air batteries, Chem. Soc. Rev. 43 (2014) 5257–5275. doi:10.1039/C4CS00015C.

[45] P. Tan, B. Chen, H. Xu, H. Zhang, W. Cai, M. Ni, M. Liu, Z. Shao, Flexible Zn– and Li–air batteries: recent advances, challenges, and future perspectives, Energy Environ. Sci. 10 (2017) 2056–2080. doi:10.1039/C7EE01913K.

[46] M.A. Rahman, X. Wang, C. Wen, High energy density metal-air batteries: A review, J. Electrochem. Soc. 160 (2013) A1759–A1771. doi:10.1149/2.062310jes.

[47] A. R. Mainar, O. Leonet, M. Bengoechea, I. Boyano, I. de Meatza, A. Kvasha, A. Guerfi, J. Alberto Blázquez, Alkaline aqueous electrolytes for secondary zinc-air batteries: an overview, Int. J. Energy Res. 40 (2016) 1032–1049. doi:10.1002/er.3499.

[48] P. Sapkota, H. Kim, Zinc–air fuel cell, a potential candidate for alternative energy, J. Ind. Eng. Chem. 15 (2009) 445–450. doi:10.1016/J.JIEC.2009.01.002.

[49] J.J. Xu, H. Ye, J. Huang, Novel zinc ion conducting polymer gel electrolytes based on ionic liquids, Electrochem. Commun. 7 (2005) 1309–1317. doi:10.1016/J.ELECOM.2005.09.011.

[50] P. Pei, K. Wang, Z. Ma, Technologies for extending zinc–air battery's cyclelife: A review, Appl. Energy. 128 (2014) 315–324. doi:10.1016/J.APENERGY.2014.04.095.

[51] J.-S. Lee, S. Tai Kim, R. Cao, N.-S. Choi, M. Liu, K.T. Lee, J. Cho, Metal-Air Batteries with High Energy Density: Li-Air versus Zn-Air, Adv. Energy Mater. 1 (2011) 34–50. doi:10.1002/aenm.201000010.

[52] D. Linden, T.B. Reddy, Handbook of batteries, McGraw-Hill, 2002.

[53] D. Stock, S. Dongmo, J. Janek, D. Schröder, Benchmarking anode concepts: The future of electrically rechargeable zinc-air batteries, ACS Energy Lett. 4 (2019) 1287–1300. doi:10.1021/acsenergylett.9b00510.

[54] J.F. Drillet, F. Holzer, T. Kallis, S. Müller, V.M. Schmidt, Influence of CO2 on the stability of bifunctional oxygen electrodes for rechargeable zinc/air batteries and study of different CO2 filter materials, in: Phys. Chem. Chem. Phys., Royal Society of Chemistry, 2001: pp. 368–371. doi:10.1039/b005523i.

[55] M.A. Al-Saleh, S. Gültekin, A.S. Al-Zakri, H. Celiker, Effect of carbon dioxide on the performance of Ni/PTFE and Ag/PTFE electrodes in an alkaline fuel cell, J. Appl. Electrochem. 24 (1994) 575–580. doi:10.1007/BF00249861.

[56] H.H. Cheng, C.S. Tan, Reduction of CO2 concentration in a zinc/air battery by absorption in a rotating packed bed, J. Power Sources. 162 (2006) 1431–1436. doi:10.1016/j.jpowsour.2006.07.046.

[57] E. Gülzow, Alkaline fuel cells: A critical view, J. Power Sources. 61 (1996) 99–104. doi:10.1016/S0378-7753(96)02344-0.

[58] E.B. Fox, H.R. Colón-Mercado, Y. Chen, W.S.W. Ho, Development and selection of ionic liquid electrolytes for hydroxide conducting polybenzimidazole membranes in alkaline fuel cells, in: ACS Symp. Ser., American Chemical Society, 2012: pp. 129–143. doi:10.1021/bk-2012-1117.ch005.

[59] U. Krewer, C. Weinzierl, N. Ziv, D.R. Dekel, Impact of carbonation processes in anion exchange membrane fuel cells, Electrochim. Acta. 263 (2018) 433–446. doi:10.1016/j.electacta.2017.12.093.

[60] Technology and IP — Wattech Power, (n.d.). http://www.wattechpower.com/technology (accessed March 15, 2019).

[61] F.R. McLarnon, E.J. Cairns, Zinc–air Battery: Understanding the structure and morphology changes of graphene-supported CoMn2O4 bifunctional catalysts under practical rechargeable conditions, J. Electrochem. Soc. 138 (1991) 645. doi:10.1149/1.2085653.

[62] A.M. Bernardes, D.C.R. Espinosa, J.A.S. Tenório, Recycling of batteries: A review of current processes and technologies, J. Power Sources. 130 (2004) 291–298. doi:10.1016/j.jpowsour.2003.12.026.

[63] J. Fu, Z.P. Cano, M.G. Park, A. Yu, M. Fowler, Z. Chen, Electrically rechargeable zinc–air batteries: Progress, challenges, and perspectives, Adv. Mater. 29 (2017). doi:10.1002/adma.201604685.

[64] V. Caramia, B. Bozzini, Materials science aspects of zinc–air batteries: a review, Mater. Renew. Sustain. Energy. 3 (2014) 28. doi:10.1007/s40243-014-0028-3.

[65] J. Pan, Y.Y. Xu, H. Yang, Z. Dong, H. Liu, B.Y. Xia, Advanced architectures and relatives of air electrodes in Zn-air batteries, Adv. Sci. 5 (2018) 1700691. doi:10.1002/advs.201700691.

[66] Q. Liu, Z. Pan, E. Wang, L. An, G. Sun, Aqueous metal-air batteries: Fundamentals and applications, Energy Storage Mater. (2019). doi:10.1016/j.ensm.2019.12.011.

[67] E. Davari, D.G. Ivey, Bifunctional electrocatalysts for Zn-air batteries, Sustain. Energy Fuels. 2 (2018) 39–67. doi:10.1039/c7se00413c.

[68] J. Zhang, Q. Zhou, Y. Tang, L. Zhang, Y. Li, Zinc-air batteries: Are they ready for prime time?, Chem. Sci. 10 (2019) 8924–8929. doi:10.1039/c9sc04221k.

[69] G. Toussaint, P. Stevens, L. Akrour, R. Rouget, F. Fourgeot, Development of a Rechargeable Zinc-Air Battery, in: ECS Trans., ECS, 2010: pp. 25–34. doi:10.1149/1.3507924.

[70] Y. Li, M. Gong, Y. Liang, J. Feng, J.E. Kim, H. Wang, G. Hong, B. Zhang, H. Dai, Advanced zinc-air batteries based on high-performance hybrid electrocatalysts, Nat. Commun. 4 (2013) 1–7. doi:10.1038/ncomms2812.

[71] A.R. Mainar, E. Iruin, L.C. Colmenares, A. Kvasha, I. de Meatza, M. Bengoechea, O. Leonet, I. Boyano, Z. Zhang, J.A. Blazquez, An overview of progress in electrolytes for secondary zinc-air batteries and other storage systems based on zinc, J. Energy Storage. 15 (2018) 304–328. doi:10.1016/j.est.2017.12.004.

[72] M. Hilder, B. Winther-Jensen, N.B. Clark, The effect of binder and electrolyte on the performance of thin zinc-air battery, Electrochim. Acta. 69 (2012) 308–314. doi:10.1016/j.electacta.2012.03.004.

[73] Z. Chen, J.-Y. Choi, H. Wang, H. Li, Z. Chen, Highly durable and active non-precious air cathode catalyst for zinc air battery, J. Power Sources. 196 (2011) 3673–3677. doi:10.1016/j.jpowsour.2010.12.047.

[74] S. Zhu, Z. Chen, B. Li, D. Higgins, H. Wang, H. Li, Z. Chen, Nitrogen-doped carbon nanotubes as air cathode catalysts in zinc-air battery, Electrochim. Acta. 56 (2011) 5080–5084. doi:10.1016/j.electacta.2011.03.082.

[75] V. Neburchilov, H. Wang, J.J. Martin, W. Qu, A review on air cathodes for zinc–air fuel cells, J. Power Sources. 195 (2010) 1271–1291. doi:10.1016/j.jpowsour.2009.08.100.

[76] X.G. Zhang, Fibrous zinc anodes for high power batteries, J. Power Sources. 163 (2006) 591–597. doi:10.1016/j.jpowsour.2006.09.034.

[77] C.W. Lee, K. Sathiyanarayanan, S.W. Eom, M.S. Yun, Novel alloys to improve the electrochemical behavior of zinc anodes for zinc/air battery, J. Power Sources. 160 (2006) 1436–1441. doi:10.1016/j.jpowsour.2006.02.019.

[78] X.-B. Zhang, Metal-air batteries : Fundamentals and applications, 2018.

[79] P. Sapkota, H. Kim, An experimental study on the performance of a zinc air fuel cell with inexpensive metal oxide catalysts and porous organic polymer separators, J. Ind. Eng. Chem. 16 (2010) 39–44. doi:10.1016/j.jiec.2010.01.024.

[80] W. Lu, C. Xie, H. Zhang, X. Li, Inhibition of zinc dendrite growth in zinc-based batteries, ChemSusChem. 11 (2018) 3996–4006. doi:10.1002/cssc.201801657.

[81] C. Chakkaravarthy, A.K.A. Waheed, H.V.K. Udupa, Zinc-air alkaline batteries - A review, J. Power Sources. 6 (1981) 203–228. doi:10.1016/0378-7753(81)80027-4.

[82] Y. Zhang, C. Li, X. Cai, J. Yao, M. Li, X. Zhang, Q. Liu, High alkaline tolerant electrolyte membrane with improved conductivity and mechanical strength via lithium chloride/dimethylacetamide dissolved microcrystalline cellulose for Zn-Air batteries, Electrochim. Acta. 220 (2016) 635–642. doi:10.1016/j.electacta.2016.10.103.

[83] H.J. Hwang, W.S. Chi, O. Kwon, J.G. Lee, J.H. Kim, Y.G. Shul, Selective ion transporting polymerized ionic liquid membrane separator for enhancing cycle stability and durability in secondary zinc-air battery systems, ACS Appl. Mater. Interfaces. 8 (2016) 26298–26308. doi:10.1021/acsami.6b07841.

[84] E.L. Dewi, K. Oyaizu, H. Nishide, E. Tsuchida, Cationic polysulfonium membrane as separator in zinc-air cell, J. Power Sources. 115 (2003) 149–152. doi:10.1016/S0378-7753(02)00650-X.

[85] H.J. Lee, J.M. Lim, H.W. Kim, S.H. Jeong, S.W. Eom, Y.T. Hong, S.Y. Lee, Electrospun polyetherimide nanofiber mat-reinforced, permselective polyvinyl alcohol composite separator membranes: A membrane-driven step closer toward rechargeable zinc-air batteries, J. Memb. Sci. 499 (2016) 526–537. doi:10.1016/j.memsci.2015.10.038.

[86] H.W. Kim, J.M. Lim, H.J. Lee, S.W. Eom, Y.T. Hong, S.Y. Lee, Artificially engineered, bicontinuous anion-conducting/-repelling polymeric phases as a selective ion transport channel for rechargeable zinc-air battery separator membranes, J. Mater. Chem. A. 4 (2016) 3711–3720. doi:10.1039/c5ta09576j.

[87] W.J. Koros, Gas separation membranes: needs for combined materials science and processing approaches, Macromol. Symp. 188 (2002) 13–22. doi:10.1002/1521-3900(200211)188:1<13::AID-MASY13>3.0.CO;2-W.

[88] L. Gubler, Membranes and separators for redox flow batteries, Curr. Opin. Electrochem. 18 (2019) 31–36. doi:10.1016/j.coelec.2019.08.007.

[89] G.-H. (Geert-H. Koops, Nomenclature and symbols in membrane science and technology : on behalf of the European Society of Membrane Science and Technology, Membrane Technology Group, University of Twente, 1995.

[90] M. Mulder, M. Mulder, Introduction, in: Basic Princ. Membr. Technol., Springer Netherlands, 1996: pp. 1–21. doi:10.1007/978-94-009-1766-8_1.

[91] B. Van Der Bruggen, C. Vandecasteele, T. Van Gestel, W. Doyen, R. Leysen, A review of pressure-driven membrane processes in wastewater treatment and drinking water production, Environ. Prog. 22 (2003) 46–56. doi:10.1002/ep.670220116.

[92] P. Arribas, M. Khayet, M.C. García-Payo, L. Gil, Advances in membrane technologies for water treatment (chapter 8) novel and emerging membranes, Elsevier, 2015. doi:10.1016/B978-1-78242-121-4.00008-3.

[93] A. Zirehpour, A. Rahimpour, Nanostructured polymer membranes, in: V. P. M., O. Nazarenko (Eds.), Nanostructured Polym. Membr. Vol. 2 Appl., Scrivener, 2016: p. 560.

[94] H. Strathmann, L. Giorno, E. Drioli, An Introduction to Membrane Science and Technology, 2006.

[95] M. Ulbricht, Nanoporous polymer filters and membranes, selective filters, in: Encycl. Polym. Nanomater., Springer Berlin Heidelberg, Berlin, Heidelberg, 2015: pp. 1360–1371. doi:10.1007/978-3-642-29648-2_357.

[96] K.S.W. Sing, D.H. Everett, R.A.W. Haul, L. Moscou, R.A. Pierotti, J. Rouquerol, T. Siemieniewska, Reporting physisorption data for gas/solid systems with special reference to the determination of surface area and porosity, Pure Appl. Chem. 57 (1985) 603–619. doi:10.1351/pac198557040603.

[97] D.M. See, R.E. White, Temperature and concentration dependence of the specific conductivity of concentrated solutions of potassium hydroxide, J. Chem. Eng. Data. 42 (1997) 1266–1268. doi:10.1021/je970140x.

[98] R.J. Gilliam, J.W. Graydon, D.W. Kirk, S.J. Thorpe, A review of specific conductivities of potassium hydroxide solutions for various concentrations and temperatures, Int. J. Hydrogen Energy. 32 (2007) 359–364. doi:10.1016/j.ijhydene.2006.10.062.

[99] X.G. Zhang, Corrosion and electrochemistry of zinc, in: Corros. Electrochem. Zinc, Springer US, Boston, MA, 1996: pp. 1–17. doi:10.1007/978-1-4757-9877-7_1.

[100] S. Hosseini, S.J. Han, A. Arponwichanop, T. Yonezawa, S. Kheawhom, Ethanol as an electrolyte additive for alkaline zinc-air flow batteries, Sci. Rep. 8 (2018) 1–11. doi:10.1038/s41598-018-29630-0.

[101] M. Xu, D.G. Ivey, Z. Xie, W. Qu, Rechargeable Zn-air batteries: Progress in electrolyte development and cell configuration advancement, J. Power Sources. 283 (2015) 358–371. doi:10.1016/j.jpowsour.2015.02.114.

[102] D.R. Dekel, Review of cell performance in anion exchange membrane fuel cells, J. Power Sources. 375 (2018) 158–169. doi:10.1016/j.jpowsour.2017.07.117.

[103] S. Maurya, S.H. Shin, Y. Kim, S.H. Moon, A review on recent developments of anion exchange membranes for fuel cells and redox flow batteries, RSC Adv. 5 (2015) 37206–37230. doi:10.1039/c5ra04741b.

[104] S. Gottesfeld, D.R. Dekel, M. Page, C. Bae, Y. Yan, P. Zelenay, Y.S. Kim, Anion exchange membrane fuel cells: current status and remaining challenges, J. Power Sources. 375 (2018) 170–184. doi:10.1016/j.jpowsour.2017.08.010.

[105] G. Merle, M. Wessling, K. Nijmeijer, Anion exchange membranes for alkaline fuel cells: A review, J. Memb. Sci. 377 (2011) 1–35. doi:10.1016/J.MEMSCI.2011.04.043.

[106] W. You, K.J.T. Noonan, G.W. Coates, Alkaline-stable anion exchange membranes: A review of synthetic approaches, Prog. Polym. Sci. 100 (2020) 101177. doi:10.1016/j.progpolymsci.2019.101177.

[107] Y.J. Wang, J. Qiao, R. Baker, J. Zhang, Alkaline polymer electrolyte membranes for fuel cell applications, Chem. Soc. Rev. 42 (2013) 5768–5787. doi:10.1039/c3cs60053j.

[108] S.C. Ramírez, R.R. Paz, Hydroxide transport in anion-exchange membranes for alkaline fuel cells, in: New Trends Ion Exch. Stud., InTech, 2018. doi:10.5772/intechopen.77148.

[109] D. Dong, W. Zhang, A.C.T. Van Duin, D. Bedrov, Grotthuss versus vehicular transport of hydroxide in anion-exchange membranes: Insight from combined reactive and nonreactive molecular simulations, J. Phys. Chem. Lett. 9 (2018) 825–829. doi:10.1021/acs.jpclett.8b00004.

[110] K.N. Grew, W.K.S. Chiu, A dusty fluid model for predicting hydroxyl anion conductivity in alkaline anion exchange membranes, J. Electrochem. Soc. 157 (2010) B327. doi:10.1149/1.3273200.

[111] M.E. Tuckerman, A. Chandra, D. Marx, Structure and dynamics of OH - (aq), Acc. Chem. Res. 39 (2006) 151–158. doi:10.1021/ar040207n.

[112] M.E. Tuckerman, D. Marx, M. Parrinello, The nature and transport mechanism of hydrated hydroxide ions in aqueous solution, Nature. 417 (2002) 925–929. doi:10.1038/nature00797.

[113] H. Takaba, T. Hisabe, T. Shimizu, M.K. Alam, Molecular modeling of OH− transport in poly(arylene ether sulfone ketone)s containing quaternized ammonio-substituted fluorenyl groups as anion exchange membranes, J. Memb. Sci. 522 (2017) 237–244. doi:10.1016/j.memsci.2016.09.019.

[114] D. Marx, A. Chandra, M.E. Tuckerman, Aqueous basic solutions: Hydroxide solvation, structural diffusion, and comparison to the hydrated proton, Chem. Rev. 110 (2010) 2174–2216. doi:10.1021/cr900233f.

[115] Grotthuss mechanism, (n.d.). http://www1.lsbu.ac.uk/water/grotthuss.html (accessed June 22, 2020).

[116] D.S. Kim, G.P. Robertson, Y.S. Kim, M.D. Guiver, Copoly(arylene ether)s containing pendant sulfonic acid groups as proton exchange membranes, Macromolecules. 42 (2009) 957–963. doi:10.1021/ma802192y.

[117] F. Song, Y. Fu, Y. Gao, J. Li, J. Qiao, X.D. Zhou, Y. Liu, Novel Alkaline Anion-exchange Membranes Based on Chitosan/Ethenylmethylimidazoliumchloride Polymer with Ethenylpyrrolidone Composites for Low Temperature Polymer Electrolyte Fuel Cells, Electrochim. Acta. 177 (2015) 137–144. doi:10.1016/j.electacta.2015.02.015.

[118] P. Choi, N.H. Jalani, R. Datta, Thermodynamics and Proton Transport in Nafion, J. Electrochem. Soc. 152 (2005) E123. doi:10.1149/1.1859814.

[119] X. Fan, J. Liu, J. Ding, Y. Deng, X. Han, W. Hu, C. Zhong, Investigation of the Environmental Stability of Poly(vinyl alcohol)–KOH Polymer Electrolytes for Flexible Zinc–Air Batteries, Front. Chem. 7 (2019). doi:10.3389/fchem.2019.00678.

[120] R. Naderi, Composite Gel Polymer Electrolyte for Lithium Ion Batteries, 2016. http://openprairie.sdstate.edu/etd (accessed June 22, 2020).

[121] M. Wang, N. Xu, J. Fu, Y. Liu, J. Qiao, High-performance binary cross-linked alkaline anion polymer electrolyte membranes for all-solid-state supercapacitors and flexible rechargeable zinc-air batteries, J. Mater. Chem. A. 7 (2019) 11257–11264. doi:10.1039/c9ta02314c.

[122] J. Zhang, T. Zhou, J. Qiao, Y. Liu, J. Zhang, Hydroxyl anion conducting membranes poly(vinyl alcohol)/ poly(diallyldimethylammonium chloride) for alkaline fuel cell applications: Effect of molecular weight, Electrochim. Acta. 111 (2013) 351–358. doi:10.1016/j.electacta.2013.07.182.

[123] J.O. Bockris, Z. Nagy, A. Damjanovic, On the deposition and dissolution of zinc in alkaline solutions, J. Electrochem. Soc. 119 (1972) 285. doi:10.1149/1.2404188.

[124] W.G. Sunu, D.N. Bennion, Transient and failure analyses of the porous zinc electrode, J. Electrochem. Soc. 127 (1980) 2017. doi:10.1149/1.2130055.

[125] P. Gu, M. Zheng, Q. Zhao, X. Xiao, H. Xue, H. Pang, Rechargeable zinc-air batteries: A promising way to green energy, J. Mater. Chem. A. 5 (2017) 7651–7666. doi:10.1039/c7ta01693j.

[126] E. Jorge Pessine, S.M. L Agostinho, L.I. O C Chagas, Evaluation of the diffusion coefficient of the zincate ion using a rotating disk electrode, n.d. www.nrcresearchpress.com (accessed February 4, 2020).

[127] E.R. Nightingale, Phenomenological theory of ion solvation. Effective radii of hydrated ions, J. Phys. Chem. 63 (1959) 1381–1387. doi:10.1021/j150579a011.

[128] T. Luo, S. Abdu, M. Wessling, Selectivity of ion exchange membranes: A review, 2018. https://www.sciencedirect.com/science/article/pii/S0376738817335779 (accessed April 28, 2019).

[129] Y. Li, S. Gregory, Diffusion of ions in sea water and in deep-sea sediments, Geochim. Cosmochim. Ac., 38, 703–714, (1974).

[130] W. Haynes, CRC handbook of chemistry and physics, 96th ed., CRC Press, CRC Press, Taylor & Francis Group, Boca Raton, London, New York, 2015.

[131] J. Xi, Z. Wu, X. Teng, Y. Zhao, L. Chen, X. Qiu, Self-assembled polyelectrolyte multilayer modified Nafion membrane with suppressed vanadium ion crossover for vanadium redox flow batteries, J. Mater. Chem. 18 (2008) 1232. doi:10.1039/b718526j.

[132] H. Zhang, H. Zhang, X. Li, Z. Mai, W. Wei, Silica modified nanofiltration membranes with improved selectivity for redox flow battery application, Energy Environ. Sci. 5 (2012) 6299–6303. doi:10.1039/C1EE02571F.

[133] H. Zhang, H. Zhang, X. Li, Z. Mai, J. Zhang, Nanofiltration (NF) membranes: the next generation separators for all vanadium redox flow batteries (VRBs)?, Energy Environ. Sci. 4 (2011) 1676. doi:10.1039/c1ee01117k.

[134] J. Duay, M. Kelly, T.N. Lambert, Evaluation of a ceramic separator for use in rechargeable alkaline Zn/MnO2 batteries, J. Power Sources. 395 (2018) 430–438. doi:10.1016/j.jpowsour.2018.05.072.

[135] I. Krejčí, P. Vanýsek, A. Trojánek, Transport of Zn (OH)42- ions across a polyolefin microporous membrane, J. Electrochem. Soc. 140 (1993) 2279. doi:10.1149/1.2220808.

[136] J. Duay, T.N. Lambert, R. Aidun, Stripping voltammetry for the real time determination of zinc membrane diffusion coefficients in high pH: Towards rapid screening of alkaline battery separators, Electroanalysis. 29 (2017) 2261–2267. doi:10.1002/elan.201700337.

[137] H. Lee, M. Yanilmaz, O. Toprakci, K. Fu, X. Zhang, A review of recent developments in membrane separators for rechargeable lithium-ion batteries, 2014. http://xlink.rsc.org/?DOI=C4EE01432D (accessed April 28, 2019).

[138] M.R. Palacín, Recent advances in rechargeable battery materials: a chemist's perspective, Chem. Soc. Rev. 38 (2009) 2565. doi:10.1039/b820555h.

[139] R. Narducci, J.-F. Chailan, A. Fahs, L. Pasquini, M.L. Di Vona, P. Knauth, Mechanical properties of anion exchange membranes by combination of tensile stress-strain tests and dynamic mechanical analysis, J. Polym. Sci. Part B Polym. Phys. 54 (2016) 1180–1187. doi:10.1002/polb.24025.

[140] P.A. and, Z. (John) Zhang, Battery separators, (2004). doi:10.1021/CR020738U.

[141] S.S. Zhang, A review on the separators of liquid electrolyte Li-ion batteries, J. Power Sources. 164 (2007) 351–364. doi:10.1016/j.jpowsour.2006.10.065.

[142] J. Fu, J. Zhang, X. Song, H. Zarrin, X. Tian, J. Qiao, L. Rasen, K. Li, Z. Chen, A flexible solid-state electrolyte for wide-scale integration of rechargeable zinc-air batteries, Energy Environ. Sci. 9 (2016) 663–670. doi:10.1039/c5ee03404c.

[143] J. Zhang, J. Fu, X. Song, G. Jiang, H. Zarrin, P. Xu, K. Li, A. Yu, Z. Chen, Laminated cross-linked nanocellulose/graphene oxide electrolyte for flexible rechargeable zinc-air batteries, Adv. Energy Mater. 6 (2016) 1600476. doi:10.1002/aenm.201600476.

[144] H. Zarrin, S. Sy, J. Fu, G. Jiang, K. Kang, Y.-S. Jun, A. Yu, M. Fowler, Z. Chen, Molecular functionalization of graphene oxide for next-generation wearable electronics, ACS Appl. Mater. Interfaces. 8 (2016) 25428–25437. doi:10.1021/acsami.6b06769.

[145] Y. Wei, M. Wang, N. Xu, L. Peng, J. Mao, Q. Gong, J. Qiao, Alkaline exchange polymer membrane electrolyte for high performance of all-solid-state electrochemical devices, ACS Appl. Mater. Interfaces. 10 (2018) 29593–29598. doi:10.1021/acsami.8b09545.

[146] J. Fang, J. Qiao, D.P. Wilkinson, J. Zhang, Electrochemical polymer electrolyte membranes, CRC Press, 2015.

[147] S. Hosseini, W. Lao-atiman, S.J. Han, A. Arpornwichanop, T. Yonezawa, S. Kheawhom, Discharge performance of zinc-air flow Bbatteries under the effects of sodium dodecyl sulfate and pluronic F-127, Sci. Rep. 8 (2018) 14909. doi:10.1038/s41598-018-32806-3.

[148] W. Lao-Atiman, S. Olaru, A. Arpornwichanop, S. Kheawhom, Discharge performance and dynamic behavior of refuellable zinc-air battery, Sci. Data. 6 (2019) 168. doi:10.1038/s41597-019-0178-3.

[149] P. Kritzer, J.A. Cook, Nonwovens as separators for alkaline batteries, J. Electrochem. Soc. 154 (2007) A481. doi:10.1149/1.2711064.

[150] K. Liu, Y. Liu, D. Lin, A. Pei, Y. Cui, Materials for lithium-ion battery safety, Sci. Adv. 4 (2018). doi:10.1126/sciadv.aas9820.

[151] W. Peng, I.C. Escobar, D.B. White, Effects of water chemistries and properties of membrane on the performance and fouling—a model development study, J. Memb. Sci. 238 (2004) 33–46. doi:10.1016/j.memsci.2004.02.035.

[152] C.C. Yang, G.M. Wu, Study of microporous PVA/PVC composite polymer membrane and it application to MnO2 capacitors, Mater. Chem. Phys. 114 (2009) 948–955. doi:10.1016/j.matchemphys.2008.11.009.

[153] Celgard LLC, Celgard high performance battery separators, 2200 (2009).

[154] F. Cheng, J. Chen, Metal–air batteries: from oxygen reduction electrochemistry to cathode catalysts, Chem. Soc. Rev. 41 (2012) 2172. doi:10.1039/c1cs15228a.

[155] A. Abbasi, S. Hosseini, A. Somwangthanaroj, A.A. Mohamad, S. Kheawhom, Poly(2,6-Dimethyl-1,4-Phenylene Oxide)-based hydroxide exchange separator membranes for zinc–air battery, Int. J. Mol. Sci. 20 (2019) 3678. doi:10.3390/ijms20153678.

[156] Y. Kiros, Separation and permeability of zincate ions through membranes, J. Power Sources. 62 (1996) 117–119. doi:10.1016/S0378-7753(96)02420-2.

[157] D.E. Turney, J.W. Gallaway, G.G. Yadav, R. Ramirez, M. Nyce, S. Banerjee, Y.C.K. Chen-Wiegart, J. Wang, M.J. D'Ambrose, S. Kolhekar, J. Huang, X. Wei, Rechargeable zinc alkaline anodes for long-cycle energy storage, Chem. Mater. 29 (2017) 4819–4832. doi:10.1021/acs.chemmater.7b00754.

[158] O.C. Wagner, Secondary Zinc-air cell investigations, 1972.

[159] Technical properties (typical values), n.d. www.innoviafilms.com (accessed March 16, 2020).

[160] B. Seymour, Cellophane membrane permeability, J. Biol. Chem. (1940) 701–707.

[161] W. Cao, Y. Li, B. Fitch, J. Shih, T. Doung, J. Zheng, Strategies to optimize lithium-ion supercapacitors achieving high-performance: Cathode configurations, lithium loadings on anode, and types of separator, J. Power Sources. 268 (2014) 841–847. doi:10.1016/j.jpowsour.2014.06.090.

[162] J. Huang, G.G. Yadav, J. Gallaway, M. Nyce, S. Banerjee, Rechargeable alkaline battery comprising metal hydroxide separator, (2019).

[163] K. Trommer, B. Morgenstern, Nonrigid microporous PVC sheets: Preparation and properties, J. Appl. Polym. Sci. 115 (2010) 2119–2126. doi:10.1002/app.31305.

[164] M. Ulbricht, Advanced functional polymer membranes, Polymer (Guildf). 47 (2006) 2217–2262. doi:10.1016/j.polymer.2006.01.084.

[165] E. Drioli, L. Giorno, Membrane Operations: Innovative Separations and Transformations, Wiley-VCH, 2009. doi:10.1002/9783527626779.

[166] M. Mulder, Phase inversion membranes, in: Ian D. Wilson (Ed.), Encycl. Sep. Sci., Academic Press, 2000: pp. 3331–3331.

[167] F. Liu, N.A. Hashim, Y. Liu, M.R.M. Abed, K. Li, Progress in the production and modification of PVDF membranes, J. Memb. Sci. 375 (2011) 1–27. doi:10.1016/j.memsci.2011.03.014.

[168] C.C. Yang, J.M. Yang, C.Y. Wu, Poly(vinyl alcohol)/poly(vinyl chloride) composite polymer membranes for secondary zinc electrodes, J. Power Sources. 191 (2009) 669–677. doi:10.1016/j.jpowsour.2009.02.044.

[169] G.M. Wu, S.J. Lin, C.C. Yang, Alkaline Zn-air and Al-air cells based on novel solid PVA/PAA polymer electrolyte membranes, J. Memb. Sci. 280 (2006) 802–808. doi:10.1016/J.MEMSCI.2006.02.037.

[170] A. Puapattanakul, S. Therdthianwong, A. Therdthianwong, N. Wongyao, Improvement of zinc-air fuel cell performance by gelled koh, Energy Procedia. 34 (2013) 173–180. doi:10.1016/j.egypro.2013.06.745.

[171] C.C. Yang, S.J. Lin, S.T. Hsu, Synthesis and characterization of alkaline polyvinyl alcohol and poly(epichlorohydrin) blend polymer electrolytes and performance in electrochemical cells, J. Power Sources. 122 (2003) 210–218. doi:10.1016/S0378-7753(03)00429-4.

[172] J.R. Kim, S.W. Choi, S.M. Jo, W.S. Lee, B.C. Kim, Electrospun PVdF-based fibrous polymer electrolytes for lithium ion polymer batteries, Electrochim. Acta. 50 (2004) 69–75. doi:10.1016/j.electacta.2004.07.014.

[173] S.W. Choi, S.M. Jo, W.S. Lee, Y.-R. Kim, An Electrospun Poly(vinylidene fluoride) Nanofibrous Membrane and Its Battery Applications, Adv. Mater. 15 (2003) 2027–2032. doi:10.1002/adma.200304617.

[174] B. Ding, J. Yu, X. Wang, Electrospinning: Nanofabrication and applications, Elsevier, 2018. doi:10.1016/C2016-0-01374-8.

[175] V.G. Gude, Emerging technologies for sustainable desalination handbook, Elsevier, 2018. doi:10.1016/C2017-0-03562-0.

[176] T.H. Cho, M. Tanaka, H. Ohnishi, Y. Kondo, M. Yoshikazu, T. Nakamura, T. Sakai, Composite nonwoven separator for lithium-ion battery: Development and characterization, J. Power Sources. 195 (2010) 4272–4277. doi:10.1016/j.jpowsour.2010.01.018.

[177] J. Zhang, Z. Liu, Q. Kong, C. Zhang, S. Pang, L. Yue, X. Wang, J. Yao, G. Cui, Renewable and superior thermal-resistant cellulose-based composite nonwoven as lithium-ion battery separator, ACS Appl. Mater. Interfaces. 5 (2013) 128–134. doi:10.1021/am302290n.

[178] G.. Zguris, A broad look at separator material technology for valve-regulated lead/acid batteries, J. Power Sources. 73 (1998) 60–64. doi:10.1016/S0378-7753(98)00022-6.

[179] S.J.H. and S.K. Ali Abbasia, Soraya Hosseinia, Discharge capacity improvement of zinc-air battery using electrospun polypropylene nanofibrous separator, ECS Meet. Abstr. (2019). http://ma.ecsdl.org/content/MA2019-04/5/229.short (accessed January 30, 2020).

[180] J. Noack, N. Roznyatovskaya, T. Herr, P. Fischer, The chemistry of redox-flow batteries, Angew. Chemie Int. Ed. 54 (2015) 9776–9809. doi:10.1002/anie.201410823.

[181] M. Cheiky, H. Wilson, Battery separator with fluoride-containing inorganic salt, 2001. https://patents.google.com/patent/US6682854 (accessed April 22, 2019).

[182] H. In Lee, D.T. Dung, J. Kim, J.H. Pak, S. kyung Kim, H.S. Cho, W.C. Cho, C.H. Kim, The synthesis of a Zirfon-type porous separator with reduced gas crossover for alkaline electrolyzer, Int. J. Energy Res. 44 (2020) 1875–1885. doi:10.1002/er.5038.

[183] P. Vermeiren, W. Adriansens, J.. Moreels, R. Leysen, Evaluation of the ZirfonS separator for use in alkaline water electrolysis and Ni-H2 batteries, Int. J. Hydrogen Energy. 23 (1998) 321–324. doi:10.1016/S0360-3199(97)00069-4.

[184] Rodríguez, Palmas, Sánchez-Molina, Amores, Mais, Campana, Simple and precise approach for determination of ohmic contribution of diaphragms in alkaline water electrolysis, Membranes (Basel). 9 (2019) 129. doi:10.3390/membranes9100129.

[185] M.B. Amunategui Vallejo, A. Ibanez Llano, M. La, Sierra De Guardia, M. Frades Tapia, D. Gonzalez, Rechargeable Zinc-air flow battery, 2014.

[186] D.E. Bergbreiter, K. Kabza, Annealing and reorganization of sulfonated polyethylene films to produce surface-modified films of varying hydrophilicity, J. Am. Chem. Soc. 113 (1991) 1447–1448. doi:10.1021/ja00004a074.

[187] G.M. Wu, S.J. Lin, C.C. Yang, Preparation and characterization of high ionic conducting alkaline non-woven membranes by sulfonation, J. Memb. Sci. 284 (2006) 120–127. doi:10.1016/j.memsci.2006.07.025.

[188] J.H. Gordon, S. Balagopal, S. Bhavaraju, J.J. Watkins, Advanced metal-air battery having a ceramic membrane electrolyte, 2007. https://patents.google.com/patent/US8012633B2/en (accessed April 29, 2019).

[189] K. Tadanaga, Y. Furukawa, A. Hayashi, M. Tatsumisago, Direct ethanol fuel cell using hydrotalcite clay as a hydroxide ion conductive electrolyte, Adv. Mater. 22 (2010) 4401–4404. doi:10.1002/adma.201001766.

[190] M.T. Tsehaye, S. Velizarov, B. Van der Bruggen, Stability of polyethersulfone membranes to oxidative agents: A review, Polym. Degrad. Stab. 157 (2018) 15–33. doi:10.1016/j.polymdegradstab.2018.09.004.

[191] M.T. Tsehaye, J. Wang, J. Zhu, S. Velizarov, B. Van der Bruggen, Development and characterization of polyethersulfone-based nanofiltration membrane with stability to hydrogen peroxide, J. Memb. Sci. 550 (2018) 462–469. doi:10.1016/j.memsci.2018.01.022.

[192] A. Le, N. Lieu, S. Pereira, Advanced polymeric and organic-inorganic membranes for pressure-driven processes item type book chapter, (2017). doi:10.1016/B978-0-12-409547-2.12275-9.

[193] N. Wang, Y. Zhao, Coaxial electrospinning, in: Electrospinning Nanofabrication Appl., Elsevier, 2019: pp. 125–200. doi:10.1016/b978-0-323-51270-1.00005-4.

[194] M.T. Tsehaye, F. Alloin, C. Iojoiu, Prospects for anion-exchange membranes in alkali metal–air batteries, Energies. 12 (2019). doi:10.3390/en12244702.

[195] J. Zhou, P. Zuo, Y. Liu, Z. Yang, T. Xu, Ion exchange membranes from poly(2,6-dimethyl-1,4-phenylene oxide) and related applications, Sci. China Chem. 61 (2018) 1062–1087. doi:10.1007/s11426-018-9296-6.

[196] H.S. Dang, E.A. Weiber, P. Jannasch, Poly(phenylene oxide) functionalized with quaternary ammonium groups via flexible alkyl spacers for high-performance anion exchange membranes, J. Mater. Chem. A. 3 (2015) 5280–5284. doi:10.1039/c5ta00350d.

[197] Y. He, J. Pan, L. Wu, Y. Zhu, X. Ge, J. Ran, Z.J. Yang, T. Xu, A novel methodology to synthesize highly conductive anion exchange membranes, Sci. Rep. 5 (2015) 1–7. doi:10.1038/srep13417.

[198] G. Jiang, M. Goledzinowski, F.J.E. Comeau, H. Zarrin, G. Lui, J. Lenos, A. Veileux, G. Liu, J. Zhang, S. Hemmati, J. Qiao, Z. Chen, Free-standing functionalized graphene oxide solid electrolytes in electrochemical gas sensors, Adv. Funct. Mater. 26 (2016) 1729–1736. doi:10.1002/adfm.201504604.

[199] H.S. Dang, P. Jannasch, Exploring different cationic alkyl side chain designs for enhanced alkaline stability and hydroxide ion conductivity of anion-exchange membranes, Macromolecules. 48 (2015) 5742–5751. doi:10.1021/acs.macromol.5b01302.

[200] N. Sun, F. Lu, A. Mariani, S. Passerini, X. Gao, L. Zheng, Anion exchange membrane electrolyte preserving inverse Ia3¯d bicontinuous cubic phase: Effect of microdomain morphology on selective ion transport, J. Memb. Sci. 605 (2020) 118113. doi:10.1016/j.memsci.2020.118113.

[201] O. Kwon, H.J. Hwang, Y. Ji, O.S. Jeon, J.P. Kim, C. Lee, Y.G. Shul, Transparent bendable secondary zinc-air batteries by controlled void ionic separators, Sci. Rep. 9 (2019) 1–9. doi:10.1038/s41598-019-38552-4.

[202] K.D. Kreuer, G. Portale, A critical revision of the nano-morphology of proton conducting ionomers and polyelectrolytes for fuel cell applications, Adv. Funct. Mater. 23 (2013) 5390–5397. doi:10.1002/adfm.201300376.

[203] F.I. Allen, L.R. Comolli, A. Kusoglu, M.A. Modestino, A.M. Minor, A.Z. Weber, Morphology of hydrated as-cast Nafion revealed through cryo electron tomography, ACS Macro Lett. 4 (2015) 1–5. doi:10.1021/mz500606h.

[204] Z. Yuan, H. Zhang, X. Li, Ion conducting membranes for aqueous flow battery systems, Chem. Commun. 54 (2018) 7570–7588. doi:10.1039/C8CC03058H.

[205] A. Münchinger, K.D. Kreuer, Selective ion transport through hydrated cation and anion exchange membranes I. The effect of specific interactions, J. Memb. Sci. 592 (2019) 117372. doi:10.1016/j.memsci.2019.117372.

[206] V.G. Artemov, A.A. Volkov, N.N. Sysoev, A.A. Volkov, Conductivity of aqueous HCl, NaOH and NaCl solutions: Is water just a substrate?, EPL (Europhysics Lett. 109 (2015) 26002. doi:10.1209/0295-5075/109/26002.

[207] N. Gupta, H.S. Wroblowa, Rechargeable cells with modified MnO2 cathodes, J. Electrochem. Soc. 135 (1988) 2415–2418. doi:10.1149/1.2095349.

[208] Y. Li, J. Fu, C. Zhong, T. Wu, Z. Chen, W. Hu, K. Amine, J. Lu, Recent advances in flexible Zinc-based rechargeable batteries, Adv. Energy Mater. 9 (2019) 1802605. doi:10.1002/aenm.201802605.

[209] A. Sumboja, M. Lübke, Y. Wang, T. An, Y. Zong, Z. Liu, All-solid-state, foldable, and rechargeable Zn-air batteries based on manganese oxide grown on graphene-coated carbon cloth air cathode, Adv. Energy Mater. 7 (2017) 1700927. doi:10.1002/aenm.201700927.

[210] M.R. Kraglund, M. Carmo, G. Schiller, S.A. Ansar, D. Aili, E. Christensen, J.O. Jensen, Ion-solvating membranes as a new approach towards high rate alkaline electrolyzers, Energy Environ. Sci. 12 (2019) 3313–3318. doi:10.1039/c9ee00832b.

[211] D. Lee, H.-W. Kim, J.-M. Kim, K.-H. Kim, S.-Y. Lee, Flexible/rechargeable Zn–air batteries based on multifunctional heteronanomat architecture, ACS Appl. Mater. Interfaces. 10 (2018) 22210–22217. doi:10.1021/acsami.8b05215.

[212] C.C. Yang, S.J. Lin, Preparation of alkaline PVA-based polymer electrolytes for Ni-MH and Zn-air batteries, J. Appl. Electrochem. 33 (2003) 777–784. doi:10.1023/A:1025514620869.

[213] C.C. Yang, S.J. Lin, G.M. Wu, Study of ionic transport properties of alkaline poly(vinyl) alcohol-based polymer electrolytes, Mater. Chem. Phys. 92 (2005) 251–255. doi:10.1016/j.matchemphys.2005.01.022.

[214] J. Fu, D.U. Lee, F.M. Hassan, Z. Bai, M.G. Park, Z. Chen, Flexible high-energy polymer-electrolyte-based rechargeable zinc-air batteries, Adv. Mater. 27 (2015) 5617–5622. doi:10.1002/adma.201502853.

[215] Y. Xu, Y. Zhang, Z. Guo, J. Ren, Y. Wang, H. Peng, Flexible, stretchable, and rechargeable fiber-shaped zinc-air battery based on cross-stacked carbon nanotube sheets, Angew. Chemie - Int. Ed. 54 (2015) 15390–15394. doi:10.1002/anie.201508848.

[216] T.N.T. Tran, H.J. Chung, D.G. Ivey, A study of alkaline gel polymer electrolytes for rechargeable zinc–air batteries, Electrochim. Acta. 327 (2019) 135021. doi:10.1016/j.electacta.2019.135021.

[217] C.-C. Yang, S.-J. Lin, Alkaline composite PEO–PVA–glass-fibre-mat polymer electrolyte for Zn–air battery, J. Power Sources. 112 (2002) 497–503. doi:10.1016/S0378-7753(02)00438-X.

[218] X. Fan, J. Liu, Z. Song, X. Han, Y. Deng, C. Zhong, W. Hu, Porous nanocomposite gel polymer electrolyte with high ionic conductivity and superior electrolyte retention capability for long-cycle-life flexible zinc–air batteries, Nano Energy. 56 (2019) 454–462. doi:10.1016/j.nanoen.2018.11.057.

[219] T.A. Witten, L.M. Sander, Diffusion-limited aggregation, a kinetic critical phenomenon, Phys. Rev. Lett. 47 (1981) 1400–1403. doi:10.1103/PhysRevLett.47.1400.

[220] G. Garcia, E. Ventosa, W. Schuhmann, Complete prevention of dendrite formation in Zn metal anodes by means of pulsed charging protocols, ACS Appl. Mater. Interfaces. 9 (2017) 18691–18698. doi:10.1021/acsami.7b01705.

[221] Q. Zhang, J. Luan, Y. Tang, X. Ji, H.-Y. Wang, Interfacial design of dendrite-free zinc anodes for aqueous zinc-ion batteries, Angew. Chemie Int. Ed. (2020). doi:10.1002/anie.202000162.

[222] A. Pei, G. Zheng, F. Shi, Y. Li, Y. Cui, Nanoscale nucleation and growth of electrodeposited lithium metal, Nano Lett. 17 (2017) 1132–1139. doi:10.1021/acs.nanolett.6b04755.

[223] M. Chamoun, B.J. Hertzberg, T. Gupta, D. Davies, S. Bhadra, B. Van Tassell, C. Erdonmez, D.A. Steingart, Hyper-dendritic nanoporous zinc foam anodes, NPG Asia Mater. 7 (2015) e178–e178. doi:10.1038/am.2015.32.

[224] J.N. Chazalviel, Electrochemical aspects of the generation of ramified metallic electrodeposits, Phys. Rev. A. 42 (1990) 7355–7367. doi:10.1103/PhysRevA.42.7355.

[225] M. Rosso, T. Gobron, C. Brissot, J.N. Chazalviel, S. Lascaud, Onset of dendritic growth in lithium/polymer cells, J. Power Sources. 97–98 (2001) 804–806. doi:10.1016/S0378-7753(01)00734-0.

[226] C. Monroe, J. Newman, Dendrite growth in lithium/polymer systems, J. Electrochem. Soc. 150 (2003) A1377. doi:10.1149/1.1606686.

[227] F.C. Porter, Zinc handbook: Properties, processing, and use in design, CRC Press, 1991. doi:10.1201/9781482276947.

[228] K. Bass, P.J. Mitchell, G.D. Wilcox, J. Smith, Methods for the reduction of shape change and dendritic growth in zinc-based secondary cells, J. Power Sources. 35 (1991) 333–351. doi:10.1016/0378-7753(91)80117-G.

[229] N.A. Hampson, A.J.S. McNeil, The electrochemistry of porous zinc V. The cycling behaviour of plain and polymer-bonded porous electrodes in koh solutions, J. Power Sources. 15 (1985) 261–285. doi:10.1016/0378-7753(85)80078-1.

[230] J.F. Parker, C.N. Chervin, E.S. Nelson, D.R. Rolison, J.W. Long, Wiring zinc in three dimensions re-writes battery performance - dendrite-free cycling, Energy Environ. Sci. 7 (2014) 1117–1124. doi:10.1039/c3ee43754j.

[231] B.-S. Lee, S. Cui, X. Xing, H. Liu, X. Yue, V. Petrova, H.-D. Lim, R. Chen, P. Liu, Dendrite suppression membranes for rechargeable zinc batteries, ACS Appl. Mater. Interfaces. 10 (2018) 38928–38935. doi:10.1021/acsami.8b14022.

[232] C. Xie, H. Zhang, W. Xu, W. Wang, X. Li, A long cycle life, self-healing zinc-iodine flow battery with high power density, Angew. Chemie. 130 (2018) 11341–11346. doi:10.1002/ange.201803122.

[233] W. Zhang, Z. Tu, J. Qian, S. Choudhury, L.A. Archer, Y. Lu, Design principles of functional polymer separators for high-energy, metal-based batteries, Small. 14 (2018) 1703001. doi:10.1002/smll.201703001.

[234] X. Yu, A. Manthiram, Electrochemical energy storage with mediator-ion solid electrolytes, Joule. 1 (2017) 453–462. doi:10.1016/j.joule.2017.10.011.

[235] L. Li, A. Manthiram, Long-life, high-voltage acidic Zn-air batteries, Adv. Energy Mater. 6 (2016) 1502054. doi:10.1002/aenm.201502054.

[236] C. Xie, Y. Liu, W. Lu, H. Zhang, X. Li, Highly stable zinc-iodine single flow batteries with super high energy density for stationary energy storage, Energy Environ. Sci. 12 (2019) 1834–1839. doi:10.1039/c8ee02825g.

Chapter 6: Porous and modified porous membranes for zinc slurry-air flow battery

1. Introduction

Redox-flow batteries (RFBs) are promising electrochemical energy storage devices for mitigating the intermittent fluctuation of solar and wind power plants [1,2]. These batteries offer several advantages, such as independent sizing of power and energy, room temperature operation, scalability, long charge/discharge cycle life and high efficiency [3]. Over the years, various types of RFBs, such as vanadium-based RFBs [4–6] and metal-air flow batteries have been developed [7–9]. Particularly, Zn-air battery presents a high potential for mobile and stationary applications because of its high theoretical energy density (1087 Wh kg^{-1}, oxygen inclusive), abundant raw materials, environmental friendliness and economic viability [10–13]. To improve its cycling and discharge performance, various studies have mainly focused on preparation and improvement of Zn electrode [14–16], electrocatalyst air electrodes [17,18] and electrolyte formulations [7,19].

In such batteries, the Zn electrode can be a semi-solid, fluidic electrode, in which particles are mixed into the electrolyte to form a slurry [9]. In other words, Zn slurry (Zn particles suspended in alkaline electrolytes) is used as the anode electrode [20,21]. Thus, the slurry, acts as both electrode and electrolyte. In these batteries, unlike conventional Zn-air batteries, the volume of tank or the amount/concentration of Zn particles in the slurry, rather than the size of the porous Zn electrode used in the system, determine the capacity of the battery [22,23]. Moreover, such Zn slurry-based configuration is believed to minimize formation of dendrites and surface passivation since the negative electrode acts only as a current collector [23–26], thus enhance battery performance.

However, some issues, such as full utilization of the Zn particles in the electrochemical reaction, blockage of the Zn particles in the electrode [26], integral battery configuration [27] and appropriate membrane development [28,29] have been impeding the development and commercialization of rechargeable Zn slurry-air flow batteries.

The membrane is used for OH^{-} ion conduction and avoiding mixing of the positive and negative active materials. To achieve this, membrane with high alkaline stability, OH^{-} conductivity, mechanical stability and low/no crossover of zincate ($Zn(OH)_4^{2-}$) ions is required. The overall performance and economic viability of this battery are greatly affected by the properties of the membrane employed [28]. Commercial Zn-air batteries usually use porous polyolefin-based membranes. The porous structure nature of these membranes permits crossover of the soluble $Zn(OH)_4^{2-}$ ions from the Zn electrode to the air electrode. An excellent review work on porous membranes for batteries can be found in the literature [30]. At the air electrode, the $Zn(OH)_4^{2-}$ can be converted to ZnO, depending on the pH, ($Zn(OH)_4^{2-} \rightarrow ZnO (s) + H_2O + 2OH^-$). The formation of ZnO layers has been reported to cause loss of battery capacity [31] and large cell polarization [11] (as the ZnO powers clog the porous air electrode). Therefore, there is a need for minimizing the crossover of $Zn(OH)_4^{2-}$ ions through the membranes.

To address this issue, the use of anion exchange membranes (AEMs) [28,32–34], inorganic-filling [35] or polymer-coating of porous membranes [36,37] have been investigated. For the former, the development of alkaline stable AEMs with well-defined and controlled ionic channels size to improve its selectivity without reducing the ionic conductivity is required. Abbasi et al. [32] prepared benzylic quaternized AEMs using poly (2,6-dimethyl-1,4-phenylene oxide) (PPO) and trimethylamine (TMA) and investigated its primary Zn-air battery discharge performance (specific discharge capacity of ~800 mAh/g_{Zn}). The PPO–TMA membrane exhibited a low $Zn(OH)_4^{2-}$ diffusion coefficient of 1.1×10^{-8} cm^2 min^{-1}.

Another promising strategy, however rarely used in Zn-air batteries is surface modification of porous membranes. One way to achieve this is to coat a thin ion-selective polymer layer. The coat is expected to allow OH^- transfer through the membrane and minimizes the migration of $Zn(OH)_4^{2-}$ ions to the cathode compartment without significantly affecting the ion conductivity. With respect to this, Nafion® 117 solution was coated on Celgard® 3401 and Celgard® 3501 membranes [36]. $Zn(OH)_4^{2-}$ ions crossover was avoided for at least 5 h by coating with a 1% Nafion® solution on Celgard® 3401 without surfactant. Furthermore, Hwang et al. [37] synthesized polymerized ionic liquid and coated it on Celgard® 5550 membrane to limit $Zn(OH)_4^{2-}$ ions crossover. A 96% decrease in $Zn(OH)_4^{2-}$ ions crossover through the membrane was reported. As a result, the lifetime of the battery was reported to increase by about 280% when compared to the pristine Celgard® 5550-based battery (104 *vs* 37 cycles). Other than these two studies, the method remains to be not explored and not tested in Zn slurry-air flow batteries. Moreover, mostly polypropylene (PP)-based Celgard® membranes have been explored, while other commercial porous membranes performance in such batteries remain to be not well-studied.

The objectives of the present work were to (i) investigate the performance of several commercial membranes in Zn slurry-air flow battery and screen out appropriate membrane for the application, and (ii) coat the porous membranes with anion-exchange polymers to improve their selectivity. Herein, six commercial membranes were tested in a 25 cm^2 Zn slurry-air flow battery and compared. Aiming at decreasing the crossover of $Zn(OH)_4^{2-}$ ions, Celgard® 3501 membrane was modified with two different anion exchange polymers. A solution of quaternized PPO and N, N- diallylpiperidinium chloride (DAPCl) was casted on the top surface of the porous membrane and cross-linked via UV irradiation in the presence of a photo-initiator. Moreover, a commercial anion exchange ionomer, Fumion FAA-3-SOLUT-10 (Fumatech, Germany) was used to modify the same support membrane for comparison purpose. DAPCl was chosen because of it high alkaline stability [38,39]. Similar UV-irradiation technique for coating N-spirocyclic quaternary ammonium monomer-based ionomer on Tetratex®PTFE porous substrate has been reported recently elsewhere [40].

2. Experiment

2.1. Materials

PPO (Mn 20,000 and Polydispersity ~ 2.5) was purchased from Polysciences, Inc. Chlorobenzene (ACS reagent, ≥ 99.5%), N-methyl-2-pyrrolidone (NMP, reagent grade), tetrahydrofuran (THF, ACS, >99%), diethyl ether (>99%), 1, 2-dichloroethane (99.8%), allyl bromide (98%), allyl chloride (98%) and chloroform (99.8%) were purchased from Alfa Aesar. Diallymethylamine (97%) and piperidine (≥99%) were bought from ABCR GmbH. Dimethyl sulfoxide-d$_6$ (DMSO-d$_6$, 99.9%) was supplied from Acros Organics. N-bromosuccinimide (NBS, 99%), 2,2'-azobis(2-methylpropionitrile) (AIBN, 98%), methanol (99.9%) and chloroform-d (CDCl$_3$-d, 99.9% D) were purchased from Sigma-Aldrich. 2-hydroxy-4'-(2-hydroxyethoxy)-2-methylpropiophenone (Irgacure D-2959) was bought from Ciba Specialty Chemicals Inc. Cellophane™ P00 was purchased from Futamura Chemical Co. Ltd. (Hamburg, Germany). Celgard® membranes were kindly provided by Celgard, LLC (France). Zirfon® and PBI® were provided by AGFA and Fumatech (Germany), respectively. All chemicals were used without further purification.

2.2. Polymer and cation preparation

PPO (6 g, 50 mmol PPO repeating unit) was dissolved in 60 mL of chlorobenzene in a 100 mL flask equipped with mechanical stirrer and a condenser under Ar gas. NBS (brominating agent) (2.07 g, 11.65 mmol) and AIBN (initiator) (0.115 g, 0.7 mmol) were added at 136 °C. Since PPO can be brominated on both its benzyl and aromatic positions, a benzyl position bromination was achieved by the high temperature used [41] while the extent of bromination was controlled by the amount NBS used [42]. The reaction continued at 136 °C for 3 hours. After 3 h of reaction, the product was precipitated in 600 mL of methanol drop wise. Finally, the product was filtered and dried at 60 °C in vacuum oven for 24 h. The obtained PPO-Br product (6.42 g, 96.8% yield) was confirmed by ^{1}H NMR. The degree of bromination was determined by ^{1}H NMR spectrum by comparing the integrals of the brominated methylene at 4.3 ppm and aromatic methyl group at 2.1 ppm. Subsequently, quaternized PPO polymer (PPO-Q) was prepared by reacting the PPO-Br polymer with diallylmethylamine [39]. PPO-Br (6.42 g) was dissolved in 150 mL THF in a 250 mL reaction flask. After the mixture was completely dissolved, diallylmethylamine (300% molar in excess with respect to the Br units in the PPO-Br) was added in excess to make sure full substitution of the Br units. The reaction continued for 48 h. The product was precipitated in diethyl ether drop wise, filtered and dried under vacuum at 35 °C overnight. The successful quaternization of the product was confirmed by ^{1}H NMR.

The preparation of DAPCl was performed in two steps based on the method reported elsewhere with slight modifications [38].

2.3. Membrane preparation

After the synthesis of the PPO-Q and DAPCl, coating over Celgard® 3501 was performed as follow: 0.075 g PPO-Q, 0.0919 g of DAPCl and 0.01023 g D-2959 initiator were dissolved in 1,2-dichloroethane. After the products were dissolved, NMP (0.62 mL) was added and stirred for 30 min. The solution was covered with aluminum foil to avoid light induced initiator decomposition. The amount and ratio of DAPCl to PPO-Q (6:1, theoretical ion-exchange capacity of 3.45 mmol OH^- g^{-1} polymer) was chosen based on preliminary optimization experiments to prepare a membrane with acceptable hydroxide ion conductivity. Once the 1, 2-dichloroethane was evaporated at room temperature, the remaining solution was poured on a 8 x 8 cm^2 Celgard® 3501 membrane and cast using doctor blade thickness of 30 µm. The coated membrane was degassed, crosslinked using UV irradiation for 3 min and dried overnight at 60 °C. The membrane prepared are denoted as PPO-3.45 + 3501.

In a separate fabrication experiment, 0.8 g of Fumion FAA-3-SOLUT-10 (12 wt.%, determined in this study by drying at 80 °C for 24 h) (referred as FAA) was coated on a 8 x 8 cm^2 Celgard® 3501 using doctor blade thickness of 30 µm. Similarly, the FAA modfiedied membrane (FAA + 3501) was dried overnight at 60 °C.

2.4. Characterization

2.4.1. Structural characterization

Chemical structures and purity of the polymer and monomer were determined by ^1H NMR spectroscopy using $CDCl_3$, deuterium or DMSO-d_6 as solvents in the Bruker Ascend™ 400 MHz Spectrometer. The polymer coating was confirmed by Bruker's VERTEX 70v FT-IR Spectrometer in range of 4000-400 cm^{-1} with resolution of 2 cm^{-1}. SEM analysis was done to study the homogeneity of the coating.

2.4.2. Electrolyte uptake

Electrolyte uptake of membranes was determined by immersing the membranes in 6 M aqueous KOH for 24 h at room temperature. Membrane samples were taken out from the solution and removed their surface solution to record their wet weight. The liquid electrolyte uptakes of the membranes were calculated from the difference of wet and dry weights of the membrane samples based on the following equation (equation 1):

$$KOH\ uptake(\%) = \frac{W_{wet} - W_{dry}}{W_{dry}} \times 100 \qquad (1)$$

where W_{dry} and W_{wet} are the weights of the membranes before and after absorbing the liquid electrolyte.

Volume swelling degree: dried membranes were immersed in 6 M KOH for 24 h at room temperature and the volume of all the membranes was measured. The difference between the wet volume and dry volume was used to calculate the swelling ratio of the membranes with the following equation (2):

$$\Delta V\ (\%) = \frac{(V_{wet} - V_{dry})}{V_{dry}} \times 100 \quad (2)$$

2.4.3. Ionic conductivity

The ionic conductivity of the membranes was measured by electrochemical impedance spectroscopy (EIS) in the frequency range 13 MHz -5 Hz at room temperature. All membranes were immersed in 6 M KOH solutions for 24 h before measuring their conductivity. The membranes were taken out from the electrolyte solution, removed the surface KOH aqueous solution and measured for their resistance. The membrane ionic conductivity (σ) was calculated by the following formula (equation 3):

$$\sigma = \frac{l}{RA} \quad (3)$$

Where *l* is the thickness of the membrane (cm), A is the active area of the membrane sandwiched between two electrodes (0.0314 cm^2) and R is the electric resistance of the membrane (Ω).

2.4.4. Rheometry

Rotational rheometry was performed using a stress-controlled rheometer Discovery HR-3 (TA instruments). PPO-DAPCl viscosity was determined with a cone-plane geometry (D = 60 mm, 1° angle), whereas FAA viscosity was determined using a bob-in-cup geometry (bob diameter = 28 mm, bob length = 42 mm and cup diameter = 30 mm), due to sample lower viscosity. Measurements were performed at 25 ºC with the aid of a Peltier plate integrated system and an anti-evaporation tool was used to prevent changes in sample properties. Steady state measurements were obtained by applying a constant shear rate from 0.01 to 100 s^{-1} and when shear stress (or torque) signal was stabilized, the measurement was taken. Validation of measurement was performed by applying decreasing steps from 100 to 0.01 s^{-1} and no significant differences were found. Lower shear rates yielded torque values out of the rheometer range of measurement, so these values were not included.

2.4.5. Polymer density

The density (ρ) of the membranes was measured by density measurement kit (Mettler-Toledo), which contains weighting pans at ambient and immersed in a solvent at 20 °C using toluene as liquid phase. The prepared membranes in OH^- form were dried at 50 °C under vacuum for 24 h.

The membranes density in g cm^{-3} was calculated by the following equation 4:

$$\rho = \frac{m_{ambient}}{m_{ambient} - m_{toluene}} \times \rho_{toluene} \quad (4)$$

where m_{ambient} and m_{toluene} are weights of the membrane at ambient and in toluene, respectively. ρ_{toluene} is density of toluene (0.87 g mL^{-1}).

2.4.6. Mercury porosimetry

Mercury (Hg) intrusion measurements (Quantachrome PoreMaster) were used to determine the intruded volume, volume of pores/mass of membrane (cm^3 g^{-1}) of the pristine and modified membranes.

2.4.7. Alkaline stability

The alkaline stability of the modified membrane (PPO-3.45+3501) was studied by immersing the membranes in a typical solution used in Zn-air batteries i.e., 6 M KOH for 10 days at room temperature. The electrolyte was replaced every 48 h. The stability of the membranes was investigated by comparing the structure (by FTIR analysis) of the membranes before and after immersion in the alkaline solution.

2.4.8. Zincate ion crossover

The crossover of $Zn(OH)_4^{2-}$ ions through both the commercial and modified membranes was tested using a self-made diffusion cell. The enriched side of the diffusion cell (left, Figure 1) consists of 0.3 M of $Zn(OH)_2$ dissolved in 6 M aqueous KOH solution (15 mL). Whereas, the deficiency chamber was filled with only 6 M KOH aqueous solution (15 mL). The membrane sample was placed between the two compartments. At predefined period of times, 0.1 mL sample was taken from the right-side chamber. The time-dependent concentration of $Zn(OH)_4^{2-}$ ions in the right chamber was then determined using atomic absorption spectroscopy (AAS, PinAAcle™ 900F). A wavelength of 213.86 nm and 0.7 nm slit was used to determine the concentration of Zn in each sample solutions. The diffusion coefficients of $Zn(OH)_4^{2-}$ ions (D) of the different membranes were calculated from the following equation (5) [43]:

$$V_B \frac{dC_B(t)}{dt} = \frac{DA}{L}(C_A - C_B(t)) \quad (5)$$

After integration, by assuming volume of the right chamber (V_B) do not change with time, equation (5) can be changed to:

$$\ln\left(\frac{C_A}{C_A - C_B}\right) = \frac{DA}{V_B L} t \quad (6)$$

Where D is the diffusion coefficient of $Zn(OH)_4^{2-}$ ions through the membrane (m^2 min^{-1}), t is the time (min), A is the effective area of the membrane (m^2), L is the thickness of the membrane (m), C_A and C_B are the zincate concentrations (mol L^{-1}) in the enriched and deficiency chambers, respectively.

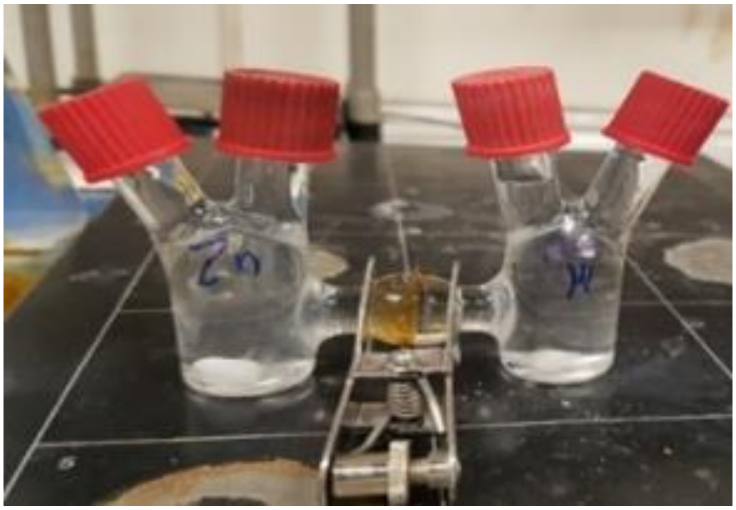

Figure 1: Image of the diffusion cell used.

2.4.9. Single cell assembly and electrochemical performance

A single cell used for this study is identical with the best performing cell design in the previous study [44] with a serpentine flow field of CuNi plate (Figure 2). A catalyst coated electrode (CCE) was used for air cathode. The catalyst ink was prepared by mixing a Pt/C catalyst (40% Pt, Alfa Aesar, Germany) with Pt loading at 1 mg cm^{-2}, isopropanol and deionized water. The prepared ink was then sonicated in an ultrasonic water bath for 15 min and sprayed on to a geometric area of 25 cm^2 (5 cm × 5 cm × 0.0235 cm) gas diffusion layer (SGL Carbon, 29BC, Germany). The catalyst-coated electrode was placed between the membranes and the cathode bipolar plate. The Zn slurry (Table 1) was prepared by same method as previous study [44] with same chemicals. Each solution was mixed at 4000 rpm for 3 minutes.

Table 1: Composition of the Zn slurry used.

Chemicals	Mass fraction (wt. %)
Zn	33.8
ZnO	4
Carbopol	0.7
KOH + H_2O	61.5

In order to perform electrochemical performances of each membrane, current–voltage characteristic curves (polarization curves) and EIS were measured. BaSyTec GSM Battery Test System (BaSyTec GmbH, Germany) was used for current-voltage characterization while Zahner IM6 workstation was used for impedance spectra. The cell resistance of the battery employing the membranes was determined from the slope of the current density-voltage (IV) curves. In addition, the ohmic resistances of the cell were assessed by EIS measurements which were carried out at 1.3 V. All membranes were immersed in 1 M KOH solutions for 24 h before measuring their resistance. During the measurements, Zn slurry was flowing into anode compartment at 160 mL min^{-1} flow rate while synthetic air was flowing into cathode at 100 mL min^{-1} flow rate. At each current density, the voltage was recorded for 30 seconds and averaged due to the fluctuation of a slurry electrode flowing into the single cell. Figure 2 presents the schematic representation and image of the Zn slurry-air flow battery used.

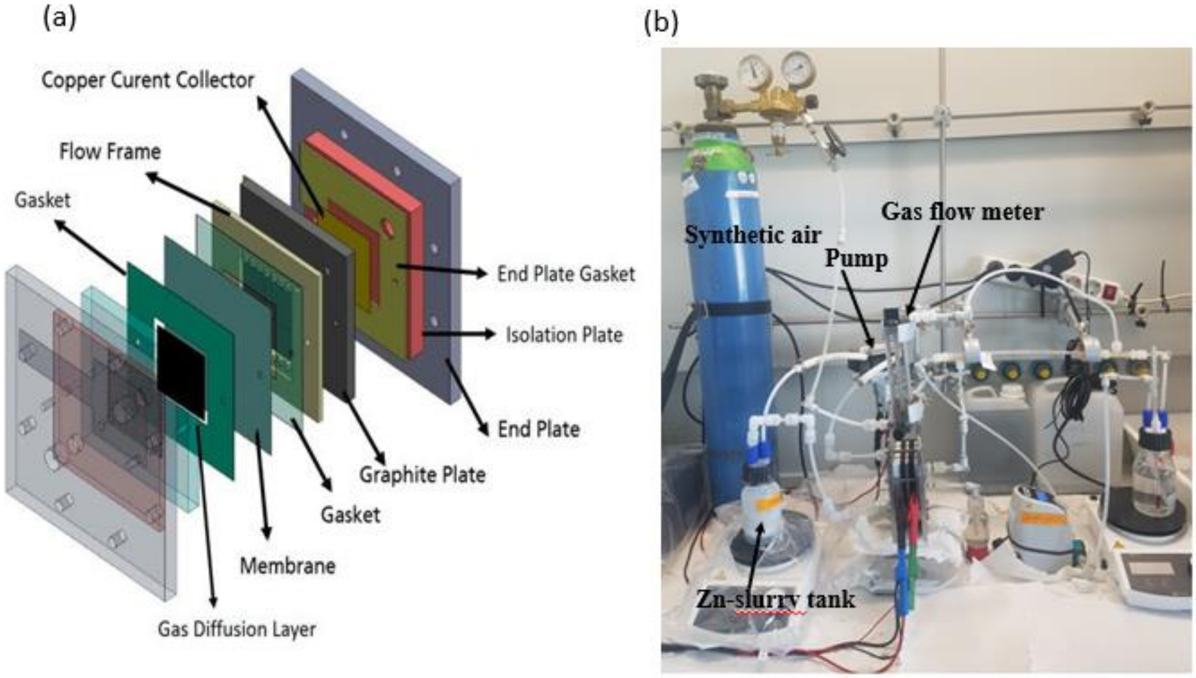

Figure 2: Schematic representation (a) [44] and image (b) of the single cell Zn slurry-air flow battery with a flow frame.

3. Results and discussion

3.1. Characterization of commercial membranes

3.1.1. Electrolyte uptake and ion conductivity

Six commercial membranes (Celgard® 3501, Celgard® 3401, Celgard® 5550, Cellophane™ 350 PØØ, PBI® and Zirfon®) were characterized in terms of electrolyte uptake and zincate ions crossover and were tested in Zn slurry-air flow battery. The composition, nature and structure of these commercial membranes are summarized in Table 2.

Table 2: Properties of the commercial membranes tested in this work

Membrane	Material	Structure	Pore size (nm)	Porosity (%)	Thickness (µm)	Ref.
Celgard® 3501	PP	Monolayer and surfactant-coated	64	55	25	[45]
Celgard® 3401	PP	Monolayer and surfactant-coated	43	41	25	
Celgard® 5550	PP	Laminated and surfactant-coated	64	55	70	
Cellophane™ 350 PØØ	Cellulose	Negatively charged	-	-	86	
PBI®	Polybenzimidazole		-	-	8	
Zirfon®	Polysulfone and ZrO_2	Porous composite diaphragm	150 ± 50	55 ± 10	500 ± 50	[46,47]

Liquid electrolyte uptake: The wettability of the membranes with the electrolyte affect both electrolyte filling time during the assembly process and the ability to retain the electrolyte solution, thus affecting the overall performance of the battery [48,49]. The wettability of a membrane, usually investigated by contact angle measurement, depends on various parameters, such as the chemical affinity between the membrane surface and the electrolyte, porosity (in the case of porous membranes), surface roughness and viscosity of the liquid electrolyte [50]. The wettability of a porous membrane influences its ability to uptake an electrolyte.

In this work, we measured the electrolyte uptake of the membranes (Table 3) and calculated the percentage of porosity filled with the electrolyte by considering the density of 6 M KOH (1.26 g cm^{-3}) and the density of the polymers (for example, 0.92 g cm^{-3} for PP-based Celgard membranes) and added in Table 3. To determine if the membranes change their volume, which indicate the swelling of the polymer matrix and can affect percentage and size of the pores, the dimensional change of the membranes in 6 M KOH was also investigated. In all studied membranes, no significant volume change was observed (all membranes recorded less than 5% volume change), therefore it can be considered that the electrolyte uptake was mainly inside the pore structure and the initial % of porosity was used in the calculation of pore filling. Similarly, electrolyte uptake-induced zero dimensional change has been reported for Celgard® 3501 elsewhere [51].

Table 3: Characterization of commercial membranes: electrolyte, swelling degree and conductivity

Membrane	Electrolyte uptake (wt. %)	Percent (%) of porosity filled with electrolyte*	Swelling degree: ΔV (%)
Celgard® 3501	98 ± 2	76	3
Celgard® 3401	49 ± 2	63	3.6
Celgard® 5550	113 ± 3	82	4.1
Cellophane™ 350 PØØ	129 ± 3	**	3.2
PBI®	36 ± 0.4	**	1.2
Zirfon®	51 ± 0.5	89	3.1

*Percent of porosity filled with electrolyte $= \frac{porosity\ filled\ with\ electrolyte}{volume\ porosity} = \frac{\frac{\left(\frac{electrolyte\ uptake\ (\%)}{1.26\frac{g}{cm3}}\right)}{\left(\frac{electrolyte\ uptake\ (\%)}{1.26\frac{g}{cm3}}\right)+\left(\frac{100}{polymer\ density}\right)}}{volume\ porosity\ (v/v)} * 100$

(Density used: PP = 0.92 g cm^{-3} and Zirfon® = 2.37 g cm^{-3}, apparent density [52]) and volume porosity are provided in Table 2.

**Porosity filled with the electrolyte are not determined as their porosity volumes are not available.

Among the PP-based Celgard® membranes, Celgard® 5550 exhibited the highest electrolyte uptake, followed by Celgard® 3501 and Celgard® 3401 with 113, 98 and 49 wt. %, respectively. As a result, 82% of the total porosity of Celgard® 5550, 76% of Celgard® 3501 and 63% of Celgard® 3401 were found to be filled with the electrolyte. The Celgard® 5550 and Celgard® 3501 membranes have the same pore size, thus the small difference in their electrolyte uptake could be attributed to the membrane morphology (induced by the manufacturing process) and the wettability of the polymer matrices which depends on the surfactant used to modify the surface of these Celgard® membranes and thus their hydrophilicity [53,54]. The lower electrolyte uptake of the Celgard® 3401 can be explained by the lower pore size (43 nm) and may be by a less hydrophilic surface modification of Celgard® 3401 membrane. Indeed, all Celgard® membranes tested in this study have surfactant coated on their surfaces, however, the nature of the surfactant is not known.

Cellophane™ 350 PØØ is made up of cellulosic material with acidic functions (– COOH) on the surface. The polymer hydrophilic character and the presence of ionic functions (-COO^-, K^+ after neutralization) explain the highest electrolyte uptake (130 wt. %) among the tested membranes. Zirfon® is a composite membrane made up of polysulfone that is a hydrophobic polymer and hydrophilic fillers (zirconia) [55]. The Zirfon® membrane is manufactured by film casting and has a thickness of about 500 ± 50 μm and a porosity of 50 ± 10%, according to the datasheet provided by Agfa [47]. Due to its higher pore size (150 ± 50 nm), compared to the other membranes, and the presence of hydrophilic ZrO_2 fillers (85 wt%, 22 m^2 g^{-1}), the electrolyte uptake corresponds to 89% of the porosity which indicates high wettability between the composite membrane and the electrolyte. Whereas, due to its dense character, the PBI membrane displayed low electrolyte uptake (36 wt.%).

Moreover, the ion conductivities of the membranes were determined by EIS. The membrane impregnated with a solution of 6 M KOH was sandwiched between two gold electrodes, the upper one is smaller and has a diameter of 2 mm. Accordingly, Celgard® 5550 membrane showed higher ion conductivity (70 ± 5.5 mS cm^{-1}) than Celgard® 3501 (17 ± 0.7) and Celgard® 3401 (14 ± 2 mS cm^{-1}) proving that the efficiency of ionic conductivity pathway depends on the electrolyte uptake and size of pores (only the porous part of the membrane is conductive). Whereas, ion conductivity of the Cellophane™ 350 PØØ membrane (56 ± 6 mS cm^{-1}) was found to be higher than that of Celgard® membranes, which can be associated to its higher hydrophilicity and electrolyte uptake. Zirfon® exhibited the highest ion conductivity (212 ± 7 mS cm^{-1}) among the tested membranes in agreement with its high electrolyte uptake. The PBI membrane (possesses a heterocyclic benzimidazole ring) with the lowest KOH uptake exhibited a conductivity of only 5.1 ± 1 mS cm^{-1}. It should be noted that the conduction mechanism in PBI has to be different as compared to the studied porous membranes, the (-N=) and (-NH-) of the imidazole interact with KOH and participate to the OH^- conductivity [56]. On the other hand, the conductivity of the 6 M KOH electrolyte was about 590 mS cm^{-1} at room temperature. However, it must be noted that the method we used to determine the porous membranes resistance is difficult due to (i) the presence of 6 M KOH electrolyte in the membranes and (ii) the electrodes which are not fully adapted for such measurements. In fact, the electrodes are in contact with the membrane under weak spring pressure and excess or lack of KOH solution in the membrane can lead to an overestimation (excess of conducting surface on the border of upper electrodes which has a smaller surface) or underestimation (if the porosity is not completely filled).

3.1.2. Zincate ions crossover

The crossover of soluble $Zn(OH)_4^{2-}$ ions from the negative to the positive electrode must be minimized/avoided in order to have working Zn-air battery. Diffusion of $Zn(OH)_4^{2-}$ through the six membranes was investigated by placing the membrane between the two compartments of the diffusion cells. The amount of $Zn(OH)_4^{2-}$ ions (in M), determined by AAS, crossed through the membranes as function of testing time/membrane thickness (normalized by membrane thickness) is shown in Figure 3. Celgard® 3501 membrane has the largest diffusion of $Zn(OH)_4^{2-}$ with a concentration of 0.077 M after 4 days. Considering the 0.3 M of $Zn(OH)_2$ used as starting concentration, about 26% of the initial $Zn(OH)_4^{2-}$ crossed through the membrane in only 4 days, half of the equilibrium concentration, 0.15 M. This can be accredited to the large pore size and porosity, good wettability and small thickness of the membrane. Celgard® 5550 and Cellophane™ 350 PØØ with a concentration of $Zn(OH)_4^{2-}$ equal to 0.074 and 0.061 M, respectively, exhibited significant crossover within about a week of testing. Whereas, Celgard® 3401 exhibited the lowest $Zn(OH)_4^{2-}$ ions crossover among the Celgard® membranes. On the other hand, nearly zero crossover of $Zn(OH)_4^{2-}$ ions was detected in the case of PBI® membrane during the week of operation, due to its dense and cationic characters. The high crossover of $Zn(OH)_4^{2-}$ ions through Zirfon® membrane could be due to the high electrolyte channels formed as a result of the large amounts of hydrophilic ZrO_2 powder within the membranes [46].

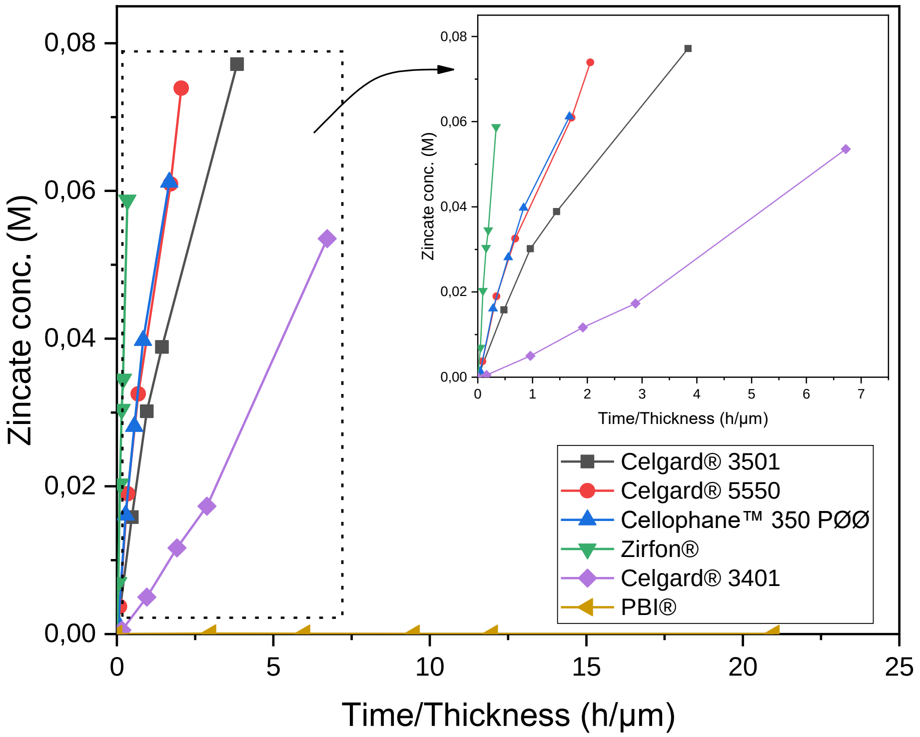

Figure 3: $Zn(OH)_4^{2-}$ crossover concentration *vs* time of Celgard® 3501, Celgard® 3401, Celgard® 5550, Cellophane™ 350 PØØ, and Zirfon® and PBI®. Lines in the figure are guide for the eye.

To measure and compare the selectiveness of the different membranes, the diffusion coefficient of $Zn(OH)_4^{2-}$ ions was determined from the slope of the plot of $\ln\left(\frac{C_A}{C_A - C_B}\right)$ vs time (equation 6) [51]. The results are summarized in Table 4. For comparison purpose, diffusion coefficient of $Zn(OH)_4^{2-}$ ions of Celgard® 3501 and Cellophane™ 350 PØØ from the literature were included in the Table 4.

Table 4: Diffusion coefficients of $Zn(OH)_4^{2-}$ ions through the membranes.

Membrane	$Zn(OH)_4^{2-}$ diffusion coefficient, D ($m^2\ s^{-1}$)	Ref
Celgard® 3501	9.2×10^{-12}	
Celgard® 3401	6.6×10^{-12}	This work
Celgard® 5550	1.4×10^{-11}	
Cellophane™ 350 PØØ	1.3×10^{-11}	
Zirfon®	6.6×10^{-11}	
PBI®	ND*	
Celgard® 3501	3.2×10^{-11}	[31]
	1.3×10^{-11}	[57]
	9.5×10^{-12}	[58]
Cellophane™ 350 PØØ	3.8×10^{-12}	[59]
	6.7×10^{-12}	[57]
	3.3×10^{-12}	[58]

* Not detected, too low to be detected by AAS within three days of experiment.

As shown in Table 4, the Cellophane™ 350 PØØ, membrane exhibited similar $Zn(OH)_4^{2-}$ ions diffusion coefficient with that of Celgard® 5550, however the two membranes have different chemical composition and structure. Cellophane™ membranes have been reported to exhibit lower $Zn(OH)_4^{2-}$ diffusion coefficient than that of Celgard® 3501 in the literature [31,57,59]. This was suggested to be due to the less porous nature [60] and negatively charge [61] of the former membrane than that of Celgard® 3501. However, it must be noted that the measuring protocols (including electrolyte type) and technique might have a significant impact on the diffusion coefficient value as can be seen in the case of Celgard® 3501 in [31] and [58] studies. For instance, Celgard® 3501 and Cellophane™ membranes were reported to have about four times larger $Zn(OH)_4^{2-}$ ions diffusion coefficient when KOH was used instead of NaOH [57]. Moreover, the Cellophane™ 350POO (Innovia Films Ltd., UK) used in [57] has a thickness of only 25 µm, which is much lower than that of the one used in this study.

In the present study, the $Zn(OH)_4^{2-}$ diffusion coefficient through the membranes was found to decrease in order as follow: Zirfon® > Celgard® 5550 ≈ Cellophane™ 350 PØØ > Celgard® 3501 > Celgard® 3401 > PBI®. This is in agreement with ion conductivities (section 3.1.1) and porous/dense structure of the membranes.

3.1.3. Zn slurry-air flow battery performance

Ohmic resistance of the system is crucial factor in fixing the performance of Zn slurry-air flow battery. The resistance of the membrane has generally a large influence on the total resistance of the system. The area resistances of the Zn slurry-air flow battery employing the different membranes was determined from the slope of IV plot and are shown in Figure 4. In addition, similar area resistance results were obtained from the EIS measurement (thus, not included here). The cell with Celgard® 3501 has the lowest area resistance (2 Ω cm^2) of all the tested cells. Among the Celgard® membranes, despite the high electrolyte uptake, Celgard® 5550 permit to exhibit the highest cell resistance of (3.2 Ω cm^2) due to its high thickness.

The area resistances obtained in the battery is different from the one determined using the conductivity measurement due to the different electrolyte used. The conductivity of the slurry used in the battery (261 mS cm^{-1}) was about 2.5 times lower than that of the conductivity of the 6 M KOH solution electrolyte (590 mS cm^{-1}) at room temperature. Additionally, the presence of particles in the slurry (Zn and ZnO) can impact the conductivity of the membranes by filling the porosity.

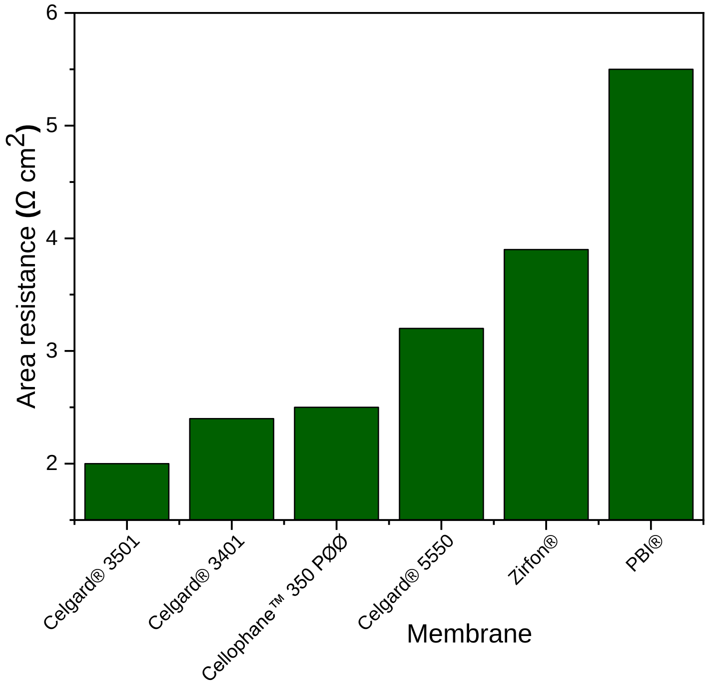

Figure 4: Cell resistance of the Zn slurry- air flow battery employing the different membranes.

Polarization curves of the membranes in Zn slurry-air battery is shown in Figure 5. The voltage and power density of the cell shows significant dependency on the discharge current. A sharp voltage decreases was seen at the beginning of the IV curves for almost all membranes, which is due to the voltage over potential that is related to the electrochemical reaction on electrodes. The about 0.7 V loss at the beginning could be due to the use of a non-optimized electrode performed without ionomer, which can limit the electrochemical reaction kinetic. In the second part, the cell ohmic loses are dominating the cell performance inducing a linear decrease of the voltage *vs* the current density [62]. The large decrease of potential at high current density is caused by the concentration polarization (probably due to transport loss into the slurry).

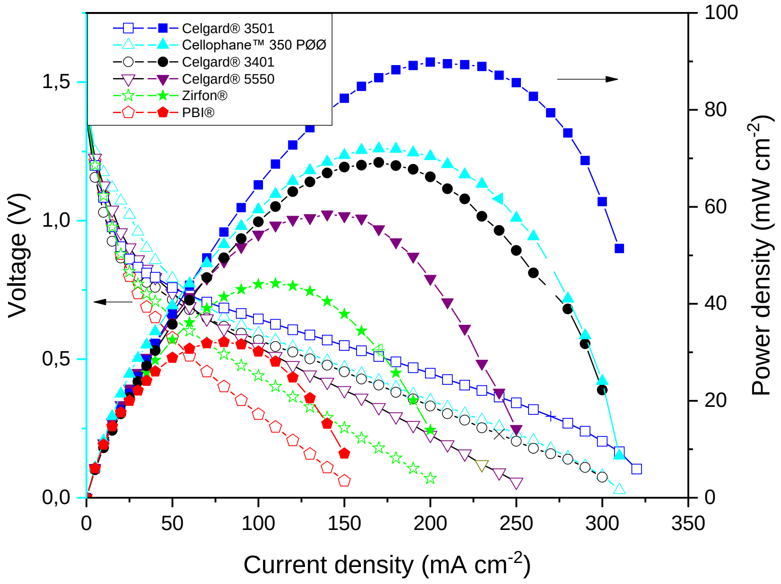

Figure 5: Polarization characteristics of the Zn slurry-air battery with the different membranes.

As shown in Figure 5, the limitation associated with mass transport occured at high current density, thus the maximum power density of the cells seems to be in agreement with their in-situ area resistances. The discharge cell performance revealed that PBI® and Zirfon®-based cell, due to their high area resistances, exhibited the lowest peak power densities among the tested membranes. The PBI®-employing cell displayed peak power density of only 32 mW cm^{-2}. Among the three Celgard® membranes tested, the cells with Celgard® 3401 and Celgard® 3501 showed maximum peak power density of 69 and 90 mW cm^{-2}, respectively, whereas Celgard® 5550-based cell showed the lowest peak power density (58 mW cm^{-2}), consistent with the highest resistance (highest thickness) of the membrane. Cellophane™ 350 PØØ membrane, with an area resistance similar to that of Celgard® 3401-based cell, displayed a peak power density of 72 mW cm^{-2}. It is interesting to note that the peak power densities delivered in decreasing order is Celgard® 3501 > Cellophane™ 350 PØØ ≈ Celgard® 3401 > Celgard® 5550 > Zirfon® > PBI®, which is in agreement with the cell resistances obtained.

Overall, $Zn(OH)_4^{2-}$ ions crossover remains an open challenge regarding the performance and lifespan of Zn-air batteries. All the membranes tested, except PBI, present too high crossover of $Zn(OH)_4^{2-}$ to be useful in a rechargeable Zn slurry-air flow battery. $Zn(OH)_4^{2-}$ crossover leads to capacity lose with cycling and cell polarization as the insoluble ZnO possibly clogs the active area of the positive electrode. However, the critical concentration at which such impact is seen in Zn-air batteries has not been investigate yet. For Zn/MnO_2 batteries, the detrimental effect of $Zn(OH)_4^{2-}$ ion on the air-cathode has been reported to occur at a concentration of ≥ 0.1 M $Zn(OH)_4^{2-}$ ion [63]. Therefore, in addition to figuring out this critical concentration, methods to lower or completely avoid the crossover of $Zn(OH)_4^{2-}$ ions through the membrane are required. The strategy followed to minimize the crossover of $Zn(OH)_4^{2-}$ ions in this work is discussed in section 3.2. Other membrane synthesis and modification strategies have been discussed in our recent review paper on the state-of-the-art membrane studies for Zn-air batteries [29].

3.2. Improving the selectivity of porous membrane by ion-selective polymers coating

3.2.1. Polymer and cation preparation

As discussed in chapter 3, the preparation of PPO-Q polymer was done in two steps, the first step being benzylic bromination of a commercial PPO polymer. DAPCl was also successfully synthesized starting from piperidine in two steps procedure, as outlined in Scheme 2. The structure of prepared cationic monomer was confirmed by ^{1}H NMR (see chapter 3). Furthermore, the successful synthesis of the polymers and DAPCl cation was also confirmed by FTIR spectroscopy (Figure S1).

3.2.2. Modified membrane structural characterization

Celgard® 3501 was chosen as a support membrane because of its low area resistance, high power density and commercial availability. Two solutions were cast on top of this support: (i) based on a mixture of PPO-Q and DAPCl with a theoretical ion exchange capacity of 3.45 mmol OH^-/g (PPO-3.45) and (ii) a commercial FAA solution. SEM and FTIR analysis were employed to confirm the successfulness of the PPO-3.45 coating. The top and cross-section of Celgard® 3501 and modified membranes are comparatively displayed in Figure 6. The pristine Celgard® 3501 membrane displays porous structures (Figure 6a and d), in which the pores are lengthened and orientated in the same direction due to the dry unidirectional stretching of Celgard® after the extrusion manufacturing process [64].

After the PPO-3.45 modification, the surface of Celgard® 3501 membrane was homogeneously covered with the ionomer (Figure 6b). Considering the weight of PPO-Q and DAPCl used, an increase of 2.6 mg cm^{-2} was expected. However, the weight change recorded before and after drying and washing with water, the modified Celgard® 3501 showed that only 2 ($\pm$ 0.1) mg cm^{-2} of ionomer was coated for the PPO-3.45 + 3501 membrane. The water soluble part, analyzed by ^{1}H NMR, was composed of the unreacted monomer DAPCl and poly(DAPCl) wtih a ratio of about 50:50. Considering the 0.6 mg cm^{-2} washed out with water, the IEC was recalculated to be 2.9 mmol OH^- g^{-1} ionomer, thus 1.64 mmol OH^- g^{-1} of composite membrane.

The modified membrane showed an increase of about 2 μm in thickness compared to the pristine membrane, as measured by micrometer. The same increase in thickness was observed in the SEM cross-section (Figure 6e). In addition, as shown in Figure 6e, it appears that some of the polymer is impregnated into the porous structure of the supporting membrane.

For the second composite membrane, a 0.8 g of FAA (12 wt. % in NMP) solution was casted on 64 cm^2 of the porous membrane, thus 1.5 mg cm^{-2} FAA polymer coating was expected. According to the manufacturer, the IEC of FAA-3-50 (membrane believed to be prepared from the FAA solution) is 1.6-2.1 mmol Cl^- g^{-1}, which is equivalent to 1.65-2.2 mmol OH^- g^{-1}. About 80 ($\underline{+}$ 2) wt.% of increase in the modified membrane was noted compared to the pristine one, corresponding to 1.2 mg cm^{-2} coating, thus the IEC was recalculated to be 0.9-1.2 mmol OH^-/(g of the composite membrane). However, no increase in thickness was noted by micrometer and SEM analysis, which indicates the complete impregnation/penetration of the polymer solution onto the porous structure of the Celgard® 3501 substrate [37]. Indeed, the SEM cross-section image (Figure 6f) show that the pores are filled partially.

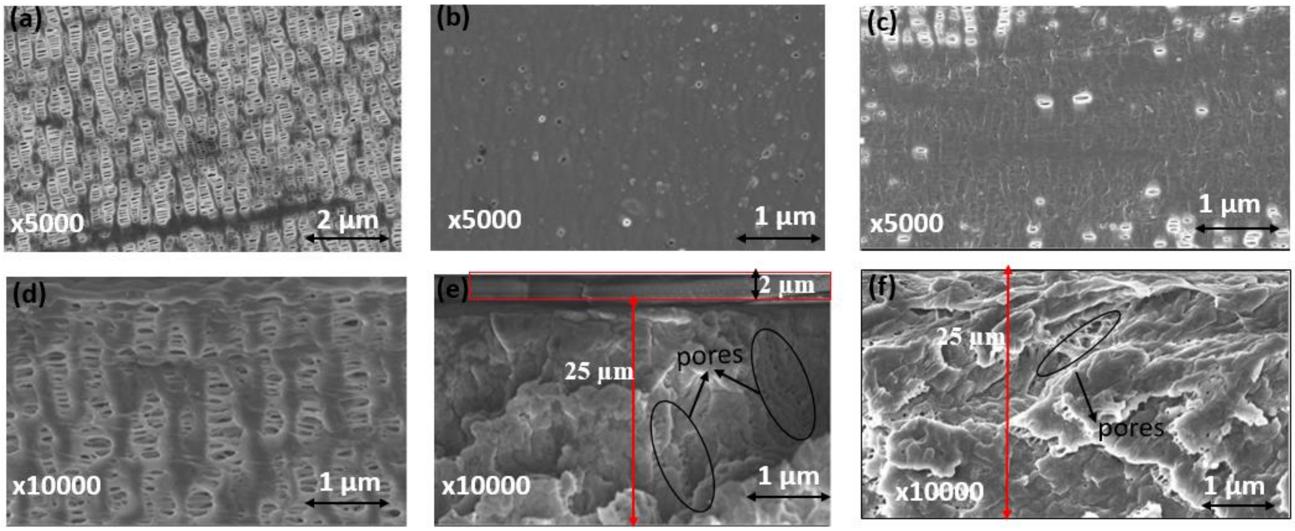

Figure 6: Surface SEM images of a) Celgard® 3501, b) PPO-3.45 + 3501, c) FAA + 3501 and SEM cross section view of d) Celgard® 3501, e) PPO-3.45 + 3501, and f) FAA + 3501 membranes. The densities of dense self-standing PPO-3.45 and FAA membranes were determined to be 1.17 and 1.14 g cm^{-3}, respectively.

Furthermore, Hg porosimetry measurement revealed that the total pore volumes of both PPO-3.45 + 3501 (0.64 cm^3 g^{-1}) and FAA + 3501 (0.72 cm^3 g^{-1}) membranes to be lower than that of the pristine Celgard® 3501 membrane (0.90 cm^3 g^{-1}). The drop of total porosity is seen as an indication of partial filling of the porous membrane with non-porous ionomers. Moreover, for both modified membranes, the larger pores seen in Celgard® 3501, 100 - 200 nm range, seem to be filled by the ionomers as shown in Figure 7.

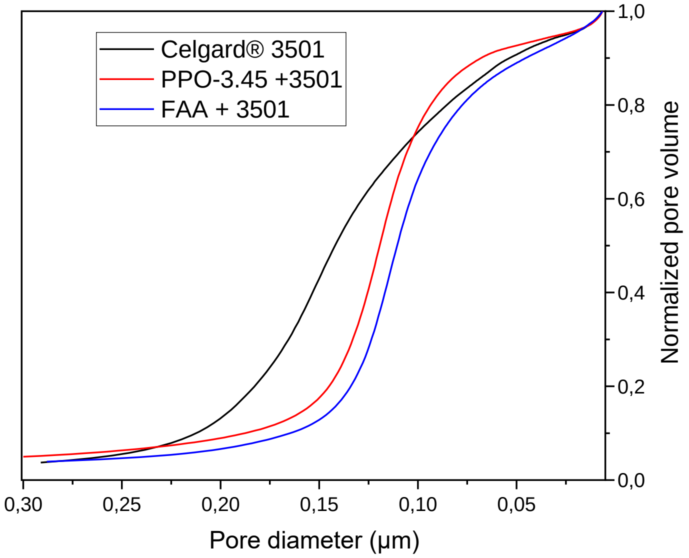

Figure 7. Measurements of Hg intrusion porosity for Celgard® 3501 and modified membranes. Normalized pore volume as a function of pore diameter of Celgard® 3501, FAA + 3501 and PPO-3.45 + 3501. Data show closure of larger Celgard® 3501 pores as a result of impregnation with the ionomers.

The coating and impregnation of the PPO-3.45 and total impregnation of FAA polymer solution could be due to the affinity/interaction between the ionomer and membrane surface in addition to the viscosity behavior of the polymer solution. Visually, the PPO-3.45 solution seems to be much more viscous than the FAA solution. To better understand the solution behavior during the casting, viscosity measurements of both PPO-DAPCl and FAA solutions are shown in Figure 8. PPO-DAPCl exhibits a non-Newtonian behavior. This means that viscosity is dependent of deformation applied to the material and in this case, PPO-DAPCl solution correspond to a shear-thinning behavior in which viscosity decreases as the shear rate (deformation) applied to the sample increases. In the range of shear rates observed, viscosity drops from 7.0 to 0.14 Pa s, decreasing 3 orders of magnitude as shear rate increases. Nevertheless, it is worth noticing that for membrane casting using a doctor blade, shear rate corresponds to a magnitude of about 555 s^{-1} (calculated by dividing casting speed (1.7 cm s^{-1}) by the 30 µm casting polymer solution used) corresponding to a high deformation regime. Using the data in Figure 8, viscosity is extrapolated to the representative shear rate and a value of 32 mPa is found. Contrastingly, FAA solution shows a Newtonian behavior as viscosity remain constant with a value of 45.7 mPa s, which is comparable to the viscosity value of PPO-DAPCl in the range of shear rate investigated. At the casting shear rate, both solutions have comparable viscosities and hence this can explain their similar behavior of large impregnation of the pore structure by the two ionomers.

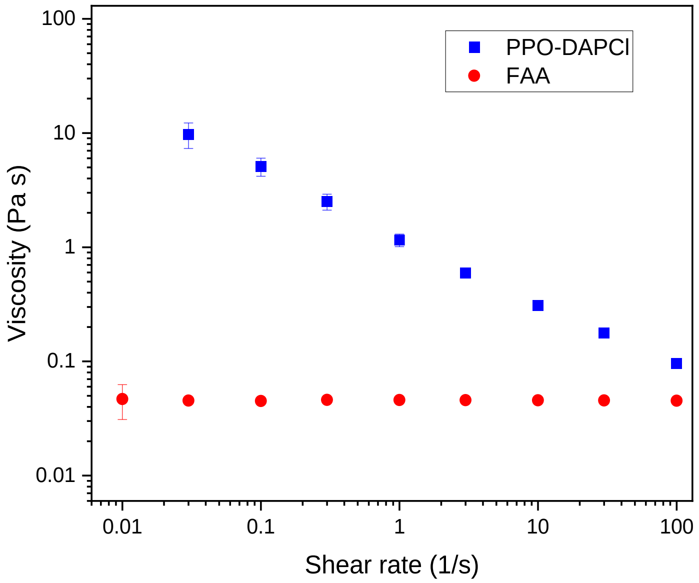

Figure 8. Viscosity as function of shear rate for polymer solutions at 25 ºC.

3.2.3. Electrolyte uptake and ion conductivity

As it can be seen from Table 5, after modifications, the electrolyte uptakes of both PPO-3.45 + 3501 and FAA + 3501 significantly decreased compared to the pristine Celgard® 3501 membrane. Celgard® 3501 was added in Table 5 for comparison purposes. The ion conductivities of PPO-3.45 + 3501 and FAA + 3501 membranes were found to be about 12 and 1 mS cm^{-1}, respectively, at room temperature. The decline in conductivity of the modified membranes, compare to the pristine Celgard® 3501, could be due to the filling of the pores, which greatly contributed to increase the resistance of these modified membranes, thus the ions (including OH$^-$ ions) are less mobile to diffuse through the pores. The difference in conductivities between the two composite-membranes could be due to the difference in IEC between them. Due to its higher IEC, as discussed in chapter 3 in detail, a self-standing membrane prepared from the PPO-3.45 has much higher water uptake than that of FAA membrane.

Table 5: Characterization of the prepared membranes: Electrolyte and ion conductivity.

Membrane	Electrolyte uptake (wt.%)	Ion conductivity (mS cm^{-1})
Celgard® 3501	98 ± 2.5	17 ± 2.5
PPO-3.45 +3501	55 ± 1.9	12.1 ± 0.9
FAA + 3501	46 ± 2.1	1 ± 0.7

3.2.4. Alkaline stability

Alkaline stability of the membranes is important in Zn-air batteries because the membranes have to work efficiently in the highly alkaline solution. The highly basic and nucleophilic OH^- might degrade the membrane. Therefore, stability of membranes in highly alkaline solution must be investigated before use in Zn slurry-air batteries. The stability of PPO-3.45 + 3501 membranes was investigated by comparing their structure before and after immersion in 6 M KOH aqueous solution for 10 days. FTIR analysis was used to investigate the alkaline stability of the membranes.

As shown in Figure 9, no appearance of new peaks of C-OH (above 3000 cm^{-1}) as a result of nucleophilic attack by the OH^- ion was observed [40,65]. Moreover, the membranes do not show any significant change in their spectrum (for example, C-N shown at around 1300 cm^{-1}) before and after immersion in the prepared solution, showing their stability in the alkaline medium. The good alkaline stability of *N*-spirocyclic cations employing AEMs can be explained by the high energy barrier value associated with the transition state during an OH^- attack [66,67].

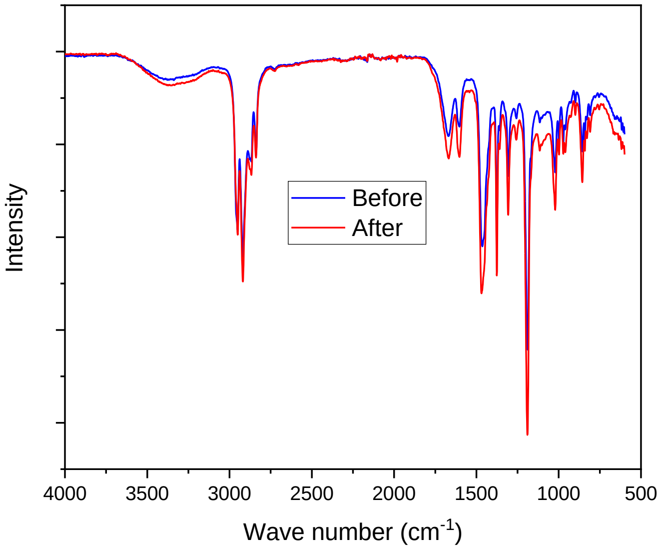

Figure 9: FTIR spectroscopy of PPO-3.45 + 3501 before and after immersion in 6 M KOH at room temperature for 10 days.

3.2.5. Zincate ions crossover

As shown in Figure 10, the PPO-3.45 + 3501 membrane exhibited the lower $Zn(OH)_4^{2-}$ crossover (0.015 M in 8 days) than that of Celgard® 3501. The diffusion of $Zn(OH)_4^{2-}$ through the PPO 3.45 + 3501 membranes was significantly diminished due to filling of the pores and thin coat layer on top of Celgard® 3501 with the ion selective polymer. With the addition of PPO-3.45 ionomer, the $Zn(OH)_4^{2-}$ ion diffusion coefficient decreased by a factor of 18. As shown in the Figure 10, much lower crossover of $Zn(OH)_4^{2-}$ ion through the FAA + 3501 membrane, compared to the PPO 3.45 + 3501 membranes, was observed which can be related to the lower IEC and electrolyte uptake of FAA+ 3501 membrane. In the case of FAA modification, the $Zn(OH)_4^{2-}$ diffusion coefficient was reduced by a factor of more than 280. A large decrease of the zincate ions crossover was reached even if all the pores were not filled completely in the dry state, the properties of the ionomers in terms of water swelling and morphology have a large impact on it. A two orders of magnitude reduction in $Zn(OH)_4^{2-}$ ions diffusion coefficient after coating Celgard® 5550 with polymerized ionic liquid has been reported elsewhere [37].

Table 6 shows the $Zn(OH)_4^{2-}$ diffusion coefficient through the modified membranes. $Zn(OH)_4^{2-}$ ions diffusion coefficient through Celgard® 3401 membrane modified with nanoparticles from the literature is included in Table 6 for comparison purpose.

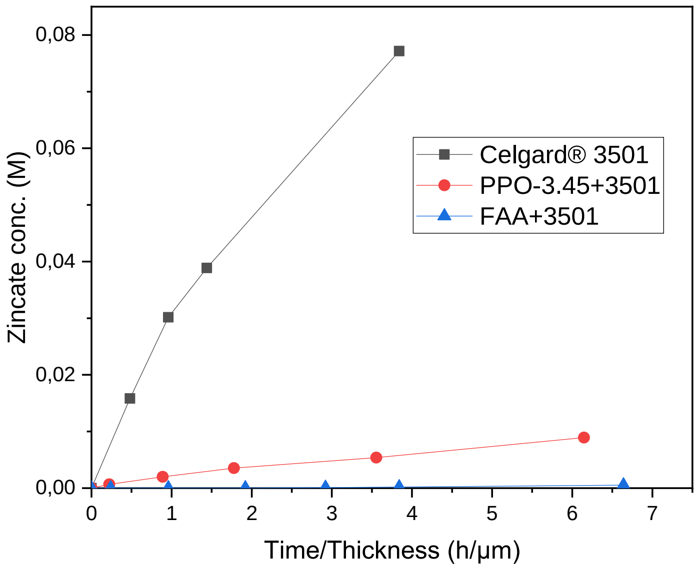

Figure 10: $Zn(OH)_4^{2-}$ crossover of Celgard® 3501, and PPO-3.45 + 3501, FAA+3501 as function of time/membrane thickness.

Table 6: Zincate ions diffusion coefficient through the modified membranes

Membrane	Diffusion coefficient ($m^2 s^{-1}$)	Ref.
Celgard® 3501	9.2 x10^{-12}	
PPO-3.45 + 3501	5.2 x 10^{-13}	This work
FAA + 3501	3.3 x 10^{-14}	
Two Celgard® 3401 coated with $Mn(OH)_2$	6.0 × $10^{−15}$	[35]

3.2.6. Zn slurry-air flow battery discharge performance

The cell resistance employing the membranes in decreasing order is FAA+3501 (5.6 Ω cm^2) > PPO-3.45 + 3501 (2.6 Ω cm^2) > Celgard® 3501 (2 Ω cm^2). The significant increase in cell resistance of the FAA + 3501 membrane, compare to the pristine Celgard® 3501, could be due to the partial filling of the pores, which greatly contributed to increase the resistance of the modified membrane, thus the (OH^-) ions are less mobile to diffuse through the pores. Whereas, the PPO-3.45 + 3501 employing cell resistance has slightly increased compared to the pristine membrane-based cell, probably due to the high IEC of the ionomer, permitting high OH^- ion conductivity and making it a good choice for the application.

The polarization characterization of the modified membranes in Zn slurry-air battery is shown in Figure 11. The decline in power density of the impregnated membranes, compared to the pristine Celgard® 3501 membrane, is due to the increase in resistance of the membranes associated with the filling of the pores with ionomers. The polarization characteristics revealed that PPO-3.45 + 3501-based cell produced a peak power density of 66 mW cm^{-2}. Whereas, the lowest cell performance was obtained when FAA + 3501 is used which could be due to the low ion conductivity of the membrane. The reduction of internal resistance by a factor near 3, in the case of FAA + 3501 membrane compared to the pristine membrane, had a high detrimental impact on the battery performance due to the ohmic drop associated with the high current density used.

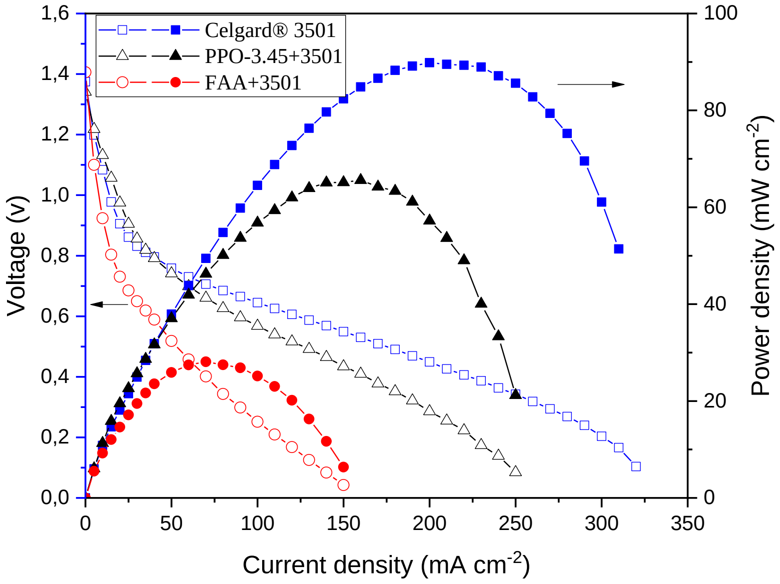

Figure 11: Polarization characteristics of the Zn slurry-air battery with the different membranes.

4. Conclusion

The order of peak power density of the cell employing the commercial membranes in decreasing was Celgard® 3501 > Cellophane™ 350 PØØ ≈ Celgard® 3401> Celgard® 5550 > Zirfon® > PBI®, in agreement with their respective cell resistances. To reduce the crossover of $Zn(OH)_4^{2-}$ ions through the porous membranes, Celgard® 3501 was modified using two different ion-selective polymers. In PPO-3.45 + 3501, the polymers were found to be coated and impregnated on the support membrane. Whereas, on the second work, due to a different rheological behavior and low viscosity, the FAA polymer impregnated into the porous structure of the commercial membrane. Compared to the pristine Celgard® 3501, the PPO 3.45+ 3501 membrane showed 18 times lower crossover of $Zn(OH)_4^{2-}$ ions (5.2×10^{-13} vs 9.2×10^{-12} m^2 s^{-1}). The modified membrane-employing battery delivered a high maximum power density 66 mW cm^{-2}, lower than that of Celgard® 3501-based cell (90 mW cm^{-2}) due to the increase in resistance of the membrane associated with the partial filling of the pores with ionomers. In summary, modified membranes are promising candidates to be used in rechargeable Zn slurry-air flow battery, even if some optimizations are required.

References

[1] B. Dunn, H. Kamath, J.-M. Tarascon, Electrical Energy Storage for the Grid: A Battery of Choices, Science (80-.). 334 (2011) 928–935. doi:10.1126/science.1212741.

[2] W. Wang, Q. Luo, B. Li, X. Wei, L. Li, Z. Yang, Recent Progress in Redox Flow Battery Research and Development, Adv. Funct. Mater. 23 (2013) 970–986. doi:10.1002/adfm.201200694.

[3] P. Alotto, M. Guarnieri, F. Moro, Redox flow batteries for the storage of renewable energy: A review, Renew. Sustain. Energy Rev. 29 (2014) 325–335. doi:10.1016/j.rser.2013.08.001.

[4] M. Rychcik, M. Skyllas-Kazacos, Characteristics of a new all-vanadium redox flow battery, J. Power Sources. 22 (1988) 59–67. doi:10.1016/0378-7753(88)80005-3.

[5] L. Li, S. Kim, W. Wang, M. Vijayakumar, Z. Nie, B. Chen, J. Zhang, G. Xia, J. Hu, G. Graff, J. Liu, Z. Yang, A stable vanadium redox-flow battery with high energy density for large-scale energy storage, Adv. Energy Mater. 1 (2011) 394–400. doi:10.1002/aenm.201100008.

[6] B. Sun, M. Skyllas-Kazacos, Modification of graphite electrode materials for vanadium redox flow battery application-I. Thermal treatment, Electrochim. Acta. 37 (1992) 1253–1260. doi:10.1016/0013-4686(92)85064-R.

[7] S. Hosseini, W. Lao-atiman, S.J. Han, A. Arpornwichanop, T. Yonezawa, S. Kheawhom, Discharge Performance of Zinc-Air Flow Batteries Under the Effects of Sodium Dodecyl Sulfate and Pluronic F-127, Sci. Rep. 8 (2018) 14909. doi:10.1038/s41598-018-32806-3.

[8] J. Ryu, H. Jang, J. Park, Y. Yoo, M. Park, J. Cho, Seed-mediated atomic-scale reconstruction of silver manganate nanoplates for oxygen reduction towards high-energy aluminum-air flow batteries, Nat. Commun. 9 (2018) 3715. doi:10.1038/s41467-018-06211-3.

[9] W. Yu, W. Shang, P. Tan, B. Chen, Z. Wu, H. Xu, Z. Shao, M. Liu, M. Ni, Toward a new generation of low cost, efficient, and durable metal–air flow batteries, J. Mater. Chem. A. 7 (2019) 26744–26768. doi:10.1039/C9TA10658H.

[10] S. Huang, H. Li, P. Pei, K. Wang, Y. Xiao, C. Zhang, C. Chen, A Dendrite-Resistant Zinc-Air Battery, IScience. 23 (2020). doi:10.1016/j.isci.2020.101169.

[11] P. Gu, M. Zheng, Q. Zhao, X. Xiao, H. Xue, H. Pang, Rechargeable zinc-air batteries: A promising way to green energy, J. Mater. Chem. A. 5 (2017) 7651–7666. doi:10.1039/c7ta01693j.

[12] J. Fu, Z.P. Cano, M.G. Park, A. Yu, M. Fowler, Z. Chen, Electrically Rechargeable Zinc–Air Batteries: Progress, Challenges, and Perspectives, Adv. Mater. 29 (2017). doi:10.1002/adma.201604685.

[13] J. Yi, P. Liang, X. Liu, K. Wu, Y. Liu, Y. Wang, Y. Xia, J. Zhang, Challenges, mitigation strategies and perspectives in development of zinc-electrode materials and fabrication for rechargeable zinc-air batteries, Energy Environ. Sci. 11 (2018) 3075–3095. doi:10.1039/c8ee01991f.

[14] C.W. Lee, K. Sathiyanarayanan, S.W. Eom, M.S. Yun, Novel alloys to improve the electrochemical behavior of zinc anodes for zinc/air battery, J. Power Sources. 160 (2006) 1436–1441. doi:10.1016/j.jpowsour.2006.02.019.

[15] M. Schmid, M. Willert-Porada, Electrochemical behavior of zinc particles with silica based coatings as anode material for zinc air batteries with improved discharge capacity, J. Power Sources. 351 (2017) 115–122. doi:10.1016/j.jpowsour.2017.03.096.

[16] D. Stock, S. Dongmo, K. Miyazaki, T. Abe, J. Janek, D. Schröder, Towards zinc-oxygen batteries with enhanced cycling stability: The benefit of anion-exchange ionomer for zinc sponge anodes, J. Power Sources. 395 (2018) 195–204. doi:10.1016/j.jpowsour.2018.05.079.

[17] Q. Wang, Y. Xue, S. Sun, S. Yan, H. Miao, Z. Liu, Facile synthesis of ternary spinel Co–Mn–Ni nanorods as efficient bi-functional oxygen catalysts for rechargeable zinc-air batteries, J. Power Sources. 435 (2019) 226761. doi:10.1016/j.jpowsour.2019.226761.

[18] Y. Wang, X. Xu, J. Chen, Q. Wang, Polyoxometalate on rice paper derived 3D mesoporous carbon paper: An electrocatalyst as cathode for asymmetric Zn-air battery, J. Power Sources. 430 (2019) 201–209. doi:10.1016/j.jpowsour.2019.05.032.

[19] S. Hosseini, S.J. Han, A. Arponwichanop, T. Yonezawa, S. Kheawhom, Ethanol as an electrolyte additive for alkaline zinc-air flow batteries, Sci. Rep. 8 (2018) 11273. doi:10.1038/s41598-018-29630-0.

[20] C. Jiratchayamaethasakul, N. Srijaroenpramong, T. Bunyangyuen, W. Arpavate, N. Wongyao, A. Therdthianwong, S. Therdthianwong, Effects of anode orientation and flow channel design on performance of refuelable zinc-air fuel cells, J. Appl. Electrochem. 44 (2014) 1205–1218. doi:10.1007/s10800-014-0737-4.

[21] C. Kupsch, L. Feierabend, R. Nauber, B. Lars, Ultrasound flow investigations at a zinc-air flow battery model, (2018).

[22] H. Ma, B. Wang, Y. Fan, W. Hong, Development and Characterization of an Electrically Rechargeable Zinc-Air Battery Stack, Energies. 7 (2014) 6549–6557. doi:10.3390/en7106549.

[23] N.H. Choi, D. del Olmo, D. Milian, N. El Kissi, P. Fischer, K. Pinkwart, J. Tübke, Use of Carbon Additives towards Rechargeable Zinc Slurry Air Flow Batteries, Energies. 13 (2020) 4482. doi:10.3390/en13174482.

[24] C. Mele, A. Bilotta, P. Bocchetta, B. Bozzini, Characterization of the particulate anode of a laboratory flow Zn–air fuel cell, J. Appl. Electrochem. 47 (2017) 877–888. doi:10.1007/s10800-017-1088-8.

[25] A. Puapattanakul, S. Therdthianwong, A. Therdthianwong, N. Wongyao, Improvement of zinc-air fuel cell performance by gelled koh, Energy Procedia. 34 (2013) 173–180. doi:10.1016/j.egypro.2013.06.745.

[26] W. Yu, W. Shang, P. Tan, B. Chen, Z. Wu, H. Xu, Z. Shao, M. Liu, M. Ni, Toward a new generation of low cost, efficient, and durable metal-air flow batteries, J. Mater. Chem. A. 7 (2019) 26744–26768. doi:10.1039/c9ta10658h.

[27] Z. Zhao, B. Liu, X. Fan, X. Liu, J. Ding, W. Hu, C. Zhong, An easily assembled boltless zinc–air battery configuration for power systems, J. Power Sources. 458 (2020) 228061. doi:10.1016/j.jpowsour.2020.228061.

[28] M.T. Tsehaye, F. Alloin, C. Iojoiu, Prospects for Anion-Exchange Membranes in Alkali Metal–Air Batteries, Energies. 12 (2019) 4702. doi:10.3390/en12244702.

[29] M.T. Tsehaye, F. Alloin, C. Iojoiu, R.A. Tufa, D. Aili, P. Fischer, S. Velizarov, Membranes for zinc-air batteries: Recent progress, challenges and perspectives, J. Power Sources. 475 (2020) 228689. doi:10.1016/j.jpowsour.2020.228689.

[30] P. Arora, Z. Zhang, Battery Separators, (2004). doi:10.1021/cr020738u.

[31] H.J. Lee, J.M. Lim, H.W. Kim, S.H. Jeong, S.W. Eom, Y.T. Hong, S.Y. Lee, Electrospun polyetherimide nanofiber mat-reinforced, permselective polyvinyl alcohol composite separator membranes: A membrane-driven step closer toward rechargeable zinc-air batteries, J. Memb. Sci. 499 (2016) 526–537. doi:10.1016/j.memsci.2015.10.038.

[32] A. Abbasi, S. Hosseini, A. Somwangthanaroj, A.A. Mohamad, S. Kheawhom, Poly(2,6-Dimethyl-1,4-Phenylene Oxide)-Based Hydroxide Exchange Separator Membranes for Zinc–Air Battery, Int. J. Mol. Sci. 20 (2019) 3678. doi:10.3390/ijms20153678.

[33] Y. Li, H. Dai, Recent advances in zinc–air batteries, Chem. Soc. Rev. 43 (2014) 5257–5275. doi:10.1039/C4CS00015C.

[34] E.L. Dewi, K. Oyaizu, H. Nishide, E. Tsuchida, Cationic polysulfonium membrane as separator in zinc–air cell, J. Power Sources. 115 (2003) 149–152. doi:10.1016/S0378-7753(02)00650-X.

[35] Y. Kiros, Separation and permeability of zincate ions through membranes, J. Power Sources. 62 (1996) 117–119. doi:10.1016/S0378-7753(96)02420-2.

[36] I. Krejčí, P. Vanýsek, A. Trojánek, Transport of Zn (OH) 4 2 − Ions across a Polyolefin Microporous Membrane, J. Electrochem. Soc. 140 (1993) 2279–2283. doi:10.1149/1.2220808.

[37] H.J. Hwang, W.S. Chi, O. Kwon, J.G. Lee, J.H. Kim, Y.G. Shul, Selective ion transporting polymerized ionic liquid membrane separator for enhancing cycle stability and durability in secondary zinc-air battery systems, ACS Appl. Mater. Interfaces. 8 (2016) 26298–26308. doi:10.1021/acsami.6b07841.

[38] D.J. Strasser, B.J. Graziano, D.M. Knauss, Base stable poly(diallylpiperidinium hydroxide) multiblock copolymers for anion exchange membranes, J. Mater. Chem. A. 5 (2017) 9627–9640. doi:10.1039/C7TA00905D.

[39] J.S. Olsson, T.H. Pham, P. Jannasch, Poly(N , N -diallylazacycloalkane)s for Anion-Exchange Membranes Functionalized with N -Spirocyclic Quaternary Ammonium Cations, Macromolecules. 50 (2017) 2784–2793. doi:10.1021/acs.macromol.7b00168.

[40] Z. Wang, J. Parrondo, S. Sankarasubramanian, K. Bhattacharyya, M. Ghosh, V. Ramani, Alkaline Stability of Pure Aliphatic-based Anion Exchange Membranes Containing Cycloaliphatic Quaternary Ammonium Cations, J. Electrochem. Soc. 167 (2020) 124504. doi:10.1149/1945-7111/abac29.

[41] X. Tongwen, Y. Weihua, Fundamental studies of a new series of anion exchange membranes: Membrane preparation and characterization, J. Memb. Sci. 190 (2001) 159–166. doi:10.1016/S0376-7388(01)00434-3.

[42] T. Xu, D. Wu, L. Wu, Poly(2,6-dimethyl-1,4-phenylene oxide) (PPO)-A versatile starting polymer for proton conductive membranes (PCMs), Prog. Polym. Sci. 33 (2008) 894–915. doi:10.1016/j.progpolymsci.2008.07.002.

[43] C. Sun, J. Chen, H. Zhang, X. Han, Q. Luo, Investigations on transfer of water and vanadium ions across Nafion membrane in an operating vanadium redox flow battery, J. Power Sources. 195 (2010) 890–897. doi:10.1016/j.jpowsour.2009.08.041.

[44] N.H. Choi, D. Del Olmo, P. Fischer, K. Pinkwart, J. Tübke, Development of flow fields for zinc slurry air flow batteries, Batteries. 6 (2020) 1–10. doi:10.3390/batteries6010015.

[45] Celgard LLC, Celgard high performance battery separators, 2200 (2009).

[46] J. Rodríguez, S. Palmas, M. Sánchez-Molina, E. Amores, L. Mais, R. Campana, Simple and precise approach for determination of Ohmic contribution of diaphragms in alkaline water electrolysis, Membranes (Basel). 9 (2019). doi:10.3390/membranes9100129.

[47] AGFA, Technical Data Sheet ZIRFON PERL UTP 500, 2020.

[48] C. Shi, J. Dai, C. Li, X. Shen, L. Peng, P. Zhang, D. Wu, D. Sun, J. Zhao, A modified ceramic-coating separator with high-temperature stability for lithium-ion battery, Polymers (Basel). 9 (2017) 10–14. doi:10.3390/polym9050159.

[49] R. Xu, H. Huang, Z. Tian, J. Xie, C. Lei, Effects of Coated Separator Surface Morphology on Electrolyte Interfacial Wettability and Corresponding Li–Ion Battery Performance, Polymers (Basel). 12 (2020) 117. doi:10.3390/polym12010117.

[50] M. Kirchhöfer, J. von Zamory, E. Paillard, S. Passerini, Separators for Li-Ion and Li-Metal Battery Including Ionic Liquid Based Electrolytes Based on the TFSI− and FSI− Anions, Int. J. Mol. Sci. 15 (2014) 14868–14890. doi:10.3390/ijms150814868.

[51] H.W. Kim, J.M. Lim, H.J. Lee, S.W. Eom, Y.T. Hong, S.Y. Lee, Artificially engineered, bicontinuous anion-conducting/-repelling polymeric phases as a selective ion transport channel for rechargeable zinc-air battery separator membranes, J. Mater. Chem. A. 4 (2016) 3711–3720. doi:10.1039/c5ta09576j.

[52] J.W. Lee, C. Lee, J.H. Lee, S.-K. Kim, H.-S. Cho, M. Kim, W.C. Cho, J.H. Joo, C.-H. Kim, Cerium Oxide–Polysulfone Composite Separator for an Advanced Alkaline Electrolyzer, Polymers (Basel). 12 (2020) 2821. doi:10.3390/polym12122821.

[53] S.J. Liu, S.P. Cui, Z.P. Qin, C.J. Fei, Y.L. Wang, H.X. Guo, A Novel Way to Modify PTFE Membrane into Hydrophilicity, Mater. Sci. Forum. 898 (2017) 1892–1895. doi:10.4028/www.scientific.net/MSF.898.1892.

[54] B. Van der Bruggen, Chemical modification of polyethersulfone nanofiltration membranes: A review, J. Appl. Polym. Sci. 114 (2009) 630–642. doi:10.1002/app.30578.

[55] P. Vermeiren, R. Leysen, H. Beckers, J.P. Moreels, A. Claes, The influence of manufacturing parameters on the properties of macroporous Zirfon® separators, J. Porous Mater. 15 (2008) 259–264. doi:10.1007/s10934-006-9084-0.

[56] J.-H. Park, J.-S. Park, KOH-doped Porous Polybenzimidazole Membranes for Solid Alkaline Fuel Cells, Energies. 13 (2020) 525. doi:10.3390/en13030525.

[57] J. Duay, T.N. Lambert, R. Aidun, Stripping Voltammetry for the *Real Time* Determination of Zinc Membrane Diffusion Coefficients in High pH: Towards Rapid Screening of Alkaline Battery Separators, Electroanalysis. 29 (2017) 2261–2267. doi:10.1002/elan.201700337.

[58] I. V. Kolesnichenko, D.J. Arnot, M.B. Lim, G.G. Yadav, M. Nyce, J. Huang, S. Banerjee, T.N. Lambert, Zincate-Blocking-Functionalized Polysulfone Separators for Secondary Zn–MnO 2 Batteries, ACS Appl. Mater. Interfaces. 12 (2020) 50406–50417. doi:10.1021/acsami.0c14143.

[59] D.E. Turney, J.W. Gallaway, G.G. Yadav, R. Ramirez, M. Nyce, S. Banerjee, Y.C.K. Chen-Wiegart, J. Wang, M.J. D'Ambrose, S. Kolhekar, J. Huang, X. Wei, Rechargeable Zinc Alkaline Anodes for Long-Cycle Energy Storage, Chem. Mater. 29 (2017) 4819–4832. doi:10.1021/acs.chemmater.7b00754.

[60] W.B. Seymour, The preparation of cellophane membranes of graded permeability, J. Biol. Chem. 134 (1940) 701–707.

[61] W. Cao, Y. Li, B. Fitch, J. Shih, T. Doung, J. Zheng, Strategies to optimize lithium-ion supercapacitors achieving high-performance: Cathode configurations, lithium loadings on anode, and types of separator, J. Power Sources. 268 (2014) 841–847. doi:10.1016/j.jpowsour.2014.06.090.

[62] S. Hosseini, W. Lao-atiman, S.J. Han, A. Arpornwichanop, T. Yonezawa, S. Kheawhom, Discharge performance of zinc-air flow Bbatteries under the effects of sodium dodecyl sulfate and pluronic F-127, Sci. Rep. 8 (2018) 14909. doi:10.1038/s41598-018-32806-3.

[63] M.A. Dzieciuch, N. Gupta, H.S. Wroblowa, Rechargeable Cells with Modified MnO 2 Cathodes , J. Electrochem. Soc. 135 (2019) 2415–2418. doi:10.1149/1.2095349.

[64] D. Djian, F. Alloin, S. Martinet, H. Lignier, J.Y. Sanchez, Lithium-ion batteries with high charge rate capacity: Influence of the porous separator, J. Power Sources. 172 (2007) 416–421. doi:10.1016/j.jpowsour.2007.07.018.

[65] Futamura, Cellophane ^{TM} PØØ technical datasheet, n.d.

[66] M.G. Marino, K.D. Kreuer, Alkaline Stability of Quaternary Ammonium Cations for Alkaline Fuel Cell Membranes and Ionic Liquids, ChemSusChem. 8 (2015) 513–523. doi:10.1002/cssc.201403022.

[67] L. Gu, H. Dong, Z. Sun, Y. Li, F. Yan, Spirocyclic quaternary ammonium cations for alkaline anion exchange membrane applications: an experimental and theoretical study, RSC Adv. 6 (2016) 94387–94398. doi:10.1039/C6RA22313C.

Supplementary information

Polymer and Cation synthesis: FTIR

Characteristic peaks of C=C stretching and C-H stretching of benzene ring in PPO appeared at around 1600 cm^{-1} and 1470 cm^{-1}, respectively [1,2]. A new characteristic peak at 987 cm^{-1}, which is attributed to the C-Br groups [3] was observed in the FTIR spectra of PPO-Br. After quaternization, the C-Br peak disappeared which confirms the reaction of CH_2Br side chains of PPO with diallylmethylamine to form the PPO-Q. The characteristic peaks in DAPCl, including C-N stretching, and quaternary ammonium are shown around 1300 cm^{-1} and 955 cm^{-1}, respectively [4]. Moreover, the C-H stretching, C=C stretching, and CH_2 bending are shown at 2977 cm^{-1}, 1635 cm^{-1}, and 1456 cm^{-1} respectively [4].

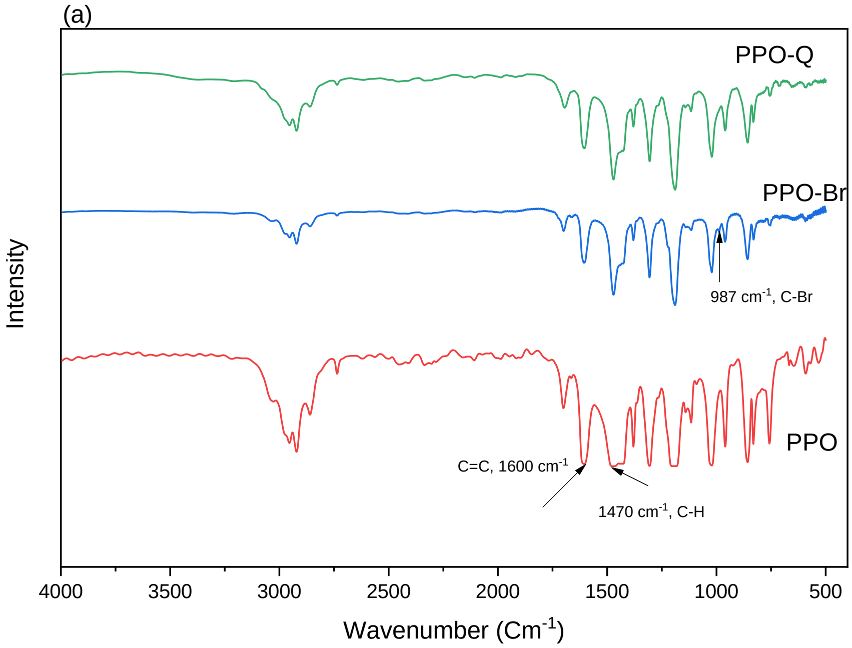

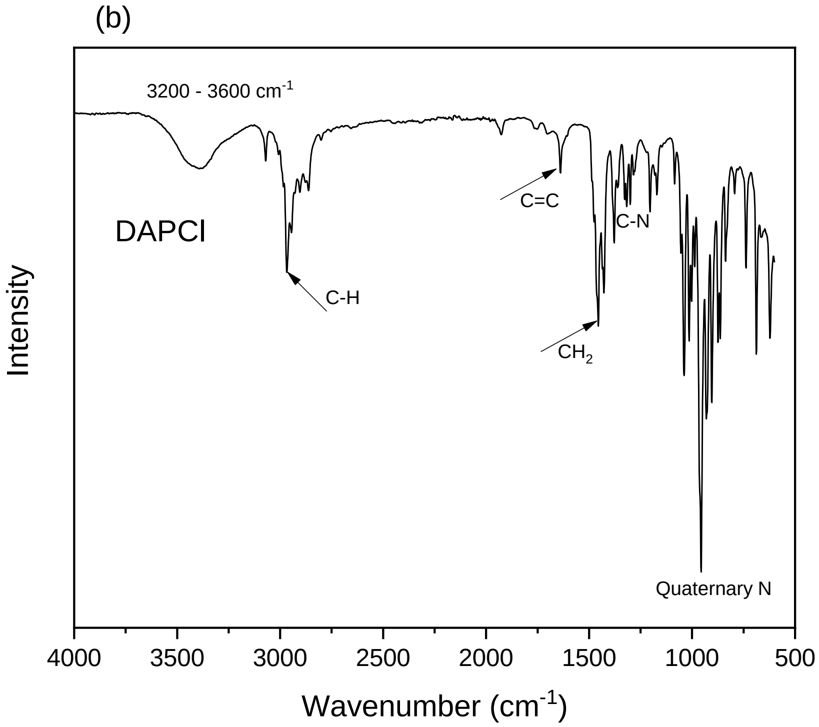

Figure S1*:* FTIR spectra of (a) PPO, PPO-Br, PPO-Q and (b) DAPCl. The spectral bands from 3600 – 3200 cm^{-1} are characteristic peaks of OH^- groups absorbed in the different samples.

References

[1] P.F. Msomi, P. Nonjola, P.G. Ndungu, J. Ramonjta, Quaternized poly(2.6 dimethyl-1.4 phenylene oxide)/polysulfone blend composite membrane doped with ZnO-nanoparticles for alkaline fuel cells, J. Appl. Polym. Sci. 135 (2018) 45959. doi:10.1002/app.45959.

[2] Y. Yang, Y. Xu, N. Ye, D. Zhang, J. Yang, R. He, Alkali Resistant Anion Exchange Membranes Based on Saturated Heterocyclic Quaternary Ammonium Cations Functionalized Poly(2,6-dimethyl-1,4-phenylene oxide)s, J. Electrochem. Soc. 165 (2018) F350–F356. doi:10.1149/2.1031805jes.

[3] L. Zhu, T.J. Zimudzi, Y. Wang, X. Yu, J. Pan, J. Han, D.I. Kushner, L. Zhuang, M.A. Hickner, Mechanically Robust Anion Exchange Membranes via Long Hydrophilic Cross-Linkers, Macromolecules. 50 (2017) 2329–2337. doi:10.1021/acs.macromol.6b01381.

[4] A.M. Patel, R.G. Patel, M.P. Patel, Nickel and copper removal study from aqueous solution using new cationic poly[acrylamide/ N,N -DAMB/ N,N -DAPB] super absorbent hydrogel, J. Appl. Polym. Sci. 119 (2011) 2485–2493. doi:10.1002/app.32818.

Chapter 7: Anion exchange membranes based on poly(phenylene oxide) with a spacer incorporating *N*-spirocyclic quaternary ammonium cation via UV irradiation for zinc slurry-air flow batteries

1. Introduction

As discussed in the previous chapter, the use of porous membranes has resulted in a significant crossover of zincate ions. On the other hand, the synthesized ion-selective polymer coated membranes displayed minimized crossover of zincate ions. However, compared to the pristine reference membrane, there was a decline in peak power density as well which is due to the increase in cell resistance and/or decrease in ion conductivity. To realize long-term rechargeable Zn slurry-air battery, it is important to employ a proper membrane with a low/no zincate crossover and high hydroxide ion conductivity (or low membrane resistance). In this chapter, we have prepared and employed dense anion exchange membranes (AEMs) which could significantly reduce the crossover of zincate ions while keeping high ion conductivity.

The use of AEMs that are only selective to the passage of OH^- ions has been widely proposed for use in Zinc-air flow batteries [1,2]. However, despite the promising use of AEMs for Zn-air batteries, to date, it remains to be a less investigated topic. Membrane containing poly(methylsulfonio-1,4-phenylenethio-1,4-phenylene trifluoromethanesulfonate) (a sulfonium cation) was reported to show lower permeation of zincate ions than a Celgard® 5550 membrane [3]. As a result, the Zn-air cell employing the prepared membrane showed six-fold higher discharge capacity than that of the polypropylene-based cell. Moreover, benzylic quaternized AEMs based on poly (2,6-dimethyl-1,4-phenylene oxide) (PPO) and three different amines, trimethylamine (TMA), 1-methylpyrolidine (MPY), and 1-methylimidazole (MIM) were prepared and tested in primary Zn-air batteries [4]. The membranes displayed low zincate ions diffusion coefficients (1.13×10^{-8} cm^2/min for the PPO-TMA membrane). This was ascribed to the formation of proper ionic channels in the polymer structure. Additionally, various AEMs, such as cationic polysulfonium [5], A201® (Tokuyama Corporation, Japan) [6,7] and FAA-3® (FumaTech, Germany) [8,9] membranes have been tested in Zn-air batteries.

Alkaline chemical stability is one of the major challenges for use of AEMs in electrochemical devices, including alkaline batteries. Chemical degradation of such ionomers can be caused by chemical instability of the cationic functional groups, of the polymer backbones and/or polymer-cationic group linkages. Specifically, the cation degradation is regarded to be the main reason why present-day polymer-based AEMs rapidly degrade in alkaline conditions beyond 80 °C and results in mechanical failure. Usually, the alkaline stability is determined by analyzing the evolution of chemical structure of ionomer, mechanical properties and/or performance of the membranes before and after immersing into an alkaline media, e.g., (1 M) KOH solution (at 80 °C), for certain time.

N-spirocyclic quaternary ammonium (QA) cations, especially 6- azonia-spiro[5.5]undecane (ASU), have been reported to have better alkaline stability compared to other ammonium species. The chemical stability of these cations against Hoffman elimination and ring-opening reaction is due to the geometric constraints of the ring on the transition state [10]. Linear polyaromatic AEMs incorporating piperidinium and ASU cations via superacid-mediated polycondensation have been reported by the same research group [11,12]. The poly(terphenyl dimethyl-piperidinium)-based AEMs showed no sign of degradation in 2 M NaOH at 60 °C after 15 days [11]. Moreover, Strasser et al. [13] prepared a multiblock AEM copolymers involving Poly(diallylpiperidinum hydroxide) cation by copolymerizing the end-functionalized polydiallylpiperidinium oligomers with polysulfone monomers. The membranes were reported to maintain 92% of their conductivity after 5 days in 1 M KOH at 80 °C. Recently, PPOs containing 3,6-diazaspiro[5.5]undecane (DSU) cation/cation strings were prepared by two steps quaternization method [14]. However, compared to ASU, the DSU cation was reported to have inferior alkaline stability because of the cation's tertiary N atom which resulted in both Hofmann elimination and SN_2 substitution.

Another issue associated with alkaline stability of AEM is that AEMs quaternized in their benzylic positions are sensitive towards chemical degradation, thus unstable especially in highly alkaline medium at high temperature [15]. Membranes with tethered benzyltrimethyl ammonium cations were reported to broken into small pieces after 3 days, whereas, comb-shaped membranes maintained acceptable mechanical properties even after 83 days when tested in 1 M NaOH at 80 °C [16]. Moreover, cations placed directly on the benzylic positions (close to the polymer backbone) restricts the local mobility of the ionic groups and minimize/avoid the distinct phase separation, which is reported to be pre-request for highly conductive AEMs [17].

In this work, to avoid the possible benzylic position instability, the PPO polymer was functionalized with methyldiallylammonium groups via a 6-C long spacer (PPO-6CH_2Q) using a two-step strategy. PPO was chosen as polymer backbone because of its high glass transition temperature of 215 °C inducing an excellent mechanical strength, good chemical, especially in alkaline medium, stability and commercial availability in a reasonable cost [18,19]. Furthermore, to overcome the challenge associated with the incorporation of N-spirocyclic ammonium cationc groups onto the polymer structures [13,20], in this work, UV curing method is employed to graft the N-spirocyclic ammonium groups onto the modified PPO polymer backbone. In order to investigate the impact of ion exchange capacity (IEC) on the water uptake, water state, ion conductivity and zincate ions crossover of the membranes, the ratio of *N*, *N*-diallylpiperidinium chloride (DAPCl) to PPO-6CH_2Q polymer was varied from 0.5 to 3. The prepared AEMs were tested for their alkaline and thermal stability and characterized by DSC and AFM. Finally, the membranes were tested in Zn slurry-air flow batteries.

2. Experimental

2.1. Materials

Poly (2,6-dimethyl-1,4-phenyleneoxide) (PPO) (Mn = 20,000, Polydispersity = 2.5) was purchased from Polysciences Inc. Chlorobenzene (ACS reagent, ≥ 99.5%), N-methyl-2-pyrrolidone (NMP, reagent grade), 1,2-dichloroethane (99.8%), allyl bromide (98%), allyl chloride (98%) and chloroform (99.8%) were purchased from Alfa Aesar. 2-hyroxy-4’-(2-hydroxyethoxy)-2-methylpropiophenone (Irgacure D-2959) was bought from Ciba Specialty Chemicals Inc. Methanol (99.9%) and chloroform (99.8%) were purchased from Fisher Scientific. Diallymethylamine (97%) and piperidine (≥99%) were bought from ABCR GmbH. 6-Bromohexanoyl chloride (97%), diethyl ether (99+ %) and chloroform-d ($CDCl_3$-d, 99.9% D) were purchased from Sigma-Aldrich. Dimethyl sulfoxide-d_6 (DMSO-d_6, 99.9%), $AlCl_3$ (98.5%, anhydrous), and N-Methyl-2-pyrrolidone (NMP, reagent grade) were supplied from Acros Organics. Chlorobenzene (ACS reagent, ≥ 99.5%) were bought from ABCR GmbH. All chemicals were used as received without further purification.

2.2. Polymer synthesis

PPO-CO-Br: As discussed in chapter 4, the synthesis of PPO with a six-carbon pendant chain spacer (PPO-6CO-Br) was carried out based on a slight modification of the method described by Hibbs [21]. The degree of bromination/functionalization was determined from the ^{1}H NMR peak areas. The polymer had approximately 0.33 mol of bromomethyl groups per polymer repeat unit.

PPO-6CH$_2$-Br: The reduction of the ketone groups in the PPO-6CO-Br polymer was carried out as follow. In a 350 mL heavy wall pressure vessel (pressure reactor purchased from chemglass), 1 g (6.85 mmol Br groups) PPO-6CO-Br was dissolved in 1,2-dichloroethane (40 mL), followed by addition of 40 mL of trifluoroacetic acid (0.685 mol, 78.1 g) and 4 mL of triethylsilane (0.0685 mol, 7.96 g). The reaction took place under pressure in order to avoid the evaporation of the solvent and increase the reaction temperature beyond the solvent-reactive mixture boiling point. The reduction reaction was carried out under oil bath temperature of 100 °C for 24 h. Once the reaction is complete, the reaction mixture was neutralized with aq. KOH solution (30 wt. %, 100 mL) till the pH becomes neutral. The organic phase was then separated using separatory funnel and precipitated in methanol. Subsequent dissolving in chloroform and precipitating in methanol were performed to remove the triethylsilane and improve the purity of the obtained product. The product was vacuum dried at 60 °C for 24 h. The degree of ketone reduction was determined from the ^{1}H NMR peak areas.

PPO-6CH2-Q: The PPO-6CH$_2$-Br polymer was first dissolved in 5 wt. % NMP at 40 °C. To fully replace the bromine groups, methydiallylamine was added in excess (2.5 molar) to the reaction flask and the reaction continued for 72 h. The quaternized product (PPO-6CH$_2$-Q) was slowly precipitated in diethyl ether and dried under vacuum at 35 °C for 72 h. The complete replacement of bromine atoms with the amine has been confirmed using ^{1}H NMR. The protocol followed to prepare PPO-6CO-Br, PPO-6CH$_2$-Br and PPO-6CH$_2$-Q is summarized in scheme 1.

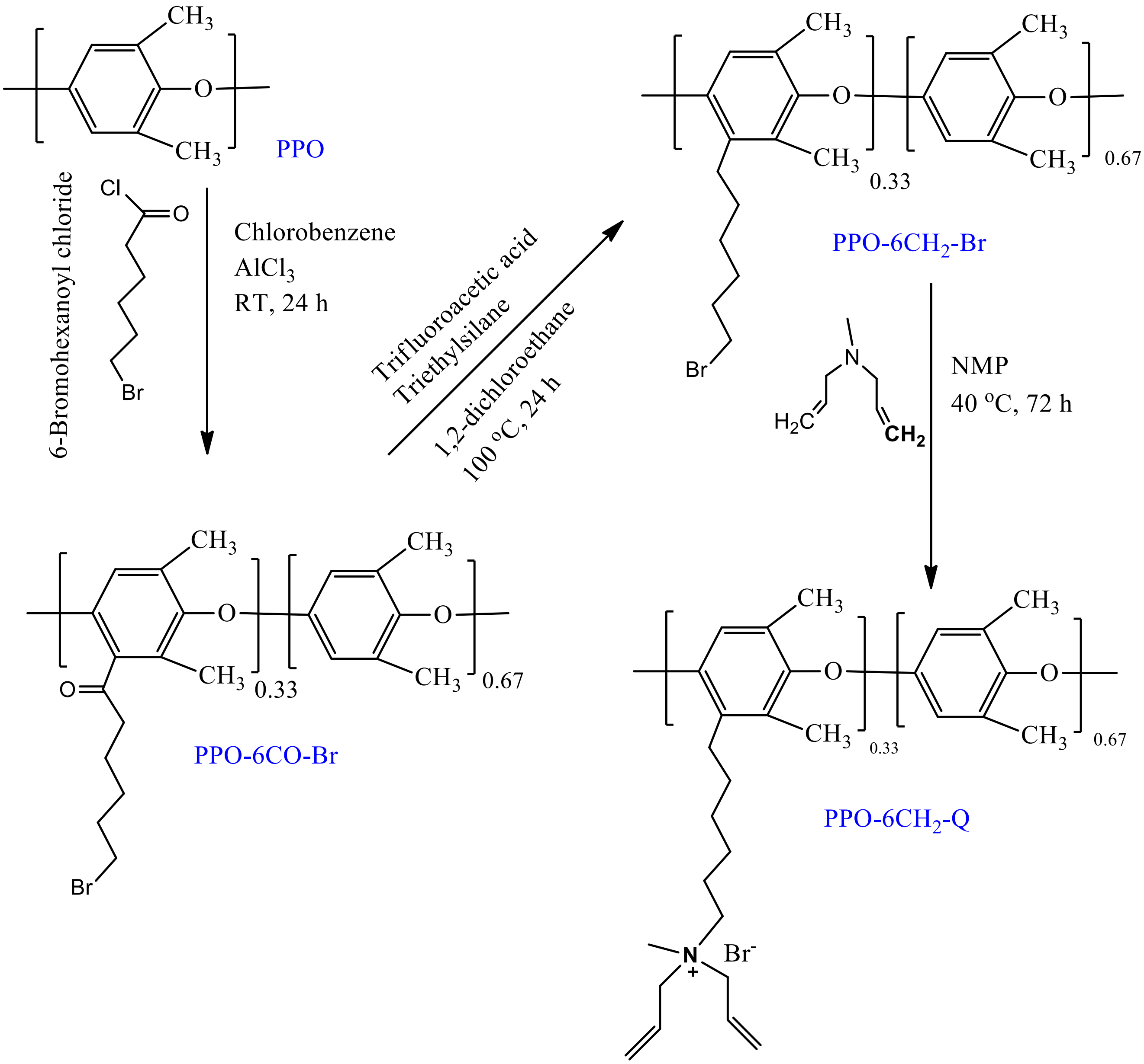

Scheme 1: Schematic representation of PPO-6CO-Br, PPO-6CH$_2$-Br and PPO-6CH$_2$-Q polymers preparation.

2.3. N, N-Diallylpiperidinum chloride (DAPCl) synthesis

The preparation of DAPCl was performed in two steps based on the method reported on chapter 3 (section 2.3).

2.4. Membrane preparation

After the synthesis of the PPO-6CH_2-Q and DAPCl, membrane preparation was performed as follow. The appropriate amounts of the different species (polymer, monomer and initiator) are solubilized in a mixture of 1, 2-dichloroethane and NMP and the solutions are cast on a petri dish. Four membranes with different IECs, by varying the ratio of DAPCl to PPO-6CH_2-Q, were prepared. For instance, to prepare AEM with a DAPCl to PPO-6CH_2-Q ratio of 3 (theoretical IEC of 2.8 mmol Br^- g^{-1}), 0.075 g PPO-6CH_2-Q (0.115 mmol diallylmethylammonium), 0.0695 g DAPCl (0.345 mmol) and 0.0155 g (20% excess with respect to the diallylmethylammonium in the polymer backbone) Irgacure® 2959 initiator were dissolved in 1.2 mL of 1, 2-dichloroethane (13 wt./v %). Next, 0.56 mL NMP (28.5 wt./v %) was added to the mixture and stirred for about 15 minutes. The prepared solution was poured into a glass petri dish (5 cm diameter) and was kept away from light by covering aluminum foil with small holes to avoid decomposition of the initiator and permit the 1, 2-dichloroethane evaporation at room temperature. The film-containing petri dish was put in a vacuum chamber and degassed to remove oxygen. The viscous homogenous solution was cross-linked using UV-radiation ((P300MT power supply, Fusion UV Systems) for 3 min under argon. After irradiation, the membrane is placed in an oven at 60 °C to evaporate the NMP. After 24 h, the membrane is removed from the petri dish and immersed in a large excess of DI water to wash out any remaining solvents, monomers and non-grafted poly(DAPCl). Figure 1 shows the schematic representation of the membrane preparation procedure.

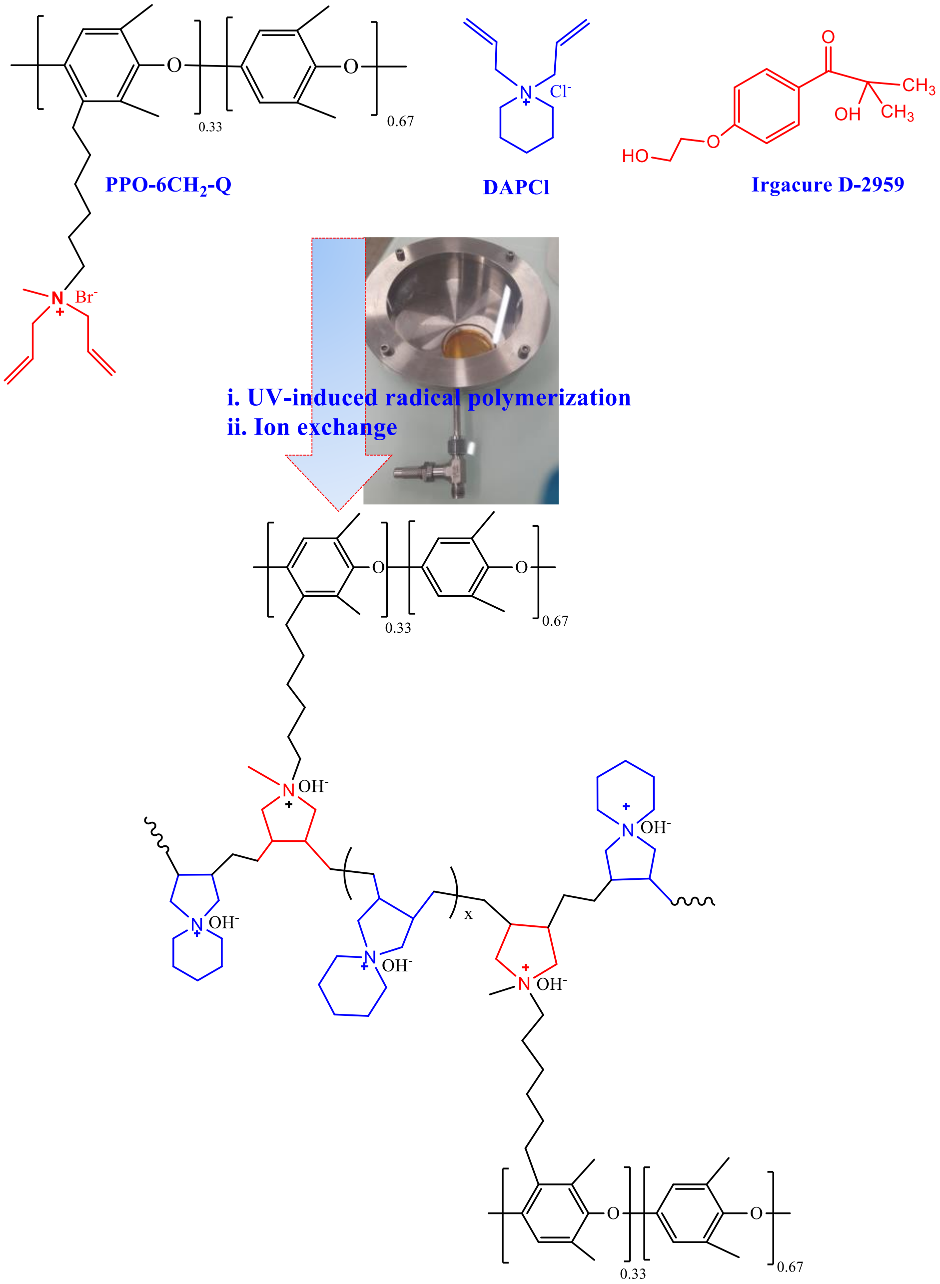

Figure 1: Schematic representation of the membrane preparation procedure.

2.5. Characterizations

2.5.1. Structural characterization

The structure of the polymers and polyelectrolyte was determined by ^{1}H NMR spectroscopy. A Bruker AV 400 NMR spectrometer was used to record the ^{1}H NMR spectra. DMSO-d_6 ($\delta = 2.50$ ppm) or $CDCl_3$ ($\delta = 7.26$ ppm) or D_2O ($\delta = 4.79$ ppm) were used as NMR solvents.

2.5.2. Morphological characterization

The surface morphology analysis of the membranes investigated by tapping mode atomic force microscopy (AFM) analysis of wet membranes in the OH^- form at room temperature. The topographical and phase images were obtained simultaneously.

2.5.3. Ionic exchange capacity and water uptake

The ion exchange capacity (IEC), number of ionic function per gram of polymer was measured by Mohr titration method. The prepared membranes were converted to Br^- form by immersing in NaBr (1 M) at 50 ^oC for 48 h. The membranes (Br^- form) were then taken out from the solution and washed with DI water several times in order to remove the excess salts. Membrane samples (~ 0.05 g) in Br^- form were dried in a vacuum oven at 50 °C for 24 h and their dry weight was recorded. The samples were then immersion in 0.2 M aq. $NaNO_3$ (25 mL) for 48 h at room temperature under stirring, thus replacing the Br^- with NO_3^{2-}. Three samples of the resulting solution were titrated with 0.01 M aq. $AgNO_3$ solution. K_2CrO_4 was used as indicator. The IEC of the membranes in Br^- form was determined using the following equation.

$$IEC_{Br-} = \frac{Volume\ x\ Concentration\ of\ AgNO_3}{g\ dry\ membrane} = \frac{0.01\ \mathrm{x}\ Volume\ \ AgNO_3}{g\ dry\ membrane} \tag{1}$$

The IEC of the AEMs in OH^- form was calculated from the IEC_{Br} using eqn (2):

$$IEC_{OH-} = \frac{IEC_{Br-}}{1-\frac{IEC_{Br-}\,(M_{Br-}-M_{OH-})}{1000}} = \frac{IEC_{Br-}}{1-0.0629\ x\ IEC_{Br-}} \tag{2}$$

Water uptake (WU) and the hydration number (λ) of the membrane samples (in OH^- form) at room temperature were determined as discussed in the chapters 3 and 4. The reported water uptake and IEC titration of the membranes are an average of at least three measurements.

2.5.4. Membrane chloride and hydroxide ion conductivity

The $Cl^-$and OH^- conductivities of the membranes were measured by exchanging the bromide/chloride mixture form of the resulting membranes in a saturated NaCl (1 M) and KOH (1 M), respectively, at room temperature for 24 h followed by immersing in excess DI water overnight to remove the excess of salt and residual KOH. The ion conductivities of the membranes were measured via through-plane electrochemical impedance spectroscopy (EIS) and a Hewlett Packard Model response analyser (HP Model 4192A LF Impedance Analyzer) by two-point probe impedance method in the AC frequency range 5 Hz to 13 MHz at room temperature. To avoid carbonation process (exchange of OH^- in the membrane for CO_3^{2-} and HCO_3^- by CO_2), the resistance measurement of the membranes in OH^- form was performed in a home-made glovebox under continuous Ar flow. The membrane ionic conductivity (σ) was calculated using formula discussed in the previous chapters.

2.5.5. Differential scanning calorimetry experiments

Differential scanning calorimetry (DSC) measurements (Mettler-Toledo DSC1 instrument) were performed to quantify the freezable and non-freezable water molecules in the membranes (OH^- form). The procedures followed are discussed in chapter 3 (section 2.5.4). Accordingly, the freezable (N_{free}) and non-freezable (N_{non}) water molecules in the membranes were determined.

2.5.6. Thermal analysis

The membrane thermal stabilities were measured by using a thermogravimetric analysis Instruments TGA Q500 (Mettler-Toledo AG). The membranes were dried at room temperature under vacuum for at least 24 h. The membrane samples were preheated at 100 °C for 30 min in the TGA to remove traces of water. The measurement was performed under a nitrogen atmosphere from 25 to 600 °C at a heating rate of 10 K/min.

2.5.7. Alkaline stability

The alkaline stability of the AEMs was tested by monitoring the changes in their Cl^- ion conductivity before and after being immersed in alkali solution for controlled lengths of time. To simulate the practical Zn slurry-air battery application, the stability of the membranes at higher concentration of KOH (6 M) and alkaline Zn slurry-air electrolytes at room temperature for 14 days was studied. Additionally, the alkaline stability of the membranes at higher temperature (60 °C) was also studied. Membranes (in OH^- form) were immersed in N_2-degassed 1 KOH (aq.) solution in sealed polypropylene container at 60 °C oven for 14 days. The KOH solution was replaced with new solution every 48 h. The AEMs samples were taken out from the container and immersed in 1 M NaCl for 24 h at 60 °C and then DI water for 24 h prior to Cl^- conductivity.

2.5.8. Zincate ions crossover

The $Zn(OH)_4^{2-}$ ions concentration crossover through the prepared AEMs and their diffusion coefficient (D, $m^2\ s^{-1}$) were quantitatively determined using home-made two-chamber diffusion cell as mentioned in chapter 6 (section 2.4.8). Moreover, permselectivity (S cm s^{-1}) of the membranes, preference of the membrane for OH^- ions over $Zn(OH)_4^{2-}$ ions, is calculated from the ratio of membrane OH^- conductivity to $Zn(OH)_4^{2-}$ ions crossover.

2.5.9. Single Zn slurry-air cell assembly and electrochemical performance

2.5.9.1. Cell design: Air cathode and Zn slurry preparation

A single Zn slurry-air cell containing air cathode, membrane and Zn slurry with a serpentine flow field of CuNi plate was used [22]. To prepare the air cathode, catalyst coated electrode (CCE) method was used. To prepare the catalyst ink, Pt/C catalyst (40% Pt, Alfa Aesar, Germany) with Pt was mixed with Fumion FAA-3 ionomer (10 wt.%, Fumatech, Germany), deionized water and isopropanol. The Pt loading was 1 mg/cm^2, whereas the ionomer content of the catalyst layer was 23 wt.%. The prepared ink mixture was sonicated in an ultrasonic water bath for 15 min and sprayed onto a gas diffusion layer (5 cm^2) (SGL Carbon, 29BC, Germany). The catalyst-coated electrode was placed between the cathode bipolar plate and the membrane. The Zn slurry containing Zn (33.8 wt. %), ZnO (4 wt.%), Carbopol (0.7 wt. %) and aqueous KOH (61.5 wt. %) was prepared as reported in previous study [22]. The chemical mixture was stirred and mixed at 4000 rpm for 3 min.

2.5.9.2. Electrochemical performance

The electrochemical performance of the cell employing the different prepared membranes was studied by current-voltage characteristic curves, polarization curves (BaSyTec GSM Battery Test System (BaSyTec GmbH, Germany). To measure the ohmic resistance of the Zn slurry-air flow battery containing the different membranes, EIS measurement was done at 1.3 V by using a Zahner IM6 workstation. The flow rates of the Zn slurry in the negative electrode and synthetic air in the air cathode were 160 and 100 mL min^{-1}, respectively. Due to the fluctuation of the Zn slurry electrode, the voltage was recorded for 30 s and averaged at each current density.

3. Results and discussion

3.1. Polymers and cation preparation

The synthesis reaction protocol followed to prepare the polymer is summarized in scheme I. The bromination, ketone reduction and quaternization reaction products involved during the preparation of PPO-6CH$_2$-Q were confirmed using ^{1}H NMR. The bromination of PPO polymer with a six-carbon pendant chain spacer containing a ketone group in the benzylic position using 6-bromohexanoyl chloride in a Friedel–Crafts acylation was carried out based on a slight modification of the method discussed in the literature [21,23] The peak at around 3.0 ppm (denoted as peak i) corresponds to the protons bonded to the carbon adjacent to the ketone group. The bromination degree was determined from the proportion of the ^{1}H NMR integrals of characteristic peak of protons of –CH$_2$Br at 4.3 ppm and the remaining CH$_3$ groups from the PPO at 2.1 ppm (Figure 2a). The functionalization ratio was fixed at 33% bromo-alkylation of PPO structural unit. The bromination was followed by ketone reduction i.e. by the shifting of peak from i position from 3 ppm to 1.7 ppm and the appearance of new peak (k) at 2.8 ppm, and reduction of ketone (96-98%) was confirmed by the changes in ^{1}H NMR spectra at (Figure 2b). In the next step, the bromine alkyl was reacted with diallylmethylamine and the quaternized with methyldiallylammonium was obtained. As shown in the NMR of the PPO-6CH-Q (Figure 2c), where new peaks matching with the protons of diallylmethylammonium appeared.

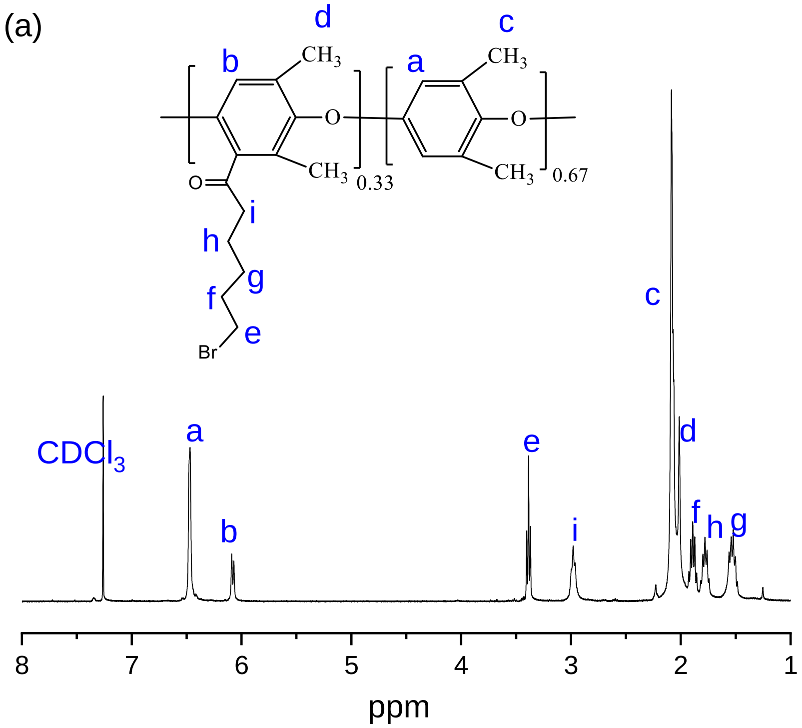
(a)
d
c
b
a
CH3
O
CH3
CH3
CH3
0.33
0.67
O
i
h
g
f
e
Br
CDCl3
a
b
e
i
c
d
f
h
g
8
7
6
5
4
3
2
1
ppm

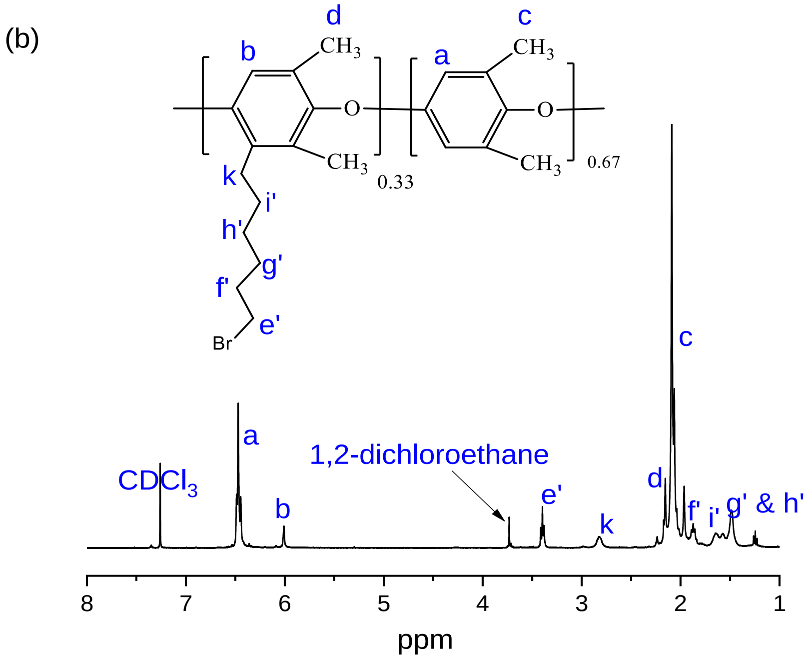
(b)
d
c
b
a
CH3
O
CH3
CH3
CH3
0.33
0.67
k
i'
h'
g'
f'
e'
Br
CDCl3
a
b
1,2-dichloroethane
e'
k
d
c
f'
i'
g' & h'
8
7
6
5
4
3
2
1
ppm

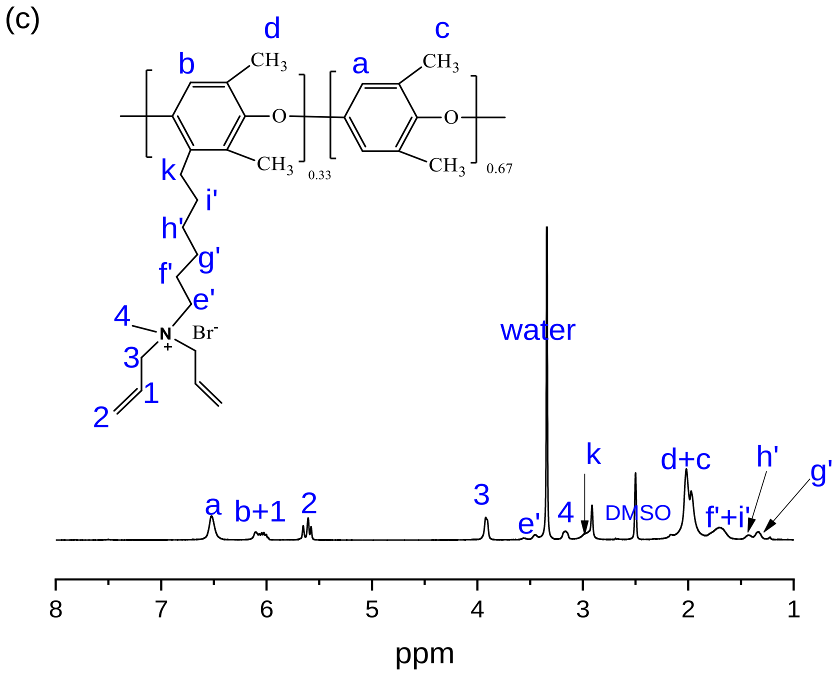

Figure 2: ^{1}H NMR spectra of (a) PPO-6CO-Br in $CDCl_3$, (b) PPO-6CH_2-Br in $CDCl_3$ and (c) PPO-6CH_2-Q in DMSO-d6.

The QA salt based on piperidine containing allyl groups, i.e., diallylpiperidinum chloride (DAPCl) was synthesized in two steps following a procedure reported in the literature [13,24]. The structure of prepared cationic monomer was confirmed by ^{1}H NMR (see chapter 3, section 3.1).

3.2. Membrane preparation, thickness and ion exchange capacity

The crosslinked AEMs with thickness between 45 and 65 µm were obtained by copolymerizing PPO-6CH_2-Q with DAPCl. The ratio between PPO quaternized ammonium side chain and DAPCl was varied between 0.5 to 3 in order to prepare membranes with theoretical IEC in the range of 2.3 to 3.6 mmol OH^-/g. Recently, the use of UV-curing method, in order to incorporate spirocylic QAs (dimethyl pyrrolinidium monomer) by copolymerization of monofunctional and difunctional monomers into an aliphatic crosslinked polymer backbone has been reported in the literature [25]. However, the cured solution-based membranes were coated on a Tetratex® porous PTFE membrane, probably due to the inability of the film to form self-standing membranes.

The prepared membranes were first characterized in terms of thickness and IEC (using Mohr titration method), the values are summarized in Table 1. The titrated IEC was found to vary between 2 and 3.4 mmol

OH^-/g, slightly lower than the theoretical one due to both incomplete polymerizations of DAPCl and the formation of poly(DAPCl) not-bonded to PPO-6CH_2-Q which were removed from the membrane during the water washing step. Based on the titrated IEC values, the practical amount of DAPCl incorporated into the PPO-6CH_2-Q was calculated (Table 1). The efficiency of degree/amount of monomer attached to the polymer backbone (DAPCl conversion %) was found to increase with increasing of DAPCl to polymer ratio due to, probably, the higher number of double bonds and/ or low viscosity of the solution.

Table 1. Chemical composition and membrane properties of the prepared AEMs.

Membrane	Thickness (µm)	IEC (mmol Br^-/g)		IEC (mmol OH^- g^{-1})*	DAPCl to PPO-6CH_2-Q molar ratio		DAPCl conversion**(%)
		Theoretical	Titration		Feed	Titration	
PPO-6CH_2-0.5x	45 ± 3	2.0	1.8 ± 0.04	2.03 ± 0.04	0.5	0.27	53
PPO-6CH_2-1x	49 ± 3	2.26	2.03 ± 0.05	2.33 ± 0.05	1	0.59	59
PPO-6CH_2-2x	55 ± 3	2.66	2.42 ± 0.03	2.85 ± 0.03	2	1.34	67
PPO-6CH_2-3x	60 ± 3	2.91	2.80 ± 0.02	3.4 ± 0.02	3	2.52	84

*Calculated from titration IEC_{Br-} using equation (2).

** DAPCl conversion (%) $= \frac{DAPCl\ to\ PPO-6CH_2-\mathrm{Q\ titration}}{DAPCl\ to\ PPO-6CH_2-\mathrm{Q\ feed}} x100$

3.3. Water uptake and ions conductivity

Sufficient water uptake in AEMs is necessary for the formation of percolating hydrated ionic domain for high ion mobility. However, the content of water uptake must be optimized to keep the mechanical strength and selectivity of the membranes. Table 2 shows the water uptake of the membranes (OH^- form) at room temperature. The water uptake of the PPO-6CH_2-0.5x reached 32 wt%. Under the same condition, PPO-6CH_2-1x and PPO-6CH_2-3x membranes took up 55 wt% and 105 wt%, respectively. The increase of IEC of the membranes induces a large water-uptake increase due to the increase of the ionic side chains, which enhances the hydrophilic character of the polymer and decreases the crosslinking stiffness i.e. the lengths of side chains between two bonded polymer chains are longer.

The OH^- ion conductivity of the AEM is an important factor in the power density performance of a battery. As the Zn slurry-air flow battery operates at room temperature, an AEM with high OH^- ion conductivity at room temperature is needed. Table 2 shows the IEC dependence of the OH^- ion conductivity in the prepared crosslinked AEMs. In addition, the chloride ion conductivity of the prepared membranes was also measured for comparison purpose. The OH^- ions conductivity of the membranes seems to be 2.7-4 times higher than that of their respective Cl^- ions conductivity mainly due to the molar conductivities of the ions (Cl^- = 7.631 and OH^- = 19.86 mS m^2 mol^{-1}), in agreement with findings reported in the literature [26].

Table 2: Water uptake and ion conductivity of prepared AEMs.

Membranes	IEC (mmol OH^- g^{-1})	Water uptake (%) *	Ion conductivity (mS cm^{-1}) **	
			Cl^-	OH^-
PPO-6CH_2-0.5x	2.03 ± 0.04	32 (± 0.7)	0.94 (±0.15)	3.3 (± 0.2)
PPO-6CH_2-1x	2.33 ± 0.05	55 (± 1.5)	1.9 (± 0.10)	5.2 (± 0.25)
PPO-6CH_2-2x	2.85 ± 0.03	80 (± 3)	3.1 (± 0.2)	13 (± 0.32)
PPO-6CH_2-3x	3.4 ± 0.02	105 (± 4)	6.6 (± 0.2)	19 (± 0.4)

*in OH^- form,

** Tested at 20 °C.

As shown in Table 2, the water uptake and ion conductivity varied significantly with the IEC of the membranes. Generally speaking, ion conductivity is dependent on the charge carrier concentration and their mobility. The increase in the IEC causes an increase in the amount of the charge carrier as well as their mobility. Indeed, the mobility of the charge carrier increases with an increase in water uptake. For instance, PPO-6CH_2-3x membrane exhibits a OH^- conductivity equal to 19 mS cm^{-1} at room temperature for fully hydrate membrane. This high value could be due to the formation of well-connected ion channels [14], which is favorable for ionic conduction, as shown in the AFM image of PPO-6CH_2-3x membrane (Figure 3). The ionic domains are shown in black regions and the non-ionic domains are the light ones. The microphase separation is caused by incompatibility between the hydrophilic cationic clusters and the hydrophobic chains.

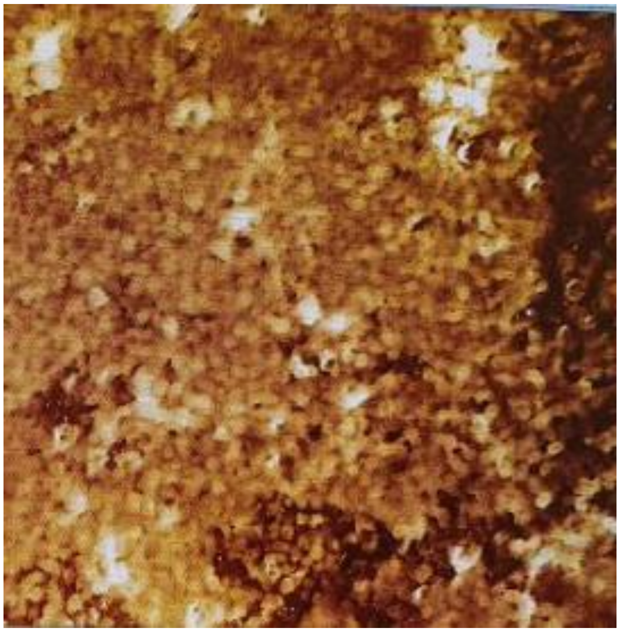

Figure 3: Tapping mode AFM phase images of PPO-6CH_2-3x membranes.

3.4. Hydration number and water states in the membrane

The hydration number (λ), the number of water molecules per functional group, of the membranes was calculated from the IEC and water uptake of the membranes using eq. (4). The λ of the membranes was found to increase with the IEC. As shown in Table 3, the λ of PPO-6CH$_2$-1x membranes have roughly three water molecules per functional group higher than that of PPO-6CH$_2$-0.5x membranes, averaging 7.8 and 11.6, respectively. Moreover, PPO-6CH$_2$-2x and PPO-6CH$_2$-3x exhibited much higher hydration number, with about 14 and 16.4, respectively. Similar values have been reported for other AEMs in the literature [14,27].

To identify whether the water molecules are in interaction with the ionic species or in water clusters, DSC measurements in the prepared AEMs were performed. As shown in Table 3, there is no freezable water detected in PPO-6CH$_2$-0.5x. Similarly, very small amount of freezable water was detected on PPO-6CH$_2$-1x membrane. It can be concluded that almost all the water absorbed in these two membranes are in strong interaction to the ionic functions [29]. Contrarily, the other two membranes showed a freezable water molecule of about 2 and 6 water molecules, indicating the presence of bulk water not associated with the ionic functions [30]. All in all, except for the PPO-6CH$_2$-0.5x membrane, regardless of the IEC and water uptake of the membranes, it seems about 10-11 water molecules/ionic function are in strong interaction with the polymer. Whereas, the excess water molecules are freely available in the membrane.

Table 3: Freezable and non-freezable water in the AEMs.

Membrane	λ_{OH-}	ΔH_f DSC (J g^{-1} wet sample) [a]	ΔH_f DSC (J g^{-1} water) [b]	Freezable water (%) [c]	λ in the membrane	
					Freezable	Non-freezable
PPO-6CH_2-0.5x	7.8 ± 0.3	0	0	0	0	7.8 ± 0.3
PPO-6CH_2-1x	11.6 ± 0.2	4.1 ± 0.7	11.6 ± 2	1.9 ± 0.33	0.22 ± 0.04	11.4 ± 0.1
PPO-6CH_2-2x	13.9 ± 0.5	31 ± 2.3	69.2 ± 5.1	16.6 ± 1.3	2.3 ± 0.16	11.6 ± 0.3
PPO-6CH_2-3x	16.4 ± 0.4	62 ± 3	121± 5.8	38.1 ± 1.8	6.23 ± 0.3	10.2 ± 0.4

a. Obtained from the DSC by integrating the DSC freezing curve area.

b. ΔH_f DSC ((J g^{-1} water) = (ΔH_f DSC, J g^{-1} wet membrane) x (sample weight, g)/ (water weight in the sample, g)

c. Freezable water (%) = $\Delta H_{f,\ DSC}/\Delta H_f$, pure water. Melting enthalpy of pure water is taken to be 334 J g^{-1}.

3.5. Thermal stability

The thermal stability of PPO-6CH_2-3x membranes was investigated with thermogravimetric analysis (TGA) under nitrogen atmosphere (Figure 4). The degradation of the membrane showed a two-step degradation behaviour. The first weight loss starting at about 300 °C belongs to the heterocyclic QA groups [31], which occurs at higher temperature than that of common QA groups [14]. The last degradation which occurred at above 400 °C is ascribed to the PPO polymer backbone, and remaining Poly(DAPCl). Similar two stages degradation of poly(DAPCl) has been reported elsewhere [31]. Therefore, the membranes are thermally stable enough for use in Zn slurry-air flow battery, which operates at room temperature.

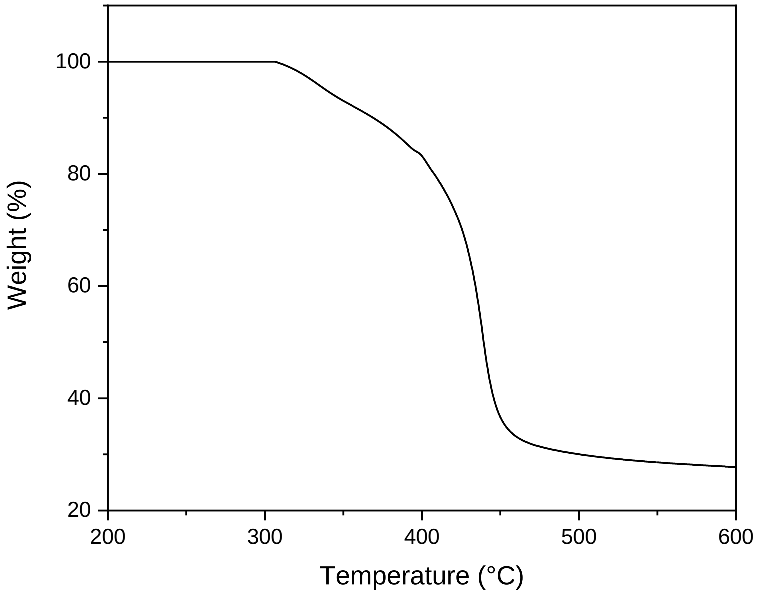

Figure 4: TGA curves of representative PPO-6CH_2-3x membranes.

3.6. Alkaline stability

The long-term alkaline stability of AEM in a highly alkaline solution is required for long-term use in Zn slurry-air flow battery. Membranes in hydroxide form were immersed in a degassed 1 M and 6 M of KOH (aq.) solution for 14 days at 60 °C and room temperature, respectively. PPO-6CH_2-3x (membrane with the highest IEC) was used as a sample to study the alkaline stability of the membranes since it is difficult to accurately determine the changes in IEC and/or ionic conductivity when membranes with low IEC are used, because of the quantification limits of the analytical techniques [23].

The Cl^- ion conductivity of the PPO-6CH_2-3x membrane remains the same before and after the membrane immersion in 6 M KOH (aq.) solution and alkaline Zn-slurry electrolyte solution at room temperature for 14 days. Moreover, the membranes retain above 92% of their chloride ion conductivity after being immersed in 1 M KOH at 60 ˚C for 14 days. Loss of ion conductivity of AEMs in alkaline media can be caused by the chemical degradation of the cation and/or polymer backbone [32]. However, it must be also noted that a minor decline in conductivity can also be caused by AEM morphology change instead of chemical degradation [33]. The mechanical flexibility and integrity of the membrane seem not to be affected after the alkaline stability tests. Chemically degraded membranes often are reported to become brittle and cracked into pieces [34].

The good alkaline stability of the membranes could be due to: (i) the constrained ring conformation of N-spirocyclic cation inducing high transition energies for Hofmann elimination and substitution degradations [10] (ii) microphase separation between the hydrophilic and hydrophobic domains which makes the hydrophobic domains less susceptible to chemical attack [35] and (iii) the crosslinking that can limit the mobility of OH^- into the hydrophilic domain [36]. Indeed, Jannasch et al. [24] prepared Poly(DAPCl) via radical-initiated cyclo-polymerization of *N*, *N*-diallylpiperidinium chloride (DAPCl) monomer and investigated its alkaline stability in 2 M KOD/D_2O solutions. The polyelectrolyte has been reported to exhibit an excellent alkaline stability, showing only minor signs of degradation at 120 °C after 14 days.

One thing worth noting is the challenge of comparing the stability of the membranes with the literature because there is no standardized testing procedure, such as immersion/testing duration, KOH concentration, temperature and methods of characterization [37]. However, a certain comparison of AEMs alkaline stability is summarized in Table 4. Indeed, both the 5-azoniaspiro[4.5]decane (ASD) and ASU-based AEMs exhibited robust alkaline stabilities in alkaline solutions at high temperature. However, most of these tests have been done for less than a month, thus long term stability of these membranes remains uncertain. In summary, compared to the most stable membranes reported in the literature, the prepared membranes showed relatively comparable and good alkaline stability for use in Zn slurry-air flow batteries, usually using (6 M aq. KOH) Zn-slurry electrolyte solution and operating at room temperature.

Table 4: Comparison of alkaline stability of synthesized AEMs with the N-spirocyclic-based AEMs in the literature.

Membrane	Cation	Test conditions: concentration, temperature and duration	Alkaline stability: retention in conductivity (σ) and/or IEC	Ref.
PSf–PDApip3	ASD	1 M KOH at 80 °C,120 h	94% (σ)	[13]
PBP-ASU-PPO	ASU	1 M NaOH at 80 °C, 2000 h	86.4% (σ)	[38]
Cr-ASU-PSF 1.92	ASU	1 M KOH at 80 ºC, 720 h	95.6% (σ)	[36]
PPO-SDSU-36	DSU	1 M aq NaOH at 80 °C, 360 h	67% (σ) and 63% (IEC)	[14]
PB-ASU	ASU	3 M NaOH at 80 °C, 2000 h	94.5% (σ)	[39]
PPO-ASU-40	ASU	10 M NaOH at 80 °C, 250 h	53.8% (σ)	[40]
ASU-PPO	ASU	1 M NaOH at 80 °C, 720 h	96.7% (σ)	[41]
[PAPi][OH]	ASU	1 M NaOH 80 °C, 168 h	98.4% (σ)	[42]
PES–NS–10%	Dense N-spirocyclic	2 M NaOH at 80 °C, 864 h	84.3% (σ) and 86.2% (IEC)	[43]
CP1	Dimethyl pyrrolinidium	1 M KOH at 80 °C, 720 h	60% (σ) and 55% (IEC)	[25]
PPO-7QPi-1.7	Quaternary piperidinium	1 M NaOH at 90 °C, 192 h	94% (σ)	[33]
PPO-6CH$_2$-3x	Poly(DAPCl)	1 M KOH at 60 °C, 336 h	92.4% (σ)	This study

3.7. Zincate ions crossover

To realize electrochemically rechargeable Zn slurry–air flow batteries, minimizing $Zn(OH)_4^{2-}$ ions crossover from the anode to the cathode is essential. To determine the good compromising between OH^- conductivity and selectivity in relation with ionic concentration and water uptake, the crossover of $Zn(OH)_4^{2-}$ ions through these membranes were measured and compared (Figure 5). As shown in Figure 5, the concentration of Zn ions in the right chamber increased with time for all the membranes. For e.g., for PPO-6CH$_2$-3x membrane, after one week, less than 5% of the Zn species crossed to the second compartment.

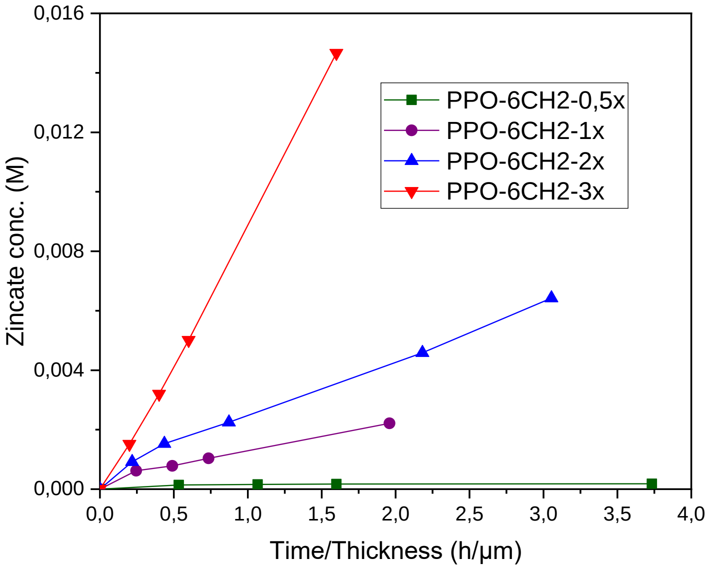

Figure 5: Plots of $Zn(OH)_4^{2-}$ ions crossover across the prepared membranes with time/thickness. Lines in the figure are guide for the eye.

Diffusion coefficients of $Zn(OH)_4^{2-}$ ions through the prepared membranes were determined and are summarized in Table 5. As can be seen in Table 5, the $Zn(OH)_4^{2-}$ diffusion coefficients of the prepared membranes relied on the IEC and water uptake of the membranes. In other words, the membranes with higher amount of freezable or bulky water exhibited a higher $Zn(OH)_4^{2-}$ ions crossover. A larger amount of water in the ionic domains is directly associated with larger size of ionic channels and, thus lower ionic selectivity. As a result, permselectivity, which shows the ratio of OH^- ions to $Zn(OH)_4^{2-}$ mobility, of the prepared membranes decreases with increase of IEC, so the selectivity decreases.

The PPO-6CH_2-0.5x membrane had lower diffusion coefficient of $Zn(OH)_4^{2-}$ (8.9×10^{-15} m^2 s^{-1}) than that of Nafion®521 (6.7×10^{-14} m^2 s^{-1}) [44] and PPO-TMA AEM (1.9×10^{-14} m^2 s^{-1}) [4]. As discussed in the previous chapter, the diffusion coefficients of $Zn(OH)_4^{2-}$ through the PPO-3.45 + 3501 and FAA + 3501 coated membranes were 5.2×10^{-13} and 3.3×10^{-14} m^2 s^{-1}, respectively. Generally speaking, the low diffusion coefficients of $Zn(OH)_4^{2-}$ ions across the prepared AEMs could be explained by the selectivity of ionic channels resulting from the nanophase separation between hydrophilic and hydrophobic blocks [4].

Table 5: Diffusion coefficient of $Zn(OH)_4^{2-}$ ions through the membranes.

Membrane	D of $Zn(OH)_4^{2-}$ (m^2 s^{-1})	Permselectivity (S.s m^{-3})
PPO-6CH_2-0.5x	8.9 x 10^{-15}	3.7 x 10^{13}
PPO-6CH_2-1x	2.8 x 10^{-13}	1.9 x 10^{12}
PPO-6CH_2-2x	9.7 x 10^{-13}	1.3 x 10^{12}
PPO-6CH_2-3x	2.3 x 10^{-12}	8.2 x 10^{11}

3.8. Single Zn slurry-air flow battery performance

High OH^- ion conductivity, alkaline stability and low $Zn(OH)_4^{2-}$ ions crossover make the prepared AEMs ideal for use in Zn slurry-air flow battery. In order to further evaluate the discharge performance properties of the prepared AEMs, Zn slurry-air flow single cells were run with the prepared AEMs. The cell resistances incorporating the different membranes were measured and are summarized in Figure 6. As expected, the IEC of the membranes, had a major impact on the cell resistance. For e.g., PPO-6CH_2-0.5x membrane–based cell exhibited the highest cell resistance (4.5 Ω cm^2) among the tested systems. Whereas, the battery using PPO-6CH_2-3x membrane displayed the lowest cell resistance (only 0.8 Ω cm^2). Similar IEC dependency and pattern was established in the OH^- ion conductivity of the membranes.

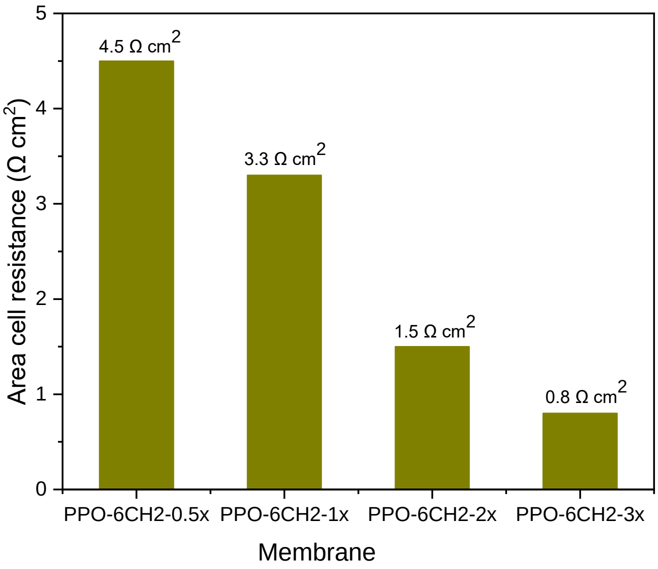

Figure 6: Cell resistance of the Zn slurry-air flow battery employing the prepared AEMs. The cell resistances were measured by EIS.

Polarization and power density curves are shown in Figure 7. All cells exhibited an OCV of about 1.4 V, showing good strength and compactness of the membranes to separate the Zn-slurry electrolyte from the air electrode [36]. As predicted, both the cell voltage and the power density of the battery were found to depend on the discharge current. The single cell voltage drop can be seen to be divided into three parts. The first component at low current density is assigned to electrochemical polarization, which is the key voltage drop in the Zn slurry-air flow battery. A large improvement was done on the electrode elaboration compared to the work presented in chapter 6, and as a result the electrochemical polarizations are notably lower than the ones obtained in chapter 6. The second part at medium current density is attributable to the ohmic polarization induced by cell resistance (mainly the AEM). However, the cell resistance determined from the current density-voltage curve was about 2-3 times higher than that of cell resistances obtained through EIS measurement. This indicates the presence of additional resistance under current which may be due to the kinetic or ion transport effects. The last part at high current density is generally due to the polarization associated with mass transport [45].

PPO-6CH_2-0.5x and 1x membranes delivered peak power densities of 35 mW cm^{-2} and 39 mW cm^{-2}, respectively. The high ohmic resistance of the membranes is really detrimental for the cell, as very high current density is used. The cell assembled with the most conductive membrane (PPO-6CH_2-3x) exhibited an excellent maximum power density (153 mW cm^{-2}) at about 200 mA cm^{-2}, which is higher than that of cell assembled with PPO-6CH_2-2x (137 mW cm^{-2}) membrane due to the higher OH^- ion conductivity. The peak power density obtained is much higher than that of the coated and porous commercial membranes (discussed in chapter 6), however, herein, the cell was further optimized, such as the use of ionomer inside the electrode, which permits to improve the electrochemical reaction kinetic. Moreover, the value obtained is, to the best of our knowledge, one of the highest values reported for Zn-air batteries. As summarized in Table 5 of chapter 5, various Zn-air batteries employing different AEMs, such as FAA®-3-based AEM (9.8 mW cm^{-2}) [46], AEM composed of poly(vinyl alcohol)/guar hydroxypropyltrimonium chloride (50 mW cm^{-2}) [47], QA-functionalized nanocellulose/graphene oxide AEM (44 mW cm^{-2}) [48], Tokuyama® A201-based (33 mW cm^{-2}) [48] has been reported to show much lower peak power densities. The cyclability of the developed system will be investigated in our ongoing work.

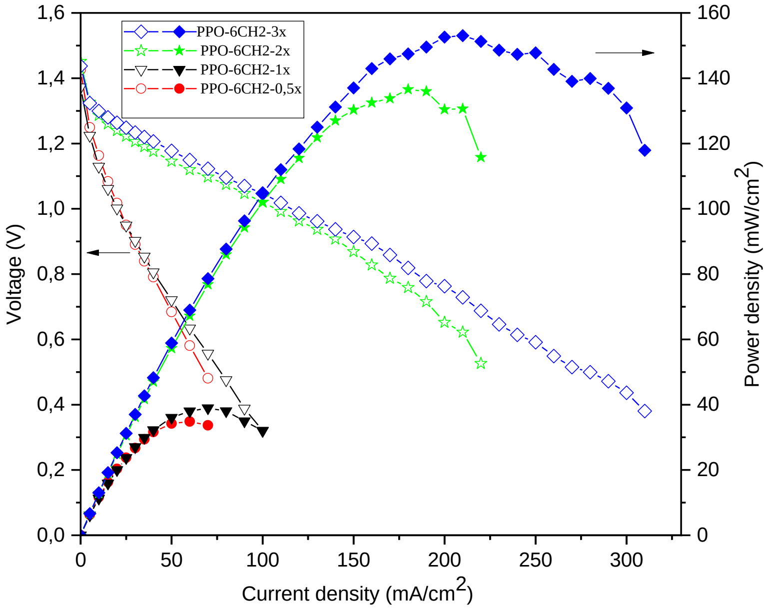

Figure 7: Power density and polarization curves of the Zn slurry-air battery with the AEMs measured at room temperature and flow rates of the Zn slurry and synthetic air 160 and 100 mL min^{-1}, respectively.

4. Conclusion

In summary, we have prepared a series of AEMs, in which the N-spirocyclic cation was grafted to the PPO backbone with 6 C spacer via UV-irradiation, by varying the ratio of DAPCl to PPO-6CH$_2$-Q. The ion conductivities, OH$^-$/ Zn(OH)$_4^{2-}$ ions selectivity of the membranes and battery performances were varied with the ratio between the polymer and monomer (IEC of the membranes). Well-defined hydrophobic-hydrophilic separation of the membranes resulted in an excellent hydroxide conductivity. The PPO-6CH$_2$-3x membrane showed 19 mS cm^{-1} at 20 °C in water. Furthermore, the membranes displayed an excellent alkaline stability in 1 M KOH at 60 °C, with a less than 8% drop in ion conductivity after alkaline stability testing for 360 h. A single Zn slurry-air flow battery testing using PPO-6CH$_2$-3x showed an OCV of 1.4 V and a maximum power density of 153 mW cm^{-2} at current density of 250 mA cm^{-2}. Therefore, given the low Zn(OH)$_4^{2-}$ ions crossovers and high peak power densities of the PPO-6CH$_2$-2x and PPO-6CH2-3x AEMs, they are promising candidates for rechargeable alkaline Zn slurry-air flow batteries.

References

[1] J. Fu, Z.P. Cano, M.G. Park, A. Yu, M. Fowler, Z. Chen, Electrically Rechargeable Zinc-Air Batteries: Progress, Challenges, and Perspectives, Adv. Mater. 29 (2017) 1604685. doi:10.1002/adma.201604685.

[2] Y. Li, H. Dai, Recent advances in zinc–air batteries, Chem. Soc. Rev. 43 (2014) 5257–5275. doi:10.1039/C4CS00015C.

[3] E.L. Dewi, K. Oyaizu, H. Nishide, E. Tsuchida, Cationic polysulfonium membrane as separator in zinc–air cell, J. Power Sources. 115 (2003) 149–152. doi:10.1016/S0378-7753(02)00650-X.

[4] A. Abbasi, S. Hosseini, A. Somwangthanaroj, A.A. Mohamad, S. Kheawhom, Poly(2,6-Dimethyl-1,4-Phenylene Oxide)-Based Hydroxide Exchange Separator Membranes for Zinc–Air Battery, Int. J. Mol. Sci. 20 (2019) 3678. doi:10.3390/ijms20153678.

[5] E.L. Dewi, K. Oyaizu, H. Nishide, E. Tsuchida, Cationic polysulfonium membrane as separator in zinc-air cell, J. Power Sources. 115 (2003) 149–152. doi:10.1016/S0378-7753(02)00650-X.

[6] J. Fu, J. Zhang, X. Song, H. Zarrin, X. Tian, J. Qiao, L. Rasen, K. Li, Z. Chen, A flexible solid-state electrolyte for wide-scale integration of rechargeable zinc-air batteries, Energy Environ. Sci. 9 (2016) 663–670. doi:10.1039/c5ee03404c.

[7] J. Zhang, J. Fu, X. Song, G. Jiang, H. Zarrin, P. Xu, K. Li, A. Yu, Z. Chen, Laminated Cross-Linked Nanocellulose/Graphene Oxide Electrolyte for Flexible Rechargeable Zinc-Air Batteries, Adv. Energy Mater. 6 (2016) 1600476. doi:10.1002/aenm.201600476.

[8] O. Kwon, H.J. Hwang, Y. Ji, O.S. Jeon, J.P. Kim, C. Lee, Y.G. Shul, Transparent Bendable Secondary Zinc-Air Batteries by Controlled Void Ionic Separators, Sci. Rep. 9 (2019) 1–9. doi:10.1038/s41598-019-38552-4.

[9] R. Soni, S.N. Bhange, S. Kurungot, A 3-D nanoribbon-like Pt-free oxygen reduction reaction electrocatalyst derived from waste leather for anion exchange membrane fuel cells and zinc-air batteries, Nanoscale. 11 (2019) 7893–7902. doi:10.1039/c9nr00977a.

[10] M.G. Marino, K.D. Kreuer, Alkaline Stability of Quaternary Ammonium Cations for Alkaline Fuel Cell Membranes and Ionic Liquids, ChemSusChem. 8 (2015) 513–523. doi:10.1002/cssc.201403022.

[11] J.S. Olsson, T.H. Pham, P. Jannasch, Poly(arylene piperidinium) Hydroxide Ion Exchange Membranes: Synthesis, Alkaline Stability, and Conductivity, Adv. Funct. Mater. 28 (2018) 1702758. doi:10.1002/adfm.201702758.

[12] T.H. Pham, J.S. Olsson, P. Jannasch, Poly(arylene alkylene)s with pendant N -spirocyclic quaternary ammonium cations for anion exchange membranes, J. Mater. Chem. A. 6 (2018) 16537–16547. doi:10.1039/C8TA04699A.

[13] D.J. Strasser, B.J. Graziano, D.M. Knauss, Base stable poly(diallylpiperidinium hydroxide) multiblock copolymers for anion exchange membranes, J. Mater. Chem. A. 5 (2017) 9627–9640. doi:10.1039/C7TA00905D.

[14] J. Xue, X. Liu, J. Zhang, Y. Yin, M.D. Guiver, Poly(phenylene oxide)s incorporating N-spirocyclic quaternary ammonium cation/cation strings for anion exchange membranes, J. Memb. Sci. 595 (2020) 117507. doi:10.1016/j.memsci.2019.117507.

[15] S.A. Nuñez, M.A. Hickner, Quantitative 1 H NMR Analysis of Chemical Stabilities in Anion-Exchange Membranes, ACS Macro Lett. 2 (2013) 49–52. doi:10.1021/mz300486h.

[16] N. Li, Y. Leng, M.A. Hickner, C.-Y. Wang, Highly Stable, Anion Conductive, Comb-Shaped Copolymers for Alkaline Fuel Cells, J. Am. Chem. Soc. 135 (2013) 10124–10133. doi:10.1021/ja403671u.

[17] H.-S. Dang, P. Jannasch, Exploring Different Cationic Alkyl Side Chain Designs for Enhanced Alkaline Stability and Hydroxide Ion Conductivity of Anion-Exchange Membranes, Macromolecules. 48 (2015) 5742–5751. doi:10.1021/acs.macromol.5b01302.

[18] J. Ran, L. Wu, Y. Ru, M. Hu, L. Din, T. Xu, Anion exchange membranes (AEMs) based on poly(2,6-dimethyl-1,4-phenylene oxide) (PPO) and its derivatives, Polym. Chem. 6 (2015) 5809–5826. doi:10.1039/C4PY01671H.

[19] C. Vogel, J. Meier-Haack, Preparation of ion-exchange materials and membranes, Desalination. 342 (2014) 156–174. doi:10.1016/j.desal.2013.12.039.

[20] T.H. Pham, P. Jannasch, Aromatic Polymers Incorporating Bis- N -spirocyclic Quaternary Ammonium Moieties for Anion-Exchange Membranes, ACS Macro Lett. 4 (2015) 1370–1375. doi:10.1021/acsmacrolett.5b00690.

[21] M.R. Hibbs, Alkaline stability of poly(phenylene)-based anion exchange membranes with various cations, J. Polym. Sci. Part B Polym. Phys. 51 (2013) 1736–1742. doi:10.1002/polb.23149.

[22] N.H. Choi, D. Del Olmo, P. Fischer, K. Pinkwart, J. Tübke, Development of flow fields for zinc slurry air flow batteries, Batteries. 6 (2020) 1–10. doi:10.3390/batteries6010015.

[23] J. Parrondo, M.J. Jung, Z. Wang, C.G. Arges, V. Ramani, Synthesis and Alkaline Stability of Solubilized Anion Exchange Membrane Binders Based on Poly(phenylene oxide) Functionalized with Quaternary Ammonium Groups via a Hexyl Spacer, J. Electrochem. Soc. 162 (2015) F1236–F1242. doi:10.1149/2.0891510jes.

[24] J.S. Olsson, T.H. Pham, P. Jannasch, Poly(N , N -diallylazacycloalkane)s for Anion-Exchange Membranes Functionalized with N -Spirocyclic Quaternary Ammonium Cations, Macromolecules. 50 (2017) 2784–2793. doi:10.1021/acs.macromol.7b00168.

[25] Z. Wang, J. Parrondo, S. Sankarasubramanian, K. Bhattacharyya, M. Ghosh, V. Ramani, Alkaline Stability of Pure Aliphatic-based Anion Exchange Membranes Containing Cycloaliphatic Quaternary Ammonium Cations, J. Electrochem. Soc. 167 (2020) 124504. doi:10.1149/1945-7111/abac29.

[26] J. Hou, Y. Liu, Q. Ge, Z. Yang, L. Wu, T. Xu, Recyclable cross-linked anion exchange membrane for alkaline fuel cell application, J. Power Sources. 375 (2018) 404–411. doi:10.1016/j.jpowsour.2017.06.073.

[27] E.A. Weiber, P. Jannasch, Ion Distribution in Quaternary-Ammonium-Functionalized Aromatic Polymers: Effects on the Ionic Clustering and Conductivity of Anion-Exchange Membranes, ChemSusChem. 7 (2014) 2621–2630. doi:10.1002/cssc.201402223.

[28] T. Zelovich, L. Vogt-Maranto, M.A. Hickner, S.J. Paddison, C. Bae, D.R. Dekel, M.E. Tuckerman, Hydroxide Ion Diffusion in Anion-Exchange Membranes at Low Hydration: Insights from Ab Initio Molecular Dynamics, Chem. Mater. 31 (2019) 5778–5787. doi:10.1021/acs.chemmater.9b01824.

[29] L. Liu, G. Huang, P.A. Kohl, Anion conducting multiblock copolymers with multiple head-groups, J. Mater. Chem. A. 6 (2018) 9000–9008. doi:10.1039/C8TA00753E.

[30] S.J. Lue, S.-J. Shieh, Water States in Perfluorosulfonic Acid Membranes Using Differential Scanning Calorimetry, J. Macromol. Sci. Part B. 48 (2009) 114–127. doi:10.1080/00222340802561649.

[31] J.S. Olsson, T.H. Pham, P. Jannasch, Poly(N,N-diallylazacycloalkane)s for Anion-Exchange Membranes Functionalized with N-Spirocyclic Quaternary Ammonium Cations, Macromolecules. 50 (2017) 2784–2793. doi:10.1021/acs.macromol.7b00168.

[32] X.Q. Wang, C.X. Lin, F.H. Liu, L. Li, Q. Yang, Q.G. Zhang, A.M. Zhu, Q.L. Liu, Alkali-stable partially fluorinated poly(arylene ether) anion exchange membranes with a claw-type head for fuel cells, J. Mater. Chem. A. 6 (2018) 12455–12465. doi:10.1039/C8TA03437K.

[33] H.-S. Dang, P. Jannasch, Alkali-stable and highly anion conducting poly(phenylene oxide)s carrying quaternary piperidinium cations, J. Mater. Chem. A. 4 (2016) 11924–11938. doi:10.1039/C6TA01905F.

[34] W. You, E. Padgett, S.N. MacMillan, D.A. Muller, G.W. Coates, Highly conductive and chemically stable alkaline anion exchange membranes via ROMP of trans -cyclooctene derivatives, Proc. Natl. Acad. Sci. 116 (2019) 9729–9734. doi:10.1073/pnas.1900988116.

[35] D.W. Shin, M.D. Guiver, Y.M. Lee, Hydrocarbon-Based Polymer Electrolyte Membranes: Importance of Morphology on Ion Transport and Membrane Stability, Chem. Rev. 117 (2017) 4759–4805. doi:10.1021/acs.chemrev.6b00586.

[36] Y. Zhang, W. Chen, X. Yan, F. Zhang, X. Wang, X. Wu, B. Pang, J. Wang, G. He, Ether spaced N-spirocyclic quaternary ammonium functionalized crosslinked polysulfone for high alkaline stable anion exchange membranes, J. Memb. Sci. 598 (2020) 117650. doi:10.1016/j.memsci.2019.117650.

[37] J. Müller, A. Zhegur, U. Krewer, J.R. Varcoe, D.R. Dekel, Practical ex-Situ Technique To Measure the Chemical Stability of Anion-Exchange Membranes under Conditions Simulating the Fuel Cell Environment, ACS Mater. Lett. 2 (2020) 168–173. doi:10.1021/acsmaterialslett.9b00418.

[38] N. Chen, C. Lu, Y. Li, C. Long, H. Zhu, Robust poly(aryl piperidinium)/N-spirocyclic poly(2,6-dimethyl-1,4-phenyl) for hydroxide-exchange membranes, J. Memb. Sci. 572 (2019) 246–254. doi:10.1016/j.memsci.2018.10.067.

[39] H. Zhu, Y. Li, N. Chen, C. Lu, C. Long, Z. Li, Q. Liu, Controllable physical-crosslinking poly(arylene 6-azaspiro[5.5] undecanium) for long-lifetime anion exchange membrane applications, J. Memb. Sci. 590 (2019) 117307. doi:10.1016/j.memsci.2019.117307.

[40] X. Chu, L. Liu, Y. Huang, M.D. Guiver, N. Li, Practical implementation of bis-six-membered N-cyclic quaternary ammonium cations in advanced anion exchange membranes for fuel cells: Synthesis and durability, J. Memb. Sci. 578 (2019) 239–250. doi:10.1016/j.memsci.2019.02.051.

[41] N. Chen, C. Long, Y. Li, C. Lu, H. Zhu, Ultrastable and High Ion-Conducting Polyelectrolyte Based on Six-Membered N-Spirocyclic Ammonium for Hydroxide Exchange Membrane Fuel Cell Applications, ACS Appl. Mater. Interfaces. 10 (2018) 15720–15732. doi:10.1021/acsami.8b02884.

[42] L. Gu, H. Dong, Z. Sun, Y. Li, F. Yan, Spirocyclic quaternary ammonium cations for alkaline anion exchange membrane applications: an experimental and theoretical study, RSC Adv. 6 (2016) 94387–94398. doi:10.1039/C6RA22313C.

[43] F.H. Liu, Q. Yang, X.L. Gao, H.Y. Wu, Q.G. Zhang, A.M. Zhu, Q.L. Liu, Anion exchange membranes with dense N-spirocyclic cations as side-chain, J. Memb. Sci. 595 (2020) 117560. doi:10.1016/j.memsci.2019.117560.

[44] H.-W. Kim, J.-M. Lim, H.-J. Lee, S.-W. Eom, Y.T. Hong, S.-Y. Lee, Artificially engineered, bicontinuous anion-conducting/-repelling polymeric phases as a selective ion transport channel for rechargeable zinc–air battery separator membranes, J. Mater. Chem. A. 4 (2016) 3711–3720. doi:10.1039/C5TA09576J.

[45] Z.F. Pan, L. An, T.S. Zhao, Z.K. Tang, Advances and challenges in alkaline anion exchange membrane fuel cells, Prog. Energy Combust. Sci. 66 (2018) 141–175. doi:10.1016/j.pecs.2018.01.001.

[46] O. Kwon, H.J. Hwang, Y. Ji, O.S. Jeon, J.P. Kim, C. Lee, Y.G. Shul, Transparent Bendable Secondary Zinc-Air Batteries by Controlled Void Ionic Separators, Sci. Rep. 9 (2019) 3175. doi:10.1038/s41598-019-38552-4.

[47] M. Wang, N. Xu, J. Fu, Y. Liu, J. Qiao, High-performance binary cross-linked alkaline anion polymer electrolyte membranes for all-solid-state supercapacitors and flexible rechargeable zinc–air batteries, J. Mater. Chem. A. 7 (2019) 11257–11264. doi:10.1039/C9TA02314C.

[48] J. Zhang, J. Fu, X. Song, G. Jiang, H. Zarrin, P. Xu, K. Li, A. Yu, Z. Chen, Laminated Cross-Linked Nanocellulose/Graphene Oxide Electrolyte for Flexible Rechargeable Zinc-Air Batteries, Adv. Energy Mater. 6 (2016) 1600476. doi:10.1002/aenm.201600476.

Chapter 8: Conclusions and future perspective

The replacement of fossil fuels with renewable energy sources is a hot research topic of the energy sector for the past some years. The main challenge of these energy sources is their intermittent energy generation, which results in a mismatch between energy supply and demand. To balance the fluctuating power output of the renewable energy sources, scalable and safe electrical energy storage is required. Among the various electrochemical energy storage systems, RFBs have promising potentials because of their scalability and decoupled energy and power output. To widely commercialize those batteries, there is a need for more research and development on their components, including the membrane.

In this work, the design, synthesis, characterization and testing of membranes in TMA-TEMPO/MV-based aqueous organic redox and Zn slurry-air flow batteries were performed. The relationships between various membrane properties and cell performances were investigated. Various types of AEMs were prepared using PPO as the backbone and the impact of their structure and properties, such as IEC, presence/absence of spacer, membrane thickness, degree of crosslinking and cation type i.e. TMA, DABCO and poly(DAPCl) were ex-situ characterized and tested in the batteries. In addition to the prepared (composite and anion exchange) membranes, several commercial porous membranes and an AEM were ex-situ characterized and tested in the Zn slurry-air flow battery.

Six commercial porous membranes were characterized in terms of electrolyte uptake, zincate ions crossover and tested in Zn slurry-air flow batteries. The electrolyte uptakes of the membranes were found to depend on various membrane parameters including the material type, composition, structure (dense or porous nature), porosity, pore size, morphology or the wettability of the polymer matrices. The order of peak power density of the cell employing the membranes was found in agreement with their respective cell resistances, the cells employing Celgard® 3501 ($2\ \Omega\ cm^2$) and PBI® ($5.5\ \Omega\ cm^2$) displayed the highest ($90\ mW\ cm^{-2}$) and lowest ($32\ mW\ cm^{-2}$) peak power densities, respectively. On the other hand, all the investigated commercial porous membranes, except PBI, exhibited high zincate ions crossover (for example, the Zirfon® and Celgard® 3501 showed 6.6×10^{-11} and $9.2 \times 10^{-12}\ m^2\ s^{-1}$ zincate ions diffusion coefficients, respectively) in agreement with their ion conductivities and porous/dense structure of the membranes. This shows the need for preparing a porous membrane with lower than $2\ \Omega\ cm^2$ cell resistance and much lower zincate ions crossover.

To reduce the crossover of $Zn(OH)_4^{2-}$ ions through the porous membranes, Celgard® 3501 was modified using two different ion-selective polymers. Due to the similar low viscosities of the ionomers used, both modifications resulted in a large impregnation of the pore structure by the two ionomers. The properties of the ionomers (such as IEC and water uptake) had a major impact on the zincate ions crossover and discharge capacity performance of the membranes. Compared to the pristine Celgard® 3501, the PPO 3.45+ 3501 membrane showed 18 times lower crossover of $Zn(OH)_4^{2-}$ ions ($5.2 \times 10^{-13}\ m^2\ s^{-1}$). The modified membrane-employing battery delivered a high maximum power density $66\ mW\ cm^{-2}$, lower than that of Celgard® 3501-based cell due to the increase in the cell resistance from 2 to 2.6 Ω cm^2 associated with the partial filling of the pores with ionomers. The performance of the coated membranes in the TMA-TEMPO/MV-based AORFB is under investigation and will be discussed in our future publication. All in all, this is a proof of concept that shows coating/impregnation of ionomer is an efficient strategy to reduce ions crossover without significantly impacting the battery performance. Further optimization of the coat thickness (by varying the viscosity of the solution) could be performed to optimize the membrane resistance, degree of crossover and minimize the negative impact on the battery performance.

In addition to the porous and modified porous membranes, AEMs were prepared, ex-situ characterized and tested in the aqueous organic redox and Zn slurry-air flow batteries. To solve the challenge associated with the incorporation of N-spirocyclic quaternary ammonium (DAPCl), which exhibits higher chemical and thermal stabilities than that of commonly used quaternary ammoniums, into the modified PPO polymer backbone, a rapid UV irradiation method was employed. Indeed, the poly(DAPCl) employing AEMs were found to be chemically stable in both TMA-TEMPO/MV aqueous organic and Zn slurry- air flow batteries. The IECs of the membranes were modified by varying the monomer to polymer ratio and was found to affect the ion conductivity, water uptake, ions crossover and cell performance. The TMA and poly(DAPCl) cations were attached to the PPO backbone either at the benzylic position or via a 6-C spacer unit. The presence of a 6-C side-chain spacer allowed the membranes to exhibit about two times higher ion conductivity at room temperature than that of the membranes without a spacer. The former membranes had slightly higher water uptake due to the possible formation of well-clustered ionic channels.

The spacer involving AEMs (such as M4 and M7) with IEC of 1.65-1.8 mmol Cl^- g^{-1} and about 60 µm thickness permitted to obtain cell resistances of about 1.5 Ω cm^2 in the TMA-TEMPO/MV-based AORFB, whereas the membranes without spacer exhibited higher cell resistance (2-2.6 Ω cm^2) regardless of the cation type. On the other hand, the PPO-6CH_2-2x AEM with IEC of 2.8 mmol OH^- g^{-1} displayed cell resistance of about 1.5 Ω cm^2 in the Zn slurry-air flow battery. As a result, the membranes with the spacer displayed an excellent battery performance. Among them, the AORFB employing M4, which exhibits 4.3 mS cm^{-1} Cl^- ion conductivity, displayed a much higher peak power density (388 mW cm^{-2}) than a well-performing commercial membrane (FAA-3-50®) (244 mW cm^{-2})-based cell at a flow rate of 16 mL min^{-1}. Whereas, the membranes without a spacer, M1.7 (2 Ω cm^2) and M8 (2.6 Ω cm^2) achieved lower maximum power densities of 258 and 183 mW cm^{-2}, respectively.

On the other hand, the Zn slurry-air flow battery employing PPO-6CH_2-3x membrane (6.6 mS cm^{-1} Cl^- and 19 mS cm^{-1} OH^- ion conductivities) reached a maximum peak power density of 153 mW cm^{-2}, much higher than the cells employing porous commercial or modified porous membranes.

Generally speaking, membranes with no or little amount of free water exhibited no or very small active species or $Zn(OH)_4^{2-}$ crossover. For instance, M7 displayed no TMA-TEMPO/MV crossover and thus excellent capacity retention after 100 consecutive charging/discharging cycles. However, it must be noted that the available capacity after 100 cycles was found to depend not only on the degree of cross-contamination but also on the current density used. In the current work, only cyclic voltammetry measurement of the TMA-TEMPO/MV active species before and after cycling was compared to estimate the degree of redox-species cross-contamination. Therefore, additional permeation experiments through the membranes to understand the mass transport mechanism of the active species is an interesting topic that requires further investigation. Similarly, the degree of $Zn(OH)_4^{2-}$ ions crossover through the tested AEMs was found to depend on the amount of freezable or bulky water in the membranes, which is associated with the size of ionic channels. Accordingly, the membranes with no (PPO-6CH_2-0.5x) and very small amount (PPO-6CH_2-1x) of freezable water had the lowest diffusion coefficient of $Zn(OH)_4^{2-}$ ions, 8.9×10^{-15} and 2.8×10^{-13} m^2 s^{-1}, respectively. Whereas, the membranes with higher amount of free water molecules exhibited higher $Zn(OH)_4^{2-}$ ions crossover. The PPO-6CH_2-2x (2.3 freezable water molecules) and PPO-6CH_2-3x membranes (6.2 freezable water molecules) showed $Zn(OH)_4^{2-}$ ions diffusion coefficients of 9.7×10^{-13} and 2.3×10^{-12} m^2 s^{-1}, respectively. Such membranes' long-term durability and impact on the lifespan of the battery should be checked by testing them in a rechargeable Zn slurry-air flow battery.

The energy efficiency of the AORFB was enhanced by decreasing the membrane resistance. Due to their moderate membrane resistance and low crossover of redox-active species, both M7 and M4 membranes permitted to obtain high energy efficiency of 80% at 80 mA cm^{-2}, which is the highest value obtained for neutral AORFBs to the best of our knowledge. Our results show an excellent membrane candidate to improve the cell performance of AORFBs. More importantly, the results obtained in this thesis work provide useful insights for preparing suitable membranes to improve the efficiency and the power capability of neutral aqueous organic redox and Zn-air flow batteries.

Last but not least, the optimized and state-of-the-art TMA-TEMPO/MV-based neutral AORFB (which uses Cl^- ion as charge carrier ion) employing optimized membrane reached a higher peak power density than the not well-optimized Zn slurry-air flow batteries (which uses OH^- ion as charge carrier ion). This confirms the fact that the charge-carrier (OH^- and Cl^-) molar conductivities and membrane property are not the only parameters that determine the polarization curves. Optimization of other parameters including, electrode, electrolyte composition, flow field design, flow rate and temperature, which is all beyond the scope of this work, are needed for further improving the Zn slurry-air flow battery's power capability.